

Understanding the Dynamics of a Mixed Sand and Gravel Coastline: A Multi-Method Approach



This thesis has been submitted in partial fulfilment of the requirements for
the degree of
Doctor of Philosophy

John Atkinson

Faculty of Science and Technology

Bournemouth University

November 2019

[Blank Page]

This copy of the thesis has been supplied on condition that anyone who consults it is understood to recognise that its copyright rests with its author and due acknowledgement must always be made of the use of any material contained in, or derived from, this thesis.

Abstract

A multi-method approach was developed to characterise the behaviour of a mixed sand and gravel (MSG) coast at Thorpeness, Suffolk, UK (52.1823°N, 1.6130°E). The field site is highly complex due to interactions of the underlying geology, bimodal sediment size distribution and great alongshore variability in the physical settings even within relatively short distances (~300 m) and has been historically impacted by short-term, focused erosion events occurring over 100-200 m of the beach frontage. The research employed a range of observational and numerical modelling techniques to understand the beach and coastal processes at the site. Analysis undertaken in this study provided insights of differing shoreline response to the same offshore drivers. Results show a combination of variable geomorphology, a bi-modal wave climate and active nearshore processes causes large differences in shoreline behaviour along short (less than 300 m) lengths of the beach frontage. Novel sediment analysis has highlighted the need to assess the vertical and surficial proportion of sand and gravel to gain better understanding of the spatial variability in mixed beach behaviour. Use of X-band radar data demonstrated that periods of prolonged northerly or southerly waves resulted in two differing offshore bathymetric configurations, these act to modify the incident wave climate and the local beach behaviour. The analysis output informed a 10-year wave hindcast model used to simulate longshore sediment transport (LST) for these two bathymetric states. The model identified a persistent long-term convergence of LST at the Ness irrespective of wave and nearshore conditions, which supports the hypothesis that sediment is recycled offshore to form a bar-like feature in moderate southerly conditions and is eroded during storms. The outputs of these analyses informed coastal management decisions, specifically that in the short-term the most sustainable and least detrimental option to reduce the impact of erosion is small-scale beach recharge using the Ness as a source of material.

Table of Contents

List of Tables	9
List of Figures	10
Acknowledgements.....	18
Author’s Declaration.....	19
Abbreviations and Nomenclature.....	20
1. Introduction.....	23
1.1 The Study Area	24
1.1.1 Geology and bathymetry.....	26
1.1.2 Metocean conditions	27
1.1.3 The effect of storms	28
1.1.4 Engineering works	29
1.2 Difficulties with MSG Beaches	30
1.3 Aim and Objectives.....	31
1.4 Thesis Structure	32
2. Mixed Sand and Gravel Beach Dynamics: Review	33
2.1 MSG Beach Surveying and Sediment Characterisation Methods.....	33
2.1.1 Sediment characterisation methods.....	33
2.1.2 Sediment movement.....	37
2.2 MSG Beach Classification	38
2.3 Morphological Features and Models of Behaviour.....	40
2.4 Hydrodynamic Characteristics.....	42
2.4.1 Porosity and hydraulic conductivity.....	42
2.4.2 Infiltration and ground water	47
2.4.3 Wave reflection.....	47
2.4.4 Transport modes and threshold of motion	47
2.4.5 Second order characteristics.....	48
2.5 Summary	49
3. The Beach Morphology and Response	50
3.1 Introduction.....	50
3.2 Methods.....	52

3.2.1	Beach topography	52
3.2.2	Wave conditions	56
3.2.3	Water level analysis.....	59
3.2.4	Statistical analysis.....	59
3.3	Results	59
3.3.1	Characterisation of metocean conditions.....	59
3.3.2	Relationships between indicators of beach change.....	65
3.3.3	Alongshore variability	65
3.3.4	Temporal changes in beach morphology	70
3.3.5	The influence of wave conditions.....	74
3.4	Discussion.....	78
4.	Sediment Distribution and Beach Change.....	80
4.1	Introduction	80
4.2	Methods	81
4.2.1	Particle size analysis.....	83
4.2.2	Proportion of sand and gravel at surface	84
4.2.3	Proportion of sand and gravel at depth.....	84
4.2.4	Statistical analysis.....	85
4.3	Results	86
4.3.1	Sediment characterisation.....	86
4.3.2	PSD relationships	88
4.3.3	Spatial and temporal variance – sand and gravel.....	92
4.3.4	Changes in the proportion of sand across and between the profiles.....	94
4.3.5	Influence of proportion of sand on beach state and mobility	95
4.3.6	Wave climate effects	98
4.4	Discussion.....	99
5.	Quantifying Nearshore Dynamics Using X-Band Radar Data	101
5.1	Introduction	101
5.2	Methods	103
5.2.1	Radar Fundamentals	103
5.2.2	Calibration of water levels.....	107
5.2.3	Calibration of wave heights	107
5.2.4	Radar-derived bathymetry	108
5.2.5	Changes in nearshore bathymetry.....	112

5.2.6	Assessing linkages between nearshore and shoreline changes and wave conditions.....	113
5.3	Results.....	114
5.3.1	Multibeam data analysis at radar resolution.....	114
5.3.2	Radar-derived nearshore volume changes	115
5.3.3	Nearshore and shoreline change analysis.....	117
5.4	Discussion.....	122
5.4.1	Nearshore dynamics and shoreline behaviour.....	122
5.4.2	Utility of Radar	123
6.	Numerical Modelling of Coastal and MSG Beach Dynamics	125
6.1	Introduction.....	125
6.2	Methods.....	126
6.2.1	Model setup and resolution	128
6.2.2	MIKE21 FMHD: Hydrodynamics	130
6.2.3	MIKE21 FMSW: Waves.....	131
6.2.4	MIKE21 FMST: Sand transport.....	131
6.2.5	Effects of bathymetric change on shoreline wave energy.....	131
6.2.6	Effects of wave direction on nearshore changes	133
6.2.7	Effects on longshore sediment transport (LST)	133
6.3	Results.....	135
6.3.1	Effects of bathymetric change on shoreline wave energy.....	135
6.3.2	Effects of wave direction on nearshore changes	137
6.3.3	Effects on longshore sediment transport (LST)	140
6.4	Discussion.....	145
7.	Discussion of Key Findings and Conclusions.....	147
7.1	Temporal and spatial variability of MSG beach morphology in relation to wave climate.....	148
7.2	The effect of the proportion of sand in mixed beach mobility.....	148
7.3	Utility of X-band radar.....	149
7.4	Nearshore variability, shoreline change and impact of a bimodal wave climate	150
7.5	Informing coastal management decisions	151
7.6	Further Research	152
7.7	Conclusions.....	152

References 156

Appendix A – Volume change error evaluation 172

Appendix B – Supplementary sediment analysis tables and figures 175

Appendix C – MIKE model supplementary information 177

 C1 – HD validation..... 177

 C2 – SW model boundary Conditions 180

 C3 – SW Validation..... 182

Appendix D – Published Materials..... 184

List of Tables

Table 1.1. Major engineering works at site until winter 2013.....	29
Table 3.1. Coordinates of starting point and azimuth of the five beach transects analysed here and their equivalent EA reference.	54
Table 3.2. Dates of topographic surveys included analysed in this chapter.	55
Table 3.3. Yearly and annual significant wave height statistics for data obtained from the West Gabbard 1 and 2 buoys, including (with some proportion of records from dominant directional dominant years highlighted).	61
Table 3.4. Yearly and annual persistence statistics for data obtained from the West Gabbard 2 buoy, between December 2006 and February 2018.....	64
Table 3.5. Statistic summary of highest annual and winter (months DJF) total water levels and surge values (elevations in ODN) from 2006 to 2017 at Lowestoft.....	64
Table 3.6. Descriptive statistics summarising changes in beach width and area (and respective dates where relevant) based on Dataset 1 for Transects A to E.	68
Table 4.1. Descriptive terms for PSD statistics used throughout the chapter (Folk and Ward 1957).84	
Table 4.2. Sediment samples used to define % sand in proportion analysis.	85
Table 4.3. Gravel and sand PSD descriptive statistics for all samples during site surveys.....	87
Table 4.4. Results of Spearman correlation tests (two-tailed) between estimates of proportion of sand at surface and at depth, beach width and cross-section area considering data from all transects for all beach levels, only for the area above MHWS and for the area between MLWS and MHWS (intertidal).	96
Table 5.1. Best matching dates between beach surveys and radar-derived bathymetry.....	113
Table 5.2. Defined periods of analysis for bathymetry, each survey and wave climate.	114
Table 5.3. Nearshore volume changes over periods of approximately 6 months.....	117
Table 5.4. Periods of focused shoreline-radar analysis and calculated volume changes between records.....	119
Table 6.1. Maximum cell area, and indicative side length (based on an equilateral triangle) used in the model gridding.	128
Table 6.2. Names, locations and temporal coverage of validation and boundary condition data sources for the SW and HD models.....	130
Table 6.3. Eastern boundary conditions for persistent northerly and southerly wave event assessment.....	133
Table 6.4. EA profiles used for the LST model. With sub cell references, longshore starting position and profile azimuth ranges indicated.....	134
Table A.1. Mean average potential error range and percentage of profile area this equates to.....	172
Table A.2. Mean average potential error range and percentage of profile area this equates to.....	174

Table B.1. Descriptive statistics of % of sand through surface and depth analysis at each Transect for all available surveys.	175
Table B.2. Gravel PSD statistics for samples above and MHWS.....	176
Table B.3. Sand PSD statistics for samples above and below MHWS.....	176

List of Figures

Figure 1.1. Thorpeness field site position and local marine map (Digimap 2004).....	25
Figure 1.2. Thorpeness village looking north towards the Ness, where the erosional hot-spot can be seen along a short stretch of the frontage (July 2010, © Mike Page).....	26
Figure 1.3. North of Thorpeness village map showing the location and extent of the coastal defences (A, Digimap 2017), including the 1970s gabions and the geobags (B and C, Photos courtesy of Suffolk Coastal District Council).	30
Figure 2.1. Variability of sediment along one beach profile in front of the cliff line north of Thorpeness. (A) Cross-shore bands of gravel in the intertidal area perpendicular to the waterline, (B) cusped formations and longshore bands of gravel parallel to the waterline above MWL, (C) gravel at the cliff toe and (D) mixed sand and gravel within the intertidal zone.....	36
Figure 2.2. She et al (2007) results of porosity experimentation of gravel with a D_{50} of 4 mm and addition of fine, medium and coarse sand against analytical prediction © Crown copyright (Defra);(2008).	46
Figure 2.3. She et al (2007) results of hydraulic conductivity experimentation of gravel with a D_{50} of 4 mm and addition of fine, medium and coarse sand against analytical prediction. R&D Technical Report FD1923/TR © Crown copyright (Defra);(2008).	46
Figure 3.1. Study area showing location of the five beach transects between Thorpeness village (south) and Sizewell nuclear power station (north) in Suffolk (East Anglia, United Kingdom), and offshore bathymetry measured in January 2017.	51
Figure 3.2. (a to e) Beach morphology along transects A to E (respectively) and (f) their approximate location within the study area shown on an oblique aerial photograph taken after an intense erosion event in 2010 (Photos a to e by L.S. Esteves; f by www.mike-page.co.uk).	53
Figure 3.3. a) Georeferenced laser scan point cloud showing the northern end of the geobags and radar site (03-Aug-2016) note the shadowing (dark areas) caused by complex geomorphology. b) Laser scanner equipment and DGPS system used for geo referencing of the point cloud at the cliffs north of Thorpeness.....	54
Figure 3.4. Example autocorrelation function correlogram from a 500-point time series over 150-time steps (lag) with the P_{ACFA} definition from k_1 to k_0 (in this case $k_0 = 35$).	57

Figure 3.5. Example of an ACF (blue) on 06-Oct-2017 0600 which equates to a to high P_{ACFA} value (98.82) but is observed to drop rapidly within 2 days and where much of the ACF curve before this is below the mean from the dataset (2007-2018). 58

Figure 3.6. Time series of (a) peak wave direction (Dir_P) and (b) significant wave height (H_s) from which the ACF was calculated in Figure 3.5. 59

Figure 3.7. West Gabbard buoy wave roses showing Dir_P and H_s (168685 records, 97.98 % data coverage) for the period Jun-2006- Mar-2018 for all waves (a) and waves exceeding 2.5 m H_s (b). 60

Figure 3.8. Area plot of percentage North-South waves over 30 days (green and grey, left y-axis) with calculated persistence in the v-component (P_{ACIV} North-South, right y-axis) and y-component (P_{ACIU} East-West) between August 2015 (the start of the radar deployment) and March 2018 (the end of the beach surveying)..... 61

Figure 3.9. Time series analysis of an (a) Dir_P and (b) H_s and persistence values (c) P_{ACIU} and (d) P_{ACIV} during a high P_{ACVI} period between 10-Oct-2015 and 25-Oct-2015. Note the steady north-east wave direction but also the range the wave heights exceeding 1 m between 13-Oct-2015 and 18-Oct-2015..... 62

Figure 3.10. Time series analysis of an (a) Dir_P and (b) H_s and persistence values (c) P_{ACIU} and (d) P_{ACIV} during a steady P_{ACIV} period between 20-Dec-2015 and 05-Jan-2016. Note the variable southerly wave direction and large range wave sizes, which lower the persistence values..... 63

Figure 3.11. Cross-shore profiles measured along Transects A–E (respectively) between January 2009 and February 2018 are shown to give an indication of the profile envelope and range of variations. Biannual measurements by the Environment Agency (EA) are shown in grey (the earliest one as a black dashed line for reference), and Dataset 2 measurements are shown in colour. Note that the areas shaded in grey were excluded from the calculations of profile area presented elsewhere in this paper. Animations of the profile evolution are available as supplementary material from Atkinson and Esteves (2018). 67

Figure 3.12. Relative change in profile area above MLWS for Transects A–E for the period between 7-Jan-2009, and 27-Mar-2018 (including Dataset 1 and Dataset 2), calculated as a proportion of the respective initial area (shown in the legend). Grey boxes indicate beach nourishment and reprofiling in the area of Transect D, with gravel taken from the area of Transect B 69

Figure 3.13. Extent of laser scan survey of the village frontage with Transects C, D and E (dashed black line) on (a) 01-Aug-2016 and (b) 27-Sep-2017 (c) calculated change between surveys with MHWS position in black (buildings are indicated behind the beach and radar position by red point)..... 72

Figure 3.14. Extent of laser scan survey of the village frontage with Transects C, D and E (dashed black line) on (a) 06-Dec-2016 and (b) 18-Jan-2017 (c) calculated change between surveys with MHWS position in black (buildings are indicated behind the beach and radar position by red point)..... 72

Figure 3.15. Extent of laser scan survey of the village frontage with Transects C, D and E (dashed black line) on (a) 21-Mar-2017 and (b) 27-Jun-2017 (c) calculated change between surveys with MHWS position in black (buildings are indicated behind the beach and radar position by red point).	73
Figure 3.16. Extent of laser scan survey of the village frontage with Transects C, D and E (dashed black line) on (a) 27-Jun-2017 and (b) 27-Sep-2017 (c) calculated change between surveys with MHWS position in black (buildings are indicated behind the beach and radar position by red point).	73
Figure 3.17. Extent of laser scan survey of the village frontage with Transects C, D and E (dashed black line) on (a) 27-Sep-2017 and (b) 24-Jan-2018 (c) calculated change between surveys with MHWS position in black (buildings are indicated behind the beach and radar position by red point).	74
Figure 3.18. Percentage of time offshore waves recorded at West Gabbard approached from northerly (Dirp: 300–60°) and southerly (Dirp: 120–240°) directions and with heights above 2.5 m (calculated for periods between consecutive surveys undertaken between 07-Jan-2009, and 27-Mar-2018).	75
Figure 3.19. Scatter plots of significant correlations between 95 th percentile of Hs and shoreline position at MLWS for (a) Transect A and (b) Transect B and (c) Transect D.	76
Figure 3.20. Scatter plots of significant correlations between the proportion of southerly waves and change in beach width (m/day) at MHWS in (a) Transect A and (b) Transect B.	76
Figure 3.21. Significant correlations between (a) maximum P _{ACIV} and change in profile area (m ² /day) above MLWS at Transect C, between maximum P _{ACIU} and (b) change in beach width at MWL and (c) change in profile area between MLWS and MWL at Transect E.....	77
Figure 4.1. Workflow schematic representing data collection and analysis methods for sediment characterisation at site. Solid boxes indicate data input and output, dashed boxes present analysis procedures	82
Figure 4.2. Representation of the sediment data along Transect A, showing: the topography on 19-Jan-2017 and in the previous survey on 13-Feb-2017; the distribution of the gravel and the mixed sediment layer (34% sand) within to top 40 cm and along the profile; and at the top, the proportion of sand at surface (the scale shows blue as 0% and yellow as 100%). Notice that although much of the profile has only a thin layer of gravel, the surface analysis only shows the presence of sand in the intertidal region.....	85
Figure 4.3. Scatter plots of sediment size (D ₅₀ , x axis) against sorting value (y axis) and elevation (where point shape indicates transect and colour indicates the elevation of the sample: blue for the intertidal zone and yellow/red above 1.25 m ODN). For gravel in Transects A and B (a) and C, D and E (b) and for sand in all transects (c).	89
Figure 4.4. Scatter plots of sediment size (D ₅₀) against skew and elevation (where point shape indicates transect and colour indicates the elevation of the sample: blue for the intertidal zone and	

yellow/red above 1.25 m ODN). For gravel in Transects A and B (a) and C, D and E (b) and for sand in all transects (c).....	90
Figure 4.5. Scatter plots of sediment size (D_{50}) against kurtosis and elevation (where point shape indicates transect and colour indicates the elevation of the sample: blue for the intertidal zone and yellow/red above 1.25 m ODN). For gravel in Transects A and B (a) and C, D and E (b) and for sand in all transects (c).....	91
Figure 4.6. Examples of sediment distributions of sand and fines <2 mm (A) across the field site on 03-Aug-2016, (B) between 03-Aug-2016 and 21-Mar-2017 at Transect A, (C) through depth at Transect B on 27-Sep-2017 and (D) the largest variances observed at site influenced by engineering work (Transect D) and natural (over wash at a gravel berm) effects.	92
Figure 4.7. Sorting values of gravel portions in the presence of sand and in pure gravel (points in which no sand was visible, and gravel ranged from +0.02 -0.30 m) for Transects A-E) in which red indicates the median value of the all PSDs, the bottom and top edges are 25 th and 75 th percentiles respectively and the whiskers extend the range of the data.	94
Figure 4.8. Box plot showing the estimated proportion of sand at surface and at depth for each beach level considering data from all transects.....	95
Figure 4.9. Scatter plots of depth analysis Transect A a) MWL shoreline change/d and %sand MLWS-MHWS; b) area change/d MLWS-MHWS and %sand MLWS-MHWS; and Transect C (c) Area change above MLWS and %sand above MLWS.....	97
Figure 4.10. Sediment and profile behaviour of Transects A (panels a – c) between 06-Dec-2016 and 19-Jan-2017 and Transect C (panels d – f) between 03-Aug-2017 and 19-Jan-2017.....	97
Figure 4.11. Scatter plots of surface analysis at Transect A a) %time above 2.5 m H_s and %sand above MLWS (surface) b) %time $S>2.5$ m H_s and %sand above MLWS (surface) (c) 95 th Percentile H_s and %sand above MLWS (depth).	98
Figure 4.12. Scatter plots of surface analysis at Transect C of a) 95 th percentile between MLWS and MHWS b) 95 th percentile above MLWS and depth analysis (c) % $N>2.5$ above MHWS	99
Figure 5.1. Bragg scattering schematic showing the reflection of X-band radar waves against capillary surface waves.	103
Figure 5.2. A raw radar image at Thorpeness with surface clutter from a SE wave direction	104
Figure 5.3. A stacked sequence of raw backscatter images, with each layer being a full rotation of the radar, the speed of this rotation being the basis of Δt and the wave inversion calculation, x and y coordinates represent Easting and Northing respectively, Δx and Δy are the window in which the wave inversion depth is calculated (adapted from Borge et al. 2004).	104
Figure 5.4. (A) The radar deployed on the cliff top and (B) position to the north of the village seen from above (with an approximate north direction indicated) on 13-Apr-2016 (Mike Page 2016)	105
Figure 5.5. Schematic of the methodology employed to produce the radar dataset used in analysis.	106

Figure 5.6. 3-day window where the synthetic model (Lowestoft) was seen to perform well (a) against the data recorded within the sluice. The bottom panels present (b) RMS analysis of harmonic model and (c) Synthetic model against observed height. Limited to >0m for observed data due to tide gauge deployment position and data quality..... 107

Figure 5.7. Radar derived wave height (calibrated) against wave buoy data. 108

Figure 5.8 The radar derived bathymetric map (A, 11-Oct-2015 05:00) and stages of quality control to remove the ‘slice’ in the radar view and highly variable data due to depth and range (B) and natural neighbour interpolation (C). 109

Figure 5.9. (A) Radar histogram of calibrated depths (blue) and the previous uncalibrated depth (red), (B) scatter plot of the multibeam and radar derived depths prior to calibration utilising the derived line equation, (C) the radar record used concurrent to the multibeam survey and (D) the resulting differences between multibeam and radar, where a negative value indicates an underestimation of the radar and orange an over estimation..... 110

Figure 5.10. Time series analysis showing consecutive records above 1m H_s threshold (blue) and points in which 24 records were exceeded and record was defined as stable. 111

Figure 5.11. The developed GUI showing two bathymetric maps (A and B) from different 'blocks' of data, the calculated difference between them (C), a diagnostic for pixel variances through each block (D), a histogram of magnitudes of difference (E) and controls in which to cycle through and define each of the records for the time series (F). 112

Figure 5.12. The three areas where largest changes in bathymetry were observed, which are the focus of the analysis, showing differences in bed level between 11-Oct-2015 and 08-Feb-2016. 113

Figure 5.13. Bathymetry data from two multibeam surveys covering the study area: (A) obtained by the EA in June 2014 and (B) obtained by the MCA in January 2017. (C) Difference in the depths recorded between the 2014 and 2017 surveys. Negative values indicate an increase in depth (usually due to sediment loss) and positive values indicate a reduction in depth (usually due to sediment gain). Areas in white represent changes within ± 0.125 m. The black boundary indicates the radar coverage used in analysis. Thorpeness beach frontage buildings are identified in all figures..... 115

Figure 5.14. Area plot of the percentage of waves from northerly (Dir_p: 300 – 60°, grey area) and southerly (Dir_p: 120 – 240°, green area) directions calculated over a rolling 30-day window from the West Gabbard buoy (left, y-axis). Radar derived volume change within areas 1-3 relative to the starting record (11-Oct-2015, right y-axis), where a reduction in volume indicates erosion of the area and an increase suggests accretion..... 116

Figure 5.15. (A) Changes in radar-derived bathymetry between the 11-Oct-2015 and 06-Feb-2016. The black line indicates the shoreline position on 02-Feb-2016 and markers indicate changes in beach width at MHWS between 05-Aug-2015 and 02-Feb-2016 Wave roses for the period 11-Oct-2015 and 06-Feb-2016 for all waves (B) and for $H_s > 2.5$ m only (C)..... 118

Figure 5.16. (A) Changes in radar-derived bathymetry between 06-Feb-2016 and 20-Aug-2016. The black line indicates the shoreline position on 27-Jul-2016 and markers indicate changes in beach width at MHWS between 02-Feb-2016 and 27-Jul-2016. Wave roses for the period 06-Feb-2016 and 20-Aug-2016 for all waves (B) and for $H_s > 2.5$ m only (C). 118

Figure 5.17. (A) Changes in radar-derived bathymetry between 20-Aug-2016 and 23-Feb-2017. The black line indicates the shoreline position on 06-Mar-2017 and markers indicate changes in beach width at MHWS between 27-Jul-2016 and 06-Mar-2017. Wave roses for the period 20-Aug-2016 and 23-Feb-2017 for all waves (B) and for $H_s > 2.5$ m only (C). 119

Figure 5.18. (A) Changes in radar-derived bathymetry between 20-Aug-2016 and 04-Dec-2016. The black line indicates the shoreline position on 06-Dec-2016 and markers indicate changes in beach width at MHWS between 03-Aug-2016 and 06-Dec-2016. Wave roses for the period 20-Aug-2016 and 04-Dec-2016 for all waves (B) and for $H_s > 2.5$ m only (C). Note large changes to the south east are likely to be artefacts of variable wave direction between records..... 120

Figure 5.19. (A) Changes in radar-derived bathymetry between the 04-Dec-2016 and 21-Jan-2017. The black line indicates the shoreline position on 18-Jan-2017 and markers indicate changes in beach width at MHWS between 06-Dec-2016 and 18-Jan-2017. Wave roses for the period the 04-Dec-2016 and 21-Jan-2017 for all waves (B) and for $H_s > 2.5$ m only (C). 121

Figure 5.20. (A) Changes in radar-derived bathymetry between the 21-Jan-2017 and 13-Feb-2017. The black line indicates the shoreline position on 13-Feb-2017 and markers indicate changes in beach width at MHWS between 18-Jan-2017 and 13-Feb-2017. Wave roses for the period the 21-Jan-2017 and 13-Feb-2017 for all waves (B) and for $H_s > 2.5$ m only (C). Note after careful interrogation large changes to the south east are likely to be artefacts of variable wave direction between records. 121

Figure 6.1. Schematic of model set up and summary of primary investigations using the models.. 127

Figure 6.2. Gridded bathymetry in the nearshore region: (a) CAM 1 from the July 2014 EA multibeam survey, (b) CAM 2 from the January 2017 MCA survey; and (c) the difference between CAM 1 and CAM 2. Positive values (green-blue) indicate accretion between 2014 and 2017 and negative values (yellow-red) indicate erosion..... 129

Figure 6.3. Google Earth © imagery overlaid with model coverage showing bathymetry and: (a) Total Tide and Tide gauge locations; and (b) NOAA WWIII points and wave buoy locations. 130

Figure 6.4. Time series of metocean conditions offshore (West Gabbard buoy) used for modelling the southerly scenario Event A: significant wave height (H_s , a) and peak wave direction (Dir_p , b) during a spring 2010 erosion event. 132

Figure 6.5. Event B: Time series of metocean conditions offshore (West Gabbard buoy) used for modelling the Winter 2016-17 erosion event (Event B). 132

Figure 6.6. Wave power plots CAM 1 (2014) and CAM 2 (2017) between Aldeburgh and Sizewell at the peak wave height for (a) southerly Event A and (b) northerly Event B. Spatial plots focusing on the Ness and beach front of the wave power differences (positive indicates an increase in

energy between CAM 1 and 2): (c) Event A; and (d) Event B. Contour lines indicate 1, 2 and 5 m depths for 2014 (red) and 2017 meshes (black).	136
Figure 6.7. Total change of bed level (greater than ± 0.25 m) from northerly waves after 14-day coupled model run, black contour lines indicate changes $> \pm 0.5$ m between 2014 and 2017 by multibeam survey. Arrows indicate areas specifically discussed in the text.	138
Figure 6.8. Total change of bed level (greater than ± 0.25 m) from southerly waves after 14-day coupled model run, black contour lines indicate changes $> \pm 0.5$ m between 2014 and 2017 by multibeam survey. Arrows indicate areas specifically discussed in the text.	139
Figure 6.9. LST total average yearly flux of medium sand ($D_{50} = 0.3$ mm) for (a) Kamphuis, (b) CERC and (c) van Rijn formulations over the 10-year dataset where a positive value denotes northerly transport and a negative value southerly transport.....	141
Figure 6.10. LST total average yearly flux of gravel fraction ($D_{50} = 14.0$ mm) for (a) Kamphuis, (b) CERC and (c) van Rijn formulations over the 10-year dataset where a positive value denotes northerly transport and a negative value southerly transport.....	142
Figure 6.11. Van Rijn computed LST for medium sand ($D_{50} = 0.3$ mm) (a) northerly dominated winter (01-Dec-2009 to 28-Feb-2010); (b) southerly dominated winter (01-Dec-2015 to 28-Feb-2016).	143
Figure 6.12. Van Rijn computed LST rates for single occurrences ($D_{50} = 0.3$ mm), (a) northerly event (17-Dec-2009 boundary conditions: $H_s = 3.67$, $Dir_p = 28$, $T_p = 8.19$) (b) southerly event (12-Dec-2014 boundary conditions: $H_s = 4.02$, $Dir_p = 210$, $T_p = 6.81$).	144
Figure A.1. Calculated profile areas for Transect D ($>MLWS$, $>MWL$, $>MHWS$) with error margins presented around points.....	173
Figure A.2. Example subsampled profiles (07-Mar-2018) at (a) Transect C and (b) Transect A. ...	174
Figure C.1. (a) Scatter plot of modelled water level against Mike FMHD water level at the location of the deployed tide gauge between 14-May-2016 and 18-May-2016. (b) time series of water level observed by the pressure sensor and predicted modelled data (note that the gauge was deployed in a tidally influenced sluice and so only covers data from a height of approximately 0.1 m).	178
Figure C.2. Time-series of current magnitude (left column) and current direction (right column) for Total Tide points (D,Q, A, B and N) used in validation of the MIKE FMHD model.....	179
Figure C.3. Significant wave height (H_s) comparison between the calibrated NOAA WaveWatch III points used within the MIKE FMSW model and the nearest deployed wavebuoy. For West Gabbard (east boundary), Felixstowe (south boundary) and Lowestoft (north boundary).....	180
Figure C.4. Peak wave direction (Dir_p) comparison between the calibrated NOAA WaveWatch III points used within the MIKE FMSW model and the nearest deployed wavebuoy. For West Gabbard (east boundary), Felixstowe (south boundary) and Lowestoft (north boundary).....	181

Figure C.5. Time -series plots showing a comparison between MIKE FMSW model predictions and Sizewell buoy data during December 2017 for: (a) significant wave height (H_s); (b) peak wave direction (Dir_p); (c) peak wave period (T_p); and (d) mean wave period (T_z)..... 182

Figure C.6. MIKE 21 FMSW model: Scatter plot between Sizewell buoy and predicted significant wave height for the period 01-Jan-2017 to 31-Dec-2017. The Nash-Sutcliffe Efficiency score of 0.66 indicates acceptable MIKE FMSW model performance for the purposes of the present modelling studies. 183

Acknowledgements

The PhD has been cofounded by Bournemouth University (BU), Suffolk Coastal District Council (SCDC) and Mott MacDonald (MM).

Many thanks to my supervisors who have guided me consistently and kept me just scared enough to rarely lose motivation, even though I do have the habit of going into Matlab explorations and technical fiddly. Dr Luciana Esteves at Bournemouth University for your late-night replies, reviews and continual guidance. Dr Jon Williams at Mott MacDonald for introducing me to the endless possibilities of modelling, writing guidance and your crazily hopped home brews. I look forward to another Blue Grass Festival with both of you. Dr Paul Bell at the NOC for allowing endless questions on the [initially] mysterious workings of the radar.

The field work could not have been completed without the support of the many people at SCDC, BU and independents: Nick Reeves, Becky Koelher, Lucy Williams, Dr Leo Clarke, Alex Wilcocks and James Bell thanks for carrying tripods and bags of gravel up and down the beach. Paul Patterson your insight into the management of the coast and field site was invaluable. Lucy Goodman, I know it was because you like a jolly, but you also took some excellent pictures and your outside insights were only ever useful, SCDC are lucky to have nabbed you. Dr Dean Burnard for getting kit sorted and listening to me complain about how much the laser scanner is causing me frustration.

Beyond fieldwork thank you to Dr David McCann (NOC) who provided a go to on many radar related issues. Modeller extraordinaire Darren Price (MM) for the enormous help and input in the creation of the numerical model I appreciate the time and mentorship.

Final thanks to my family and friends, who have put up with my ever-decreasing reliability, specifically Lucy for not getting rid of me over the last three years of grumpiness. I love you all.

Author's Declaration

I declare that the work in this dissertation was carried out in accordance with the requirements of the University's Code of Practice for Research Degrees and that it has not been submitted for any other academic award. Except where indicated by specific references in the text, the work is the candidate's own. Work done in collaboration with, or with the assistance of others, is indicated as such:

Chapter 3 has its basis in the paper published collaboratively with Luciana S. Esteves:

Atkinson, J. and Esteves, L., 2018. Alongshore Variability in the Response of a Mixed Sand and Gravel Beach to Bimodal Wave Direction. *Geosciences*, 8 (12), 488.

Abbreviations and Nomenclature

Symbol	Description
ACF	Autocorrelation Function
ADC	Analogue to Digital Converter
BEEMS	British Energy Estuarine and Marine Studies
BGS	British Geological Survey
BODC	British Oceanographic Data Centre
c_0	Variance of a time series
CAM	Coastal Area Model
Cefas	Centre for Environment, Fisheries and Aquaculture Science
CERC	Coastal Engineering Research Center
C_g	Group velocity
\cos	Cosine
Defra	Department of Environment and Rural Affairs
DGPS	Differential Global Positioning System
DHI	Danish Hydraulic Institute
Dir_M	Mean wave direction
Dir_P	Peak wave direction
DTM	Digital Terrain Model
d_r	distance of the reflective sub surfaces
EA	Environment Agency
FM	Flexible Mesh
g	Acceleration due to gravity (9.81 m/s^2)
GUI	Graphical User Interface
h	Water depth
H_0	Deep water wave height
HAT	Highest Astronomical Tide
HD	Hydrodynamic (model)
h_e	Energy loss in Hagen-Poiseuille law
H_s	Significant wave height
H_{sb}	Breaking wave height
i	Hydraulic gradient
IEEE	Institute of Electrical and Electronics Engineers
k	CERC coefficient
K_g	Kurtosis
k_g	Hydraulic conductivity gravel
ki	Hydraulic conductivity
k_n	Wave number
kn	Time lag
k_s	Hydraulic conductivity sand
L_0	Deep water wave length
LAT	Lowest Astronomical Tide
LDA	Linear Discriminant Analysis
LiDAR	Light Detecting and Ranging

Symbol	Description
LST	Longshore Sediment Transport
mbar	millibar
MCA	Maritime and Coastguard Agency
MDir	Mathematical Direction (where East = 0 degrees)
MHWS	Mean High Water Springs
MLWS	Mean Lower Water Springs
MSG	Mixed Sand and Gravel
MWL	Mean Water Level
NAO	North Atlantic Oscillation
n_e	Porosity of sediment
n_g	Porosity of gravel
n_s	Porosity of sand
ODN	Ordnance Datum Newlyn
P_{ACFA}	Persistence Via Autocorrelation Function
P_{ACI}	Persistence Via Autocorrelation Integral
P_{ACIU}	Persistence Via Autocorrelation Integral u velocity
P_{ACIV}	Persistence Via Autocorrelation Integral v velocity
PDF	Probability Density Function
PSD	Particle Size Distribution
Q	Volumetric transport rate
r	Pearsons correlation coefficient
RFID	Radio Frequency Identification
rk	Correlation
r_s	Spearman's correlation coefficient
RTK	Real-time kinematic
SCDC	Suffolk Coastal District Council
SDBC	Sizewell-Dunwich Bank Complex
Sk_I	Skew
SNR	Signal to Noise Ratio
ST	Sand Transport (model)
SW	Spectral Wave (model)
T_0	Deep water peak period
$\tan\beta$	Beach slope
T_m	Mean period
T_p	Peak wave period
T_{pb}	Peak wave period at breaker point
u	Velocity east-west
UAV	Unmanned Aerial Vehicle
v	Velocity north-south
v_s	Velocity
$v_{seepage}$	Seepage velocity
Wp	Wave power
θ	Wave Direction relative to the shoreline
θ_b	Incident 'Bragg' angle

Symbol	Description
λ	Percentage of sand by weight (mixed sediment)
λ_c	Critical porosity
λ_t	Transmitted wave length
μ	Dynamic viscosity of water
ξ	Irribarren number
ξ_n	Open pore space volume
ρ	Water density
ρ_s	Sediment density
σ	Wave frequency
σ_l	Sorting
ϕ	Krumbien Phi scale of sediment Sizes

1. Introduction

Quantifying magnitudes of coastal change and understanding drivers of temporal and spatial variability are paramount to support sound coastal management decisions (Pye and Blott 2006; Smit et al. 2007). Despite their pervasiveness in higher latitudes (Forbes et al. 1995), only a few studies have focused on mixed sand and gravel (MSG) beaches worldwide (Kirk 1975, 1980; Mason and Coates 2001; Bergillos et al. 2016; Bergillos et al. 2017a). Gravel and sand behave differently to hydrodynamic forcing, adding complexity to beach response and the effort required in data collection and analysis. As a result, little is known about the characteristics of MSG coasts and how they vary in space and time.

Most studies on MSG beaches published in English were undertaken in New Zealand, Canada, the USA, and the UK. Earlier research focused mainly on the description of sedimentary characteristics of MSG beaches in New Zealand (McLean 1970; Kirk 1975, 1980). This continued through to the turn of the century (Nolan et al. 1999; Dawe 2001; Kulkarni et al. 2004; Miles and Russell 2004), after which, some research focused on categorisation of beach types of which mixed systems were considered (Jennings and Shulmeister 2002; Scott et al. 2011; López et al. 2015). The interest in gravel and MSG beaches has increased in the last two decades in response to the need to better understand the behaviour of nourishment schemes (Mason and Coates 2001; Horn and Walton 2007; She et al. 2007; Bergillos et al. 2016; Zarkogiannis et al. 2018) and the role of gravel berms to dissipate wave energy and provide significant coastal protection (Van Wellen et al. 2000; Buscombe and Masselink 2006; Ruiz de Alegria-Arzaburu et al. 2010). In most MSG coasts, gravel is a finite resource and difficult to replace once removed from the system. Therefore, long-term monitoring (Elsner et al. 2015) and methods for defining transport rates (Stark and Hay 2016) have been applied to understand MSG beach mobility better.

Sediment grain size is an important factor determining the rate of erosion, deposition, and transport (Cheng and Liu 2015). However, sediment characterisation is laborious and time-consuming, particularly in MSG systems. The presence of bimodal sediment distributions on MSG beaches makes characterising their variability (in space and time) a difficult task. For example, quantifying particle size distribution (PSD) requires the application of different methods for the sand and the gravel fractions, and the presence of coarse fractions requires collection of larger sediment samples weighing from 5 kg (Dornbusch et al. 2005; Horn and Walton 2007) to some cases 1500 kg (Eikaas and Hemmingsen 2006). Samples of this size limits the number that can be feasibly collected and analysed, which often leads to oversimplifications of methods or the sampling temporal and spatial coverage. As a result, there are no widely accepted standardised sampling and surveying methods that would allow a more robust characterisation of MSG beaches (Horn and Walton 2007). Therefore, very little is known about the temporal and spatial variability in the proportion of sand and gravel in mixed beaches and the influence they exert on beach mobility.

The ability to accurately and consistently monitor beach and nearshore processes provides the foundation for understanding beach dynamics (Davidson et al. 2007). There are a number of well-established methods to monitor changes in beach topography through recurrent surveys, e.g. Differential Global Positioning System, DGPS, Light Detection and Ranging, LiDAR (Burvingt et al. 2017), video systems (Holman and Stanley 2007; Smit et al. 2007; Holman et al. 2013) and the increasingly popular Unmanned Aerial Vehicles, UAV (Elsner et al. 2015). Assessing changes in nearshore bathymetry requires greater effort and investment; therefore, regular monitoring is much less affordable. Bathymetric surveys and measurements of nearshore waves, hydrodynamic and sediment processes are traditionally obtained by *in situ* surveys from vessels or deployment of equipment at sea, often with limited spatial and temporal coverage. Land-based remote sensing offers a cost-effective alternative to monitor nearshore waves and the seabed, through installations of X-band radar (Bell et al. 2004) or video systems (Bell et al. 2004; Holman et al. 2013).

Numerical models are often used to investigate the effects of varying driving conditions on coastal and nearshore dynamics (Roelvink et al. 2009; Hequette and Aernouts 2010; Dissanayake et al. 2015). The models used to achieve this are limited to the quality and coverage of their calibration and input data, in some cases using single bathymetric datasets (e.g. Burningham and French 2016), or single sediment size values to best describe a mixed system (Bergillos et al. 2017b).

It is clear that, in isolation, each of the methods mentioned here have limited capacity to advance the current knowledge of the interactions between driving forces (waves, surges and meteorological parameters) and the associated nearshore and beach changes. Utilising a multi-method approach is a necessity to gain a coherent understanding of the interactions influencing coastal and nearshore changes, particularly in a complex system characterised by: (1) mixed sediment (e.g. Horn and Walton 2007); (2) variable dominant wave climates (e.g. Harley et al. 2017); and (3) complex nearshore bathymetry (e.g. Limber et al. 2017).

This research applied a combination of field, remote sensing and modelling methods to advance the current knowledge on the temporal and spatial variability in the characteristics of MSG beaches and their response to driving factors. The area around Thorpeness (Suffolk, East Anglia, England) was used as the study site due to the pressing need to improve the understanding of drivers of coastal change to inform local coastal management strategies. Further, the area offers an ideal opportunity to investigate the effects of interactions between complex physical settings (i.e. antecedent geology and varying beach morphology), the presence of coastal protection, and a very dynamic system driven by bimodal dominant wave directions.

1.1 The Study Area

This research focuses on a 2-km long stretch of the North Sea MSG coast in Suffolk, East England, extending from Thorpeness, (52.182°N, 1.613°E) to the prominent cusped gravel foreland named Thorpe Ness (herein the Ness), between Aldeburgh and Sizewell nuclear power station (Figure 1.1).

Here the coastal morphology is greatly variable (Figure 1.2), changing from the (often multiple) gravel ridges at the Ness, which reduce in size to the south, to unconsolidated and retreating (~10-m high) cliffs and the urban frontage of Thorpeness village in the south.

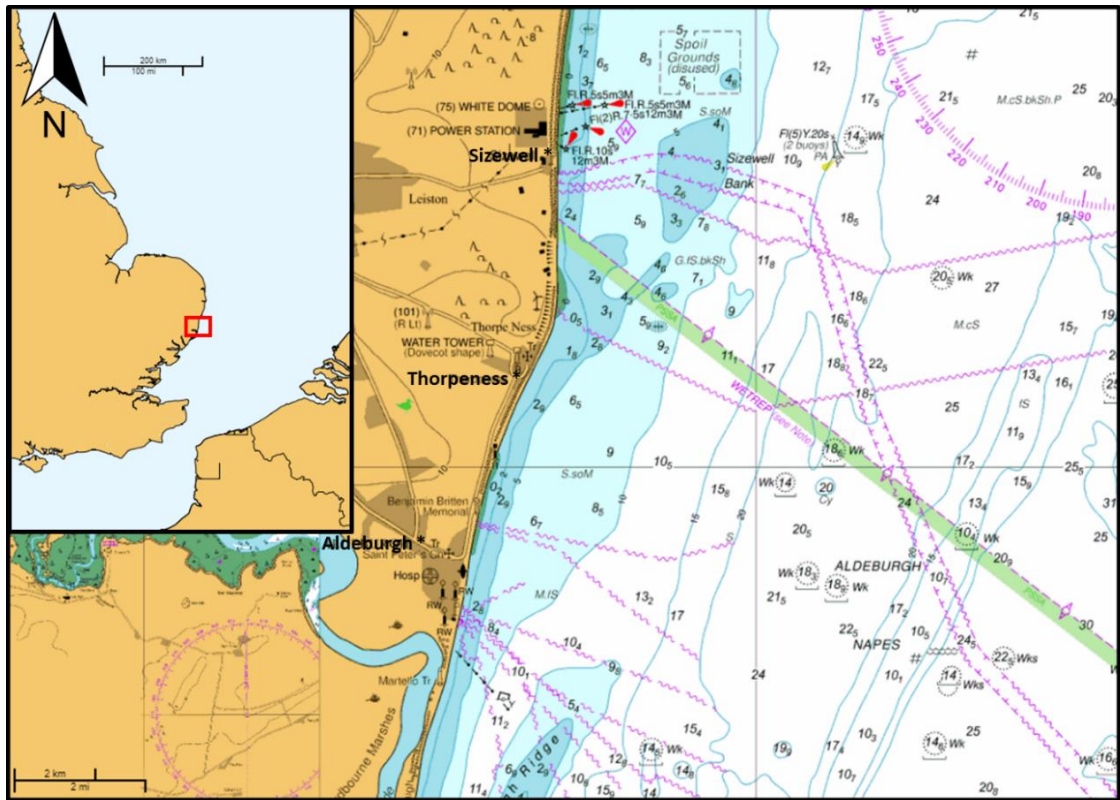


Figure 1.1. Thorpeness field site position and local marine map. (© British Crown and OceanWise, 2017. All rights reserved. Licence No. EK001-20180802. Not to be used for Navigation).

The presence of gravel foreland ‘Nesses’ occurs elsewhere along the Suffolk coast, such as at Kessingland, Southwold and Orford. The origin and behaviour of these features is uncertain, with one theory suggesting that they are a sink for offshore sediment (Robinson 1980), providing a bridge between the coast and nearshore sediment banks in which material is moved onshore. Others suggest that they are formed due to longshore transport convergence point from which sediment is transported offshore (McCave 1978; Carr 1981). In general, these features are generally observed to migrate north or south with the dominant sediment transport (Pye and Blott 2006). However, Thorpe Ness has been observed to be relatively stable and ‘fixed’ to the coast (Williams 2014; Burningham and French 2017). This stability is in part attributed to the underlying geology of the Coralline Crag ridges running NE/SW from Aldeburgh.



Figure 1.2. Thorpeness village looking north towards the Ness, where the erosional hot-spot can be seen along a short stretch of the frontage (July 2010, © Mike Page).

The Suffolk coast has been subject of many reviews and studies of short and long-term erosion (Pye and Blott 2006; Brooks and Spencer 2012; Burningham and French 2017). Between 1881 and 2013, 62% of this coastline has shown erosion rates of $>0.5 \pm 0.08 \text{ m y}^{-1}$. At some locations, mean rates of change are more extreme than those observed at Thorpeness, with retreat of up to 4.6 m y^{-1} observed between Southwold and Benacre Broad), and progradation of 2.2 m y^{-1} at Benacre Ness. When analysing shoreline change only over decades Thorpeness has shown a relatively stable beach face, (for example accreting by 0.23 m y^{-1} between 1990 and 2001 as shown in Pile, 2003). The threats posed to the beach front properties at Thorpeness occurs in short, focused erosion events along 50-200 m of coastline. These erosion events have sporadically threatened the beachfront properties since the 1920s and as a result, gabions, gravel-filled geobags and beach recharge have been implemented along the affected coastline (Figure 1.2).

1.1.1 Geology and bathymetry

The field site is characterised by (a) ~10-m high soft cliffs formed by Holocene alluvial and windblown sand; and (b) an underlying harder geology, particularly the Pliocene Coralline Crag formation. Previous studies indicate that this cliff line is more resilient than similar systems along the Norfolk and Suffolk coast. Historic map analysis between 1883 and 2000 suggested that cliff retreat was within the error of the analysis (Pile 2003) and an annual contribution to the sediment budget between 1881 and 2013 was estimated to be $1984 \text{ m}^3 \text{ y}^{-1}$ (Burningham and French 2016),

which is negligible when compared to $33340 \text{ m}^3 \text{ y}^{-1}$ at Dunwich (10 km north) and $64517 \text{ m}^3 \text{ y}^{-1}$ at Covehithe (21 km north).

The cliff system overlays the Pliocene geology of the Coralline Crag formation (cemented fine sands and silts rich in bryozoan and bivalve shells formed in a shallow shelf environment (Long and Zalasiewicz 2011). Offshore of Thorpeness, the Coralline Crag formation is prominent in the nearshore, forming underwater ridges extending 12 km with a SW-NE orientation (Pye and Blott 2006; Long and Zalasiewicz 2011). As stated previously, the interaction between these Coralline Crag ridges and the Sizewell-Dunwich Bank Complex (SDBC) to the north of the study area is believed to promote the stability and anchoring of the Ness (Lees 1983). This stationarity contrasts with the mobility of Benacre and Orford Ness (Burningham and French 2016). Carr (1979) suggested that the SDBC acts as a sink for fine and medium sand from the north and south; which may be the case also at Thorpe Ness, in turn, likely to influence loss and gain of sediment at Thorpeness (Bamber 1965).

1.1.2 Metocean conditions

The meteorologic and oceanographic (hence referred to as metocean) forcing on the Suffolk coast result in bimodal wind directions. The most intense winds are caused by low-pressure systems forming over Greenland and travelling south into the North Sea, while relatively less destructive winds approach from the SW (Spencer et al. 2015). The resulting wave energy is the primary driver of significant coastal impact and change in the North Sea (Burningham and French 2016). Pye and Blott (2006) analysed a hindcast analysis of 13 years of data (1986-1999) from the Meteorological Office UK Waters Wave Model, from a location 48 km east of Dunwich, concluded that most waves approached from the north and northeast ($345 - 045^\circ$) or south and southwest ($165 - 225^\circ$). At this location, 37.7% of waves were less than 1 m, and 76% less than 2 m high. The highest waves were from the northeast (in line with the maximum fetch), with 1 in 100-year wave heights estimated to reach 7.3 – 7.8 m, in contrast of 5.4 - 6.7 m waves from a southwest and southeast direction. Numerical modelling studies indicate that the inter-annual variability in the bimodal wave climate affects sediment transport rates along the Suffolk coast (Burningham and French 2016; Pethick 2017). However, there has been little or no investigation into the effects of storm clustering and persistent moderate conditions, which have been observed to have a slower but significant impact on beach dynamics elsewhere (Karunaratna et al. 2014; Dissanayake et al. 2015; Angnuureng et al. 2017).

At the study area, the inshore wave dynamics are more complex as interactions with the SDBC system and the Aldeburgh Napes affect the energy arriving inshore. The SDBC is reported to reduce the size of the waves through refraction and energy dissipation, by up to 1.3 m (to a maximum of 3 m inshore of the bank), providing protection to the Sizewell coast (BEEMS 2012). At Thorpeness, however, the influence of the nearshore features (SDBC, Coralline Crag and Aldeburgh Napes) has

not been studied. Williams (2014) suggested that, under specific conditions, these offshore features may lead to concentration of wave energy, which may cause the local erosion 'hot-spot'.

The tidal regime on the Suffolk coast is semidiurnal with ranges (Lowest astronomical to highest astronomical tide, LAT, HAT) of 2.90 m in Lowestoft increasing to 4.30 m in Felixstowe (Admiralty Tide Tables, 2004). The tidal stream offshore is rectilinear and runs almost parallel to the coast (north to south), with a flood dominance (around 20% stronger than the ebb) peaking at 1.7 and 0.9 m s⁻¹ during spring and neap flood respectively, and 1.4 and 0.8 m s⁻¹ during spring and neap ebb (Williams 2014). In the Thorpeness area, the effect of nearshore bathymetry on the tidal currents has had little investigation since initial observations by Lees (1983), suggesting the shoreline at Thorpeness causes a lee eddy during ebb tides which results in a longer southerly flow to the north of the Ness.

1.1.3 The effect of storms

The Suffolk and East Anglia coast has been impacted by several significant erosion and flooding events in recorded history. These events are primarily observed when high waves coincide with high storm surge. The combination of shallowing and narrowing of the shelf in the SW North Sea towards the English Channel and the longest fetch make the East Anglia coast particularly exposed to northerly storm (Spencer et al. 2015).

The meteorological and oceanographic forcing of storm surge events for the North Sea has been widely studied (Lamb 1991; Horsburgh and Wilson 2007; Brooks and Spencer 2014; Spencer et al. 2015). The two most prominent and destructive storm surge events over the last 60 years occurred between 31st January and 1st February 1953 and 5th – 6th December 2013 (Spencer et al. 2015; Wadey et al. 2015a; 2015b). Both these storms resulted in super-elevated water levels (3.78 m ODN in 1953 and 3.17 m in 2013 at Aldeburgh, 5 km from the field site). At the study site, the impacts of these two storms were minimal. The major 1953 flood that devastated many coastal locations in the UK and around northern Europe (Wadey et al. 2015a) had relatively little impact at Thorpeness. A large and well-developed berm is believed to have saved the village and surrounding area from the worst of the storm (Williams 2014). The 2013 storm coincided with low beach levels in front of the village, causing damage to existing engineering works but minimal impact to the protected beachfront properties.

Existing records of major coastal erosion at the study area suggest that they occur as a result of prolonged stormy periods when impacts of later storms are enhanced due to a state of sediment depletion caused by earlier storms. The earliest well-recorded erosion event in Thorpeness occurred in October 1911, when a storm caused ~10 m of cliff recession undermining beachfront properties and the local coastguard station (Williams 2014). A period of relative stability followed, as no destructive events were recorded until the mid-1970s. In 1975, severe weather reduced beach levels by 2 m along a stretch of approximately 200 m at the north of the village; gabions were then placed

to protect the cliff. Another period of relative stability followed as the next noted erosion occurred in the April and May 2010 followed by 12 months of chronic erosion along the Thorpeness beach frontage (Williams 2014), a situation aggravated by a destructive storm on 19th June 2010, which exposed the 1970s gabions (Royal Haskoning 2010). Gravel-filled geobags were then placed in front of the gabions as a temporary measure to prevent damage to beachfront properties. Storms in April and May 2013 reduced beach levels, exposing and damaging the geobags and gabions of newly installed defences, some recovery occurred over summer however further erosion occurred in October requiring further beach nourishment. This recurring erosion along 200 m of the Thorpeness village (Figure 1.2), while the neighbouring beach is often unaffected, have been described as an erosion 'hot-spot' (Williams 2014).

1.1.4 Engineering works

The major erosion events of mid-1970s, 2010 and 2013 have led to coastal protection works (Table 1.1) to reduce cliff retreat and the threat to beachfront properties. Major, documented works at the field site began after the erosion events of 1975, rock-filled gabions were installed running approximately 250 m along the beachfront at the north of the village and covered with shingle. These were exposed by storms in June 2010, after which emergency protection works consisting of geotextile bags filled with sand and shingle were installed along 500 m of beach frontage in two phases (Figure 1.3). Phase 1 (winter 2010-11) focused on the installation of geobags extending 300 m south from the southern end of the gabions overlaid with 989 m³ of gravel extracted from the Ness (Environment Agency 2011). Phase 2 (winter 2011-12) extended the installation of geobags north of Phase 1, along the toe and around the northern end of the gabions. These works were co-funded by Thorpeness residents, the Environment Agency (EA) and Suffolk Coastal District Council (SCDC). The geobags were covered by gravel nourishment in the spring of 2012 and October 2013, with gravel sourced from the Ness and south of the protected coastline, respectively.

Table 1.1. Major engineering works at site until winter 2013.

Date	Engineering Work	Size	Region
1975-1980	Rock filled gabions (40° slope), gravel nourishment.	250 m	North beach frontage
Summer 2010	Gabion repair, Phase 1 geobag installation.	250 m	South of gabion defences
Winter 2010 - 2011	Gravel nourishment at gabions sourced from Ness	300 m 989 m ³	North beach frontage
Summer 2011	Phase 2 Geobag installation	250 m	North beach frontage
Winter 2011-2012	Gravel nourishment over geobags sourced from the Ness	500 m 1000 m ³	Covering all defences
Oct-2013	Gravel nourishment sourced from south of engineering works	1500 m ³	South defences

After the storm damage to the geobags in 2013, studies were commissioned to appraise the coastal erosion issue at Thorpeness (Williams 2014) and assess the feasibility of coastal management options (Williams and Herbert 2015) to reduce risk to the beachfront properties over the next 30-50 years. A key finding was that a better understanding of local coastal processes leading to the erosion hot-spot was required to inform coastal management decisions.



Figure 1.3. North of Thorpeness village map showing the location and extent of the coastal defences (A, © Ordnance Survey and Crown copyright and database rights 2017, 100025252), including the 1970s gabions and the geobags (B and C, Photos courtesy of Suffolk Coastal District Council).

1.2 Difficulties with MSG Beaches

MSG beaches show a range of sediment characteristics which can range from deep coarse and fine gravels to a sandy surface and mixed sand and gravel layers. A key difficulty in management of the system is that the sedimentary processes in mixed systems are complex. This is due to the hydrodynamic processes changing as a result of these varying proportions of sand and gravels (Mason and Coates 2001). Defining a standard particle size distribution (PSD) from which to characterise behaviour is difficult and mixed beaches have therefore often been overlooked in research (Horn and Walton 2007).

Typically, an MSG beach contains sediment sizing on the Udden-Wentworth Scale (Wentworth 1922) from fine sand ($62.5 \mu\text{m}$, 4ϕ) to coarse gravel and cobbles (64 mm , -8ϕ). Although there is no clear-cut definition for what constitutes a mixed beach, many definitions have been proposed in literature: McLean (1970) proposed MSG beaches having equal portions of sand and gravel. Mason and Coates (2001) however, explored the definition more broadly, noting that even 'pure' gravel beaches rarely comprise of pure gravel and often contain proportions of fine material varying temporally and spatially cross- and longshore. This variation between definitions in the literature is pronounced with mixed beaches in New Zealand defined as being composed of between 17% and 63% sand (Matthews 1983), 30% in Suffolk, UK (Pontee et al. 2004) and 53% on the Beaufort Sea Coast, Canada (Hill 1990). Defra (2003) summarised the pattern of MSG beaches within the UK as consisting of bimodal sediments, one being sand and the other gravel with an approximately 20-30% sand portion, although the composition is observed to vary spatially and temporally. These definitions are broad, primarily due to the variation that can be observed not just between beaches

but on single beaches over time and space. In its simplest sense, an MSG beach is a beach in which the bimodality of the PSD has a direct impact on the dynamics and behaviour observed.

Published reviews on the understanding of mixed beaches are limited. Kirk (1980) provided an overview of MSG processes in New Zealand and Mason and Coates (2001) provided an extensive review of the literature in relation to management issues. Buscombe and Masselink (2006) reviewed gravel beaches but highlighted within that although some processes of MSG beaches were like that of pure gravel beaches, the dynamics as a system were distinct and significantly different. More recently, Holland and Elmore (2008) reviewed heterogeneous sediment systems of which MSG beaches were one of the foci.

Although comparable to pure gravel beaches, MSG beaches are more complex, exhibiting properties of pure gravel and pure sand beaches, dependent on tidal range and level. This can mean the hydro- and sediment dynamics at any one beach can change throughout a single tidal cycle, showing reflective beach properties during high tide and dissipative properties at low (Wright and Short 1984). This is also evident in the sorting of sand and gravel deposits cross-shore, where swash and breaking wave dynamics are the core driver of coarse sediment movement above and in the inter-tidal zone cross-shore and tidal currents are observed to be a primary cause of fine material movement seaward of the low water level (Single and Hemmingsen 2001). In addition to this natural complexity, management of beaches through nourishment results in a beach which rarely reaches equilibrium of sediment distribution and profile shape. With some nourishment schemes observed to enhance erosion or cause cliffing (Zarkogiannis et al. 2018); due to compaction and the dynamics associated with varying proportion of sands and gravels (She et al. 2006, 2007).

1.3 Aim and Objectives

The overall aim of this research is to advance the understanding of the temporal and spatial variability of MSG beaches in response to driving factors, such as varying wave conditions and changes in nearshore bathymetry. To achieve this, a multi-method approach was used to investigate beach and nearshore changes and sediment characterisation. The specific objectives to answer the overarching aim are:

1. To advance the current knowledge on the spatial and temporal variability of MSG beach morphology and how these are influenced by wave conditions
2. To assess MSG beach sediment characterisation and test whether there is an association between the calculated proportion of sand and beach mobility;
3. To establish and apply a robust and cost-effective method to quantify changes in nearshore bathymetry, at temporal scales of weeks and seasons, using X-band radar technology, and quantify associated uncertainties;
4. To improve the understanding of the effects of bimodal wave directions on the temporal variability and interaction of MSG beaches with nearshore changes;

5. To identify linkages between nearshore and shoreline changes, particularly the effects of antecedent nearshore bathymetry on longshore sediment transport;
6. To utilise the evidenced-knowledge obtained in this research to inform coastal management decisions to mitigate the effects of erosion at Thorpeness.

1.4 Thesis Structure

The thesis is organised into seven chapters. Here in Chapter 1, an overview of the key research challenges addressed in this study, the characterisation of the study area and the overall research aim and objectives are presented. The current state of knowledge related to MSG beaches is summarised in Chapter 2. Chapters 3, 4 and 5 describe the primary and secondary data analysed in this study to advance the understanding of how MSG beaches vary in response to changing driving conditions. These chapters are self-contained and include the description of methods, analysis of results and discussion.

More specifically, Chapter 3 assesses the temporal and spatial variability of the morphology at the site and how wave conditions influence this, with an aim to achieve objective 1. Chapter 4 analyses the sedimentological variability at site to accomplish objective 2. This is done through deriving the proportion of sand and gravel within the beach to establish how it influences beach mobility in relation to wave climate. Chapter 5 seeks to accomplish both objectives 3 and 4. This is done through first establishing a robust methodology for the use of X-band radar in coastal and nearshore modelling (objective 3). Before applying the methodology to understand the nearshore variability at site with a focus on the influence of bimodal wave direction and the interaction between the nearshore and shoreline (objective 4). Chapter 6 uses the data and knowledge gained from previous chapters to inform numerical modelling simulations. Aiming to assess the influence of varying wave conditions and nearshore bathymetry on the rates and direction of longshore sediment transport in the study area (objective 5) before exploring how this can be used to inform local management decisions (objective 6). Chapter 7 synthesises the key findings of this research and critically evaluates if the project aims and objectives have been reached, before further exploring the relevance of the findings to inform local coastal management (objective 6) and how they contribute to advance the understanding of MSG beaches and current practices.

2. Mixed Sand and Gravel Beach Dynamics: Review

The complexities inherent within MSG beaches (outlined in 1.2) make characterising MSG dynamics difficult and a standard method has thus far not been established. This chapter seeks to establish current methods for surveying and characterising MSG beaches and how they have historically been classified within beach behaviour models. This is followed by exploration of the hydrodynamics of mixed systems and how they are distinct from their pure gravel and sand counterparts before identifying the key research knowledge gaps that will be addressed in this thesis.

2.1 MSG Beach Surveying and Sediment Characterisation Methods

A range of methods have been applied for surveying and characterising MSG beaches to suit specific research focus. This section assesses the methods used in (1) *sediment* characterisation; and 2) *sediment movement*. Monitoring of beach topography is central to assessing changes in beach morphology. The methods used in MSG beach are the same used elsewhere, varying from traditional surveying methods, using DGPS, total station, or terrestrial LiDAR, or the increasingly common unmanned aerial vehicle high-resolution photogrammetric mapping.

2.1.1 Sediment characterisation methods

Traditional measurement of sediment sizing for both coastal and riverine applications has tended to favour manual sieving, laser diffraction or settling (Buscombe and Masselink 2006). The large range in sediment size of MSG beaches, however, limits methods to those which can handle the largest and smallest particles together or necessitates a combination of more than one method, and so sieving and manual measurement have often been the foundation for research (Kirk 1975; Dawe 2001; Horn and Walton 2007; Bergillos et al. 2016; Stark and Hay 2016).

To mitigate time and reduce the logistical difficulties of large sample analysis the use of manual and automated measurement of grain size from photographs has been explored within morphodynamics since at least the 1960's; both in riverine and beach settings. This began with manual measurement directly from photographs, as well as the use of an optical size analyser, where the intermediate *b*-axis of particles was measured using an adjustable light spot to match the particle and an automated measurement taken for each particle prior to the PSD being calculated (Ritter and Helley 1969). With the introduction of digital photography and higher resolution cameras, the manual measurement of particles became slightly easier and a number of studies have utilised bespoke processing tools (particularly in riverine systems where fine and coarse grains are present) for particle analysis and measurement which minimises preparation, measurement and statistical analysis time (Matthew et al. 2011; Turley et al. 2016).

The length of time for manual image measurement (both digital and analogue) however is still high and this has led to the development of a number of automated methods for image analysis approached through two distinct techniques: 1) edge detection, where individual grains are established through artificially spacing of the grains on a uniform background or image filtering (Butler and Place 2001; Sime and Ferguson 2003); and 2) statistical analyses, where the ‘texture’ of an image is analysed and a statistical function utilised to establish PSD (Rubin 2004; Buscombe and Masselink 2009; Warrick et al. 2009; Buscombe 2013). MSG adds additional complexity to the analyses due to the sediment sizes spanning more than one order of magnitude and when attempted has proved unreliable when compared to unimodal sediments (Pontee et al. 2004; Pentney and Dickson 2012; Buscombe 2013).

Even at its most accurate, measurement of particles from field photographs is limited by the orientation of the clasts, although particles will tend to fall into an orientation with the *b*-axes facing the camera (Buscombe 2013), the effect of stacked or overlaying particles tend to skew the image measured axis to less than a physical measurement. Kellerhals and Bray (1971) found the mean particle size to be 5 mm less when measured from an image and Adams (1979) concluded multiplication of a factor 1.07 for mm measurements or the subtraction of 0.1 ϕ correction factor.

Whether through traditional techniques or images, PSD analysis of MSG beaches is more difficult and time consuming than that of pure sand or gravel beaches. It is important when designing a survey to accurately capture the variance on the beach face and through depth using a method or combination of methods which do not instil a bias towards the fine or coarse fraction which may influence conclusions drawn or model outputs. Unfortunately, no standardised methodology for defining MSG variance is followed in literature; primarily because every site exhibits different characteristics, and what may be utilised at one site may not be applicable to another.

Little is known about morphodynamic influence of cross-shore grain size variations on MSGs (Roberts et al. 2013) and so the need to characterise sediment variance in space and time is crucial for understanding the behaviour observed and the modelling of future beach states. Logistically, sampling gravel and MSG beaches for PSD is difficult; with some literature suggesting large samples of more than 100 grains at each 0.25 ϕ fraction required to fully quantify variation (Gale and Hoare 1992), whilst others argue that due to the complexity, spatial and temporal variation in sediment size that several smaller samples would better characterise a site (Dornbusch et al. 2005; Horn and Walton 2007) or simply that the research aims dictate the sampling required (Dunkerley 1994); ideally large samples would be taken at every proportion and size change, both on the surface and through depth, however, the expense and practicalities mean an ideal is all but impossible in an environment where variance is a key characteristic (Figure 2.1).

The difficulty in characterising this variance has resulted in some studies having a larger focus on sediment analysis for characterisation (Dawe 2001; Horn and Walton 2007; She et al. 2007) and others using fewer samples due to a focus on sediment movement and modelling (Bramato et al. 2012; Stark et al. 2014; Dornbusch 2017). Neither of which is incorrect but instead, a side effect of

research objectives, focus and related time constraints. The use of airborne drones for beach surveying is a relatively new method and still in the process of being proven for capturing beach height and in the case of MSG beaches to map gravel distribution (Elsner et al. 2015), though this can only ever provide surface analysis.

These difficulties and time-consuming methods for PSD analysis has resulted in often simplified, minimal samples to characterise sediment distribution as part of a larger analysis campaign or intensive large-scale sediment collection analysis to be utilised as a single piece of research focusing on characterising single moments in time (e.g. McLean and Kirk 1969; McLean 1970a; Dawe 2001) or spatial sampling (characterising entire regions by limited cross-shore bulk samples e.g. Eikaas and Hemmingsen 2006). Pontee et al. (2004) assessed a range of characteristics along three transects on the Suffolk coast incorporating profile analysis, internal architecture (through ground penetrating radar) and conceptual beach models. The PSD analysis, however, assessed surface sizing through a combination of sieving (for two surveys) and image analysis for all other visits, cross-shore only (every 2 – 3 m, though only results of three per profile were presented), ignoring change through depth and longshore. This contrasts with Dawe (2001) who assessed PSD across 16 beach profiles for sediment mapping (size, sorting and kurtosis) along an 8 km stretch of beach in Kaikoura, New Zealand at a single point in time, collecting between 1 and 15 kg of sediment at each site (totalling ~250 kg), a method logistically difficult and potentially destructive to a beach if utilised for the longer-term, regular surveying outlined in Pontee et al. (2004).



Figure 2.1. Variability of sediment along one beach profile in front of the cliff line north of Thorpeness. (A) Cross-shore bands of gravel in the intertidal area perpendicular to the waterline, (B) cuscate formations and longshore bands of gravel parallel to the waterline above MWL, (C) gravel at the cliff toe and (D) mixed sand and gravel within the intertidal zone.

2.1.2 Sediment movement

Observation and monitoring of the hydrodynamics associated with beach change (waves, tides and wind) and the resulting movement of particles is generally more difficult than beach level and sediment measurement. This is due to the energetic area in which change most rapidly occurs requiring expensive equipment and logistically challenging installation which is difficult to monitor over a longer period. There have been a number of studies focusing on capturing hydrodynamics occurring in the swash zone through combinations of physical models (López de San Román Blanco 2003; López de San Román-Blanco et al. 2006; Antoniadis 2012, 2013), field hydrodynamic measurement (Kirk 1980; Ivamy and Kench 2006; Stark and Hay 2016) and particle tracking (Ciavola et al. 2009; Dickson et al. 2011; Miller et al. 2011; Stark et al. 2014) and often the methods used in field can parallel or be replicated between those of pure sand and gravel, in these cases; the sediment multi-modality is not as much as an issue.

The characterisation of swash zone dynamics follows much of the same methodologies as those for pure sand and gravel research, relying on frames mounted with instrumentation within the intertidal zone. Instrument arrays on the frames can consist of (but not limited to) single- and multi-point current meters, pressure sensors for wave estimation, sediment traps and side scan sonar for bed monitoring. MSG beach research has focused on a number of conditions with the impact of moderate conditions and tidal forcing explored by Kulkarni et al. (2004) and Ivamy and Kench (2006) and high energy conditions by (Kirk 1975, recorded swash processes at breaker heights of up to 2.44 m) and Stark and Hay (2016, during storm conditions exceeding 2 m H_s).

The observation and analysis of sediment movement through particle tracking techniques allows a better understanding of transport speed, rates and direction than the inference of mass sediment movement through monitoring of beach levels and volume. It has shown considerable investment since the turn of the century (Stark and Hay 2016) and can consist of a number of methods for identification of sediments, ranging from magnetic synthetic tracers (Black 2012), fluorescent paint (Ciavola et al. 2009; Stark and Hay 2016) and embedded radio frequency identification tags (RFID, Curtiss et al. 2009; Miller et al. 2011) and with the range of clast sizes found on an MSG beach often a combination of tracer types is utilised in ratio to the amounts of each clast size found at site. In its simplest form, it allows an understanding of the transport rates, volume and dispersion occurring at site in a Lagrangian nature; particles are released into the system and then recovered elsewhere, the location and concentration noted.

The methods and guidance employed during particle tracking are well defined in literature (Black 2012), with MSG beach research simply able to employ a combination of the methods used in pure sand and pure gravel applications. Initially, tracers are prepared to match as closely as possible the size, shape and density and hydrodynamic characteristics of the natural sediment (Curtiss et al. 2009) for gravel and coarse sediments this often means the collection and marking of the natural sediment at site. Tracing particles finer than fine gravel (4 – 8 mm, -2ϕ) is more complex, with methods based

on the use of coated natural sediments or labelled synthetic tracers (Black et al. 2007). The sediment is then released into the system within the area of interest (often the intertidal or swash zone) and then recovered on various time scales dependent on transport rates needed and research focus. For large particles recovery is simply retrieval and identification of the particle where marking and sizes of the gravel are observed to have a considerable impact on recovery rates: RFID tags observed to have a recovery rate exceeding 80% (Osborne 2005) and fluorescent paint recovery dependent on conditions and time frames, ranging from 100% (low energy) to 50% (high energy storm event, Stark and Hays 2016). Fine particles require spatial sediment sampling to assess the movement where the sample is returned to lab and tracer concentrations calculated through grain counting (Ingle 1966; McComb and Black 2005) or in the case of synthetic tracers separated through magnetism of the tracer coating (Black 2012).

2.2 MSG Beach Classification

This characterisation and classification of beaches has been a foundation for understanding beach behaviour since early systems employed by the Australian beach model (Chappell and Eliot 1979; Short 1979; Wright and Short 1984). The utility of these systems is based on the ability to predict and understand behaviour based on their morpho- and hydrodynamic characteristics which can also be applied to the safety issues and dangers associated with differing systems (Short 2006) and to define frameworks for ecologists (Rodil and Lastra 2004). Though papers by Jackson et al. (2005) and Scott et al. (2011) both urge caution in the use of models and classification systems, concluding ‘a universal beach model does not exist’. Within MSG beach research and at the project field site this is further evident due to the inherent variance and complexity within the system, changing seasonally and alongshore and when the application of differing survey methods is liable to end in a range of conclusions.

A number of studies have attempted to classify MSG beaches with varying degrees of complexity. Jennings and Shulmeister (2002) proposed a tripartite classification of gravel and MSG beaches based on morphology, sedimentology and hydrodynamics drawing on data from 42 coarse grained beaches on New Zealand’s South Island. These beaches were classified based on: beach width, storm berm height, number of berms, beach slope (from the top of the highest berm to low tide mark, and the high and low tide points on the survey day), grain size, metocean parameters, wave climate and tidal range. To differentiate between wave breaking types the Iribarren Number (Battjes 1974) was calculated for the two beach slope parameters:

$$\xi = \frac{\tan\beta}{(H_0/L_0)} \quad (2.1)$$

Where $\tan\beta$ is the beach face slope, H_0 is the offshore wave height (m) and L_0 is the offshore wavelength (m).

Linear discriminant analysis (LDA) was applied to the measured values; this analysis method utilises all the parameters collected to identify the patterns within the data which can be used to identify the features which best characterise and differentiate beach type.

The study identified three dominant beach forms:

- Pure Gravel: contains majority coarse particles (>2 mm) and forms a linear slope, with minor berms and is similar to the simple linear slope class described in Carter and Orford (1993), steepest slope of all identified beach forms, with average beach slope of $\tan\beta = 0.18$, and sediment grading increasing with increasing distance towards the storm berm;
- MSG beach: contains both sand and gravel well mixed through depth and cross- and long-shore with no defined regions of pure gravel or pure sand, average $\tan\beta = 0.08$; and
- Composite: distinct separation between coarse and finer particles, with finer grades below MWL and larger particles in the mid to high tidal ranges, low average beach slope $\tan\beta = 0.1$, and sediment grading towards the storm berm.

Using cluster analysis Scott et al. (2011) took 24 variables to define nine distinct beach types in the UK ranging from sand to pure gravel. From these 9 beach classifications, there were three coarse grained (>10% gravel) based types identified:

- Reflective Low-energy (Group 1): highly reflective, low energy, slopes ranging from 4-10°, upper and lower beach face consists of medium to coarse gravel (>50%);
- Reflective High-energy (Group 2): reflective, slopes of 5-7°, low to high energy (H_{S50} 0.4-1.2 m); and
- Low-tide terrace/non-barred dissipative, Low-energy (Group 4): distinct break in slope from upper reflective to dissipative lower beach.

López et al. (2015) characterised 34 coarse sediment beaches along the Alicante coastline, Spain, by first visually splitting the beaches into five types:

- Type 1: Sand and gravel beaches;
- Type 2: Sand and gravel separated beaches;
- Type 3: Gravel and sand beaches;
- Type 4: Gravel and sand separated beaches; and
- Type 5: Pure gravel beaches.

A similar technique to Scott et al. (2011) was then employed, defining 45 variables from sediment characteristics, wave conditions, boundary conditions (environmentally dependent variables from which source materials occur) and geometry. The number of variables was then reduced to 25 through two by two analyses and discriminant method (essentially assessing whether a range of variables are effective in predicting categories or membership to a group), to compare and differentiate the elements (Jennings and Shulmeister 2002). These analyses were then validated against data collected in January, March, April and May 2014, for five of the 34 beaches, along three

cross sections. Here the objective was to understand the effect of seasonal and spatial beach changes and to quantify the sensitivity of the variables in the discriminant analysis. The outputs from the analysis were that the five visually defined beaches categories were statistically different and different enough that any temporal variation within the validation beaches was not large enough to change the classification. Although this survey period only covered 5 months, which would not fully capture seasonal or longer-term cycles of change it does support the idea that a visual assessment of a site and its morphology can provide a basic understanding of core dynamics.

The primary issue with these classification systems is that many sites can show variability alongshore and through time. When visually assessing the field site, it becomes obvious that a number of these categories could be applied along the beach frontage: in some cases, having distinct transitions between sand and the intertidal and gravel berms, whilst in other cases the berm is not present and instead the profile is dominated by a mixed gravel and sand substrate. Paired with a range of natural and man-made structures above high water the behaviour and response to driving forces is unlikely to be uniform and so categorising and then defining likely behaviour becomes difficult.

2.3 Morphological Features and Models of Behaviour

Much like gravel beaches, it appears the spatial and temporal homogeneity of PSD are both an expression and control of the resulting morphodynamics (Buscombe and Masselink 2006), however the shallower library of MSG research and the distinct variability in behaviour results in a limited number of conceptual models and as previously explored a universal model is advised against (Jackson et al. 2005; Scott et al. 2011). The focus of MSG (and pure gravel) research is generally the swash zone hydrodynamics, this is due to the largest and most significant changes occurring in this area (Pedrozo-Acuña et al. 2006). Resulting general conceptual models of MSG beach behaviour are limited, there are however a number of studies in which behaviour is defined (Kirk 1980; Ivamy and Kench 2006; Bergillos et al. 2016) or are directly applicable to the project field site due to geographic proximity (Pontee et al. 2004).

Although MSG profiles are highly variable there are a number of common features present. The presence of a coarse-grained fraction results in a beach steepness higher than that of sand but lower than that of gravel, this middle ground results in an MSG profile often containing a narrow surf zone where much of the energy is dissipated (Kirk 1980), and an active and dynamic swash zone where the major coarse grain transport occurs and the active geomorphology is developed (Kirk 1974). The peak of the swash zone is generally associated with a high tide berm which accretes or erodes dependent upon the wave energy and tidal phase; in some cases, being removed completely during storm conditions causing a flatter profile, or driven further up the beach, which can produce multiple relict berms caused by storm conditions followed by longer periods of low or moderate energy (Pontee et al. 2004; Bergillos et al. 2016). Below the mean water level, a steep break-point step or nearshore face is often present where depth increases and is the cause of the relatively short breaking

zone and characteristic plunging or surging breakers associated with mixed and pure gravel beaches (Kirk 1975; Ivamy and Kench 2006).

The behaviour of these features and reaction to wave and tidal forcing is debated. The Duncan model (Duncan 1964) states accretion occurs when the swash lens passes over unsaturated sediment, the infiltration of water then reduces capacity and a portion of suspended (or bed load) sediment remains above the saturated level. When the tide and associated swash lens drops the exfiltration of the groundwater is added and the backwash velocities are increased, causing erosion. This has been supported by observation on sand beaches (Waddell 1976) though direct field observation of this process within MSG beach research is conflicting: Kulkarni et al. (2004) observed significant erosion during the beginning of the rising tide which reduced with tidal height, stating the cause of this maybe due to a thinning of the boundary layer/swash lens increasing the near bed velocity, though could not corroborate this with observed data. Mason (1997) and Ivamy and Kench (2006) support this observation and state the increased sediment mobility is likely due to the lower hydraulic conductivity of MSG sediment in comparison to both pure-sand and gravel. This infiltration is directly related to the proportions of sand and gravel in the beach face and has been a key focus within MSG beach research; affecting porosity and related hydraulic conductivity (Mason 1997; She et al 2006; 2007, explored extensively in Section 2.4.1).

The Suffolk profiles of Pontee et al. (2004) provide a key overview to the dynamics on the Suffolk coast; but more importantly the distinct behavioural difference between MSG profiles based on their composition, structure and engineering works. Three conceptual models were derived, these consisted of: 1) a soft cliff backed mixed beach (Dunwich); 2) a mixed beach overlaid by a large gravel berm (Aldeburgh/Thorpeness); and 3) a heavily engineered beach within a groyne field (Slaughden). These three profiles show direct parallels with the range of morphodynamics observed at Thorpeness, the large gravel berm observed at the south beach and Ness, engineering works around the erosion prone areas and soft cliffs observed to the north of the village before the Ness headland.

The beach response model of Aldeburgh/Thorpeness defined three types of beach accretions: 1) low energy conditions causing accretion on the lower foreshore; 2) large swell waves, high water levels and plentiful sediment supply causing accretion on large portions of the foreshore; and 3) large waves and high water levels causing accretion in the upper beach. These three accretion patterns were observed to be in both the internal architecture and relic ridges at the site and provide an understanding of the sediment supply to the system and preceding conditions and were a result of the permeable beach face associated with the coarse sediments of the gravel berm.

The behaviour associated with cliff lined and heavily engineered beaches were said to be similar to that of the large gravel berms in optimum conditions, however large erosion events resulted in the profile being less likely to recover naturally. This was even more pronounced in the engineered beach where nourishment schemes and hard engineering had limited the sources of naturally occurring sediment and resulted in low- or impermeable surfaces, whereas the cliff lined beach was

observed to retreat and therefore supply some finer sediment into the system. A key issue on the engineered beach studied was in some cases the engineering was observed to promote erosion and limit recovery, enhancing scour and providing a physical barrier to onshore sediment movement. These issues appear to be echoed at Thorpeness, where recurring erosional issues are observed in relatively short stretches of the engineered beach, though the question of whether the area is a region of wave focusing which has resulted in the need to protect the beach front needs to be assessed.

2.4 Hydrodynamic Characteristics

The conceptual models outlined in the previous section are based upon the observation of behaviour in the field or physical models, these models often show conflicting behaviour between sites or due to the profile parameters. It is important to note within beach hydrodynamics research that there has been a historic trend of pure sand research leading the field, defining concepts and understanding, followed by pure gravel and MSG being often overlooked or over simplified. A recent example of this is the development of the numerical profile evolution model XBeach (Roelvink et al. 2009), which was adopted, modified and validated into XBeach-G (Williams et al. 2012; McCall et al. 2015) for pure gravel beaches and although an MSG module has been developed, validation with mixed sediment distributions has not been carried out and studies using it on MSG beaches have instead opted to use a single representative median grain size (Bergillos et al. 2017b). The key reason for this is the complexity of MSG beach processes being strongly linked to the bi- or multi-modal sediment size distribution. To analytically, numerically or even conceptually model an MSG system requires a larger understanding of the range (spatially: vertically, long- and cross-shore and temporally) of sediment sizing and proportions from which its behaviour can be established through the response of the differing sediment size and proportions to hydrodynamic forcing.

Mason and Coates (2001) reviewed mixed beach hydrodynamic characteristics to the year 2000. In this, the hydrodynamic processes were grouped into first and second order characteristics, first order characteristics were deemed to have the most influence on behaviour and consisted of porosity/hydraulic conductivity, infiltration and ground water, wave reflection and threshold of motion whilst second order have a relatively smaller impact on beach behaviour and consists of clast shape, tidal range, specific gravity (of particles), armouring and chemical processes. This section seeks to establish the major research outputs since this review, expanding on the important features of MSG beach dynamics and establishing current trends and foci in the hydrodynamics of MSG beach in literature.

2.4.1 Porosity and hydraulic conductivity

The ease at which water can move through the pores of sediment is defined as its hydraulic conductivity (k). This parameter within pure gravel and MSG beaches is fundamental in defining and characterising the sediment transport processes within the swash zone and is the primary control of beach slope (Inman and Bagnold, 1963).

Arguably porosity and the resulting hydraulic conductivity are the key parameters which affect MSG beach behaviour; directly altering infiltration and energy dissipation. It is one area within MSG beaches that has seen a strong focus in research (Mason 1997; López de San Román Blanco 2003; López de San Román-Blanco et al. 2006; She et al. 2006, 2007), driven by the need to understand the effect of beach nourishment and how the range of sediment sizes dredged offshore can affect the dynamics in the long- and short- term.

Greater wave energy dissipation attributable to greater bed roughness was theorised to be the reason for steeper profiles and demonstrated partially by the field and laboratory of experiments of (Powell 1989; Carter et al. 1990). This assertion conflicts with Quick and Dyksterhuis (1994) who suggested the steeper faces were caused by net onshore sediment transport due to bed shear stress asymmetry occurring during the wash and backwash cycle.

Taking uniform sediment as a starting point, hydraulic conductivity is dependent upon sediment size and sorting and clast shape. The hydraulic conductivity of gravel is observed to decrease with an increasing percentage of sand, and so understanding the range of sand ratios within the beach profile is essential to characterise profile response and swash dynamics in the same way gravel beaches are observed to have vastly different swash zone hydrodynamics to pure sand beaches a mixed beach of varying proportions can show varying swash processes based on the proportion of sand and gravel. Mason (1997) measured exceedance of 25% sand (20% for fine sand) as the critical value, reducing the hydraulic conductivity of the substrate by up to two orders of magnitude as sand increases from 20 to 30% proportion by weight. This observation was investigated along with porosity in López de San Roman-Blanco (2003) based on initially categorising the mix proportions by porosity of the gravel particles in relation to the sand content:

Where λ is percentage of sand by weight, porosity of gravel is n_g and sand is n_s and the density of gravel and sand is equal and represented by ρ_s .

Under-filled – the sand does not fully fill the pores between gravel grains:

$$n_{under-filled} = \frac{n_g - \lambda}{1 - \lambda} \quad (2.2)$$

Over-filled – there is more sand than space within the pores of the gravel:

$$n_{over-filled} = \frac{\lambda n_s - \lambda}{1 - n_s(1 - \lambda)} \quad (2.3)$$

Fully-filled – the sand fully fills pores between gravel grains; a transition zone between the two occurring when the sand volume is equal to the gravel pore volume and is termed the ‘critical point’ ($n_{under-filled}=n_{over-filled}$):

$$\lambda_c = \frac{n_g(1 - n_s)}{1 - n_s n_g} \quad (2.4)$$

She et al. (2006; 2007) explored porosity and hydraulic conductivity of mixed grains based on these categories. Conceptually the process can be simplified to a series of steps. Water will always find the path of least resistance, and so in pure gravel, this is simply defined by the pore diameter. As sand is added (to an under filled state) two pathways are created. The first being through the gravel pores and the second through any sand present. As this system approaches a fully-filled state hydraulic conductivity decreases due to a reduction in the area in which water can flow. Once fully-filled the cross-sectional area in which water can flow is at a minimum and the gravel then acts to only reduce the cross-sectional flow area. As more sand is added the system becomes ‘overfilled’ and tips the hydraulic conductivity towards that of pure sand, increasing sand percentage further increases hydraulic conductivity from the low observed at ‘fully filled’.

Porosity (n) of bimodal sediments can be calculated through one of two equations (2.6 and 2.7) dependent on the percentage of sand in relation to critical porosity (λ_c)

$$\lambda_c = \frac{n_g(1 - n_s)}{1 - n_g n_s} \quad (2.5)$$

$$n = \frac{\lambda n_s}{1 - n_s(1 - \lambda)} \quad (\lambda \geq \lambda_c) \quad (2.6)$$

$$n = \frac{n_g - \lambda}{1 - \lambda} \quad (\lambda \leq \lambda_c) \quad (2.7)$$

$$n = \frac{\lambda n_s}{1 - n_s(1 - \lambda)} \quad (\lambda \geq \lambda_c) \quad (2.8)$$

Quantifying porosity allows the hydraulic conductivity to be defined based on the portions of sand and gravel. Letting k_s and k_g be the hydraulic conductivity of sand and gravel respectively, a number of assumptions need to be made:

- Laminar flow through the substrate obeys Darcy’s law:

$$v_s = k_i i \quad (2.9)$$

where v_s is velocity and i is hydraulic gradient;

- Flow through the sediment is analogous to flow through parallel pipes of length L and diameter d where d is proportional to sediment size and porosity and;
- The Hagen-Poiseuille law describes the laminar pipe flow, where energy loss h_e is related to the seepage velocity $v_{seepage}$, μ is the dynamic viscosity of water, g is the acceleration due to gravity, and ρ is fluid density:

$$h_e = \frac{32\mu Lv_{seepage}}{\rho g d^2} = \frac{Lv_{seepage}}{Cd^2} \quad (2.10)$$

OR

$$i = \frac{h_e}{L} = \frac{v_{seepage}}{Cd^2} \quad (2.11)$$

From here the three conditions (under-, fully-, and over-filled) can be defined. In the case of under-filled gravel, two pathways are available, one through the sand and one through any remaining pore space within the gravel which remains open:

$$k_{underfilled} = k_g(1 - \xi_n)^2 + k_s n_g \xi_n \quad (2.12)$$

where:

$$\xi_n = \frac{(1 - n_g)\lambda}{n_g(1 - n_s)(1 - \lambda)} \quad (2.13)$$

In the case of over-filled sediment, the only pathway available is through the sand, and the gravel simply decreases the available cross section of the sand pathways by volume, and so:

$$k_{overfilled} = \frac{k_s \lambda}{\lambda + (1 - n_s)(1 - \lambda)} \quad (2.14)$$

The critical point for the sediment mix can then be calculated through the porosity n_g and calculated hydraulic conductivity of sand k_s :

$$k_c = n_g k_s \quad (2.15)$$

$$k = k_g(1 - \xi)^2 + k_s n_g \xi_n \quad (\lambda \leq \lambda_c) \quad (2.16)$$

$$k = \frac{k_s \lambda}{\lambda + (1 - n_s)(1 - \lambda)} \quad (\lambda \geq \lambda_c) \quad (2.17)$$

These analytical models have been tested in the laboratory and results compared with previous studies (López de San Román Blanco (2003) for porosity and Mason (1997) for hydraulic conductivity). Figure 2.2 and Figure 2.3 show good agreement between the results of the laboratory experiments and the analytical predictions. Most importantly previous observations by Mason (1997) of critical sand ratios of 20% to 30 % showing the largest change in characteristics were confirmed.

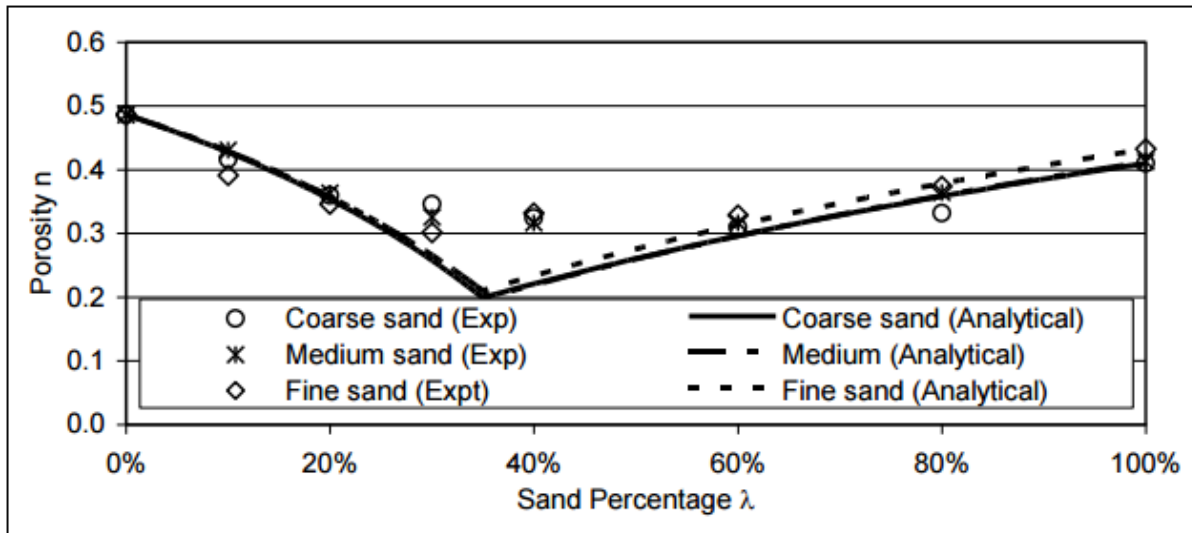


Figure 2.2. She et al (2007) results of porosity experimentation of gravel with a D_{50} of 4 mm and addition of fine, medium and coarse sand against analytical prediction © Crown copyright (Defra);(2008).

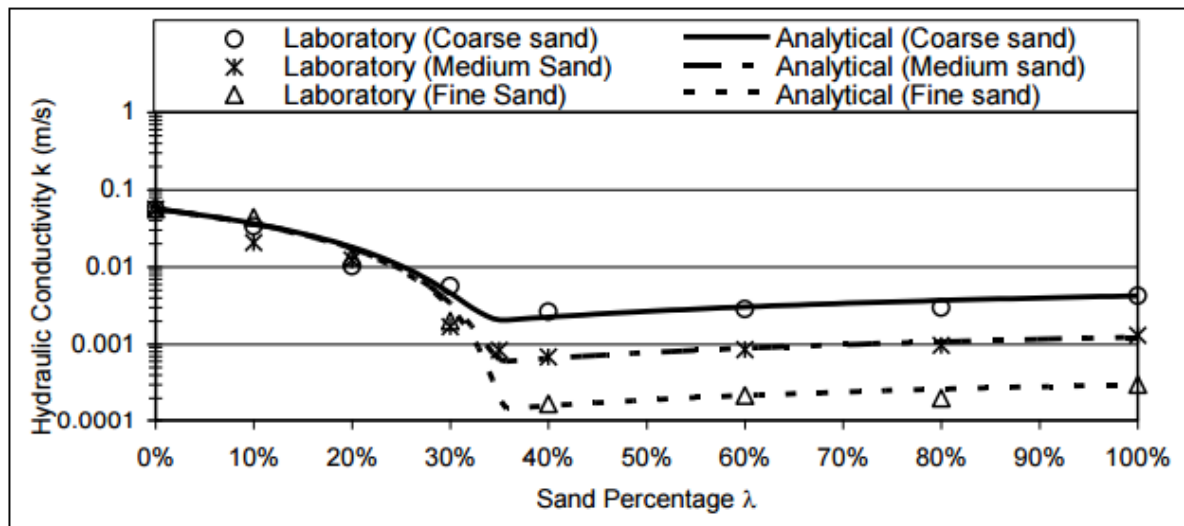


Figure 2.3. She et al (2007) results of hydraulic conductivity experimentation of gravel with a D_{50} of 4 mm and addition of fine, medium and coarse sand against analytical prediction. R&D Technical Report FD1923/TR © Crown copyright (Defra);(2008).

The effect of this phenomena is likely to be the biggest factor in understanding the response of an MSG beach to the driving forces of waves and currents and understanding how the behaviour differs from that of pure gravel and sand systems. In the laboratory defining proportions of sand and gravel for experimentation is simple as samples can be controlled. In contrast, there exists no robust methodology for defining this proportion in the field and the variance of MSG beaches make sampling regimes difficult to define. Significant sources of sand (from the cliff face) and gravel (from the Ness) at site compound these difficulties. Within the project, the effect of how sediment (surface and through depth) is sampled will be investigated as well as how defined proportions can be linked with the behaviour of the system.

2.4.2 Infiltration and ground water

The infiltration of water is directly related to hydraulic conductivity of the sediments. A higher infiltration during swash and backwash leads to an asymmetry of kinetic energy between swash and back wash (loss of energy due to flow of water through the substrate, Mason and Coates 2001), which directly effects bed load and suspended sediment movement. The spatial and temporal variability of this hydraulic conductivity caused by differing sediment proportions can have significant effects on the infiltration and resulting groundwater and due to this complexity, this behaviour on MSG beaches has not been explored to the same extent as pure sand and pure gravel beaches (Mason 1997). The effect is important as demonstrated by (Antoniadis 2012, 2013) who shows by physical modelling that the effect of lower infiltration for MSG beaches resulted in less energy dissipating in the swash zone. Consequently, beach crest elevations were observed to be higher than a pure gravel variant.

2.4.3 Wave reflection

The steepness of a beach directly affects the presence and degree of wave reflection. On pure and mixed gravel beach types, the coarser grains allow steeper beach profiles to form (Section 2.2). MSG beaches tend to form steep upper beach profiles and shallower low tide terraces due to the variation in sediment sizes (gravel berms on the upper beach and sands in the inter tidal) which can enhance and decrease reflectivity dependent on tidal level and the spring-neap cycle. However, the conductivity of the sediment also plays a role in reflectivity, with coarser grains absorbing rather than reflecting the energy, this was reported when Kobayashi et al. (1991) investigated the reflectivity of irregular incident wave trains in the laboratory reported that a thick permeable gravel layer greatly reduced reflectivity when compared with an impermeable slope. This has been verified subsequently by numerical simulations by Kobayashi and Wurjanto (1993). López de San Roman-Blanco et al. (2006) alludes to an in-preparation study by Pedrozo-Acuña et al. (2006) focused on wave reflection, concluding that there is a marked difference between MSG and pure gravel beach reflectivity, correlated with grain size and the surf-similarity parameter (Iribarren number) though it appears the scope of this paper changed and the published and the following paper (Pedrozo-Acuña et al. 2007) was instead focused on pure gravel behaviour and an empirical approach to evaluating pure and MSG beach behaviour respectively.

2.4.4 Transport modes and threshold of motion

Quantification of the velocity required to mobilise individual grains as bed- or suspended-load is required for calculation of sediment transport. This ‘threshold’ velocity is generally related to a characteristic sediment grain size. However, with MSG the combination of multi-modal sediment components allowing infill and reducing bed velocities it is difficult to define a single threshold of motion that correctly represents a threshold for the mixed sediment (Mason and Coates 2001).

Laboratory work of Kuhnle (1993) and Wilcock et al. (2001) are most relevance to MSG beach dynamics. Both considered unidirectional flow over bi-modal sediments, the first analysing mixtures of 0, 10, 25, 45 and 100% gravel, the second 66, 73, 79, 85 and 96% gravel. Mason and Coates (2001) highlighted that the Kuhnle (1993) study did not represent the mixture proportions reported in mixed beach studies. This was addressed by Wilcock et al. (2001) using sediment mixtures with the critical range (0-30% sand) described previously for hydraulic conductivity and infiltration. Kuhnle (1993) found that with all mixtures, the sand portion was observed to move at approximately the same shear stress, but gravel fractions movement were a function of grain size. Wilcock et al. (2001) concluded that total transport rate is heavily dependent of sand content. With gravel transport rates increased by an order of magnitude as sand content increased (within the same flow velocity). This increase was observed to be the most rapid between sand content of 14-27%, again suggesting a link with the filled and over-filled pores outlined within 2.4.1 and being of critical importance when designing nourishment schemes.

Many threshold of motion experiments have examined unidirectional flows over flat beds of sediment. To understand fundamentals this is important, however, it neglects the differing effects of swash and back wash and the impact of turbulent multi-directional flow caused by wave impact from which substantial sediment movement occurs on MSG beaches. The research of Ivamy and Kench (2006) suggests that this asymmetry in wave shear stress generally results in the dominance of uprush sediment transport, occurring in 80% of cases (in moderate and low conditions), the 20% when back rush was dominant only occurred during a falling tide suggesting the combination of backwash, gravity and tidal influence can cause net movement offshore.

2.4.5 Second order characteristics

The second order characteristics (Mason and Coates 2001) of clast shape, tidal range, specific gravity (of particles), armouring and chemical processes were generally said to have a smaller influence of the hydrodynamics and behaviour on an MSG beach. Overall this seems to continue, with less direct focus on these properties in contemporary literature though some advances have been observed.

At the time of Mason and Coates (2001), the effect of chemical processes on MSG dynamics were limited to the initial observations of McFarland et al. (1994) on the steep scarps occurring on nourished beaches being a result of chemical cementation and physical compaction. These assumptions have only recently been extensively investigated by Zarkogiannis et al. (2018). Whom investigated this beach scarping through textural, geochemical and mineralogical analyses of the sediment utilising physical PSD measurement (sieving and laser diffraction), pH, moisture content, X-ray and isotopic/organic carbon analysis. The study identified a series of conditions which promoted the scarping of nourished beaches: 1) techniques and machinery used to distribute and shape the beach causing compaction and grain fracture; reducing porosity; 2) water (from swash and precipitation) percolating the fine and medium sediments through to a deeper intermediate layer; 3) this densely packed layer promoting interaction between clay minerals (calcium cations), weakly

cementing the sediment; and 4) a wave or erosion event promoting the formation of the scarps. These processes directly affect beach management schemes and it is suggested that coastal managers attempt to source nourishment sediment with the lowest possible fine and medium grain portions whilst the methods of placement and formation of the artificial beach needs to be considered to lower impaction and grain fracture associated with heavy machinery.

The effect of clast shape on entrainment and related beach sorting was explored by Bluck (1967) and Orford (1975) where shape sorting is related to how flat the clast is and the dominant energy in a system; if the energy is close to the threshold of motion sorting occurs with the flatter clasts moved landward and more spherical casts moved with the backwash and gravity seaward. If the energy vastly exceeds this threshold no sorting occurs as all particles are mobilised. Field observations by Stark and Haye (2016) concur with this model where particle tracking showed flat particles travelling the largest distance (generally upslope) and spherical tracers travelling less distance in the same conditions (generally seaward).

2.5 Summary

The characterisation of MSG beaches is difficult. In this thesis an MSG beach is simply defined as a system in which there are two or more modes of sediment, split between sand ($62.5 \mu\text{m}$, 4ϕ) to gravel and cobbles (64 mm , -8ϕ) and that the size of these modes have a significant impact on the hydrodynamic and morphological characteristics of the beach.

Due to the complexity of the systems, no standard methodology has been defined for characterising PSDs and the relative proportions of sand and gravel. Instead, studies utilise a range of methods to define the sediment of the system including large but a limited number of bulk samples or numerous smaller ones. The contrast in these methodologies can ultimately mean that a range of results and conclusions can be defined from the same system.

Sand and gravel proportions are integral to the behaviour of MSG beaches due to how it effects porosity and the resulting hydraulic conductivity, which in turn impact the beach slope, reflectivity, swash processes and sediment transport. A mixed beach is hypothesised to show similar characteristics to a gravel or sand beach based on the proportion of sand. Though this behaviour becomes more distinct with increasing coarse or fine materials. A beach is least porous and conductive when at a 'fully filled' state, in which all pores between gravel are filled with sand.

3. The Beach Morphology and Response

3.1 Introduction

This chapter describes the spatial and temporal variability of beach morphology at Thorpeness and analyses the effects wave climate on beach mobility in the very complex coastal setting of the study area. The content replicates the aspects presented in Atkinson and Esteves (2018) and includes additional investigation into the effects of high-water levels (tides and storm surges), spatial changes through terrestrial laser scanning and persistence of wave conditions on beach behaviour. Persistence analysis is commonly applied in atmospheric sciences as a forecasting element and refers to “the atmosphere’s tendency to maintain its current state” (Franzke and Woollings 2011). Here, a similar concept is used to quantify the persistence of wave conditions (herein wave persistence), using a novel approach that considers the stability of both wave height and direction over time.

Significant changes in sedimentary coasts are often associated with extreme storms (Brooks et al. 2017; Burvingt et al. 2017), storm clusters (Davidson et al. 2013; Karunarathna et al. 2014; Dissanayake et al. 2015; McSweeney and Shulmeister 2018), storm surges (Gomes et al. 2018), and their interaction with complex nearshore bathymetry (Hegermiller et al. 2017; Limber et al. 2017). Recent studies have investigated the effects of both bimodal seas and bimodal wave directions. Bimodal seas refer to swell and sea waves simultaneously occurring, forming a bimodal wave energy spectrum (Coates and Hawkes 1998). Bimodal seas may cause a larger impact on coasts due to a combination of higher wave heights from sea waves and a longer period from swell waves, leading to longer run-up and the potential for overtopping (Mason and Dhoop 2018). Bimodal wave directions refer to locations where the dominant wave direction oscillates through time, causing significant changes in the direction of longshore sediment transport and associated shoreline changes (Adams et al. 2011; Burningham and French 2016; McSweeney and Shulmeister 2018). In Suffolk, the interaction of bimodal wave directions with nearshore features (e.g. sand banks) increases the longshore variability of beach response (Burningham and French 2016), as parts of the coast may be more sheltered from one wave direction and exposed to others.

Although the duration of stormy conditions is recognised as a factor contributing to coastal erosion (e.g. Esteves et al. 2012), the effects of prolonged periods of consistent conditions are rarely investigated. Local observation at site has suggested that continual erosion issues are associated with moderate and continual wave and wind from the south. To assess this the analysis of wave persistence can provide a quantitative assessment that reflects time periods in which conditions (e.g. wave height and direction) showed little change. The technique is often used to assess climate variability (Franzke and Woollings 2011; Lenton et al. 2017), particularly in the analysis of wind speed and direction trends (Vogel et al. 2007; Koçak 2008, 2009; Cancino-Solórzano et al. 2010).

These analyses have been applied to assess potential windfarm yield (Villegas et al. 2017), or to inform plans to mitigate forest fire spread and pollutant dispersion (Koçak 2008). The concept of persistence has been used within the identification of thresholds (the amount of time wave height exceeds a certain value) for engineering purposes (Kuwashima and Hogben 1986; Feld et al. 2015). Persistence analysis methods have not been applied to studies of coastal processes though has been considered indirectly, through the effects of climatology phenomena (such as the North Atlantic Oscillation) on coastal change (Masselink et al. 2014).

The analysis focuses on beach morphology measured along five cross-shore transects within a 2-km-long shoreline between Thorpeness and the Sizewell nuclear power station (Figure 3.1) over a period of nine years. With an emphasis on (1) identifying alongshore variability in beach mobility based on biannual topography surveys from January 2009 and March 2018 and at shorter time periods based on 11 surveys between July 2016 and March 2018, and (2) establishing possible relationships between beach mobility and wave conditions.

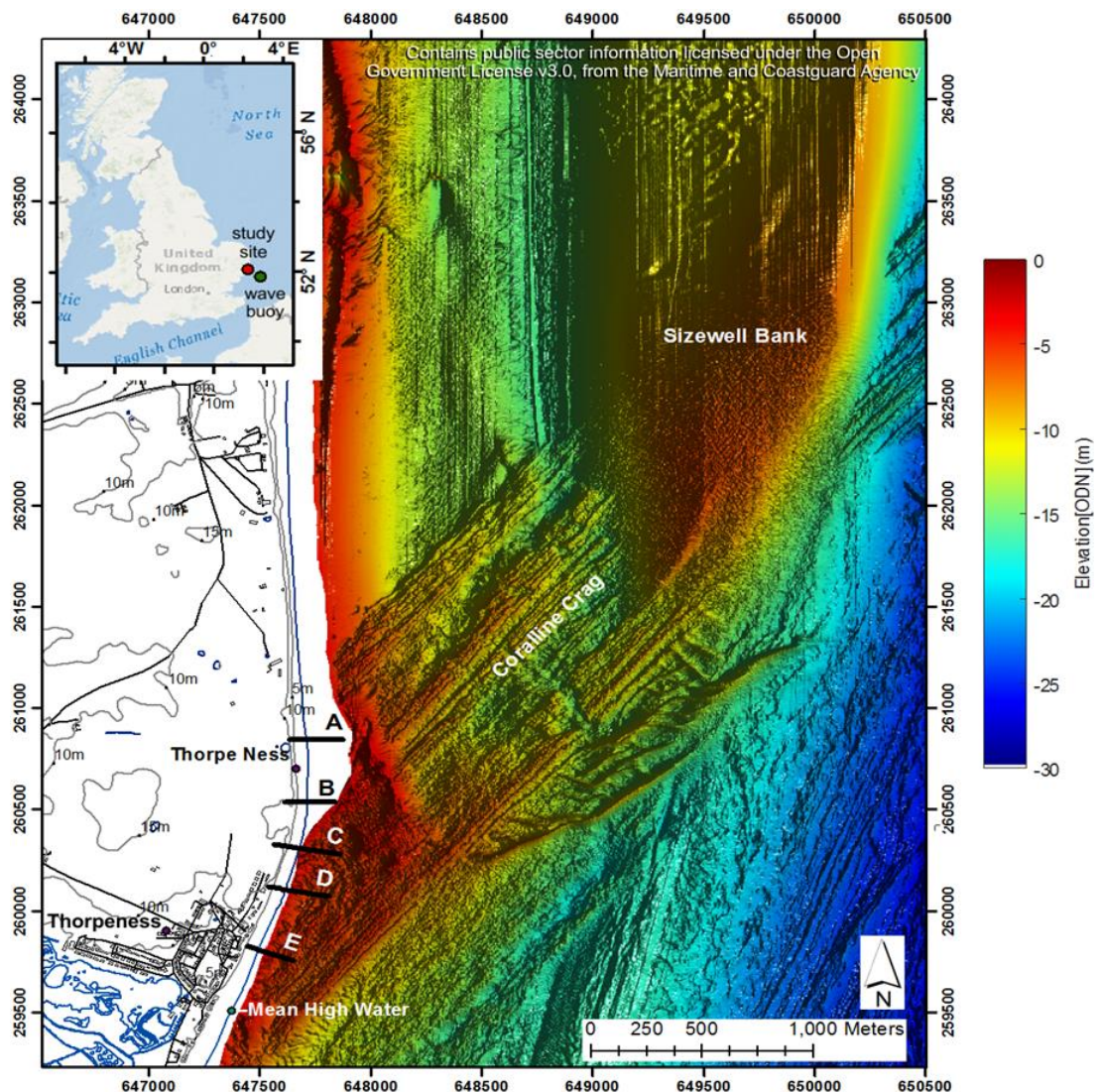


Figure 3.1. Study area showing location of the five beach transects between Thorpeness village (south) and Sizewell nuclear power station (north) in Suffolk (East Anglia, United Kingdom), and offshore bathymetry measured in January 2017.

3.2 Methods

3.2.1 Beach topography

Beach topography data were used to characterise beach morphology and quantify magnitudes and rates of change. Three sets of data were analysed: (1) 19 biannual beach profiles measured from 2009 to 2018 by the Environment Agency (EA) along five selected cross-shore transects; (2) 15 Real-Time Kinematic Differential Geographical Positioning System (RTK-DGPS) topographic surveys along the same five cross-shore transects conducted at variable intervals (seasonal, monthly, and pre- and post-storm) between July 2016 and March 2018; and (3) nine terrestrial laser scanner surveys covering Thorpeness urban seafront between the transects. Whenever possible, the surveys were conducted during spring tides, to enable the largest possible intertidal coverage.

The terrestrial laser scanner (Leica C10 terrestrial laser scanner coupled with Leica GPS Viva GS10 rover and base station) enabled acquisition of high-resolution beach and cliff elevation data (Figure 3.2) with a vertical and horizontal accuracy of 0.8 cm and 1.5 cm, respectively. The point cloud was processed using the proprietary Leica cyclone software to remove spurious data (e.g. water and sun reflections, beach tents, people etc.). Additional quality control flagged areas of low point coverage caused by shadowing of morphologic features (Figure 3.2a) or the removal of spurious data and removed them from analysis if there were no points within a 1 m radius. Then, natural neighbour interpolation was applied to create a digital terrain model with a spatial resolution of 0.1 m using Matlab ®.

The EA beach monitoring programme has been gathering topography data at cross-shore transects in the study area biannually since 2009 (using the same RTK-DGPS instrumentation), sometimes at shorter time intervals to cover beach nourishment projects or periods of critical erosion. Five transects (Figure 3.1 and Figure 3.2) from the EA coastal monitoring scheme were selected for analysis here as they reflect the distinct local settings and morphological features. These five transects are herein identified sequentially from north to south as Transects A to E (their equivalent EA reference, coordinates of starting point and azimuth are given in Table 3.1):

- Transect A (EA profile TN007) is located at the north end of the study area crossing the gravel ridges of the Ness.
- Transect B (EA profile TN013) crosses the south flank of the Ness, where a gravel berm is often prominent and backed by a vegetated and eroding cliff talus.
- Transect C (EA profile TN017) is characterised by the presence of a rapidly retreating soft cliff, a gravel upper beach, and a sandy lower beach (although temporal variations occur).
- Transect D (EA profile TN021) crosses a local erosion hot-spot, where the beach profile is influenced by gabions, geobags, and gravel nourishment. The gabions were placed in the 1970s and the geobags in 2011 after a storm exposed and damaged the gabions in the spring

of 2010. These structures are periodically exposed during storms, with gravel nourishment occasionally used to restore the beach profile and cover the structures.

- Transect E (EA profile TN026) is located south of the coastal protection structures, approximately at the centre of the village's seafront housing.



Figure 3.2. (a to e) Beach morphology along transects A to E (respectively) and (f) their approximate location within the study area shown on an oblique aerial photograph taken after an intense erosion event in 2010 (Photos a to e by L.S. Esteves; f by www.mike-page.co.uk).

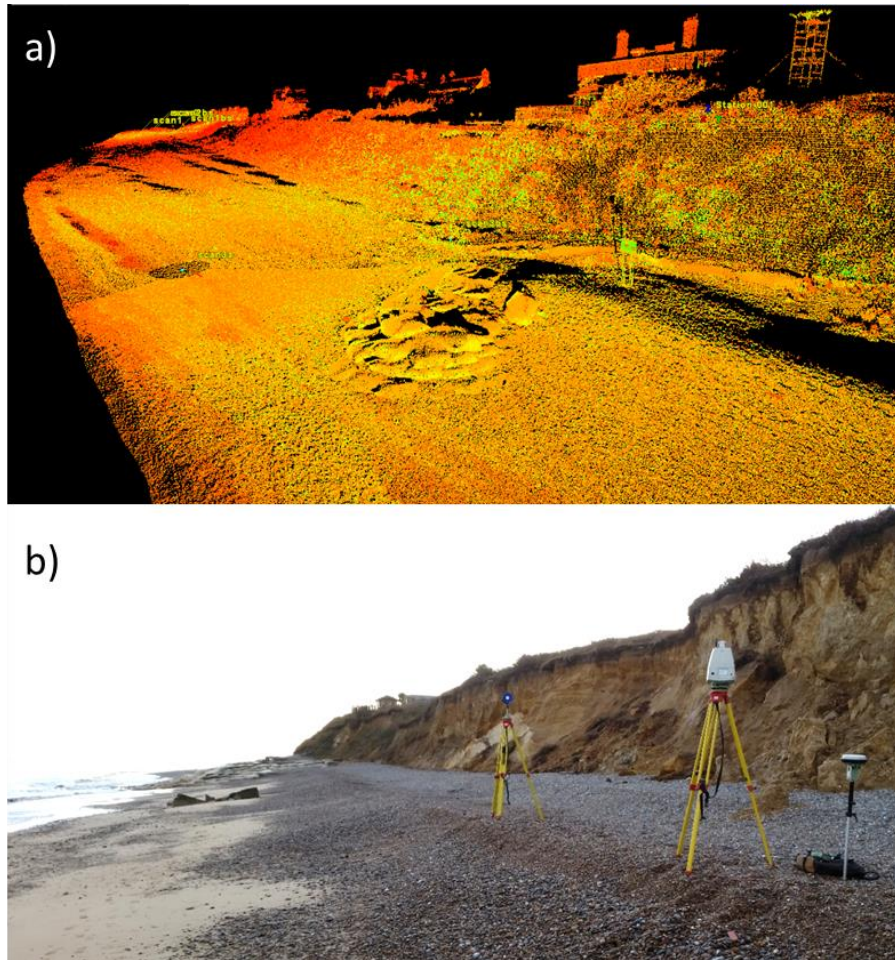


Figure 3.3. a) Georeferenced laser scan point cloud showing the northern end of the geobags and radar site (03-Aug-2016) note the shadowing (dark areas) caused by complex geomorphology. b) Laser scanner equipment and DGPS system used for geo referencing of the point cloud at the cliffs north of Thorpeness.

Table 3.1. Coordinates of starting point and azimuth of the five beach transects analysed here and their equivalent EA reference.

Transect	EA Ref.	Easting (m)	Northing (m)	Azimuth (°)
A	TN007	647628	260845	90
B	TN013	647699	260535	90
C	TN017	647565	260318	100
D	TN021	647541	260119	100
E	TN026	647440	259827	110

Considering the temporal distribution of the beach topography data, analyses were undertaken on two sets of data: (1) Dataset 1 consisted of 19 biannual monitoring surveys conducted by the Environment Agency (EA) from 2009 to 2018; (2) Dataset 2 consisted of 15 beach surveys conducted at variable intervals between July 2016 and March 2018; and Dataset 3 consisted of the quality controlled laser scan surface data over 9 surveys at site (Table 3.2). Dataset 1 provided a longer-term context, in which interannual variability and the effects of shorter-term changes could be analysed, including beach recharge works and the stormy winter of 2013–2014. Dataset 2 and 3 included seasonal, monthly, and pre- and post-storm surveys aiming to better understand beach response, magnitudes of change, and spatial variability that are not captured through regular biannual monitoring. The inter-comparison of profiles collected by the EA and within this thesis were analysed for uncertainty to

establish how different sampling rates and error caused by instrument precision impacted volume calculations. The results (outlined in Appendix A) showed the magnitude of changes occurring at site were much larger than these errors (not exceeding 2.5 % of calculated profile area) and so inter-comparison of datasets and profiles were acceptable.

Table 3.2. Dates of topographic surveys included analysed in this chapter.

Date	Dataset 1	Dataset 2	Dataset 3
07-Jan-2009	x		
27-Jul-2009	x		
07-Jan-2010	x		
20-Jul-2010	x		
27-Jan-2011	x		
22-Jun-2011	x ^a		
22-Dec-2011	x		
26-Jul-2012	x		
06-Feb-2013	x		
18-Jul-2013	x		
08-Feb-2014	x		
05-Aug-2014	x		
29-Jan-2015	x		
05-Aug-2015	x		
02-Feb-2016	x		
26-Jul-2016	x	x	
03-Aug-2016		x	x
22-Oct-2016		x ^b	x
06-Dec-2016		x	x
09-Jan-2017		x ^c	
19-Jan-2017		x	x
13-Feb-2017	x	x	x
21-Mar-2017		x	x
27-Jun-2017		x	x
20-Jul-2017	x	x	
27-Sep-2017		x	x
16-Jan-2018		x	x
26-Feb-2018	x	x	
07-Mar-2018		x	
27-Mar-2018		x	

^a Transect A and C measured on 8–9 June; ^b unavailable for Transect C; ^c available only for Transects A and B.

3.2.1.1 Indicators of coastal change

For each transect and survey date (Table 3.2), the beach width at mean low water springs (MLWS), mean water level (MWL) and mean high water springs (MHWS) were estimated. These tidal levels were defined relative to ODN: MHWS = 1.22 m, MWL = 0.16 m, and MLWS = -1.01 m (Williams 2014). Similarly, for each transect and survey date, the profile cross-section area above and between MLWS, MWL and MHWS was estimated using the trapezoidal approximation (interpolated 0.25 m cross-shore). For consistency, beach widths and profile areas were calculated using a fixed landward boundary that encapsulated the area of change observed in each transect across the period of analysis. Additionally, where required (i.e., when surveys were undertaken during higher tidal levels), profiles were linearly extended to intersect the MLWS using the average inter-tidal beach slope of each transect. The changes in beach width and profile area between consecutive surveys in each dataset and the respective changes per day were also calculated.

Indicative spatial and volume changes were assessed through the laser scan derived digital terrain models (DTMs). Volumes of accreted, eroded and total changes were calculated above and below

MHWS between each of the laser scan surveys and periods indicating significant changes or morphological evolution were investigated further. The results of which are presented in 3.3.4.

3.2.2 Wave conditions

Offshore wave data were obtained from the Cefas West Gabbard (2006–2016, 51°58.88' N 002°04.73' E) and West Gabbard 2 (2016–2018, 51°57.17' N 002°06.53' E) ~40 km southeast of the field site. Initially, basic annual (Jan-Dec) and winter (DJF) statistics from the previous 10 years (2007 – 2017) were calculated to establish the range of conditions between years and the (generally) most energetic months within the North Sea (Fugro Geos 2001; Feld et al. 2015):

- mean deep-water significant wave height measured in meters (H_s);
- 95th percentile of H_s ;
- mean wave power (Wp), calculated using Equation (3.1, Davidson et al. 2013), where T_p is the peak period measured in seconds:

$$Wp = H_s^2 T_p \quad (3.1)$$

- percentage of time of northerly waves (Dir_p : 300 – 60°);
- percentage of time of southerly waves (Dir_p : 120 – 240°);
- percentage of time wave heights exceeded 2.5 m, following a storm threshold defined by Bennett et al. (2016);
- percentage of time wave heights exceeding 2.5 m approached from a northerly direction (300–60°);
- percentage of time wave heights exceeding 2.5 m approached from a southerly direction (120–240°); and

To assess the influence of the wave energy and two dominant wave directions on beach response, the parameters were then calculated for the time periods between beach surveys in Dataset 1 and Dataset 2 and statistical analysis (see 3.2.4) used to identify links.

3.2.2.1 Wave Persistence

Within the atmospheric sciences, an autocorrelation function (ACF) is often utilised to statistically define persistence (Wylie et al. 1985; Vogel et al. 2007; Franzke and Woollings 2011). The ACF is a technique for measuring the correlation (r_k) of observations (y) as a function of the time lag (k_L , k_2, \dots, k_n) between them (y_t and y_{t+k}):

$$r_k = \frac{c_k}{c_0} \quad (3.2)$$

Where c_0 is the variance in the time series of duration T and:

$$c_k = \frac{1}{T} \sum_{t=1}^{T-k} (y_t - \bar{y}) (y_{t+k} - \bar{y}) \quad (3.3)$$

In this case, the time lag is the time between records (30 minutes). Each ACF begins with an unshifted series of data (r_0), where $r_0 = 1$, as an unshifted data series will show perfect correlation with itself. Persistence is then calculated through the area of the triangle (Figure 3.4) between the first shift (r_1) and the first shift in which the autocorrelation function is equal to 0 (k_0) defined as the ‘persistence via autocorrelation function approach’ (P_{acfa} , Koçak 2008).

$$P_{ACFA} = \frac{1}{2} r_1 (k_0 - 1) \quad (3.4)$$

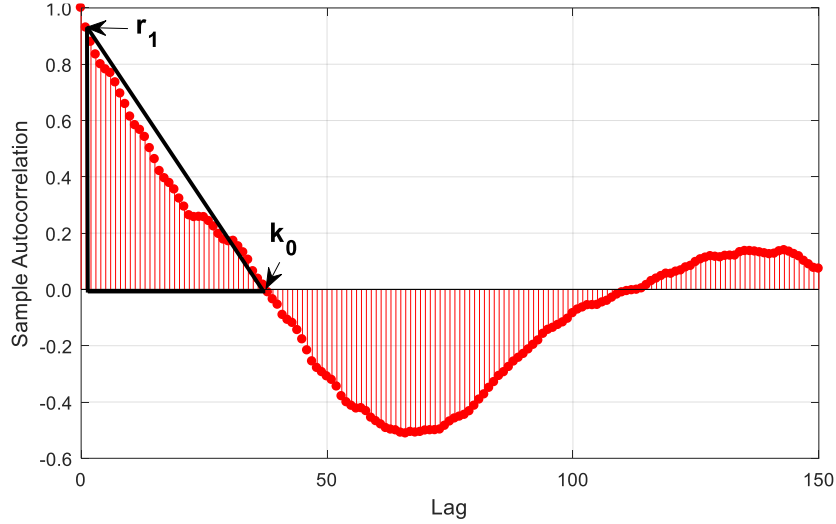


Figure 3.4. Example autocorrelation function correlogram from a 500-point time series over 150-time steps (lag) with the P_{ACFA} definition from k_1 to k_0 (in this case $k_0 = 35$).

An introduction of a directional component to persistence analysis adds complexity, directional data is difficult to statistically analyse when incorporating mean average calculations inherent within the ACF (Fisher and Lee 1994). A simple example of this is the mean of two directions 359 and 1 is 180, whereas in directional space it would be 0. With a direction (in this case peak wave direction) having an associated magnitude (significant wave height) the time series can be analysed as its meridional velocities of u (east-west) and v (north-south, Vogel et al. 2007).

To assess persistence at the field site the data from the West Gabbard buoy (between January 2015 to February 2018) were analysed. The time series of H_s and Dir_P were transposed to their zonal and meridional velocities of u (east-west) and v (north-south) respectively, through the equations 3.5 and 3.6:

$$u = H_s * \cos(MDir) \quad (3.5)$$

$$v = H_s * \sin(MDir) \quad (3.6)$$

Where $MDir$ defines the mathematical direction (of East = 0 degrees, rather than oceanographic direction of east = 90 degrees). The u and v component time series were then analysed within a 30-day moving window with a 1000 lag (approximately 20 days) ACF at each measurement point.

Within each 30-day window, missing data was flagged and periods with >1% missing were removed from the record.

In some cases, an ACF can continue near 0 (k_0) but not drop below (Vogel et al. 2007). This increases the persistence value derived from the calculation of P_{ACFA} even though the correlation itself is low. To mitigate this the k_0 can be shifted to 0.05 (Vogel et al. 2007) but on investigation, this method can still result in high P_{ACFA} values when the ACF indicates relatively low persistence. Figure 3.5 provides an example of an ACF calculated from the v -component time series at the West Gabbard buoy at 05:00 06-Oct-2017. This ACF reports relatively high P_{ACFA} values though is observed to drop rapidly to 0.051 within 2 days before increasing again and finally reaching k_0 after 4.5 days.

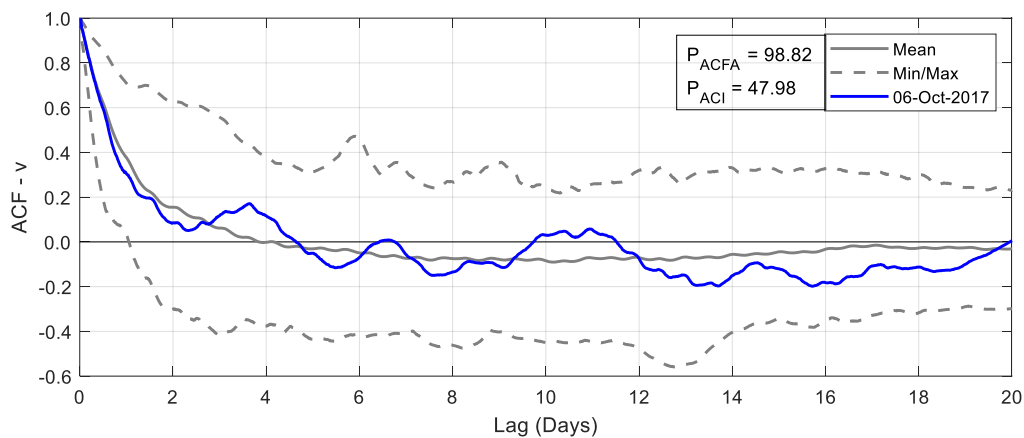


Figure 3.5. Example of an ACF (blue) on 06-Oct-2017 0600 which equates to a to high P_{ACFA} value (98.82) but is observed to drop rapidly within 2 days and where much of the ACF curve before this is below the mean from the dataset (2007-2018).

Interrogation of the wave conditions over this period (Figure 3.6) show this rapid drop and then recovery of the ACF is due to a southerly wave event occurring after a period of northerly waves, which is then followed by northerly conditions (08-Oct-2017). To mitigate instances where this occurs an integration of the curve instead is calculated to provide a value more indication of the stability of the ACF (Persistence via Autocorrelation Integral, P_{ACI}) for the u (P_{ACIU}) and v (P_{ACIV}) components. This results in the persistence value dropping from $P_{ACFA} = 98.82$ to $P_{ACIV} = 47.96$.

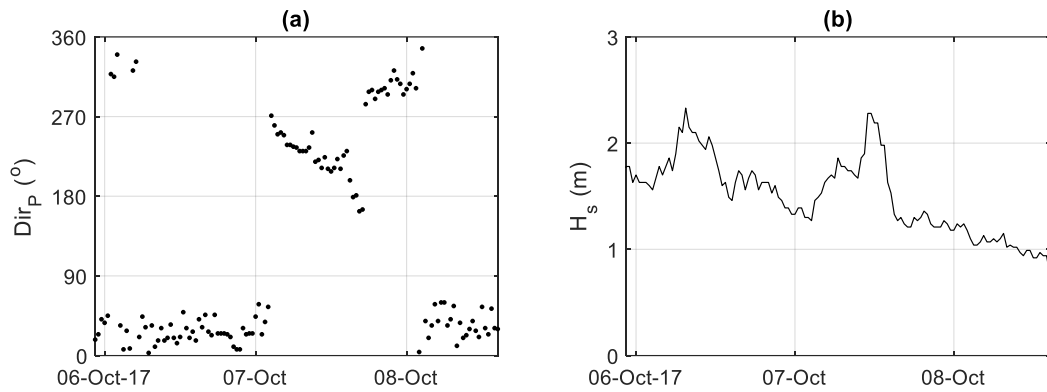


Figure 3.6. Time series of (a) peak wave direction (Dir_P) and (b) significant wave height (H_s) from which the ACF was calculated in Figure 3.5.

The maximum, mean and 95th percentile of each (P_{ACIU} and P_{ACIV}) time series were then used for statistical analysis (3.2.4) against the beach survey data.

3.2.3 Water level analysis

Total water levels are defined as the combination of astronomic tides and tidal residuals. These values were taken from Lowestoft (about 35 km north of Thorpeness), which is the closest Class 1 tidal gauge to the study site. The tidal residuals are calculated by the British Oceanographic Data Centre (BODC) as the difference between predicted astronomical tide (calculated from harmonic constituents and mean sea level pressure: 1013.25 mbar) and observed water level. A positive value indicates a higher than predicted tidal level, a negative value indicates a lower than predicted tidal level. A positive residual is referred to as a storm surge and occurs due to low pressure and onshore winds.

3.2.4 Statistical analysis

Correlation analyses were used to assist the identification of relationships between beach change and driving factors, i.e. wave conditions, wave persistence and water levels values. Pearson's correlation coefficient (r) was calculated only when the assumptions for parametric tests were met by the data. Otherwise, Spearman's rank correlation coefficient (r_s) was used. Analyses were undertaken in IBM SPSS Statistics 24® and Matlab®.

3.3 Results

3.3.1 Characterisation of metocean conditions

Analysis of the historic wave climate provides insight into the variability of the area and establishes how the conditions over the project period compare to previous years. The West Gabbard buoy time-series (Jun-2006 to Mar-2018) indicates a strong bimodality in the direction of offshore waves (Figure 3.7). When considering all wave heights (Figure 3.7a), 43% of the waves approached from the north ($300 - 60^\circ$) whilst 43% approached from the south ($120 - 240^\circ$, Table 3.4). When

considering $H_s > 2.5$ m (3% of all records), waves approaching from the SSW dominate, reflecting 53% of records, while waves approaching from the NNE represent 41% of the records (Figure 3.7b).

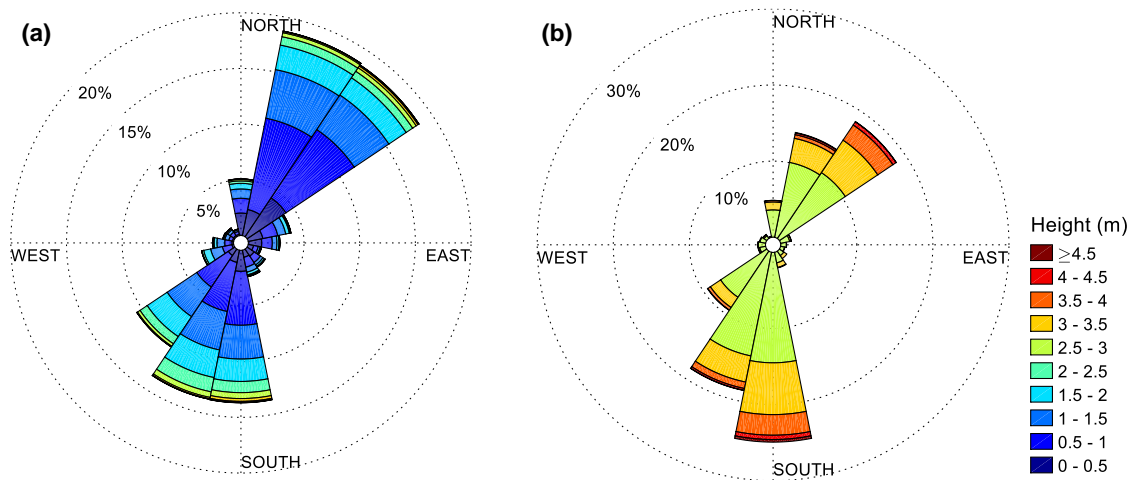


Figure 3.7. West Gabbard buoy wave roses showing Dir_p and H_s (168685 records, 97.98 % data coverage) for the period Jun-2006- Mar-2018 for all waves (a) and waves exceeding 2.5 m H_s (b).

The analysis of yearly and winter statistics (Table 1.1) show inter-annual variability in directional dominance. In most years (8 out of 11) southerly waves are more frequent than northerly waves. Differences between the proportion of waves approaching from a northerly or southerly direction vary from 2-3% (e.g. 2010, 2013, 2015, 2017) to 25% (more northerly waves in 2011). Differences are magnified when only winter months are analysed. Southerly waves are also more frequent than northerly waves in most winters (8 out of 12). However, differences in the proportion of waves approaching from a northerly or southerly direction vary from about 4% more northerly waves in 2012-2013 to as much as 66% more southerly waves in 2013-2014 (when 79% of the time waves approached from a southerly direction and 13% from a northerly direction).

The calculation of persistence parameters provides a quantification of both direction and magnitude of wave energy and time series of the resulting P_{ACIV} and P_{ACIU} values (Figure 3.8) show distinct differences to the underlying proportion of northerly and southerly waves. When the calculated P_{ACIV} (persistence of the N-S, v-component) and P_{ACIU} (E-W, u component) is compared to the proportion of northerly and southerly approaching waves (within a 30-day window), peaks in the P_{ACIV} value (also derived from 30-day analysis) tend to coincide with an increasing directional dominance but often this value reduces even if the period is dominated by northerly or southerly waves (e.g. the winter of 2015-2016).

Table 3.3. Yearly and annual significant wave height statistics for data obtained from the West Gabbard 1 and 2 buoys, including (with some proportion of records from dominant directional dominant years highlighted).

Year	Significant Wave Height (m)				Direction			
	95%ile	Max	Mean	N (%)	S (%)	%Records Hs>2.5	N (%)	S (%)
All Data	2.32	5.25	1.09	43.44	43.02	3.56	1.45	1.87
2007	2.23	4.09	1.13	32.44	48.77	3.35	0.50	2.82
2008	2.41	5.25	1.14	49.28	37.93	3.07	1.66	1.22
2009	2.23	5.06	0.96	39.17	45.98	4.66	1.49	2.88
2010	2.32	4.55	1.07	41.60	43.88	2.86	1.25	1.55
2011	2.14	4.09	1.05	57.09	31.87	4.16	3.16	0.86
2012	2.23	4.24	1.04	36.46	49.48	1.59	0.26	1.20
2013	2.51	5.06	1.12	42.62	45.99	3.28	1.31	1.59
2014	2.32	4.39	1.10	48.98	38.03	5.06	2.71	2.07
2015	2.28	4.42	1.11	42.88	45.63	3.82	0.43	3.03
2016	2.37	4.83	1.11	38.18	47.78	3.07	0.42	2.48
2017	2.15	4.50	1.02	42.32	45.04	3.93	1.59	2.17
Winter (DJF)								
2006-07	2.71	4.09	1.39	33.16	52.13	7.72	0.48	6.75
2007-08	2.61	4.72	1.37	23.94	57.73	7.48	0.32	6.56
2008-09	1.89	3.94	0.73	53.42	32.30	2.39	0.46	1.90
2009-10	2.82	5.06	1.36	55.49	32.72	7.11	6.50	0.40
2010-11	2.32	4.55	1.24	49.82	38.79	4.14	3.04	1.11
2011-12	2.51	3.94	1.32	34.96	46.82	6.02	1.98	3.25
2012-13	2.51	3.40	1.33	44.28	40.72	5.13	1.42	3.12
2013-14	3.04	5.06	1.61	12.94	79.34	15.14	0.15	14.64
2014-15	2.57	3.82	1.39	38.61	44.36	6.04	1.23	4.08
2015-16	2.78	4.04	1.57	20.63	70.35	10.21	1.65	8.24
2016-17	2.23	3.48	1.08	32.26	51.54	2.13	1.18	0.58
2017-18	2.67	4.18	1.39	36.78	42.60	7.27	2.75	3.36

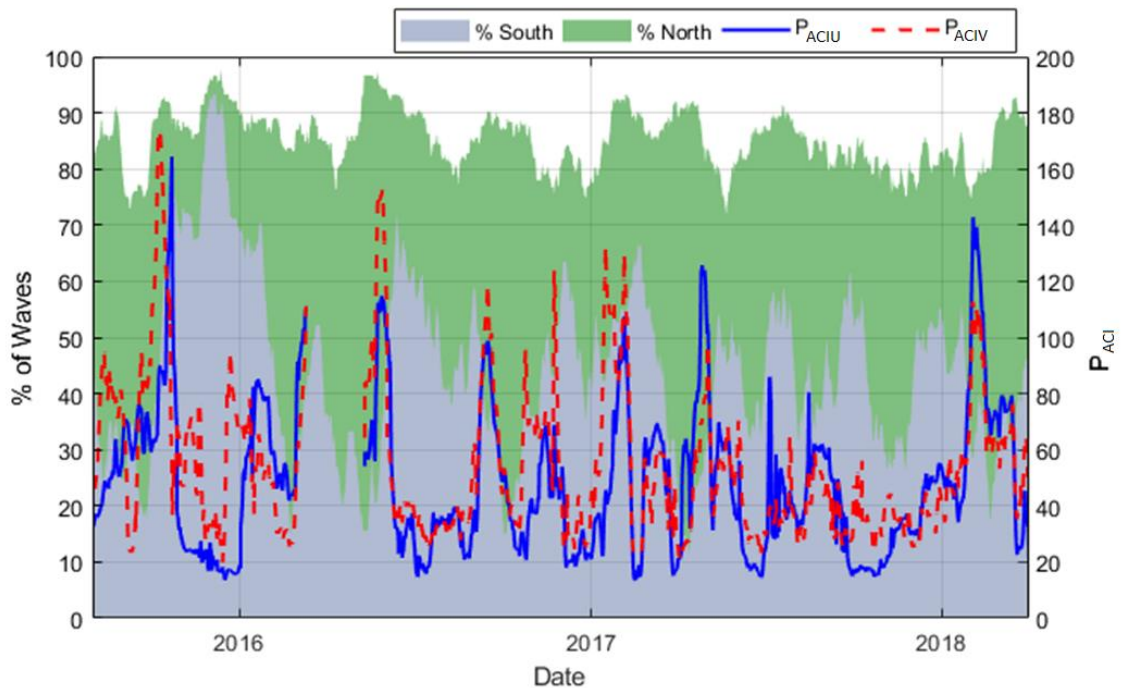


Figure 3.8. Area plot of percentage North-South waves over 30 days (green and grey, left y-axis) with calculated persistence in the v-component (P_{ACIU} North-South, right y-axis) and y-component (P_{ACIU} East-West) between August 2015 (the start of the radar deployment) and March 2018 (the end of the beach surveying).

Two examples to illustrate how and why these values are influenced by wave height and direction are presented for a high P_{ACIV} northerly dominated period (Figure 3.9) and lower P_{ACIV} southerly period (Figure 3.10):

- The northerly event (Figure 3.9) shows a high peak in P_{ACIV} (175) which slowly degrades over 14 days, the wave direction over this period are consistent, from the north-east as well as a period (~6 days) where significant wave height exceeded 1 m. This persistent period is followed by a distinct change between northerly and southerly waves, which results in a drop in the P_{ACIV} ; and
- The southerly event (Figure 3.10) has a lower overall persistence value ($P_{ACIV} = 98$) and this is due to larger variance in wave height throughout the period (ranging from <1 m to >3 m), the wave direction over this period is also observed to show more variance (swinging between ESE and SSW over the course of 2 weeks).

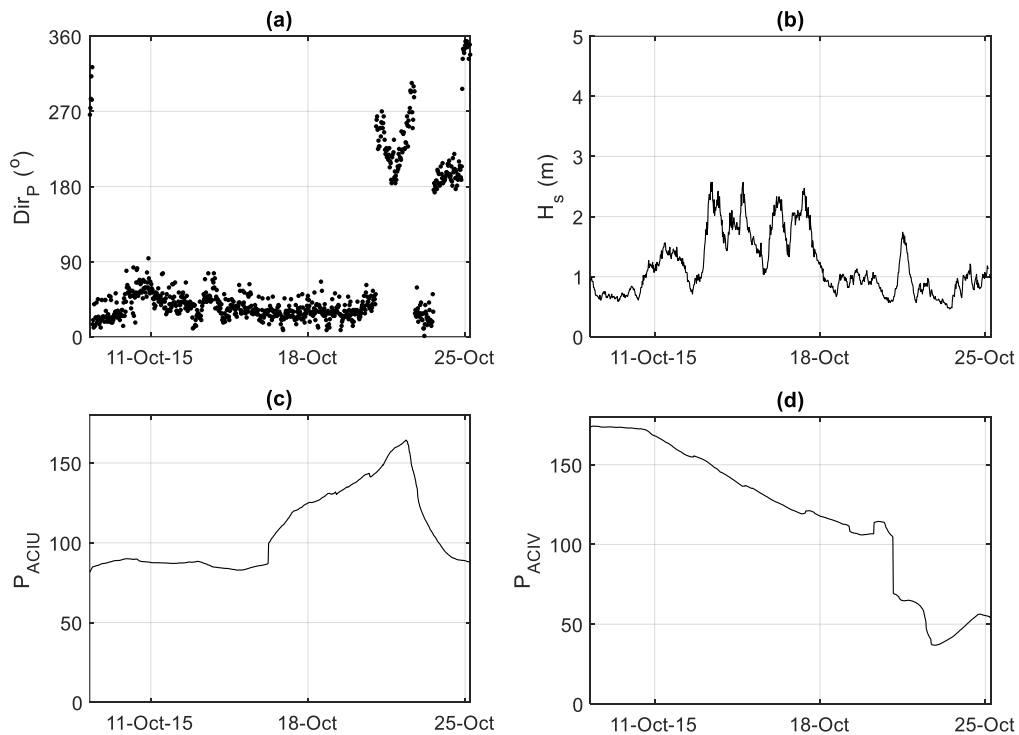


Figure 3.9. Time series analysis of an (a) Dir_P and (b) H_s and persistence values (c) P_{ACIV} and (d) P_{ACIV} during a high P_{ACIV} period between 10-Oct-2015 and 25-Oct-2015. Note the steady north-east wave direction but also the range the wave heights exceeding 1 m between 13-Oct-2015 and 18-Oct-2015.

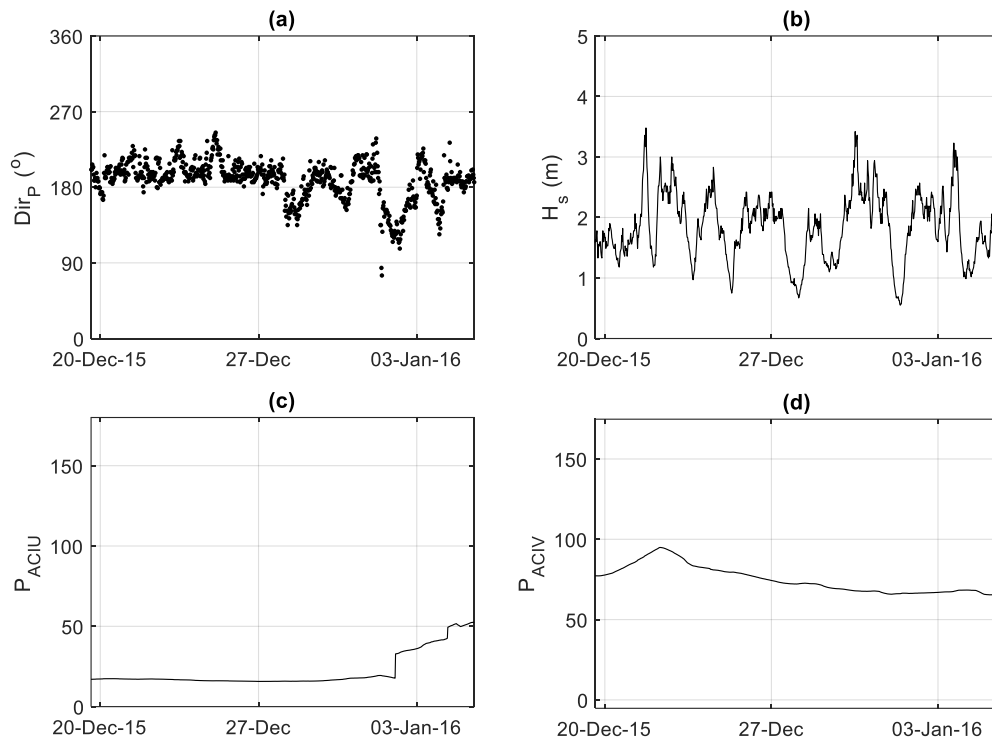


Figure 3.10. Time series analysis of an (a) Dir_P and (b) H_s and persistence values (c) P_{ACIU} and (d) P_{ACIV} during a steady P_{ACIV} period between 20-Dec-2015 and 05-Jan-2016. Note the variable southerly wave direction and large range wave sizes, which lower the persistence values.

The formulation of these persistence values provides a combined measure of both the wave direction and wave height which is distinctly different from the analysis of wave direction only. Although periods of northerly and southerly domination can result in peaks in the persistence this is not sustained. This is particularly true with southerly dominated periods which show a larger more balanced spread of directions (Figure 3.7).

The annual and winter statistics of the persistence values (Table 1.1) show that these parameters are as also show strong inter-annual variability. Generally, the largest persistence values occur outside of winter, which is likely due to the effect of large changes in wave height impacting the ACF (as outlined previously) Between years significant ranges are observable in maximum and 95th percentile values, though the annual and winter seasonal mean values tend to range between 40 and 60 for both P_{ACI} and P_{ACIV} .

Table 3.4. Yearly and annual persistence statistics for data obtained from the West Gabbard 2 buoy, between December 2006 and February 2018.

Year	P _{ACIU}			P _{ACIV}		
	95 th ile	Max	Mean	95 th ile	Max	Mean
2007	104.20	142.72	50.86	94.72	129.05	49.91
2008	112.92	127.19	58.40	109.69	140.80	57.42
2009	119.33	163.21	55.30	127.68	183.93	61.81
2010	111.99	161.45	58.03	148.81	175.20	60.24
2011	125.35	169.50	55.64	116.15	160.64	56.21
2012	96.06	180.23	42.79	70.19	119.40	47.16
2013	113.13	161.12	53.17	141.15	164.17	63.31
2014	98.50	152.80	50.68	93.01	123.87	53.91
2015	120.86	164.41	51.91	114.65	174.23	56.43
2016	98.39	114.81	48.93	110.06	152.56	55.21
2017	87.50	125.77	43.31	97.85	132.25	45.47
Winter (DJF)						
2006-07	119.34	128.14	61.96	70.74	78.88	43.01
2007-08	65.71	70.34	41.40	106.32	108.14	54.64
2008-09	70.49	128.40	48.91	86.12	171.04	53.07
2009-10	91.93	110.36	65.65	125.12	132.63	75.28
2010-11	96.85	102.71	50.70	49.94	51.13	38.37
2011-12	169.40	180.23	81.36	111.41	119.40	56.45
2012-13	57.35	64.45	30.49	92.75	105.58	37.80
2013-14	80.10	81.42	55.82	103.23	104.61	54.56
2014-15	119.34	128.14	61.96	70.74	78.88	43.01
2015-16	82.45	89.37	45.37	80.15	94.90	49.42
2016-17	92.94	107.51	41.22	116.35	132.25	57.65
2017-18	132.48	142.88	63.57	106.25	112.58	55.97

The statistics summary of highest annual and winter total water levels and surge values from 2006 to 2017 (Table 3.5) indicates that the majority of the largest surges (and therefore total water levels) occur over the winter months, though exceptions exist (2007, 2009, 2011). When a large storm surge and high spring tides coincide, the total water level is observed to reach a maximum of 3.26 m ODN (05-Dec-2013) at Lowestoft. Conditions during the period of primary data collection for this project are within the range observed since 2006. The highest annual total water level (2.38 m) occurred during spring tides on 14-Jan-2017 and was the third highest since 2006. The highest 95th percentile of total water levels over the eleven-year period occurred in 2017 (1.09 m) suggesting that higher water levels were relatively more frequent in that year. Storm surges were relatively higher in the winter 2017-2018 as the 95th percentile value was one of the highest (>0.50 m).

Table 3.5. Statistic summary of highest annual and winter (months DJF) total water levels and surge values (elevations in ODN) from 2006 to 2017 at Lowestoft.

Year	Total Water Level (m)		Surge Value (m)		Winter	Total Water Level (m)		Surge Value (m)	
	95 th ile	Max	95 th ile	Max		95 th ile	Max	95 th ile	Max
2006	1.02	2.24	0.37	1.87	2006-07	1.11	2.14	0.55	1.87
2007	1.07	2.63	0.20	1.07	2007-08	1.10	2.11	0.53	2.09
2008	1.01	2.11	0.34	1.92	2008-09	0.97	1.67	0.34	1.11
2009	0.99	1.84	0.28	0.92	2009-10	1.05	1.68	0.33	0.95
2010	1.03	1.68	0.32	0.95	2010-11	1.00	1.57	0.34	1.15
2011	1.03	2.33	0.36	1.49	2011-12	1.20	2.14	0.54	1.49
2012	1.03	2.14	0.29	1.45	2012-13	1.05	1.73	0.33	0.92
2013	1.04	3.26	0.32	2.18	2013-14	1.03	3.26	0.38	2.18
2014	1.03	2.02	0.30	1.74	2014-15	1.13	2.23	0.44	1.74
2015	1.06	2.23	0.38	1.63	2015-16	1.11	1.69	0.43	1.26
2016	1.06	1.69	0.32	1.38	2016-17	1.12	2.38	0.40	1.56
2017	1.09	2.38	0.36	1.56	2017-18	1.14	1.98	0.52	1.47

3.3.2 Relationships between indicators of beach change

It is usually expected that beach accretion (and erosion) results in both an increase (decrease) in beach width and cross-section area. However, in some cases, the amount of accretion (and erosion) differs below and above the MHWS, affecting the profile morphology. To assess whether these differences are observed in the study area, the relationship between beach width at MHWS, MWL and MLWS and cross-section area above and between MHWS, MWL and MLWS were tested through statistical correlation.

Strong significant positive correlations were observed between the beach width and the area within the different beach compartments in all transects, albeit with differences. Significant correlations are found between all measurements of beach width and the area in all beach compartments in Transects B and D. These results indicate that changes along Transects B and D are likely to occur as parallel displacement. In Transects A, C and E no significant correlations are found with the area above MHWS. Thus accretion (erosion) above MHWS in those transects not always reflect an increase (decrease) in beach width, suggesting occasional effects from cross-shore exchange of material between the upper and lower beach. In fact, the area between MWL-MHWS or MLWS-MHWS show significant correlation with beach width at all levels for all transects, with the weakest correlation ($r=0.647$, $p=0.012$) in Transect E with beach width at MLWS. Therefore, variations in profile area below MHWS throughout the study period follow closely the variations in beach width.

3.3.3 Alongshore variability

The analysis of all cross-shore profiles measured between January 2009 and February 2018 (Figure 3.11) indicated a very dynamic system with large variations in the magnitudes and direction of changes within the 2-km-long shoreline covered by the five transects. The beach width at the MWL varied as little as 18.0 m in Transect E and 48.8 m in Transect B. In both locations the mean beach width is about 68 m (Table 2). The largest change in elevation (~8.5 m) was observed in Transect C (Figure 3.11c) as a result of a 12-m cliff retreat in the 2016–2017 winter. Maximum changes in beach elevation (around 4 m) occurred in the upper beach in Transect B, toward the central part of the profile in Transects C and D and in the lower beach in Transects A and E. As with beach width, Transect E showed the smallest changes in beach elevation (a maximum of 2.5 m). Profiles measured in 2016–2018 (Dataset 2) tended to be positioned seaward of earlier measurements in Transects A and E and landward in Transects B and C (Figure 3.11b to C), suggesting relative accretion and erosion, respectively. However, these trends were not continuous through time and seemed to have reversed in the period 2016–2018 (Figure 3.12). In Transect D there was a greater overlap in the position of profiles through time.

Summarising beach change through descriptive statistics of key indicators (Table 3.6) provided a general overview of differences and similarities across transects. For example, it is evident that the largest erosion (i.e., reduction in area) in all transects occurred between July (summer) and January or

February (winter), but the largest beach retreat (i.e., landward movement of the shoreline position) showed variation of this pattern in Transects A and C. The largest accretion (i.e., increase in area) and beach growth (i.e., increase in beach width) occurred between the winter and the summer, except in Transect A. The maximum and minimum values of both beach width and area did not always result from the largest growth and accretion and retreat and erosion, respectively, suggesting that gradual changes can have significant effects. The range (i.e., the difference between the maximum and the minimum values) of both beach width and area suggests that Transect D showed the highest relative mobility (i.e., the range was relatively high in relation to the mean value). However, descriptive statistics provided little insight into the temporal and spatial variability in beach mobility.

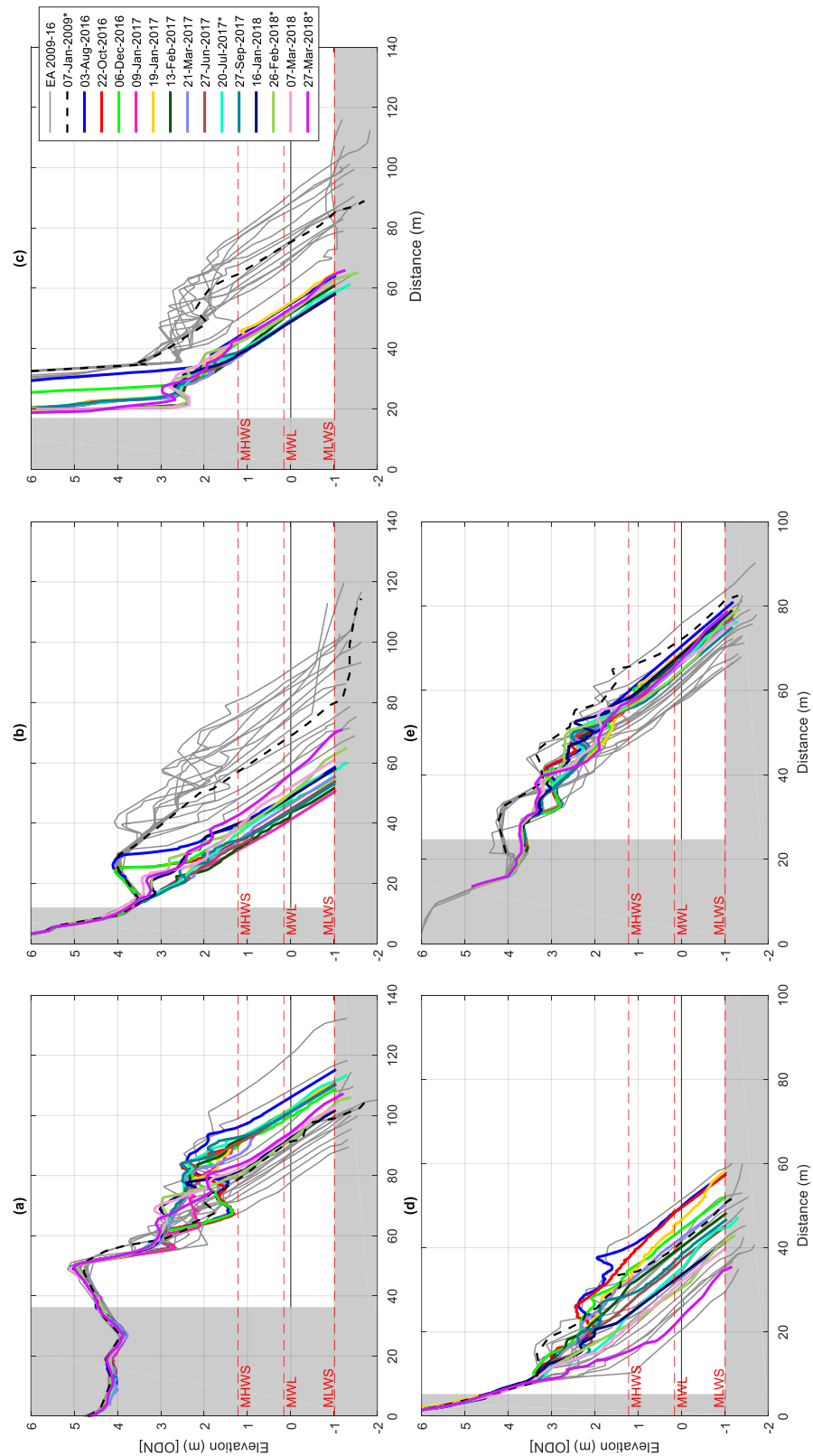


Figure 3.11. Cross-shore profiles measured along Transects A–E (respectively) between January 2009 and February 2018 are shown to give an indication of the profile envelope and range of variations. Biannual measurements by the Environment Agency (EA) are shown in grey (the earliest one as a black dashed line for reference), and Dataset 2 measurements are shown in colour. Note that the areas shaded in grey were excluded from the calculations of profile area presented elsewhere in this paper. Animations of the profile evolution are available as supplementary material from Atkinson and Esteves (2018).

Table 3.6. Descriptive statistics summarising changes in beach width and area (and respective dates where relevant) based on Dataset 1 for Transects A to E.

Transects	A	B	C	D	E
Beach width at MWL (m)					
Mean	91.1	67.8	70.2	32.6	67.3
Range	42.3	48.8	41.8	31.0	18.0
Minimum	76.0 8-Feb-2014	40.8 13-Feb-2017	47.8 20-Jul-2017	19.3 21-Jul-2010	61.3 22-Dec-2011
Maximum	118.3 2-Feb-2016	89.5 20-Jul-2010	89.5 27-Jan-2011	50.3 26-Jul-2016	79.3 27-Jul-2009
Largest beach growth	29.8 Aug 2015 – Feb 2016	12.8 Feb 2013 – Jul 2013	26.5 Feb 2010 – Jul 2010	10.0 Feb 2016 – Jul 2016	5.75 Feb 2016 – Jul 2016
Largest retreat	-11.0 Feb 2016 – Jul 2016	-14.0 Jul 2016 – Feb 2017	-15.5 Feb 2016 – Jul 2016	-12.0 Jul 2009 – Feb 2010	-5.75 Jul 2010 – Jan 2011
Area above MLWS (m²)					
Mean	214.5	207.9	271.1	88.3	134.0
Range	116.9	194.2	221.1	101.9	75.4
Minimum	169.7 08-Feb-2014	90.1 13-Feb-2017	119.7 13-Feb-2017	42.1 21-Jul-2010	106.2 08-Feb-2014
Maximum	286.7 02-Feb-2016	284.4 20-Jul-2010	340.8 27-Jan-2011	144.1 26-Jul-2016	181.6 27-Jul-2009
Largest accretion	78.4 Aug 2015 – Feb 2016	36.1 Jan 2010 – Jul 2010	67.4 Feb 2010 – Jul 2010	27.8 Feb 2016 – Jul 2016	17.7 Feb 2016 – Jul 2016
Largest erosion	-35.5 Jul 2017 – Feb 2018	-66.3 Jul 2016 – Feb 2017	-87.6 Jul 2016 – Feb 2017	-46.5 Jul 2009 – Feb 2010	-23.2 Jul 2010 – Jan 2011

There were large differences in beach width and area between the transects, where Transect A was the widest, Transect D was the narrowest, and Transect C had the largest cross-sectional area (Table 3.6) due to the presence of the cliff. Therefore, assessing temporal changes in relation to the initial profile area facilitated visualisation of alongshore variations (Figure 3.12). An end-point type of assessment would indicate overall erosion, more pronounced in Transects C (-184.4 m^2 , a 60.4% reduction in area) and D (-64.8 m^2 , a 53.7% reduction in area), with accretion observed only in Transect A (19.3 m^2 , a 9.3% increase in area). However, patterns of change varied in the period, with periods of relative erosion, stability, and accretion that did not necessarily coincide for the five transects (Figure 3.12). The spatial variability was evidenced by the lack of correlation in patterns of beach change between transects. In Dataset 1, significant correlations were found only between Transects B and D, which showed a significant moderate negative correlation for changes in area above MLWS ($r_s = -0.581$, $p = 0.011$, $N = 18$), above MWL ($r_s = -0.511$, $p = 0.030$, $N = 18$), and below MHWS ($r_s = -0.606$, $p = 0.008$, $N = 18$). In Dataset 2, a negative significant correlation was found for Transects D and E for changes in area above MLWS ($r = -0.560$, $p = 0.046$, $N = 13$), and a strong positive significant correlation was found for Transects A and B for changes in area below MHWS ($r_s = 0.600$, $p = 0.023$, $N = 14$).

Broadly, patterns of change seem to shift every 2–3 years as a response to major storms with no seasonality (winter and summer profiles and/or profile volumes) observed. The storms that exposed the 1970s gabions (along Transect D) in October 2010 seemed to have slowed or reversed the accretion and erosion trends observed until then along Transects B (accretion), C, D (erosion), and E

(Figure 3.12). Afterwards, despite temporal and spatial variations, Transects B and C were roughly in a state of relative stability or accretion and Transects D and E were in a state of erosion up to mid-2013. The extended stormy period from October 2013 to February 2014 (which exposed the geobags installed in 2011) seemed to have triggered another shift in the patterns of change. Transects A, D, and E responded with accretion and Transects B and C with erosion (Figure 3.12). The Ness (Transect A) was not greatly affected by these storms, remaining relatively stable after the storms in 2010, with considerable accretion (116.9 m²) observed between February 2014 and February 2016, after minor erosion during the 2013–2014 winter. At different times in 2016, trends changed once again, with erosion starting in Transects A and D and accretion or stability in Transects B, C, and E. In 2016, the loss of area in Transect C was due to cliff retreat, while the beach remained relatively stable.

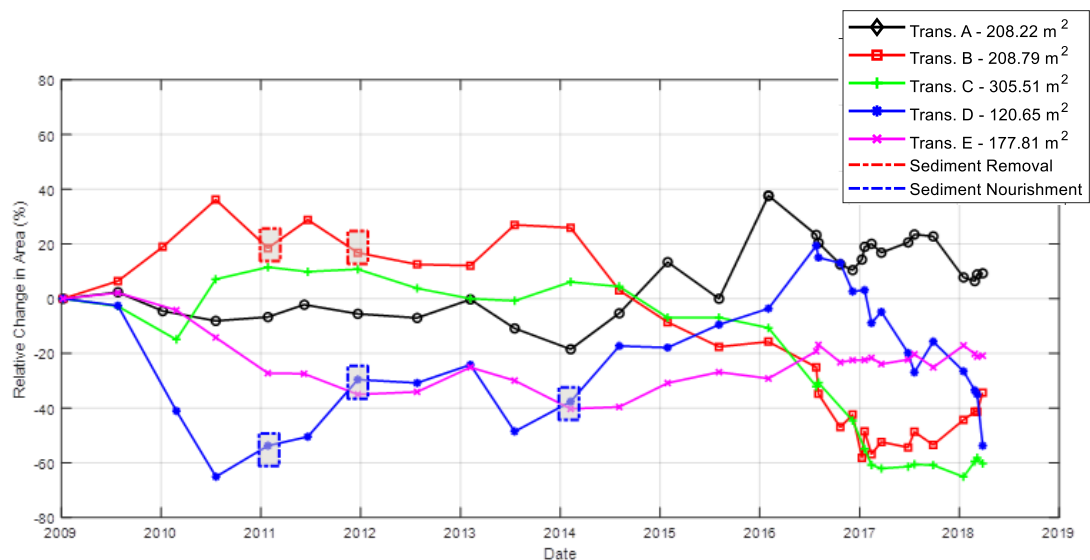


Figure 3.12. Relative change in profile area above MLWS for Transects A–E for the period between 7-Jan-2009, and 27-Mar-2018 (including Dataset 1 and Dataset 2), calculated as a proportion of the respective initial area (shown in the legend). Grey boxes indicate beach nourishment and reprofiling in the area of Transect D, with gravel taken from the area of Transect B

Interestingly, in 2010 the 1970s gabions were exposed when Transect D was the most eroded (42 m² cross-sectional area, 65% less than the initial area). Since then and up to mid-2016, an overall accretion trend was observed in that area (Figure 3.11 and Figure 3.12), with exposure of the geobags in 2013 occurring when the area was considerably more accreted (75 m² cross-sectional area) than in 2010. The geobags were more exposed to waves as they were placed seaward of the gabions, resulting in a narrower beach and, therefore, less natural dissipation of wave energy. Additionally, in 2013 there were prolonged periods of waves higher than 2.5 m, and they were dominantly from a southerly direction, while in 2010 higher waves were lower, less frequent, and dominantly from the northeast. Small-scale nourishment works occurred in the area of Transect D after storms in 2010 and 2011 with materials (around 1000–1500 m³) sourced from the area of Transect B and in 2013 sourced from an area south of Transect E. Although these works might have helped in protecting the already damaged protection structures, they caused only a small and temporary effect, not affecting the

overall trend either in Transect B or D. However, the area of Transect B has experienced considerable erosion since 2014 (loss of 173 m² >MLWS), despite some recovery since 2017 (Figure 3.12), which may preclude further extraction of material to nourish areas further south. The continued erosion at Transect D has resulted in the further uncovering of the geobag ‘groyne’ placed at the end of the gabion baskets to the north of the village. It is also concerning that the last survey (March 2018) at Transect D showed a state of erosion almost as critical as the one observed after the 2010 storm (Figure 3.12). Therefore, identifying suitable and sustainable sources for beach nourishment requires better understanding of the longer-term trends and variability of beach responses.

3.3.4 Temporal changes in beach morphology

The analysis of profile evolution is particularly useful in understanding cross-shore variations in beach change. In the study area, most often and in all transects, the profile showed a parallel displacement seaward or landwards (i.e., no major changes to the overall shape). However, sometimes changes differed below and above the MHWS, affecting the profile morphology, mainly as a result of movement of gravel, particularly gravel ridges. Gravel ridges were observed in all transects, but there were alongshore differences in their size, response and movement time-frame, and the effects on profile morphology. Although the analysis of profile changes based on biannual data (Dataset 1) was useful to visualise general patterns of change, the more frequent surveys in Dataset 2 helped in understanding the movement of gravel ridges and their effect on beach morphology.

The Ness (Transect A) is characterised by the presence of (sometimes multiple) gravel ridges above MHWS (Figure 3.11a), which can have steep flanks and be over 1 m high (higher if further up the beach). Here beach retreat occurs as the gravel ridge closest to the waterline migrates up the beach, as observed between late July 2016 and January 2017 and also in the following year. Although the beach slope below MHWS remained unchanged, the ridge became narrower and steeper above MHWS, where the retreat was largest. The retreat below MHWS halted when the ridge above MHWS spread out landwards, becoming flatter and wider as it welded to the next gravel ridge. This migration continued until all ridges coalesced, resulting in a higher and flatter beach above MHWS, as seen in 19-Jan-2017. Below MHWS, the beach became a less steep and featureless sandy surface. The existing data suggested the presence of a single gravel ridge from late winter to the spring, with others forming during the summer (as evident from June–September 2017).

The gravel movement observed in Transect B, although similar to Transect A, seemed to occur in shorter time frames. A well-developed gravel berm present at MHWS in early December 2016 had completely disappeared by 09-Jan-2017 (Figure 3.11b) when the profile was greatly eroded (an area loss of 33 m²). After erosion, the gravel that was dominantly above MHWS was observed to be more evenly distributed across the profile. Just 10 days later, a gravel ridge had formed just below MHWS, with the profile recovering 20 m². By 13-Feb-2017, almost all this gain had been lost when the gravel ridge migrated well above the MHWS (around 2.5 m ODN), resulting in a flattened and retreated sandy profile below MHWS. Only minor changes were observed between late winter and early

summer. Over the summer 2017, the featureless profile remained, with gravel ridges apparent in September. A similar pattern of erosion and accretion associated with gravel ridge migration was observed between January and March 2018.

In Transect C, the cliff face retreated 6 m between 03-Aug-2016 and 06-Dec-2016 (Figure 3.11c), and a further 5 m by 19-Jan-2017 (Figure 3.14), with tragic consequences. Just a few meters from this transect, the cliff failure resulted in the death of a man who was walking his dog along the beach close to the cliff face (due to high tide) on 14-Jan-2017. Prior to this, the beach had been stable since July 2016, with no significant change in area below MHWS.

Multiple gravel ridges occurred above MHWS in Transect D (Figure 3.11d), and they influenced changes in morphology, similar to those observed in Transect A. Here, the gravel ridge closest to the waterline seemed to control changes further up the beach. Multiple gravel ridges seemed to develop during the summer, with the topography becoming flatter across the winter. During summer (26-Jul-2016 to 3-Aug-2016), the gravel ridge closest to the waterline migrated up the beach, becoming wider and less defined until it coalesced with other ridges in late autumn and early winter. Without the gravel ridge, the profile below MHWS eroded, while changes above MHWS were negligible. The upper beach is fixed by the presence of gabions. The pattern of ridge formation in the summer (Figure 3.16) and migration and fading in the autumn and early winter seemed to occur in 2017.

In the period 2016–2018, Transect E was relatively stable despite showing a gravel ridge migration similar to Transect B (Figure 3.11e also noted in the DTM between August 2016 and September 2017, Figure 3.13). Here the ridges remained well-formed, showing little change during the summer and persisting during the winter, albeit much less developed. It is worth noting that the beach below MHWS retreated in early autumn and showed little change or slight accretion during the winter.

The variable longshore, temporal response at site can be observed by comparing the digital terrain models of the village frontage and cliff face (Figure 3.13 to Figure 3.17). The continued erosion issues at Transect D between 2016 and 2018 around the edge of the engineering works continues even when the rest of the beach remains stable (21-Mar-2017 to 27-Jun-2017, Figure 3.14) and shows only minimal recovery periods (27-Jun-2017 and 27-Sep-2017, Figure 3.16). This focused erosion occurs along a relatively small length of the beach (200-300 m) and has shifted north since the major erosion events in 2010 and 2013: starting at 100 m south of Transect D and extending north beyond Transect C over longer periods (01-Aug-2016 to 27-Sep-2017, Figure 3.13) but over shorter time periods stopping prior (21-Mar-2017 to 27-Jun-2017, Figure 3.14). The winter of 2017-2018 (Figure 3.17) indicates variable responses to the wave climate with migration of two gravel berms up the beach at Transect E which is seen to shift to erosion at Transect D. Beyond the geobag groyne (where data coverage was limited due to equipment failure) the cliff line shows retreat while the beach

accretes. At Transect C the cliff retreat slows and instead erosion of the beach face increases.

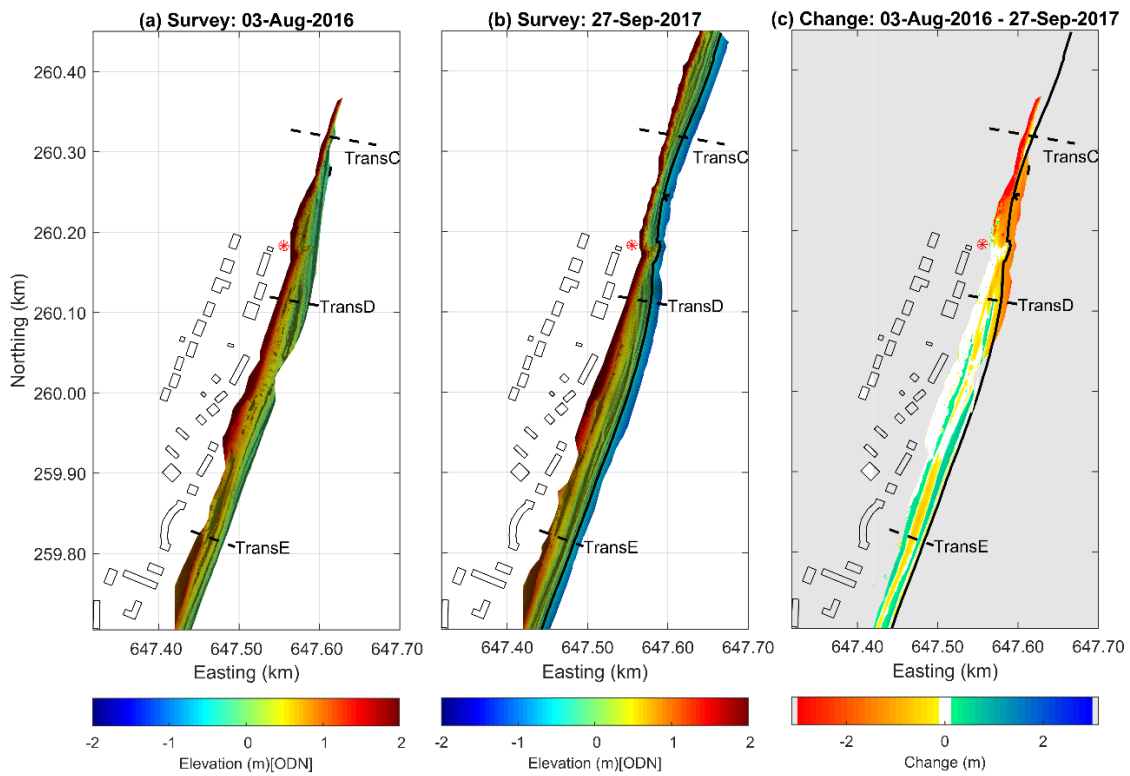


Figure 3.13. Extent of laser scan survey of the village frontage with Transects C, D and E (dashed black line) on (a) 01-Aug-2016 and (b) 27-Sep-2017 (c) calculated change between surveys with MHWS position in black (buildings are indicated behind the beach and radar position by red point).

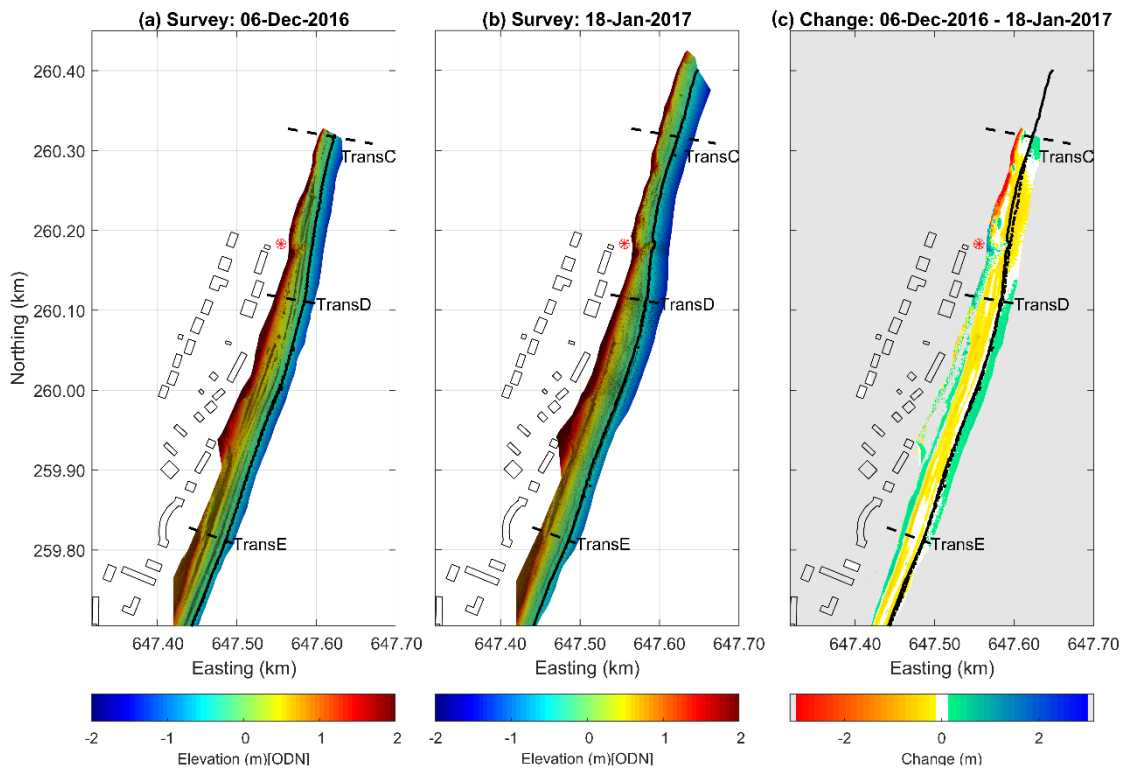


Figure 3.14. Extent of laser scan survey of the village frontage with Transects C, D and E (dashed black line) on (a) 06-Dec-2016 and (b) 18-Jan-2017 (c) calculated change between surveys with MHWS position in black (buildings are indicated behind the beach and radar position by red point).

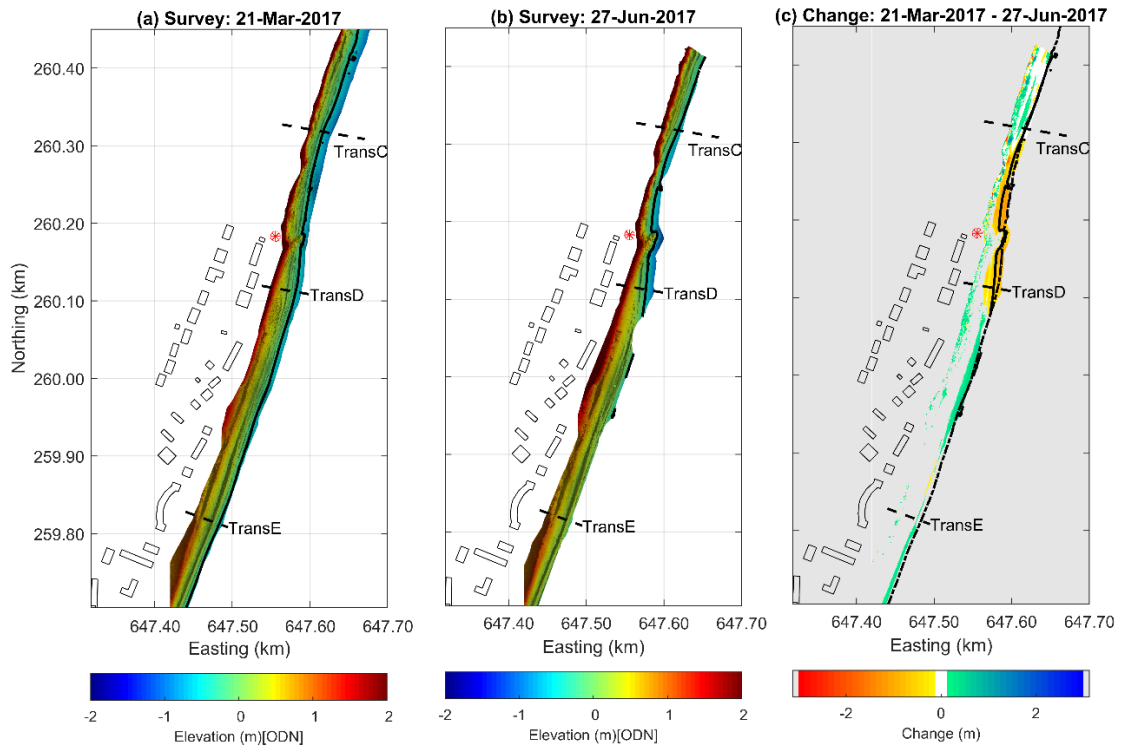


Figure 3.15. Extent of laser scan survey of the village frontage with Transects C, D and E (dashed black line) on (a) 21-Mar-2017 and (b) 27-Jun-2017 (c) calculated change between surveys with MHWS position in black (buildings are indicated behind the beach and radar position by red point).

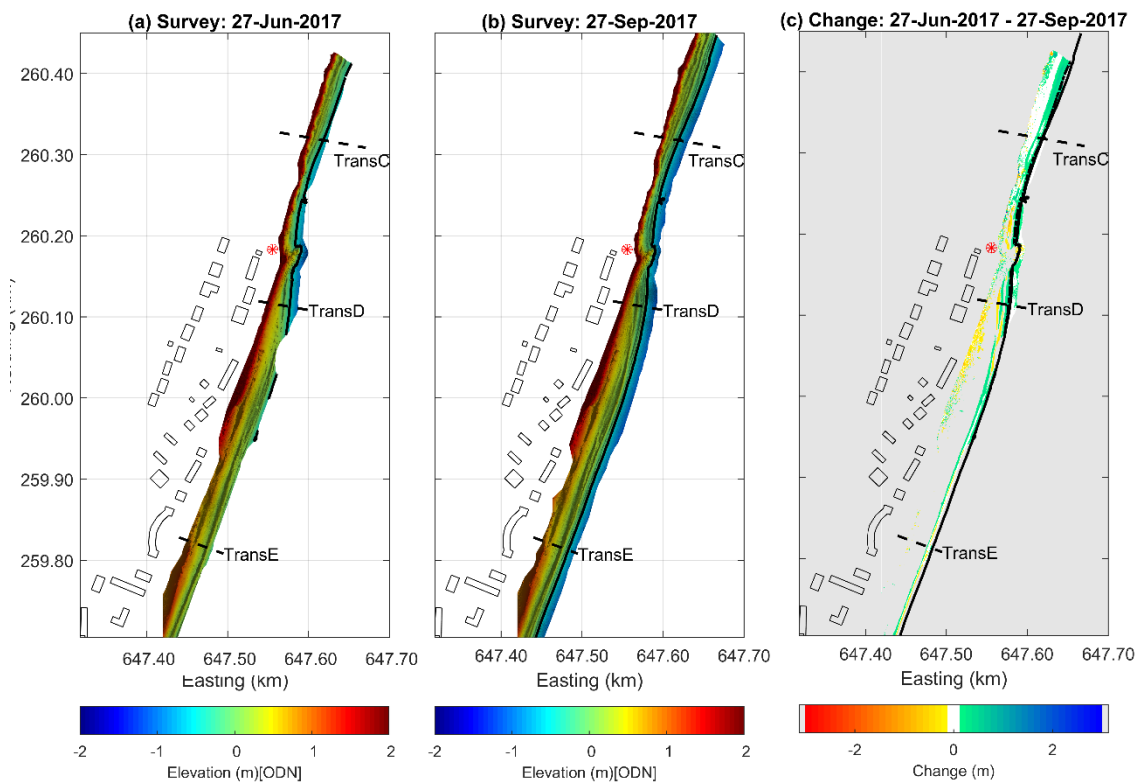


Figure 3.16. Extent of laser scan survey of the village frontage with Transects C, D and E (dashed black line) on (a) 27-Jun-2017 and (b) 27-Sep-2017 (c) calculated change between surveys with MHWS position in black (buildings are indicated behind the beach and radar position by red point).

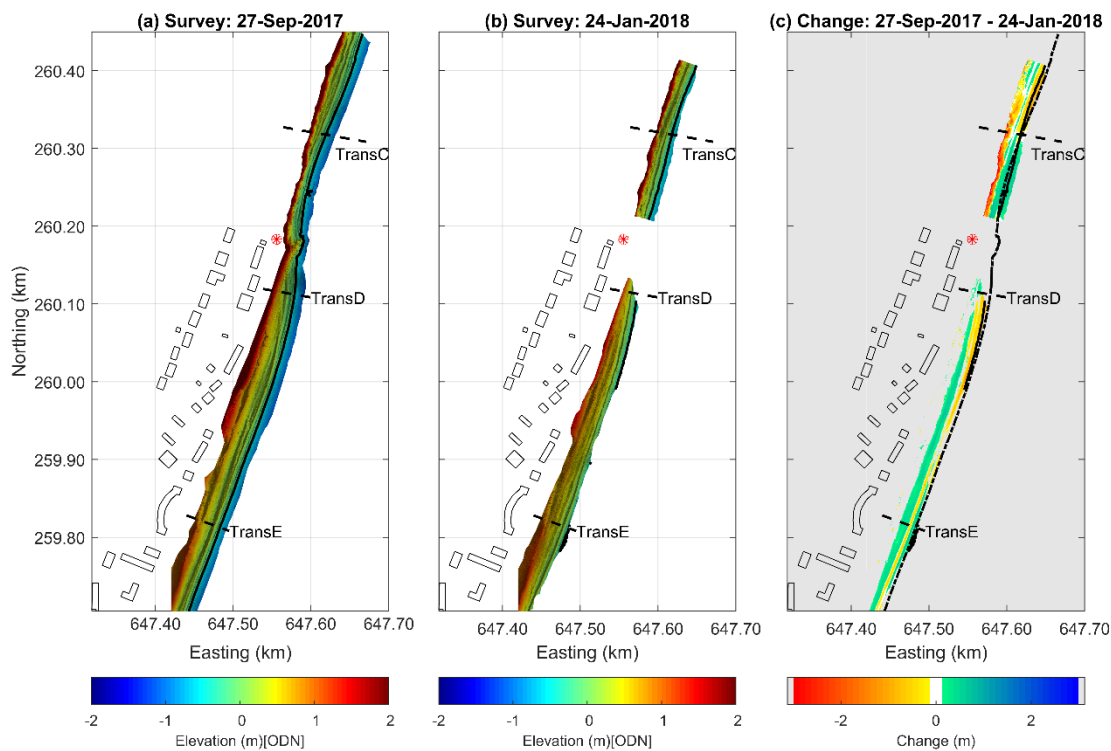


Figure 3.17. Extent of laser scan survey of the village frontage with Transects C, D and E (dashed black line) on (a) 27-Sep-2017 and (b) 24-Jan-2018 (c) calculated change between surveys with MHWS position in black (buildings are indicated behind the beach and radar position by red point).

3.3.5 The influence of wave conditions

About 80–90% of the time, offshore waves approached from a northerly or southerly direction, generally with the former dominating from January to July and the latter dominating from July to January (Figure 3.18), with exceptions. At times, northerly and southerly waves could dominate for extended periods (~18 months), as observed between January 2010 and June 2011 and from August 2014 to February 2016, respectively. Deviations from this pattern occurred when shorter periods of time were considered (Dataset 2, 2016–2018) (e.g., northerly waves dominated from early August to early December 2016 and southerly waves from 19-Jan-2017 to 21-Mar-2017). Additionally, waves higher than 2.5 m could be dominantly from a southerly direction in periods when waves were predominantly from a northerly direction, and vice versa. Waves exceeding 2.5 m in height could have a dominant southerly or northerly direction for long periods (~3 years), such as from the winter of 2013–2014 to the summer of 2016, when they were southerly dominant (Figure 3.18). Considering the biannual surveys (Dataset 1), waves higher than 2.5 m from all directions could occur as little as 0.58% of the time (January to June 2011) or as much as 7.12% of the time (July 2013 to February 2014). These high waves were usually concentrated in shorter periods of high energy lasting about a month. For example, from 26-Feb-2018 to 27-Mar-2018, waves higher than 2.5 m occurred 28.2% of the time in the first 9 days and 14% of the time in the last 20 days, dominantly from a northerly direction.

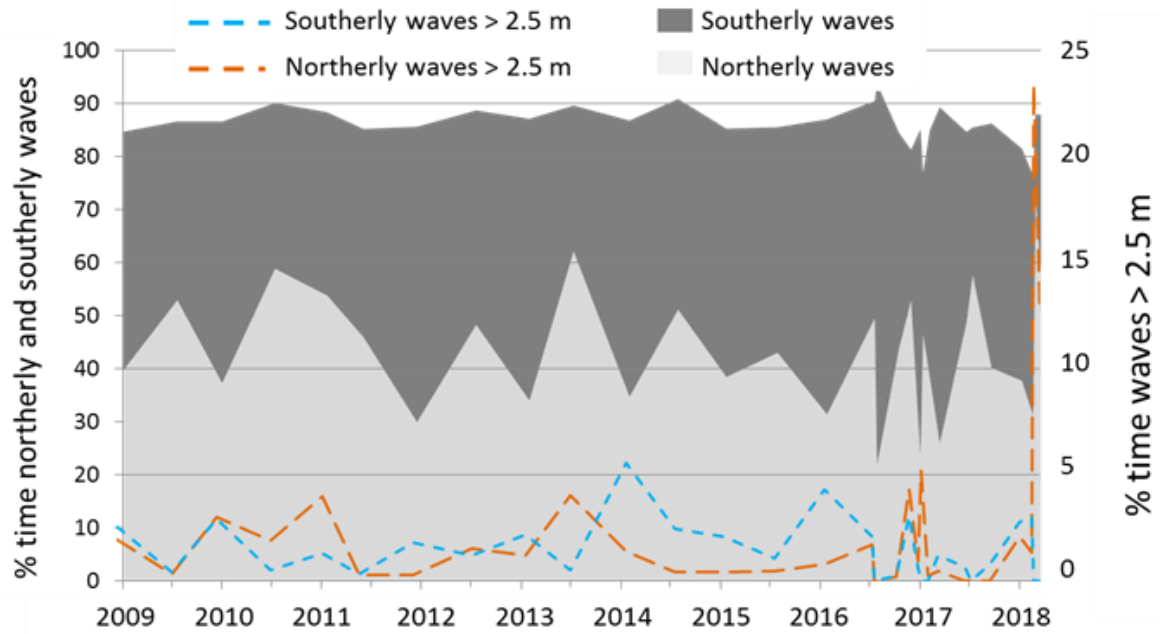


Figure 3.18. Percentage of time offshore waves recorded at West Gabbard approached from northerly ($Dir_P: 300-60^\circ$) and southerly ($Dir_P: 120-240^\circ$) directions and with heights above 2.5 m (calculated for periods between consecutive surveys undertaken between 07-Jan-2009, and 27-Mar-2018).

Considering the relationship usually found between shoreline changes and offshore wave power (Davidson et al. 2013), a number of indicators were used to test correlations to elucidate the influence of wave energy and bimodal wave direction on the direction and magnitude of shoreline changes. Indicators of shoreline change drawn from Dataset 1 (biannual surveys) showed significant correlations only for Transect A and when considering the percentage of time northerly waves exceeded heights of 2.5 m. For Transect A, significant moderate negative correlations were found between the percentage of time northerly waves exceeded heights of 2.5 m and changes in beach width (m/day) at MLWS ($r_s = -0.508, p = 0.031, N = 18$) and changes in profile area (m/day) within all beach compartments ($r_s = -0.494$ to $-0.512, p = 0.030$ to $0.037, N = 18$), except above MHWS ($r_s = -0.398, p = 0.102, N = 18$). These results suggested that erosion rates in Transect A were likely to increase with an increase in the occurrence of high northerly waves. However, a more detailed analysis of the data suggested that the relationship was less evident for the periods beach accretion was observed. Accretion rates in Transect A also seemed to increase with an increase in the occurrence of high northerly waves when these occurred less than 1% of the time.

In contrast, a number of significant correlations were identified for indicators drawn from Dataset 2, with variations between the five transects. Considering first the indicators of wave energy irrespective of wave direction, correlations indicated that an increase in wave energy would result in a reduction in beach width and area in all Transects, except Transect B, which showed an inverse relationship. Only the 95th percentile of H_s showed significant correlations with indicators of beach change for all transects, particularly with beach width at MLWS in Transect A (Figure 3.19a, $r = -0.650, p = 0.009, N = 15$), Transect B (Figure 3.19b, $r = 0.537, p = 0.039, N = 15$) and Transect D (Figure 3.19c, $r = -0.534, p = 0.049, N = 14$); area above MHWS in Transect C ($r_s = -0.615, p =$

0.015, $N = 15$); and changes in area above MWL (m^2/day) in Transect E ($r = -0.694$, $p = 0.009$, $N = 13$). Note that for Transects C, D, and E, these were the only indicators of beach change showing significant correlations with indicators of wave energy. The strongest correlation was found between H_s and beach width at MHWS in Transect A ($r = -0.752$, $p = 0.001$, $N = 15$).

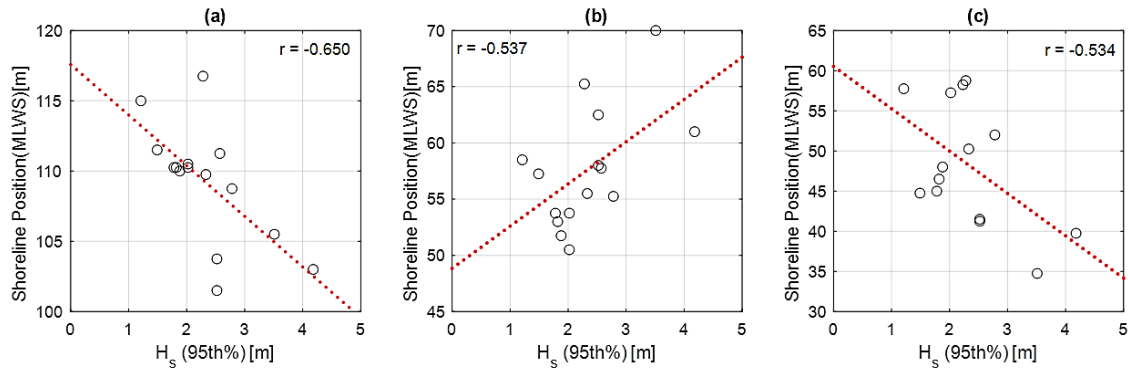


Figure 3.19. Scatter plots of significant correlations between 95th percentile of H_s and shoreline position at MLWS for (a) Transect A and (b) Transect B and (c) Transect D.

Correlations involving indicators reflecting wave direction suggested that the percentage of time southerly waves occurred may have had a greater influence on beach changes than other indicators. This was the only indicator showing significant correlations with all transects, except Transect C. More southerly waves tended to enhance erosion along Transects A and B and beach growth in Transects D and E. The strongest correlations were found for changes in beach width (m/day) at MHWS for both Transects A (Figure 3.20a, $r = -0.622$, $p = 0.018$, $N = 14$) and B (Figure 3.20b $r = -0.717$, $p = 0.004$, $N = 14$), and at MLWS for (Transect E $r = 0.585$, $p = 0.036$, $N = 13$). For Transect D, moderate positive significant correlation was found between the percentage of time southerly waves occurred and beach width at MLWS ($r = 0.534$, $p = 0.049$, $N = 14$). These were the only significant correlations found for Transects D and E.

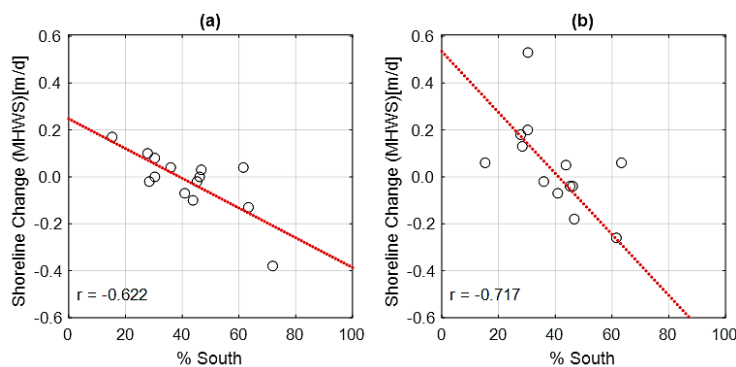


Figure 3.20. Scatter plots of significant correlations between the proportion of southerly waves and change in beach width (m/day) at MHWS in (a) Transect A and (b) Transect B.

Interestingly, significant correlations involving the percentage of time northerly waves occurred were found only for Transect A, suggesting that more northerly waves resulted in enhanced accretion ($r = 0.697$, $p = 0.006$, $N = 14$ for changes in beach width, m/day). However, an increase in the proportion of time northerly waves exceeded heights of 2.5 m was likely to result in a decrease in beach profile

area above MLWS ($r_s = -0.654$, $p = 0.008$, $N = 15$), as also observed in the analysis of Dataset 1. In contrast, an increase in the proportion of time northerly waves exceeded heights of 2.5 m was likely to enhance beach accretion in Transects B and C, for changes in beach width (m/day) above MWL ($r_s = 0.651$, $p = 0.012$, $N = 14$) and for area below MHWS ($r_s = 0.551$, $p = 0.033$, $N = 15$), respectively.

No significant correlations between indicators of beach change and wave persistence parameters for Dataset 1 were found and when assessing Dataset 2, significant correlations were found only for data from Transects C and E. Transect C shows a negative correlation between changes in profile area (m^2/day) and the 95th percentile ($r_s = -0.594$, $p = 0.045$, $N = 12$) and maximum of P_{ACIV} ($r_s = -0.629$, $p = 0.032$, $N = 12$) above MLWS suggesting persistent energy from the north and south cause a reduction in beach area (Figure 3.21a). Transect E, presents a number of significant correlations between indicators of change, below MHWS only and P_{ACIV} . The strongest of which with change in beach width (m) at MWL (Figure 3.21b, $r_s = -0.737$, $p = 0.004$, $N = 14$) and with change in profile area (m) between MLWS and MWL ($r_s = -0.703$, $p = 0.010$, $N = 14$, Figure 3.21c).

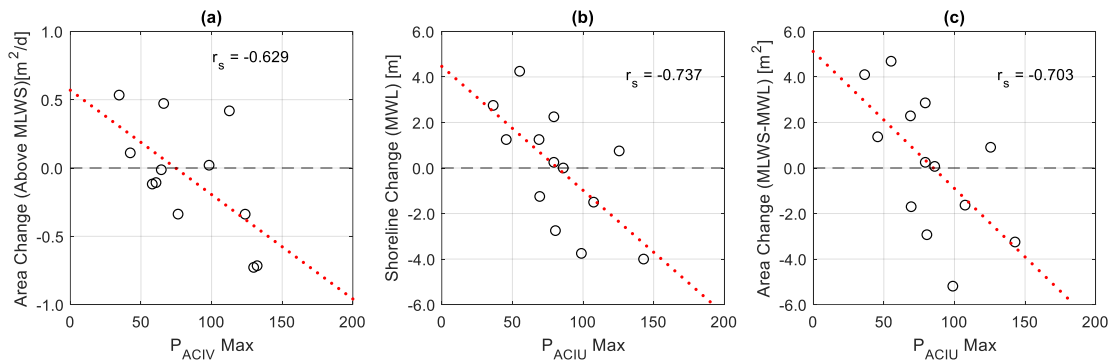


Figure 3.21. Significant correlations between (a) maximum P_{ACIV} and change in profile area (m^2/day) above MLWS at Transect C, between maximum P_{ACIV} and (b) change in beach width at MWL and (c) change in profile area between MLWS and MWL at Transect E.

Results from the analysis of wave persistence suggest that areas relatively stable under the higher energy conditions from the dominant southerly or northerly directions (such as Transect E), seem to respond to prolonged less energetic conditions. In these areas, beach response (particularly below MHWS) tend to involve steady changes of lower magnitudes, instead of the faster and larger changes driven by southerly or northerly high energy conditions observed in the more dynamic transects (particularly Transects A and B). In these more dynamic transects, the effects of wave persistence tend to be negligible.

The lack of correlation with indicators based on Dataset 1 for all wave and persistence values was likely due to the episodic nature of large shoreline changes. The largest magnitudes of shoreline changes tended to occur within short periods of time as a response to changes in wave conditions. Therefore, commonly used indicators may not be appropriate for analysis at longer time frames. Indicators reflected either extreme values (which could have varying effects depending on whether they were evenly distributed or occurred at either end of the time period) or average conditions (which indiscriminately evened out effects across the period). Both types provided limited

information on conditions throughout the period of time, restricting the identification of relationships. The effects of localised settings, such as the presence of an eroding cliff or coastal defences, also contributed to the alongshore variability of beach response at all spatial scales. Erosion of the soft cliff in Transect C could provide sand to the beach, counteracting beach retreat or area loss. The presence of gabions and geobags in Transect D seemed to enhance beach mobility, particularly erosion.

3.4 Discussion

The relationship between shoreline changes and indicators of wave power are widely recognised and demonstrated for sandy (Short 1979; Loureiro et al. 2012; Angnuureng et al. 2017) and gravel (Ruiz de Alegria-Arzaburu et al. 2010; McCall et al. 2015) beaches. In the study area, this relationship was precluded or limited due to the large spatial variability in beach response observed within the 2-km-long coastline at a range of temporal scales. This large variability is likely attributed to the presence of mixed sand and gravel, the bimodal wave direction, wave interactions with nearshore features, localised settings (e.g., the presence of engineering works), or a combination of these factors.

The limited number of studies on the effects of bimodal wave directions suggests that even small differences in wave offshore direction can affect transport rates at the shoreline (McSweeney and Shulmeister 2018). More often these differences are attributed to wave interactions with nearshore bathymetry (Adams et al. 2011; Burningham and French 2016; Hegermiller et al. 2017), affecting the distribution of energy arriving at the shore (Limber et al. 2017). The presence of stationary Coralline Crag ridges and the dynamic Sizewell sand bank makes the nearshore bathymetry in the study area very complex, which could result in a local divergence of longshore transport around Thorpeness (Burningham and French 2016) or a focusing of wave energy causing erosion hot-spots at the coast (Williams and Herbert 2015). The presence of the Ness may be a result or a cause of divergence of longshore transport, as suggested at Orford Ness (H.R Wallingford 2010) and Benacre Ness (Burningham and French 2016). At these locations, local longshore transport divergence is associated with headlands, underwater geology, or a combination of both. Results from this study showed a contrasting response between Transect A (at the Ness) and B (south of the Ness), which may suggest an effect of longshore transport boundaries. Transect A eroded, and Transect B accreted, with increasing wave energy, particularly due to high northerly waves. Similarly, when high southerly waves were dominant for extended periods (e.g., from 2014 to mid-2016), Transect A accreted and Transect B eroded. Targeted modelling simulations could provide further insights into the occurrence and potential influence of local divergences of longshore transport and nearshore wave focusing.

The novel wave persistence analysis provided few correlations to beach change, though the significant correlations at Transect C and E give an indication that some beach segments are more responsive to the conditions which result in high persistence values. In Transect C this was based on P_{ACIV} and at Transect E (which showed very fewer significant correlations to any of the wave parameters) P_{ACIU} had impact on both change in shoreline position and profile area. The fact no

significant correlations were observed in the more active profiles except Transect C suggests that the other wave parameters may have a larger impact than that of persistence. Whereas in the more historically stable Transect E persistent energy and direction may cause steady changes in the beach face.

MSG beach response is modulated by the proportions of sand and gravel (Mason 1997; López de San Román Blanco 2003; She et al. 2007). Additionally, the distribution of sand and gravel can show considerable variations through time both alongshore and cross-shore, making patterns of beach response less obvious (Mason and Coates 2001). However, little is known about how the proportion of sand and gravel changes temporally and spatially in MSG beaches and how the different mixes may influence beach mobility (Horn and Walton 2007). Laboratory experiments and limited observations on MSG beach nourishment have suggested enhanced beach mobility when the sediment mixture is formed by 30%–40% of sand (Mason and Coates 2001; She et al. 2007). Corroboration from studies on natural beaches and in a range of settings would contribute to demonstrating the validity of these suggestions.

Better understanding the role of the proportion of sand and gravel is warranted to prevent undesirable effects, such as enhancing erosion as a result of beach nourishment that has inadvertently created sediment mixtures with unfavourable proportions of sand (She et al. 2007; Zarkogiannis et al. 2018), or to assess whether erosion of a sandy cliff may enrich the beach with a 30% sand mixture that may lead to increased erosion. Elucidating the drivers influencing the large alongshore variability observed within the 2-km-long coastline requires further investigation to adequately inform and support management decisions.

These results highlight the intricate range of factors, natural and human-derived, that interact along modern coastlines influencing beach response. The understanding of temporal and spatial variability in the response of MSG beaches is still limited, particularly in complex settings, such as under the influence of bimodal wave direction. The analysis of biannual topographic surveys has proven useful in detecting longer-term trends of shoreline changes and how they vary (in magnitude and direction) alongshore and through time. However, it was only through the analysis of more frequent surveys that key aspects of beach morphology changes and how they vary alongshore could be elucidated. In particular, these surveys helped identify the role of gravel ridges in beach stability and erosion and, to some extent, the influence of bimodal wave direction on beach mobility. Therefore, there is a case to be made for more frequent surveys as part of coastal monitoring to advance the understanding of MSG beach behaviour, which is required to inform coastal management schemes.

4. Sediment Distribution and Beach Change

4.1 Introduction

This chapter characterises and assesses the PSD in the study area, particularly the spatial and temporal variation in the proportion of sand and gravel and assesses whether it influences beach changes. Field data from eleven surveys across two years were analysed to: (a) characterise the temporal and spatial variability in the PSD and proportion of sand, and (b) identify whether there is evidence of increased beach mobility with increased sand proportion.

Previous studies identifying the effects of proportion of sand on MSG beach mobility were based on known proportions of sand and gravel in sediment used in experiments (e.g. She et al. 2006) or as beach fill (e.g. Bergillos et al. 2016). Consequently, these studies do not define or discuss how and where the proportion of sand should be measured. Therefore, the definition of a method that is reasonably robust and yet rationale to the time and effort required in fieldwork and laboratory analysis was a considerable requirement to accomplish this chapter's objectives.

Sediment grain size is an important factor determining the rate of erosion, deposition and transport (Cheng and Liu 2015). Gravel and sand behave differently to hydrodynamic forcing, adding complexity to the MSG beach response in comparison to pure sand or gravel systems (Zenkovich 1967, p.271). Even a sediment grain size characterisation, which is a relatively simple task in pure sand or gravel beaches, is not as straight forward in mixed systems (Horn and Walton 2007). Understanding the temporal and spatial variability in the proportion of sand and gravel and their influence on beach morphology changes is laborious and time consuming; as a result, very little is actually known about it. Studies often resource from approximations and oversimplifications either due to sparse temporal (focusing on characterising single moments in time e.g. McLean and Kirk 1969; McLean 1970a; Dawe 2001) or spatial sampling (characterising entire regions by limited cross-shore bulk samples e.g. Eikaas and Hemmingsen 2006) or limitations of the methods used (e.g. digital image analysis or sampling sediment at surface only, disregarding sub-surface grain size variations; Miller and Warrick 2012).

Hydrodynamic processes in MSG beaches are controlled primarily by porosity/hydraulic conductivity, wave reflection and threshold of motion (Mason and Coates 2001). In simple terms, higher hydraulic conductivity results in higher dissipation of wave energy, reduced wave reflection and therefore, increased beach stability. In MSG beaches, sand tends to occupy the spaces between gravel clasts reducing porosity and hydraulic conductivity. Laboratory tests showed that hydraulic conductivity is highest in pure gravel and decreases rapidly with the addition of sand, reaching a minimum when the volume of sand is equal to the pore space between gravel particles (She et al. 2006). Sand proportions of 30-40% or above seem to be linked with increased beach mobility in laboratory tests and nourished beaches (e.g. Mason 1997; López de San Román Blanco 2003; She et

al. 2006). It seems then relevant to investigate whether the effect of increasing proportion of sand is evident in the behaviour of natural MSG beaches.

4.2 Methods

The field sites sediment distributions are complex. The beach can range from deep and shallow coarse gravel berms and ridges, mixed sand and fine gravel, as well as pure sand patches (usually less than 0.02 m thick) overlaying mixed or relatively pure gravels. The variation in sediment distributions can occur over less than ten metres both cross and longshore, which makes characterising an 'average' sediment size for a transect or of the entire system difficult.

Many of the techniques to define sediment characteristics have initially been developed in riverine systems (Folk and Ward 1957 sediment size parameters, Wolman 1954 pebble and grid counts). Riverine research has also been historically more focused on the issues caused by defining bimodal PSDs (Kellerhals and Bray 1971; Wilcock 1993; Smith et al. 1997; Bunte and Abt 2001). This is primarily due to the prevalence of multi-modal sediments in river systems. In some studies, the degree of bimodality has been defined through a 'bimodality' parameter in which the average sediment sizes of the coarse and fine modes is assessed in relation to their respective proportions (Wilcock 1993). Though the use of them as a single parameter to confidently define the PSD is warned against (Smith et al. 1997). With this in mind and the recent investigations into the effect of sand proportion on behaviour instead, this study assesses the PSDs of the gravel (>2mm) and sands and fines (<2mm) separately, before taking the effect of relative proportions into consideration.

The method employed in this study to represent the spatial and temporal variability in the sediment distribution was devised considering the trade-offs between accuracy and time-effort (e.g. Dornbusch et al. 2005; Horn and Walton 2007). To optimise field time and reduce the need for large bulk samples to be collected and analysed in the laboratory, a combination of digital image analysis and laser diffraction was used in the sediment size characterisation (Figure 4.2). The analysis focused on determining the variation in grain size along Transects A-E across 11 beach surveys. Sediment characterisation and/or samples were obtained from the surface (image analysis and surface sand sampling) and through depth (up to 0.4 m deep) at locations where there were visible changes in the proportion of sand and gravel at surface. At times, data collection was limited due to bad weather and/or poor light (affecting the quality of digital images) or high tidal levels.

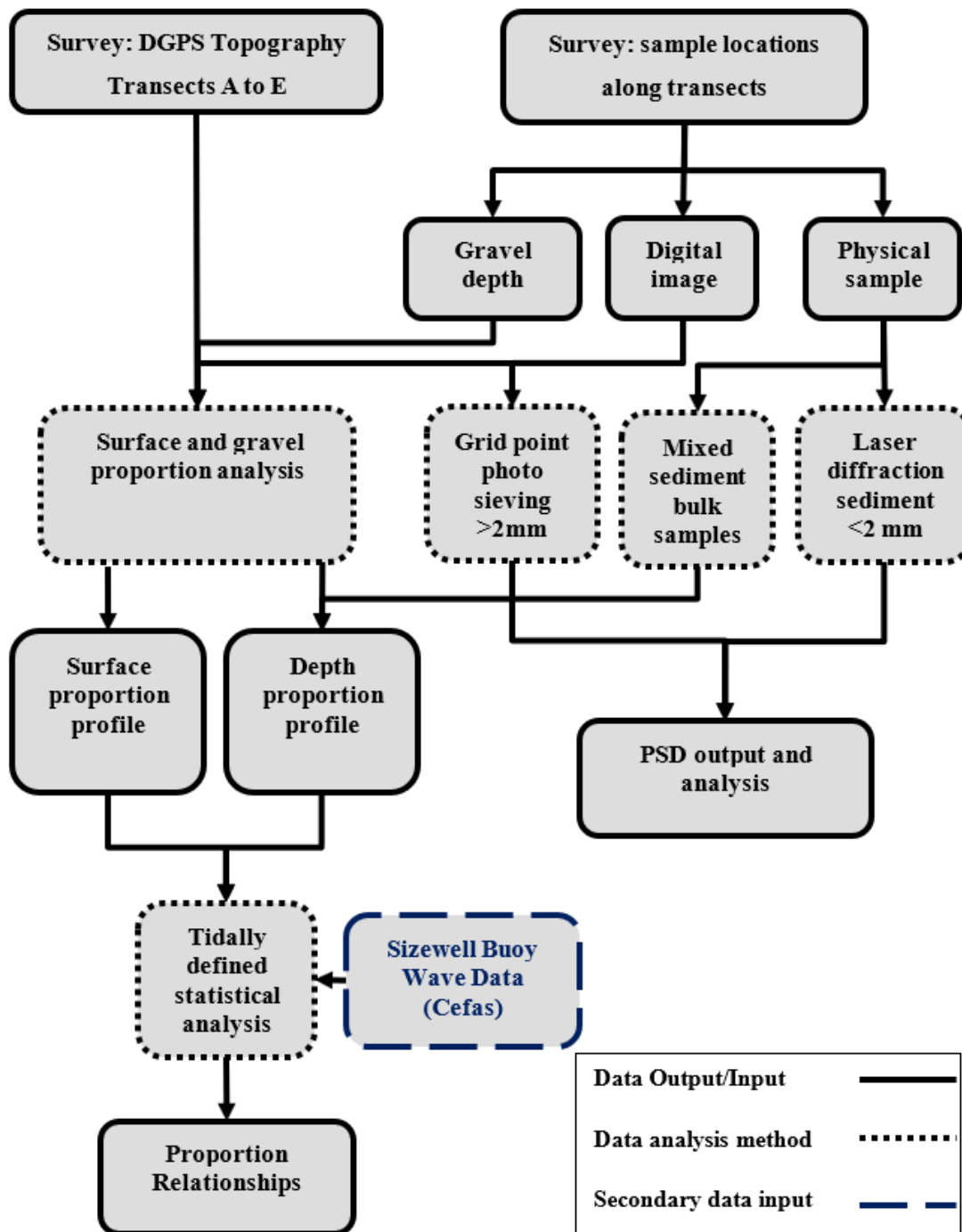


Figure 4.1. Workflow schematic representing data collection and analysis methods for sediment characterisation at site. Solid boxes indicate data input and output, dashed boxes present analysis procedures

4.2.1 Particle size analysis

Defining the particle size distribution of mixed beaches has traditionally involved large bulk samples and manual measurement (Horn and Walton 2007). Image analysis provides an option for intensive sampling without the need for bulk samples to be removed from the site, enabling good coverage in an environment that show considerable spatial and temporal variability. Although photography for sediment characterisation has been utilised since the early 1970s (Kellerhals and Bray 1971), recent developments in digital photography and automated PSD calculation through look-up-catalogue (Rubin 2004), edge detection (Zhang et al. 2018), the auto-correlation (Warrick et al. 2009) and transferable wavelet (Buscombe 2013) methods have allowed faster analysis. Applications of these methods for mixed sediments in coastal settings have shown limitations due to increase in error with a decrease in sorting (Warrick et al. 2009), and the obscuration of image areas containing smaller grains by the presence of larger clasts (Pentney and Dickson 2012).

Systematic tests were undertaken to establish the viability of automate image analysis of pure sand, pure gravel and mixed samples through the transferable wavelet (Buscombe 2013) and auto-correlation (Warrick et al. 2009) methods. The results indicated errors of up to $D_{50} \pm 50\%$ in lab tests when compared with traditional sieving for pure sand and gravel but also an inability to define bimodal distributions. As the more automated methods were considered to have large errors, a more time-consuming approach was utilised using a combination of supervised image analysis for fractions larger than 2 mm and sample collection and laser diffraction analysis using a Malvern Mastersizer 3000 for particles smaller than 2 mm.

On each transect, measurements (generally between 4 and 9) were taken at points of major morphological change and features along each transect (gravel grading and berms, areas of over washed sand, inter-tidal terrace). In each point, a digital image was taken using a Nikon D5300A 24.2-megapixel camera mounted on a horizontal tripod 0.40 m above the ground. If sand was present, samples were collected and for laser diffraction analysis in the laboratory.

A simple grid count method (Hey and Thorne 1983; Yuzyk and Winkler 1991) was used to estimate the size distribution of the gravel fraction through digital image analysis. The images were overlain with digital a 10 x 10 grid (100 points, Bunte and Abt 2001). PSD was determined through measuring intermediate axis of the nearest full particle at each grid cross section through the Jann5s Measure Tool function (v2.01) in Matlab, which converts from pixel size to mm based on a size reference (steel ruler) within the photograph. These sizes were then calibrated through a correction factor (*1.07) outlined by Adams (1979) based on the particle size difference between manual calliper and photo measurement.

The gravel and sand distributions were then analysed through SANDY (Ruiz-Martinez et al. 2016) a Matlab procedure in which the D_{50} and statistics (Folk and Ward 1957, Table 4.1) of sorting (equation (4.1)), skewness (4.2) and kurtosis (4.3) were derived separately for all sediments

below 2 mm (sand and fines) and all above 2 mm (gravel, cobbles and boulders) where ϕ_{nn} indicates the nn percentile of the PSD curve:

$$\sigma_l = \frac{\phi_{84}\phi_{16}}{4} + \frac{\phi_{95}\phi_5}{6.6} \quad (4.1)$$

$$Sk_1 = \frac{\phi_{16} + \phi_{84} - (2)(\phi_{50})}{(2)(\phi_{16} - \phi_{84})} + \frac{\phi_5 + \phi_{95} - (2)(\phi_{50})}{(2)(\phi_{95} - \phi_5)} \quad (4.2)$$

$$K_G = \frac{\phi_{95} - \phi_5}{(2.44)(\phi_{75} - \phi_{25})} \quad (4.3)$$

Table 4.1. Descriptive terms for PSD statistics used throughout the chapter (Folk and Ward 1957).

Sorting (σ_l)		Skewness (Sk_l)		Kurtosis (K_G)	
V. well sorted	<0.35	V. fine skewed	+1.0 to +0.3	V. platykurtic	<0.67
Well sorted	0.35 to 0.50	Fine skewed	+0.3 to +0.1	Platykurtic	0.67 to 0.90
Mod. well sorted	0.50 to 0.70	Symmetrical	+0.1 to -0.1	Mesokurtic	0.90 to 1.11
Moderately sorted	0.70 to 1.00	Coarse skewed	-0.1 to -0.3	Leptokurtic	1.11 to 1.50
Poorly sorted	1.00 to 2.00	V. coarse skewed	-0.3 to -1.0	V. leptokurtic	1.50 to 3.00
V. poorly sorted	2.00 to 4.00			Extr. leptokurtic	>3.00
Extr. poorly sorted	>4.00				

4.2.2 Proportion of sand and gravel at surface

At each sampling point, the proportions of sand and gravel at surface and at depth were estimated. The method for surface proportion utilised the same photographic grid count method, instead defining each grid intersection as sand or gravel. These proportions at each sample point were then used to establish the proportion for each beach compartment defined by the selected tidal. To do so, the characteristics of each sampling point were extended to the midpoint between each of the sample locations (Figure 4.2) and up to 0.40 m depth (see explanation in the next section). It was assumed that the proportion of sand and gravel found at the surface was the same at depth (subsurface).

4.2.3 Proportion of sand and gravel at depth

At each sample point where gravel was present, the thickness of the gravel layer was measured with a ruler by digging a small trench until sand was the dominant grain size. This method allowed trenches up to a maximum depth of 0.30 – 0.35 m, if no sand was present, the gravel layer was assumed to be deeper than 0.35 m. As measurements were limited to the top 0.35 m, and to allow indication of thicker gravel layers, the representation of thickness was limited to the top 0.40 m.

In sampling points where gravel layers were not found at surface, the sediment was formed by a mixture of sand and gravel sizes. To characterise the proportion of sand and gravel, six bulk samples were collected from the intertidal zone of Transects B and D on 27-Sep-2017 at surface, 0.02 and 0.10 m depths. The proportions of sand and gravel (by weight) were measured for each sample (Table 4.2). The average proportion of sand of all subsurface samples (34%) was used to represent the proportions found in the mixed sand and gravel composite below the surface (>0.02 m) along the profile. The proportion of sand and gravel in each beach compartment was calculated following the same approach described in Section 4.2.2.

Table 4.2. Sediment samples used to define % sand in proportion analysis.

Sample (27-Sep-2017)	Depth (m)	Gravel (g)	Sand (g)	Gravel (%)	Sand (%)	Average Surface % Sand (weight)	Average Depth % Sand (weight)
B6A	0	282	199	58.63	41.37	54.19	33.53
B6B	0.02	1478	743	66.55	33.45		
B6C	0.10	1006	697	59.07	40.93		
E7A	0	196	398	33.00	67.00		
E7B	0.02	1122	526	68.08	31.92		
E7C	0.10	797	307	72.19	27.81		

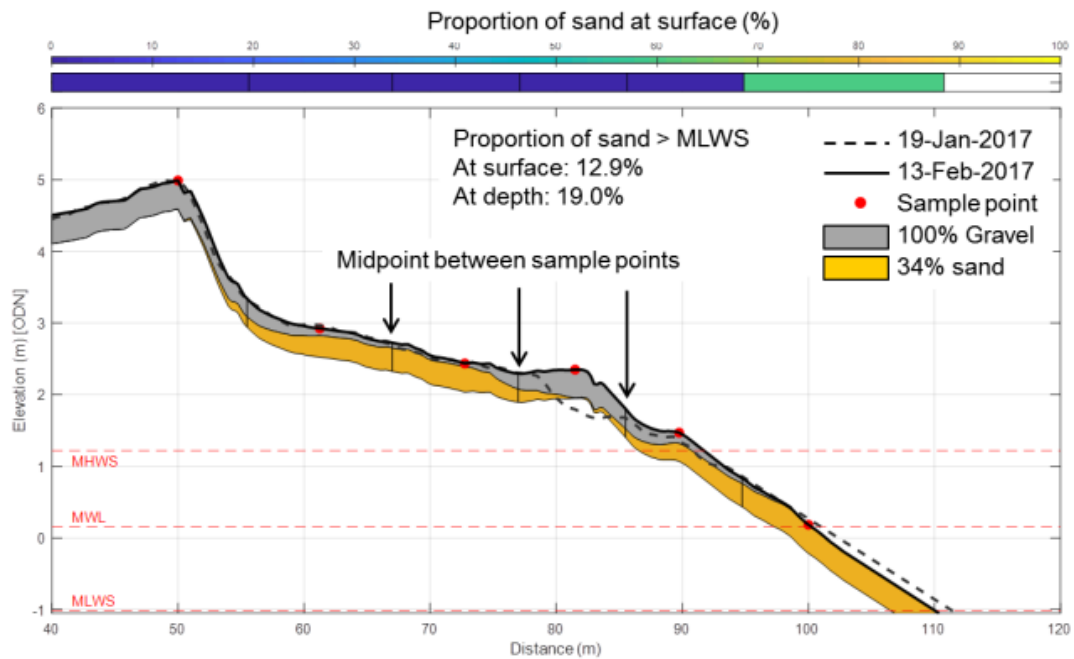


Figure 4.2. Representation of the sediment data along Transect A, showing: the topography on 19-Jan-2017 and in the previous survey on 13-Feb-2017; the distribution of the gravel and the mixed sediment layer (34% sand) within to top 40 cm and along the profile; and at the top, the proportion of sand at surface (the scale shows blue as 0% and yellow as 100%). Notice that although much of the profile has only a thin layer of gravel, the surface analysis only shows the presence of sand in the intertidal region.

4.2.4 Statistical analysis

To assess whether the proportion of sand present in MSG beaches influences beach mobility, a statistical approach (as in Chapter 3, section 3.2.4) was used. Correlations between the proportion of sand at depth and surface in the defined beach compartments and indicators of beach state (shoreline position, profile area), beach change (shoreline position change/d, beach area change/d) and wave parameters (see 3.2.4).

The relationships between beach state and wave parameters were calculated based on the assumption that the proportion of sand was the result of these variables. i.e. the wave climate between survey 1 and 2 resulted in the proportion of sand identified in survey 2. When assessing rates of change the assumption was instead that the proportion of sand caused the identified rate of change. i.e. the proportion of sand calculated in survey 1 resulted in the rate of change (shoreline position or area) that occurred between survey 1 and 2.

4.3 Results

4.3.1 Sediment characterisation

Although there are no strong temporal variations of sediment sizes with season (Appendix B). The gravel at site is variable across the profiles and between transects and ranges from very fine (a minimum of 3.39 mm at Transect A) to very coarse (a maximum of 35.67 mm at Transect B, Table 4.3). The mean D_{50} of each transect however are all classed as medium gravel (between 12.64 and 15.28 mm, -3.5 to -4.0 ϕ) and Mann-Whitney tests between all transects show there are no significant differences in sizes. The sorting values of the site ranges from poorly sorted (1.34 at Transect A) to well sorted (0.36 at Transect C), Transect A has the largest range and standard deviation of sorting but again the spread of the mean values is relatively small; all transects being moderately well sorted between 0.58 (Transect D) and 0.66 (Transect B). The mean kurtosis and skew values indicate on average the gravel portion is symmetrical (0) and mesokurtic (normal distribution, 1), though some samples in all transect are observed to be platykurtic and leptokurtic.

Comparing the gravel samples above and below MHWS (Appendix B) indicates that the mean D_{50} is greater above MHWS for Transects A-D (increases of between 0.96 and 4.62 mm) and smaller for Transect E (reduction of -2.42 mm). The same trend is observed for mean sorting values, which are observed to be more sorted above MHWS for Transects A-D (by 0.10 to 0.26), and less well sorted in Transect E (0.03). Skew and kurtosis differences are not as pronounced, with Transect A-D all staying within symmetrical ranges for above and below MHWS (between -0.04 and 0.09), whereas Transect E is observed to be finely skewed below MHWS (0.14) with mean values for all transects (above and below MHWS) being mesokurtic.

The sand fraction statistical descriptors show the general uniformity of the sand and fines (<2 mm) within the system. Mean D_{50} values for all transects sit within medium sand (0.30 – 0.36 mm, 1.5 ϕ) and is on average, moderately well or well sorted (0.44 to 0.55), symmetrical (-0.03 to 0.03) and mesokurtic (0.91 to 1.01). Below and above MHWS (Appendix B) however show some distinct differences. Above MHWS the samples are on average less well sorted for all transects (0.47 to 0.60 above MHWS and 0.43 to 0.49 below MHWS) which most likely occurs to the lack of sorting action of waves within the intertidal zone. Above MHWS the samples tend to be more leptokurtic (0.98 to 1.08 above MHWS and 0.87 to 0.91 below MHWS) though mean values for both show little skew and remain symmetrical (-0.05 to 0.07).

Table 4.3. Gravel and sand PSD descriptive statistics for all samples during site surveys.

Gravel		D₅₀ (mm)				Sorting (σ_I)				Kurtosis (K_G)				Skewness (Sk_I)			
Transect		Min	Mean	Max	StDev	Min	Mean	Max	StDev	Min	Mean	Max	StDev	Min	Mean	Max	StDev
A		3.39	13.22	25.88	5.29	0.37	0.63	1.34	0.20	0.70	1.03	1.52	0.17	-0.54	-0.02	0.16	0.13
B		4.46	13.25	35.67	6.30	0.44	0.66	0.92	0.13	0.73	1.00	1.28	0.13	-0.40	0.02	0.33	0.17
C		5.41	12.64	20.75	4.62	0.36	0.64	0.97	0.15	0.70	1.00	1.32	0.15	-0.39	-0.01	0.18	0.13
D		4.02	14.62	24.30	5.23	0.41	0.58	0.85	0.10	0.82	1.02	1.34	0.12	-0.28	-0.01	0.14	0.10
E		7.05	15.28	28.73	5.56	0.38	0.62	0.92	0.12	0.79	1.06	1.39	0.13	-0.19	0.08	0.32	0.11
Sand		D₅₀ (mm)				Sorting (σ_I)				Kurtosis (K_G)				Skewness (Sk_I)			
Transect		Min	Mean	Max	StDev	Min	Mean	Max	StDev	Min	Mean	Max	StDev	Min	Mean	Max	StDev
A		0.26	0.33	0.42	0.05	0.44	0.55	0.85	0.12	0.84	1.01	1.47	0.19	-0.06	0.03	0.30	0.11
B		0.28	0.34	0.44	0.05	0.39	0.50	0.75	0.10	0.84	0.95	1.09	0.07	-0.20	-0.02	0.05	0.07
C		0.21	0.30	0.37	0.05	0.41	0.44	0.51	0.04	0.85	0.92	1.05	0.08	-0.08	-0.01	0.06	0.05
D		0.31	0.36	0.48	0.07	0.43	0.52	0.75	0.12	0.85	0.95	1.04	0.07	-0.07	-0.03	0.04	0.04
E		0.28	0.30	0.33	0.02	0.41	0.46	0.52	0.04	0.85	0.91	0.99	0.06	-0.07	-0.01	0.03	0.04

4.3.2 PSD relationships

The gravel fraction of Transect A and B show a wide spread of sorting values, between well and poorly sorted (Figure 4.3a). However, with increasing grain size the spread of the sorting values decreases, sizes between 20 and 40 mm are all between moderately and well sorted. The gravel fractions of Transects C-E (Figure 4.3b) show a similar, though less pronounced relationship. The sand fraction of all transects (Figure 4.3c) displays a strong grouping of well sorted samples between 0.27 and 0.34 mm, within the intertidal area, samples above and near to MHWS, however, show more variability both in sorting and size. There appears to be no polynomial fit of sorting against mean grain size as identified in other MSG beach studies (McLean and Kirk 1969; McLean 1970) however this may be due to the approach taken by these studies, in which mean grain size was taken based on the whole PSD, including sand and fine grains.

The link between height and sorting/grain size within the gravel portion is less defined; Transect A shows a grouping of well sorted gravel samples at an elevation between 5-6 m and of D_{50} approximately 9–14 mm (Figure 4.3a, red points). This grouping occurs at the top berm, which was stable throughout the project. The intertidal zone shows a large spread of both sediment sizing and sorting within the gravel fraction and tends to be less well sorted. This is likely due to gravel particles sitting on the surface of sand dominated areas rather than being sorted through the percolation of smaller particles through larger gravel particles. The largest D_{50} within the intertidal zone, however, exceeded 35 mm and was well sorted, appearing well outside the grouping of all other points, this occurred below MWL (at -0.33 m) in a rare gravel dominated area (06-Dec-2016).

Kurtosis and skew relationships are less defined within the gravel fractions (Figure 4.4a, b and Figure 4.5a, b) with coarse and finely skewed samples throughout transects and elevations. Though in Transects B-E the only very skewed samples (both fine and coarse) were taken in the intertidal zone.

The kurtosis of the sand samples are relatively evenly spread between platykurtic (flattened), mesokurtic (normal) and leptokurtic (peaked). The same grouping of intertidal points and a spread/variation above MHWS is evident, however, a distinct curvilinear relationship of both kurtosis and skew is observed. At the D_{50} of 0.3 mm, the samples indicate no skew (symmetrical) and are platykurtic (more peaked than normal distribution). An increase in grain size results in an increase in skewness (indicating the addition of coarser grains) and a shift towards mesokurtosis. A decrease in grain size appears to have a lesser effect on the skew (remaining symmetrical) but kurtosis again approaches mesokurtosis. Though these changes are small and unlikely to effect the overall behaviour of the system considering the much larger variability of the gravel PSD and the known effect of sand/gravel proportion previously discussed.

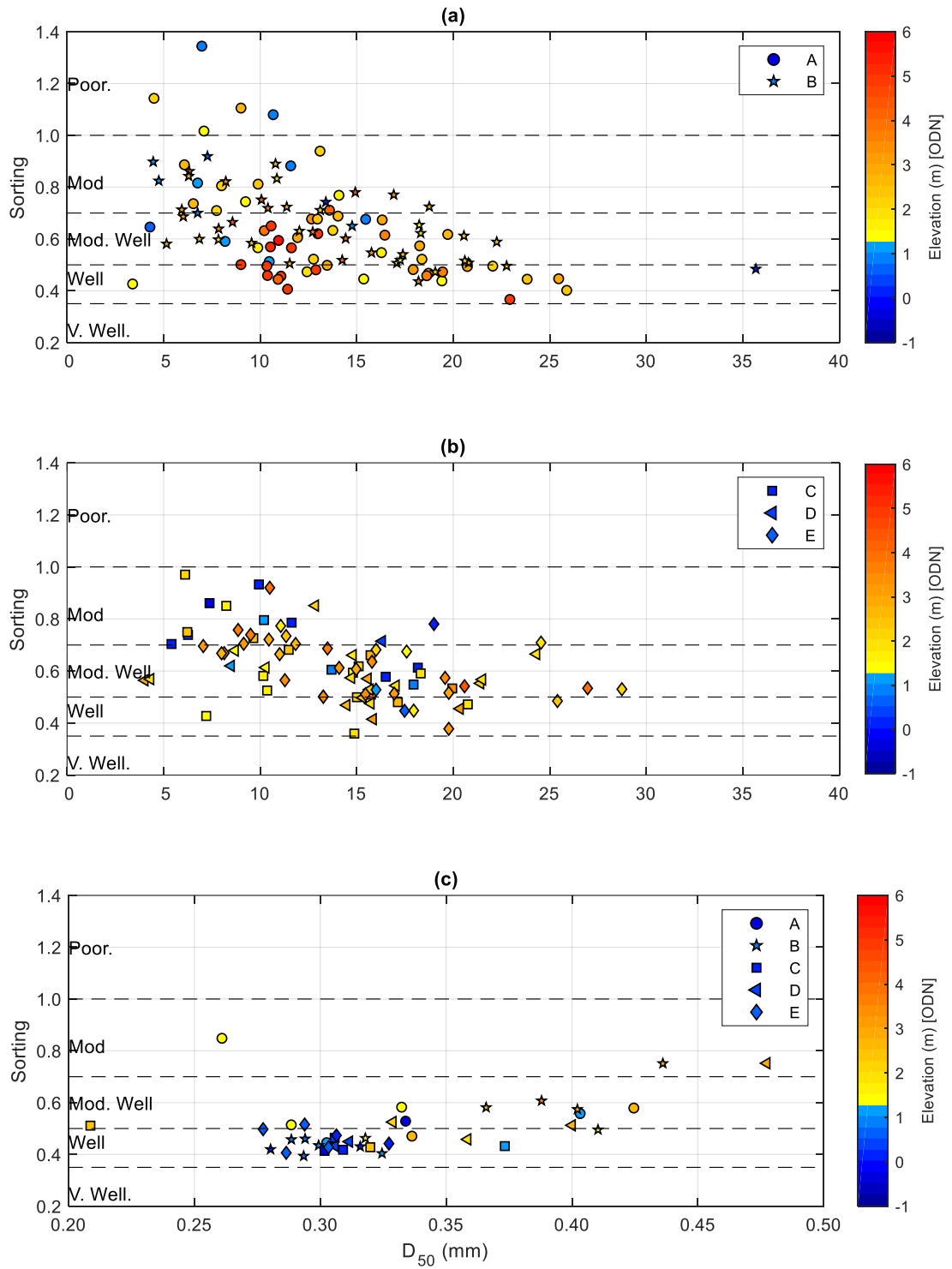


Figure 4.3. Scatter plots of sediment size (D_{50} , x axis) against sorting value (y axis) and elevation (where point shape indicates transect and colour indicates the elevation of the sample: blue for the intertidal zone and yellow/red above 1.25 m ODN). For gravel in Transects A and B (a) and C, D and E (b) and for sand in all transects (c).

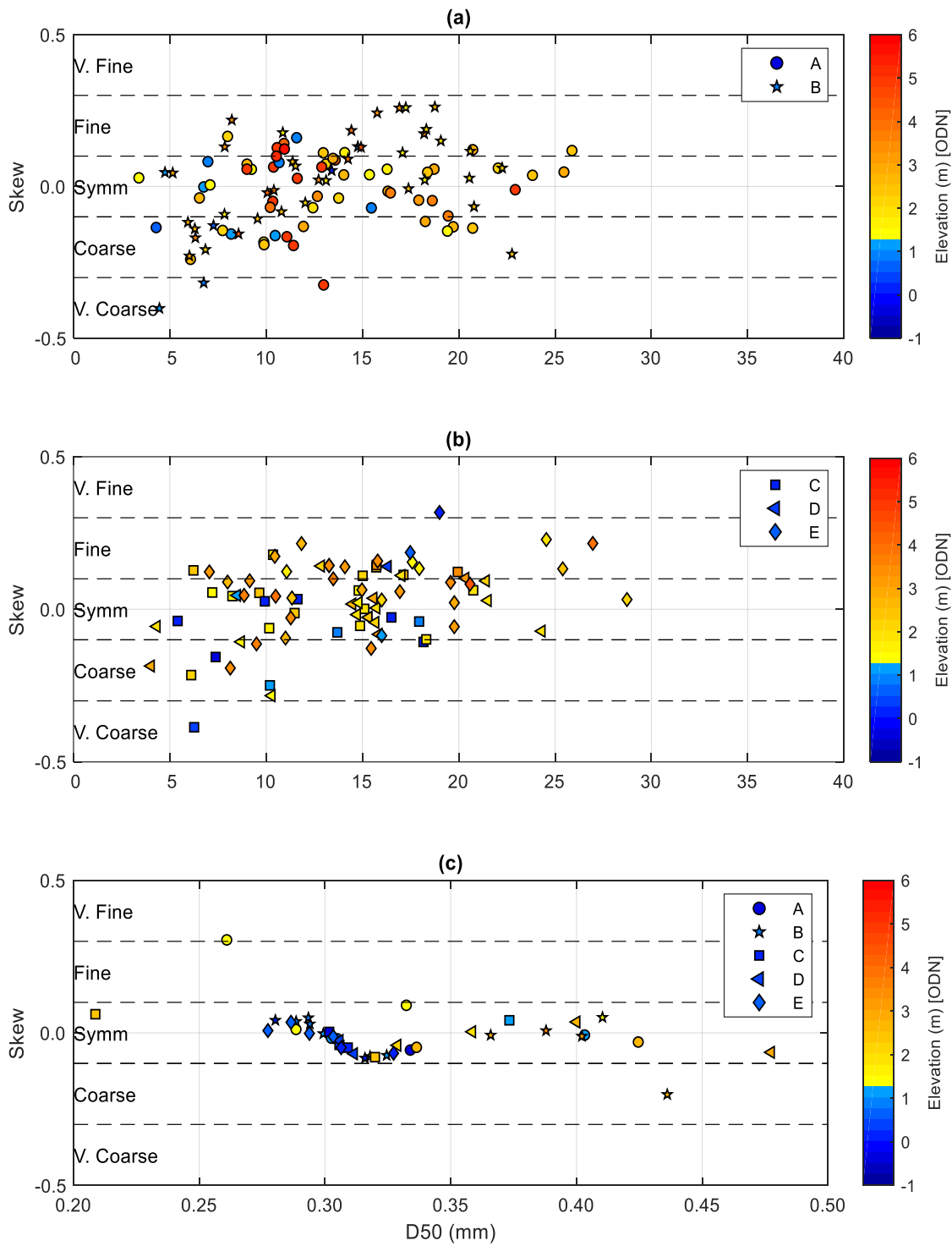


Figure 4.4. Scatter plots of sediment size (D_{50}) against skew and elevation (where point shape indicates transect and colour indicates the elevation of the sample: blue for the intertidal zone and yellow/red above 1.25 m ODN). For gravel in Transects A and B (a) and C, D and E (b) and for sand in all transects (c).

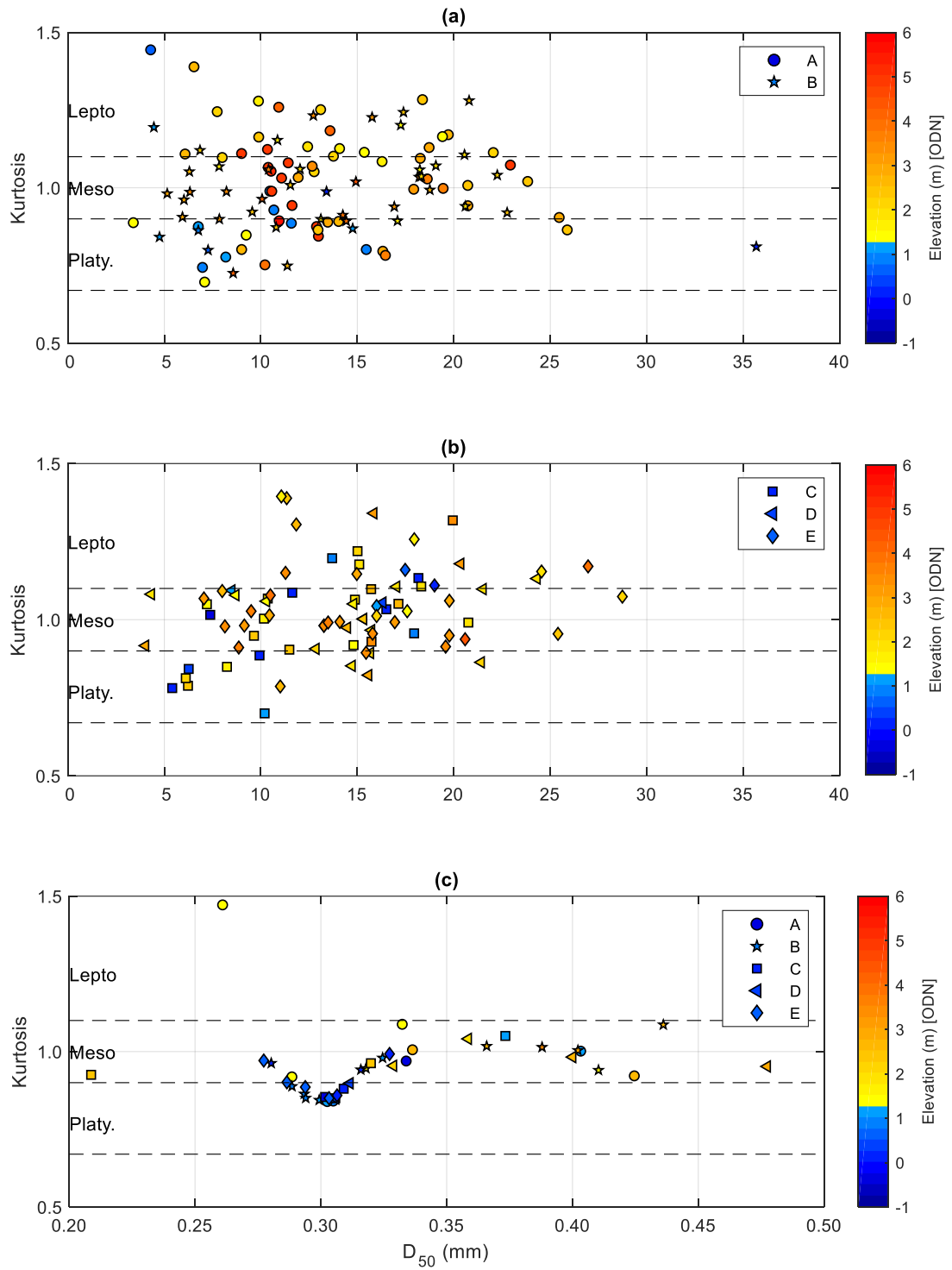


Figure 4.5. Scatter plots of sediment size (D_{50}) against kurtosis and elevation (where point shape indicates transect and colour indicates the elevation of the sample: blue for the intertidal zone and yellow/red above 1.25 m ODN). For gravel in Transects A and B (a) and C, D and E (b) and for sand in all transects (c).

4.3.3 Spatial and temporal variance – sand and gravel

The sand within the system is observed to be relatively uniform through space and time when compared with gravel. This is particularly true within the intertidal zone where the D_{50} of the sand component exclusively sits within medium sand (1-2 ϕ , averaging 0.3 mm) throughout all transects (Figure 4.6a) and a similar value can be observed through time: D_{50} variance of 0.05 mm over the 9 month period presented (Figure 4.6b). Through depth the change is observed to be even smaller; with D_{50} having a range of <0.02 mm in the bulk depth samples analysed at Transect B (Figure 4.6c). The largest variability in D_{50} (spatially and temporally) of the sand portion is above the intertidal area. Specifically, at points where over wash of berms occurs (on the Ness) and around regions affected by engineering works (Figure 4.6d), resulting in more fines and coarser fractions respectively. The low variance in sediment size in the intertidal area suggests the sizes and proportion of gravel maybe the controlling sedimentary driver in variable beach response, the relatively small changes in sand and fines dominated by the swash and over wash processes occurring above MHWS.

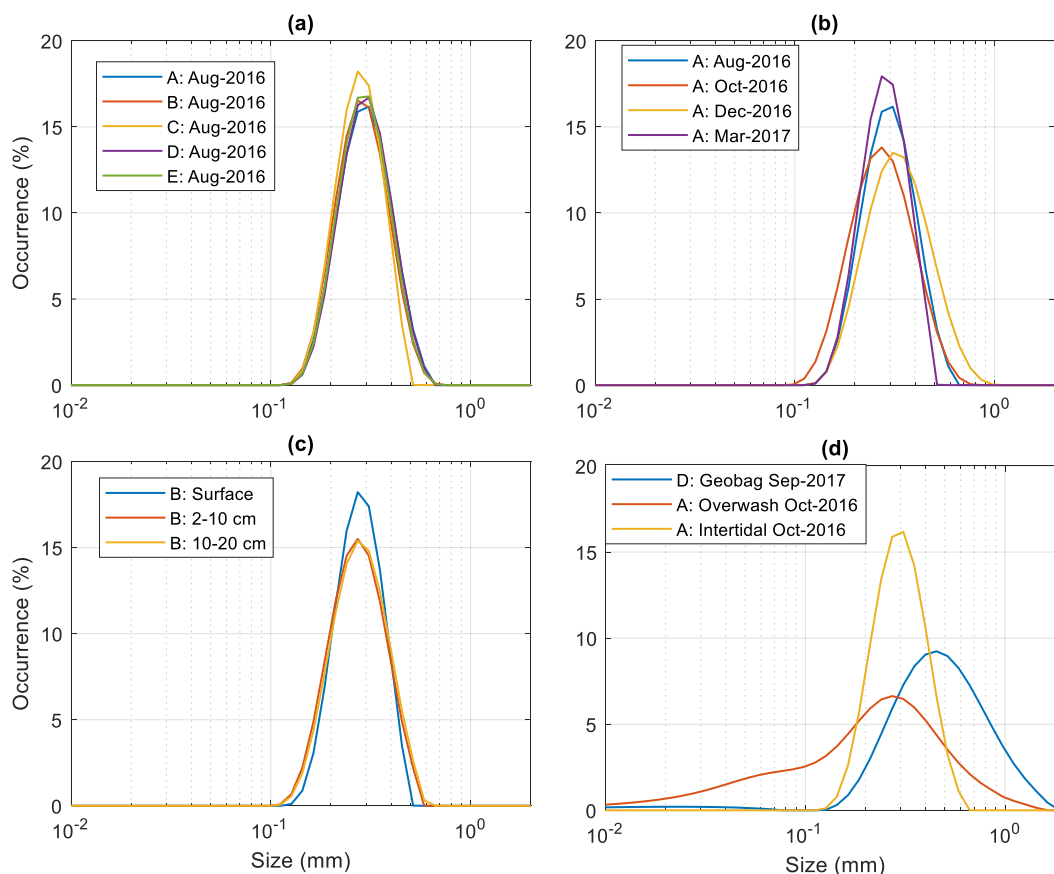


Figure 4.6. Examples of sediment distributions of sand and fines <2 mm (A) across the field site on 03-Aug-2016, (B) between 03-Aug-2016 and 21-Mar-2017 at Transect A, (C) through depth at Transect B on 27-Sep-2017 and (D) the largest variances observed at site influenced by engineering work (Transect D) and natural (over wash at a gravel berm) effects.

Within the gravel fraction temporal changes were found to be indistinct, with sizes and sorting having considerable ranges for each survey with no seasonal or temporal trends (Appendix B). When

considering spatial changes, the data samples were split between transects (A-E) as well as the presence of surface sand (Figure 4.7). There are significant differences between gravel samples at each transect when in the presence of sand (gravel sitting over a visible sand and gravel composite) and where pure gravel (deeper than 0.02 m) occurs. In all transects where sand is present the median D_{50} value is less than in pure gravel samples, Transects A-D show significant differences, whilst Transect E does not:

- Transect A D_{50} : (Mann–Whitney $U = 249$, $n_1 = 18$, $n_2 = 47$, $p < 0.000$);
- Transect B D_{50} : (Mann–Whitney $U = 266$, $n_1 = 26$, $n_2 = 30$, $p < 0.000$);
- Transect C D_{50} : (Mann–Whitney $U = 269$, $n_1 = 18$, $n_2 = 17$, $p < 0.000$);
- Transect D D_{50} : (Mann–Whitney $U = 47.5$, $n_1 = 11$, $n_2 = 14$, $p < 0.003$); and
- Transect E D_{50} : (Mann–Whitney $U = 140$, $n_1 = 17$, $n_2 = 36$, $p < 0.42$)

Differences are also evident (though to a lesser extent) with sorting (Figure 4.7b), where Transects A-C show significant differences between pure gravel (better sorted, with a smaller range) and mixed samples (more poorly sorted with a larger range):

- Transect A Sorting: (Mann–Whitney $U = 748$, $n_1 = 18$, $n_2 = 47$, $p < 0.000$);
- Transect B Sorting: (Mann–Whitney $U = 543$, $n_1 = 26$, $n_2 = 30$, $p < 0.000$);
- Transect C Sorting: (Mann–Whitney $U = 269$, $n_1 = 18$, $n_2 = 17$, $p < 0.000$);
- Transect D Sorting: (Mann–Whitney $U = 94.5$, $n_1 = 11$, $n_2 = 14$, $p < 0.205$); and
- Transect E Sorting: (Mann–Whitney $U = 189.5$, $n_1 = 17$, $n_2 = 36$, $p < 0.308$)

Spatially, the sediment sizes of Transects A-C in the presence of sand (median 8-10 mm, Figure 4.7a) are the most uniform. In fact, Transects A-C show similar trends between both sorting and size, with the less sorted, smaller samples generally where sand is present and better sorted, larger samples in pure gravel measurements. Transects D and E show the same trends though to less of an extent, with the median values of size in sand being smaller than that of gravel.

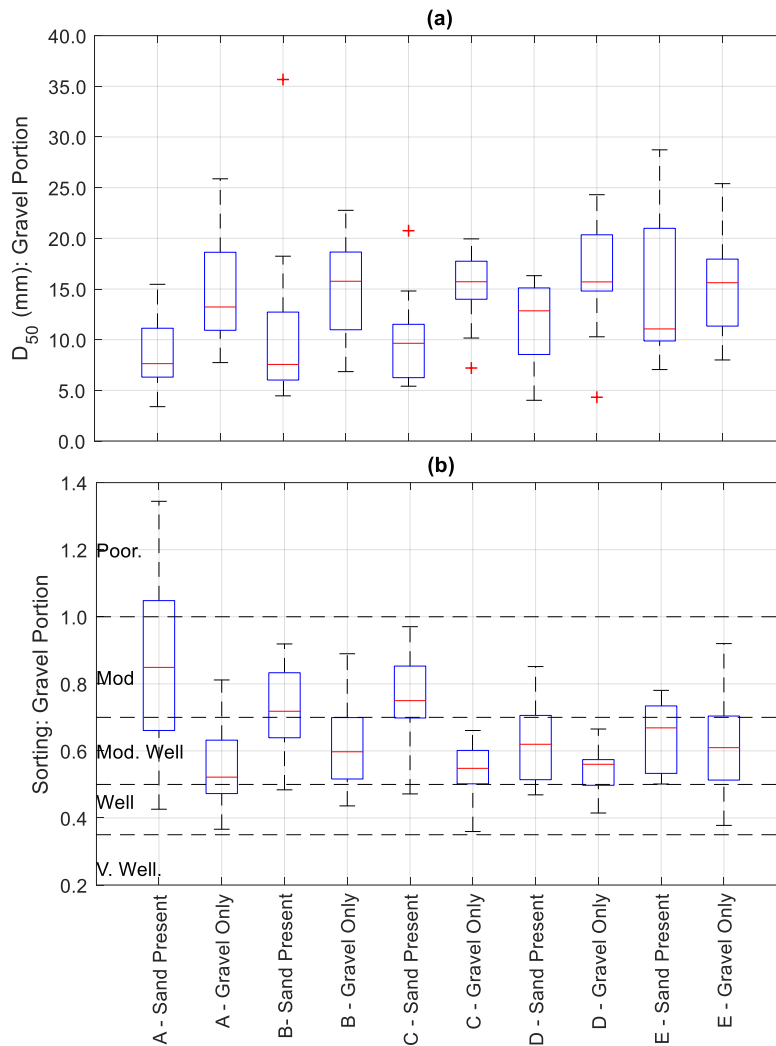


Figure 4.7. Sorting values of gravel portions in the presence of sand and in pure gravel (points in which no sand was visible, and gravel ranged from +0.02 -0.30 m) for Transects A-E) in which red indicates the median value of the all PSDs, the bottom and top edges are 25th and 75th percentiles respectively and the whiskers extend the range of the data.

4.3.4 Changes in the proportion of sand across and between the profiles

When considering data from all transects together, the proportion of sand is significantly higher in areas below than above MHWS (Figure 4.8) both at surface (Mann–Whitney $U = 67$, $n_1 = n_2 = 45$, $p < 0.000$) and at depth (Mann–Whitney $U = 33$, $n_1 = n_2 = 45$, $p < 0.000$). The median proportion of sand at surface is 61.2% for areas below MHWS and 7.3% for areas above MHWS, while at depth it is 34.9% and 21.8%, respectively. Therefore, on average, the proportion of sand at surface tends to be significantly higher than at depth in the intertidal (Mann–Whitney $U = 279$, $n_1 = n_2 = 45$, $p < 0.000$) and lower in areas above MHWS (Mann–Whitney $U = 332.5$, $n_1 = n_2 = 45$, $p < 0.000$). However, there is no significant difference between the proportion of sand at surface and at depth when the areas above and below MHWS are considered together, i.e. areas above MLWS (Mann–Whitney $U = 830$, $n_1 = n_2 = 45$, $p = 0.141$) and above MWL (Mann–Whitney $U = 771.5$, $n_1 = n_2 = 45$, $p = 0.052$).

There is a large variation in the proportion of sand at the surface than at depth in all beach compartments, the difference is more pronounced in the intertidal area. While there is a significant difference in the proportion of sand at depth across all beach compartments, no significant difference was found within the intertidal area for the proportion of sand at surface ($X^2(2)=4.49$, $p=0.106$). Results of these analyses suggest that quantifying the proportion of sand (and gravel) at surface only and in the intertidal area alone will not provide a good reflection of the characteristics within the mobile beach sediment layer. Therefore, measurements at surface and depth both in the intertidal and supratidal areas are needed to obtain a more accurate estimate of the volume of sand and gravel that forms the mobile layer of an MSG beach.

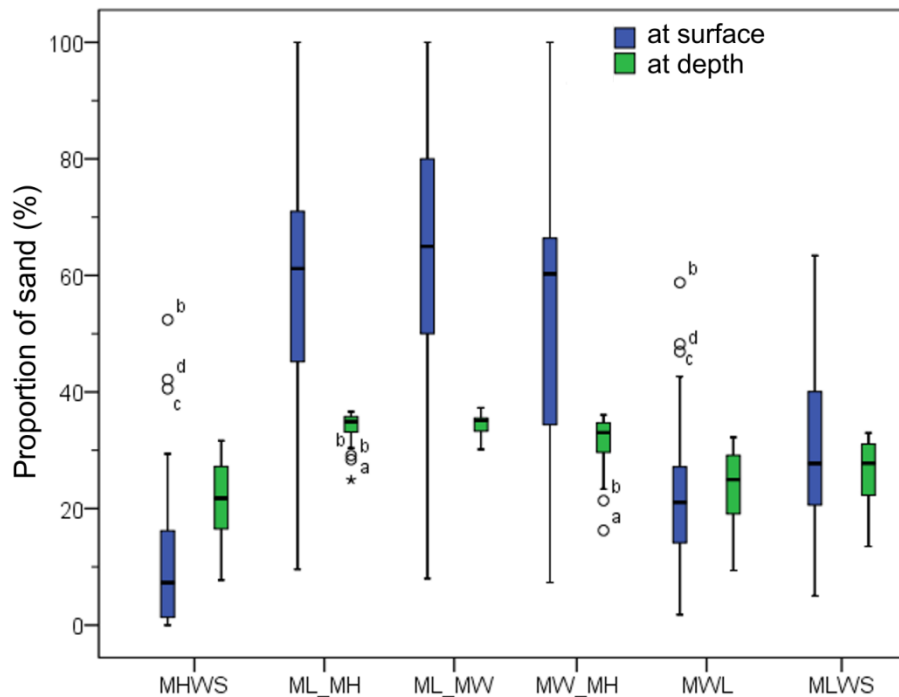


Figure 4.8. Box plot showing the estimated proportion of sand at surface and at depth for each beach level considering data from all transects.

4.3.5 Influence of proportion of sand on beach state and mobility

Important differences were found in the correlation between the proportion of sand at surface and at depth and indicators of the beach state (i.e. beach width and cross-section area) when beach levels above and below MHWS are considered (Table 4.4). Significant positive correlations were found between the proportion of sand at surface and at depth for areas above and below MHWS. However, the correlation is considerably stronger when data from all beach compartments are analysed ($\rho=0.806$, $n=270$, $p<0.000$). For areas below MHWS (the intertidal), no significant correlations were found between the proportion of sand at surface or at depth and the respective cross-section area or beach width. On the other hand, for the data above MHWS, significant negative correlations were found between the proportion of sand at depth and beach width ($\rho=-0.68$, $n=45$, $p<0.000$) and also cross-section area ($\rho=-0.512$, $n=45$, $p<0.000$). Therefore, these results suggest an association between higher proportions of sand above MHWS and reduction of beach width and area.

Table 4.4. Results of Spearman correlation tests (two-tailed) between estimates of proportion of sand at surface and at depth, beach width and cross-section area considering data from all transects for all beach levels, only for the area above MHWS and for the area between MLWS and MHWS (intertidal).

Variable 1	Variable 2	All data	Above MHWS	MLWS-MHWS (intertidal)
Proportion sand at surface	Proportion of sand at depth	rho=0.806 n=270, p<0.000	rho=0.413 n=45, p=0.005	rho=0.504 n=45, p<0.000
	Beach width	rho=-0.087 n=135, p=0.157	rho=-0.230 n=45, p=0.129	rho=-0.027 ^a n=45, p=0.858
	Cross-section area	rho=-0.167 n=270, p=0.003	rho=-0.164 n=45, p=0.283	rho=-0.086 n=45, p=0.573
Proportion sand at depth	Beach width	rho=-0.435 n=135, p<0.000	rho=-0.680 n=45, p<0.000	rho=-0.053 ^a n=45, p=0.730
	Cross-section area	rho=-0.275 n=270, p<0.000	rho=-0.512 n=45, p<0.000	rho=-0.194 n=45, p=0.202

^a Results are shown for analysis considering beach width at MHWS (results were also not significant for beach width at MLWS).

When assessing the rate of change (both area and shoreline position change per day) significant relationships were found primarily at Transect A and C, with a single relationship at Transect E. Transect A showed exclusively positive relationships with proportion of sand i.e. an increase in profile area, or movement of the shoreline seaward was accompanied by an increase in the proportion of sand. Shoreline position relationships ranged from strong to very strong for depth analysis: change at MWL against percent MLWS-MHWS ($r=0.88$, $p=0.003$, $n=8$, Figure 4.9a), MLWS change against MLWS-MHWS ($r=0.86$, $p=0.006$, $n=8$) and MHWS change against MWL-MHWS ($r=0.85$, $p=0.006$, $n=8$) all showing positive relationships. Area change significant relationships were found only within the intertidal region between MLWS and MHWS ($r=0.88$, $p=0.004$, $n=8$, Figure 4.9b) and between MWL and MHWS ($r=0.78$, $p=0.020$, $n=8$) with their respective proportion values. In comparison Transect C shows very strong negative correlations for rates of area change throughout the profile (depth analysis) above MLWS ($r=-0.94$, $p=0.000$, $n=8$, Figure 4.9c), Above MWL ($r=-0.85$, $p=0.008$, $n=8$) and above MHWS ($r=-0.90$, $p=0.002$, $n=8$) but also for above MHWS for surface analysis ($r=-0.81$, $p=0.014$, $n=8$). A single significant relationship was found at Transect E above MWL (surface analysis) against area rate of change ($r=-0.71$, $p=0.049$, $n=8$).

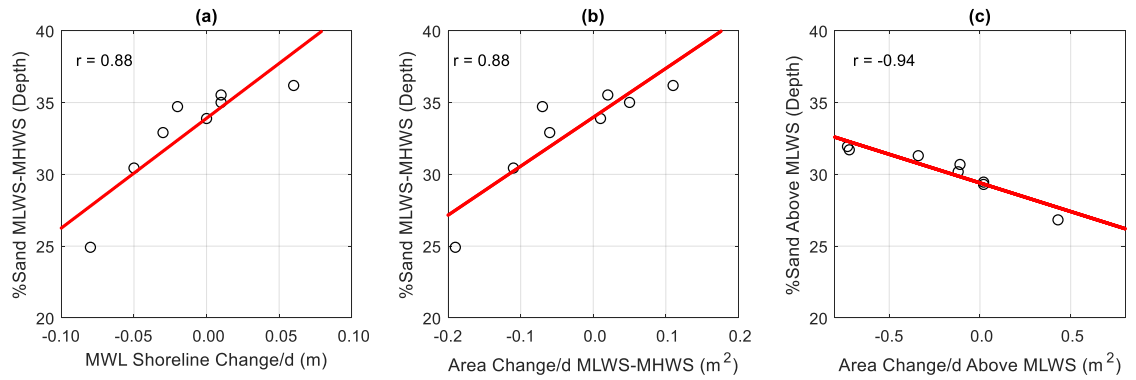


Figure 4.9. Scatter plots of depth analysis Transect A a) MWL shoreline change/d and %sand MLWS-MHWS; b) area change/d MLWS-MHWS and %sand MLWS-MHWS; and Transect C c) Area change above MLWS and %sand above MLWS.

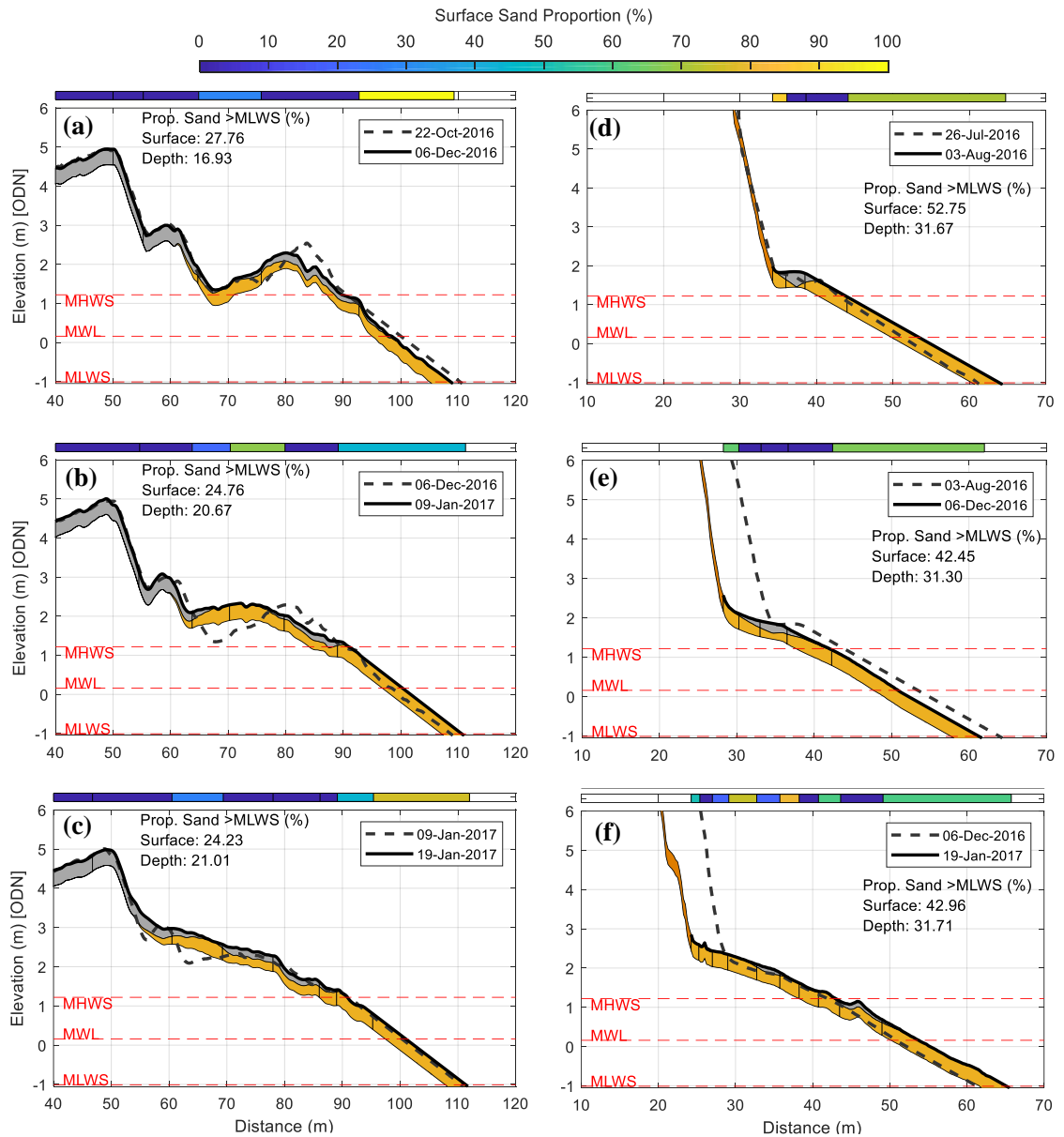


Figure 4.10. Sediment and profile behaviour of Transects A (panels a – c) between 06-Dec-2016 and 19-Jan-2017 and Transect C (panels d – f) between 03-Aug-2016 and 19-Jan-2017.

The contrary trends observed between Transect A and C maybe linked with the distinct morphological differences in the profiles as well as the dominant LST processes over the project. Both Transects have a considerable but differing sediment sources above MHWS: Transect A consists of gravel dominated berms and Transect C sandy cliffs. In the case of Transect A, an increase in area over the winter of 2016-2017 coincided with an increase in sand proportion at depth (Figure 4.10a to c), where three distinct gravel berms meld into a more planar profile which was primarily the composite sand/gravel mix. The source of this sand is unclear, though the southerly (32/51% N/S) dominated winter and cliff recession at Transect C (Figure 4.10d to f) suggests LST north towards the Ness. The proportion of sand (depth analysis) at Transect C is less volatile (Figure 4.9C) remaining consistent (changing by less than 0.5% >MLWS between August 2016 and January 2017), even with rapid erosion of the cliff face likely to introduce considerable amounts of sand into the system (though it is worth noting the sediment in the cliff face is not included in the proportion calculations).

4.3.6 Wave climate effects

When assessing the wave climate effects on sand and gravel proportions Transects A and C again show strong though opposite relationships, Transect D and E show no significant correlations.

At Transect A significant strong negative relationships were found between the proportion of sand at surface (e.g. above MLWS) and the duration of waves higher than 2.5 m ($r=-0.72$, $p=0.020$, $n=10$, Figure 4.11a), particularly from a southerly direction ($r=-0.93$, $p=0.000$, $n=10$, Figure 4.11b). A wider range and further negative correlations are found for proportion of sand at depth (for areas above MLWS, MWL and MHWS) and indicators of wave energy, i.e. 95th percentile of wave height (the strongest, $r=-0.66$, $p=0.037$, $n=10$, Figure 4.11c), mean H_s , duration of waves higher than 2.5 m and wave power. Transect B shows similar correlations with wave power though no other parameters at MLWS ($r=-0.72$, $p=0.020$, $n=10$), MWL ($r=-0.73$, $p=0.016$, $n=10$) and MHWS ($r=-0.66$, $p=0.036$, $n=10$). Unsurprisingly, these results indicate that higher wave energy tends to be associated with a lower proportion of sand along the beach profile.

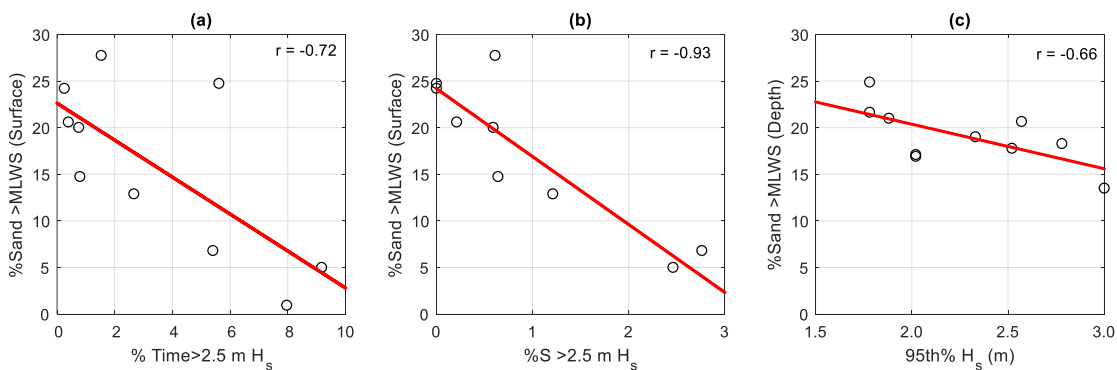


Figure 4.11. Scatter plots of surface analysis at Transect A a) %time above 2.5 m H_s and %sand above MLWS (surface) b) %time $S >2.5$ m H_s and %sand above MLWS (surface) (c) 95th Percentile H_s and %sand above MLWS (depth).

Perhaps the most interesting relationships are found at Transect C, where much like the rate of change explored in the previous section, oppose those seen at Transect A. These relationships could be linked to the cliff recession observed during the project, providing a pure sand source to the system. Increasing wave energy and directional components are linked exclusively to an increase in sand which impacts the surface analysis most strongly. Significant correlations are found at above MLWS and within the intertidal cells, with the strongest of these being associated with the mean ($r=0.90$, $p=0.003$, $n=8$, Figure 4.12a) and 95th percentile of wave height ($r=0.88$, $p=0.003$, $n=8$, Figure 4.12B) between MLWS and MHWS. Similar significant relationships also occurred for wave power and % time >2.5 m (Above MLWS and for all intertidal cells) with the surface analysis methodology. Depth analysis, relationships are not as abundant, though proportion between MLWS and MWL was correlated with 95th percentile ($r=0.75$, $p=0.030$, $n=8$), mean wave height ($r=0.85$, $p=0.008$, $n=8$) and wave power ($r=0.79$, $p=0.019$, $n=8$). When assessing the directional parameters surface analysis indicates significant positive correlations with North%>2.5 m above MLWS ($r=0.74$, $p=0.037$, $n=8$) and, between MWL and MHWS ($r=0.82$, $p=0.013$, $n=8$) and between MLWS and MHWS ($r=0.79$, $p=0.019$, $n=8$). The intertidal (MLW-MHWS) also showed a positive correlation with South%>2.5 m utilising surface analysis, though a negative correlation above MHWS ($r=-0.74$, $p=0.035$, $n=8$, Figure 4.12c) for the depth analysis.

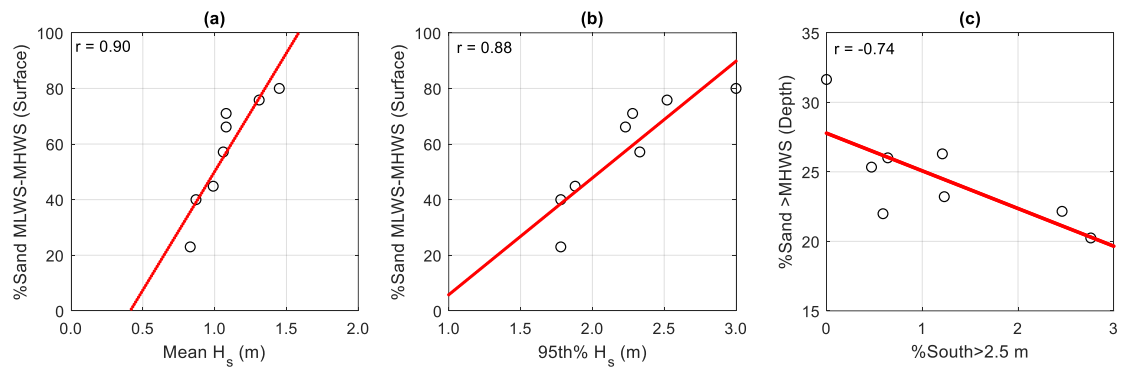


Figure 4.12. Scatter plots of surface analysis at Transect C of a) 95th percentile between MLWS and MHWS b) 95th percentile above MLWS and depth analysis (c) % N>2.5 above MHWS

4.4 Discussion

The methodologies employed, although using several assumptions and simplifications have shown to characterise much of the variance (spatially and temporally) that can be seen at site. It has also highlighted the need and current lack of frameworks for the analysis of sediment characteristics on MSG beaches. Although extensive sampling of MSG systems has been done historically (McLean and Kirk 1969; McLean 1970) and more recently (Dawe 2001; Horn and Walton 2007) sampling and analysis is often only taken as a snapshot (Dawe 2001) or in relation to nourishment works (Horn and Walton 2007; Zarkogiannis et al. 2018), and so the understanding of long-term behaviour and the relationship with external drivers is limited. The recent focus on the effect of sand proportion on beach behaviour (Mason 1997; Mason and Coates 2001; López de San Román Blanco 2003; She et al. 2006, 2007) hypothesise that a hydraulic conductivity low occurs at ~34% sand content, which

in turn influences the rate of erosion. This hypothesis has been proven through lab tests (López de San Román Blanco 2003; She et al. 2007) where proportions can be accurately controlled, however when transferring this to the field the task becomes more difficult. The research highlights the variability in calculated sediment proportion both through the methodology used (surface and depth) and through space and time, demonstrating the difficulty in defining the proportion of sand in a system particularly at sites such as Thorpeness, where the beach above MHWS can comprise of deep gravel berms, sandy cliffs or engineering works and a sand-gravel mix within the intertidal zone.

The fact rates of change and wave climate show numerous though opposing significant correlations with the proportion of sand at Transect A and C suggests variability maybe caused due to complexity in the environment. Both transects display considerable sediment sources above MHWS; for Transect A this is gravel berms and at Transect C the sandy cliff. As a result, in Transect A increasing wave energy was observed to increase the proportion of gravel (sand proportion reduced) in surface and depth analysis for the whole profile, indicating a spread of this gravel component to the lower sections of the profile. In Transect C the opposite occurred, with erosion of the cliff face resulting in an increase in the proportion of sand. This adds complexity to identifying the links between sand proportion and erosion rates, as it is difficult to assess the sediment deeper in the profile without heavy machinery operations (such as Neal et al. 2002) and the associated destructive effects on the natural profile.

The limitations of the methods used are primarily based on the assumptions made to define both the PSD and proportion of sand/gravel. Defining the PSD of the gravel through a 100 point analysis provided a middle ground between the logistical difficulties of bulk sampling gravel and the speed (though inaccuracy) of automated digital analysis (Rubin 2004; Warrick et al. 2009; Buscombe 2013) on mixed systems (Pentney and Dickson 2012). It also shows limitations in the sand dominated regions within the intertidal zone, where a sand veneer often overlays a gravel dominated composite mix. The effect of this within proportion analysis was a highly variable surface and a more stable depth analysis proportion, the first skewed by the assumption of the surface spatial proportion representing through depth and the second regulated by the predefined 34/66% sand/gravel composite definition. Improvements on this would require more physical samples to be taken of the composite mix to understand changes occurring below the surface sand veneer and beneath the gravel berms. Recent improvements in photogrammetry and unmanned aerial vehicle (UAV) use for defining sediment distributions (Elsner et al. 2015) would allow spatial change and movement of gravel patches to be assessed both long- and cross-shore. Unfortunately, the fundamental issue, particularly in mixed environments is that the surface composition can vary vastly from what occurs at depth. Therefore, methods to accurately characterise a system need to evaluate these differences and it seems currently the most robust method for this is manual sampling.

5. Quantifying Nearshore Dynamics Using X-Band Radar Data

5.1 Introduction

This chapter seeks to establish a robust methodology for the use of X-band radar in coastal and nearshore modelling; establishing processing standards and analysis techniques. The derived methodology is then applied to understand the nearshore variability at site, with a focus on the influence of bimodal wave direction and the resulting interaction between the nearshore and shoreline.

The nearshore zone is defined as the area between the low tide line and the water depth where storm waves cease to impact the seabed (Davidson-Arnott and Greenwood 2003). In the nearshore, wave refraction and dissipation processes occur and influence the alongshore distribution of wave energy, which in turn controls the rate of coastal change (e.g. Hequette et al. 2009). The control on waves by changing nearshore bathymetry has been the subject of increased research interest (Elko et al. 2014), primarily to understand and predict shoreline positions (e.g. Ruessink et al. 2004; Hequette et al. 2009; Hequette and Aernouts 2010; Stokes et al. 2015). In these studies, a growth in nearshore sediment volume has been shown to provide protection to the coast during the first high energy events that follow periods of low energy (Dissanayake et al. 2015). On the other hand, the occurrence of erosion hot-spots has been attributed to concentration of wave energy caused by focusing with complex nearshore geology (e.g. Browder and McNinch 2006; Schupp et al. 2006). These processes are further controlled by seasonal or longer-term changes in the incident wave climate (Hegermiller et al. 2017) and by wave direction bimodality (Burningham and French 2016).

The effect on wave energy distribution and associated sediment transport attributable to changes in nearshore waves has been investigated in the field (e.g. Malvarez and Cooper 2000; Bender and Dean 2003; Van Lancker et al. 2004) and through modelling studies (e.g. Burningham and French 2016; Hegermiller et al. 2017; Limber et al. 2017) where relationships between offshore wave conditions, nearshore bathymetry and alongshore wave energy distributions have been established (e.g. Cooper and Navas, 2004). Most conceptual and numerical models developed to describe shoreline behaviour focus on sandy systems (e.g. Masselink et al. 2014; Bergsma et al. 2016). Studies of MSG beaches are much more limited (e.g. Van Lancker et al. 2004; Roberts et al. 2013).

Models used to investigate how changes in the nearshore sea bed affect shoreline behaviour require accurate bathymetric data acquired on at least two occasions. The time between repeat surveys must reflect the local rates of bathymetric changes and capture the movement of features that affect the incident waves. While vessel-based bathymetric surveys are accurate to ± 20 -30 cm horizontally and ± 2 -8 cm in elevation (Ernstsen et al. 2006; Hequette et al. 2009; McCall et al. 2015; Bergillos et al.

2017a), they are also expensive and limited by weather and sea conditions. Stormy periods when offshore changes in bathymetry may be largest can therefore be missed. However, this limitation has been overcome to some extent by remote sensing techniques which enable higher frequency measurements of the nearshore at a fraction of the cost of vessel-based surveys even during high energy periods (Esteves et al. 2007).

Camera-based optical systems, such as Argus (Holman et al. 1991; Smit et al. 2007), are passive remote sensing tools that use one or more cameras and image analysis techniques to derive water depth and basic wave and current parameters (e.g. Holman and Stanley 2007). These systems have been employed in numerous beach study campaigns concerned with, for example, bar dynamics and storm impacts (e.g. Masselink et al. 2014), long-term coastal evolution (Smit et al. 2007) and in support of coastal management (Davidson et al. 2007). The use of camera-based systems is limited by daylight hours and weather-related visibility and requires image rectification and other geometric corrections if wind or other factors give rise to camera movements. Further, with an absolute range of ~1000-1500 m per camera, pixel resolution at 1500 m from the camera exceeds 40 m (Holman and Stanley 2007). Optical systems are most useful in studies of the wide dissipative beaches in macro-tidal regimes that enable quantification of morphology for large exposed intertidal areas (van Dongeren et al. 2008; Hequette and Aernouts 2010; Masselink et al. 2014; Stokes et al. 2015; Bergsma et al. 2016). Most recently, cBathy (Holman et al. 2013) has been applied to derive nearshore bathymetric information from the camera images.

Radar offers an alternative to optical remote sensing that required no image correction and can be operational irrespective of the daylight and weather conditions. Through analysis of X-Band radar images of the sea surface, information related to bathymetry, waves and surface currents can be derived over an area with a radius of up to 5 km offshore (e.g. Bell et al. 2016). The use of wave inversion techniques to calculate bathymetry has been long established with X-band radar (Bell 1999; Hessner and Bell 2009; Ludeno et al. 2015) and is discussed further in the sections below.

Evidence suggests that mobile sea bed features offshore from Thorpeness may influence the incident wave climate and contribute in part to the temporal and spatial occurrence of episodic erosion events at locations along the village frontage (Williams 2014). Similar effects were observed elsewhere off the Suffolk coast by Burningham and French (2016) who identify the controls on wave climate by offshore sand bank systems and the hard geology of the sea bed. With the aim of establishing if changes in nearshore bathymetry at the Thorpeness study site are influential in the behaviour of the shoreline, this chapter presents results from the analysis of radar-derived hydrodynamic, wave and bathymetric data collected over 19 months. While past studies of the Suffolk coast have examined broad-scale, relatively long-term coastal behaviour using beach and coastal monitoring data, the understanding of localised episodic erosion events have received much less attention. Thus, this chapter seeks use radar data to understand the effects of bimodal wave climate and changing bed features on observed shoreline behaviour.

5.2 Methods

5.2.1 Radar Fundamentals

X-band radar (Radio Detection and Ranging) is defined by IEEE (Institute of Electrical and Electronics Engineers) as microwave energy within the frequency of 8 and 12 GHz and wavelength of 2.50 to 3.75 cm. It has been traditionally used for nautical navigation and collision avoidance however in the late 20th century adopted as a method for deriving sea state parameters (Young et al. 1985), surface currents and bathymetry for a range of oceanographic purposes.

This wavelength allows the resolving of relatively small surface ripples (caused by wind speeds >3 m s^{-1}) on the water surface through an understanding of Bragg scattering (Bragg and Bragg 1913). The reflection of these radar pulses causes constructive interference (Figure 5.1) which is received by the radar; the received signal strength and speed in relation to distance can be used to understand the size and shape of the ocean surface through equation:

$$d_r = \frac{\lambda_t}{2 \cdot \cos\theta_b} \quad (5.1)$$

Where: d_r = distance of the reflective sub surfaces, λ_t = transmitted wave length, θ_b = incident 'Bragg' angle.

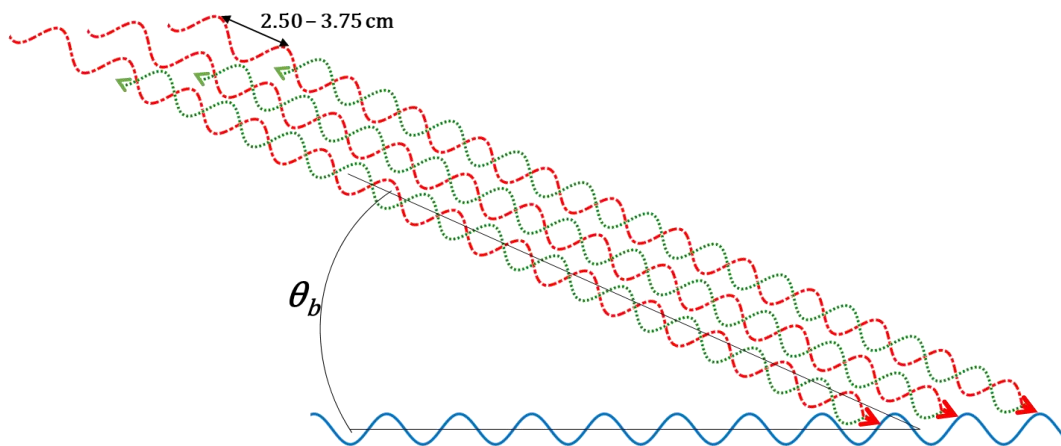


Figure 5.1. Bragg scattering schematic showing the reflection of X-band radar waves against capillary surface waves.

This back-scatter intensity is then mapped based on the rotation of the radar into polar coordinates. For each rotation of the radar the raw analogue image is converted through an Analogue-to-Digital converter (ADC) and projected onto a Cartesian grid. This sequence of images can then be 'stacked' (Figure 5.3) and forms the basis of deriving of all parameters. When deployed in offshore deep water, the whole radar image can be assumed to be homogenous, in coastal applications the effect of refraction must be considered and so the radar image is split into smaller subsections from which

wave spectra are derived (Ludeno et al. 2015). The understanding of wave behaviour due to the underlying bathymetry is then used to derive water depth within each smaller subsection (see 5.2.4).

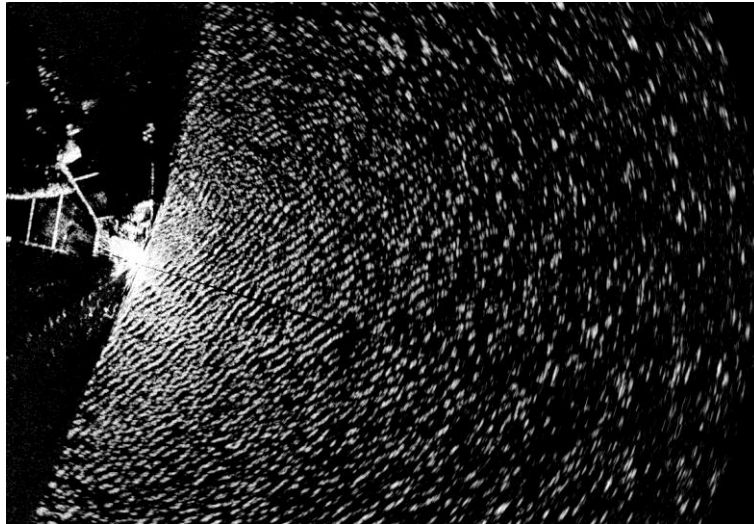


Figure 5.2. A raw radar image at Thorpeness with surface clutter from a SE wave direction

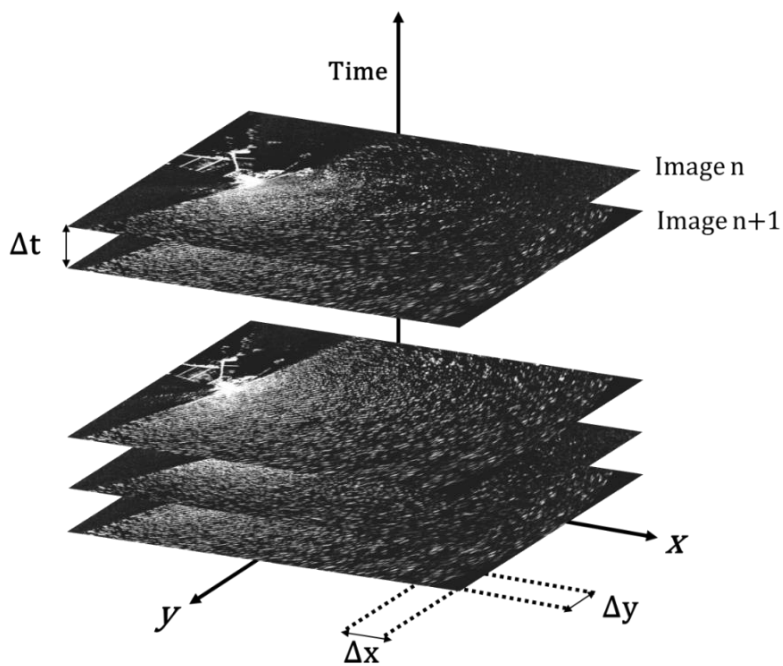


Figure 5.3. A stacked sequence of raw backscatter images, with each layer being a full rotation of the radar, the speed of this rotation being the basis of Δt and the wave inversion calculation, x and y coordinates represent Easting and Northing respectively, Δx and Δy are the window in which the wave inversion depth is calculated.

As part of a NERC-funded project¹, a Kelvin Hughes 10kW, 9.8 GHz marine X-band radar system was deployed at Thorpeness by the National Oceanographic Centre Liverpool (NOC) in August 2015 (Figure 5.4). The study focused on an area of 3.3 km² (1.5 km alongshore x 2.2 km offshore) at a spatial resolution of 40 x 40 m. The analogue radar images of the sea surface were digitised by the OceanWaves WaMoS II ADC at ~0.8-degree horizontal resolution. Wave parameters (H_s , T_p , T_m , Dir_M , Dir_P) were calculated using WaMoS II, a well-established commercial software used to measure sea state conditions from X-band radar data following algorithms well documented in the literature (Reichert et al. 1999; Wyatt et al. 2003; Hessner et al. 2014, 2015).

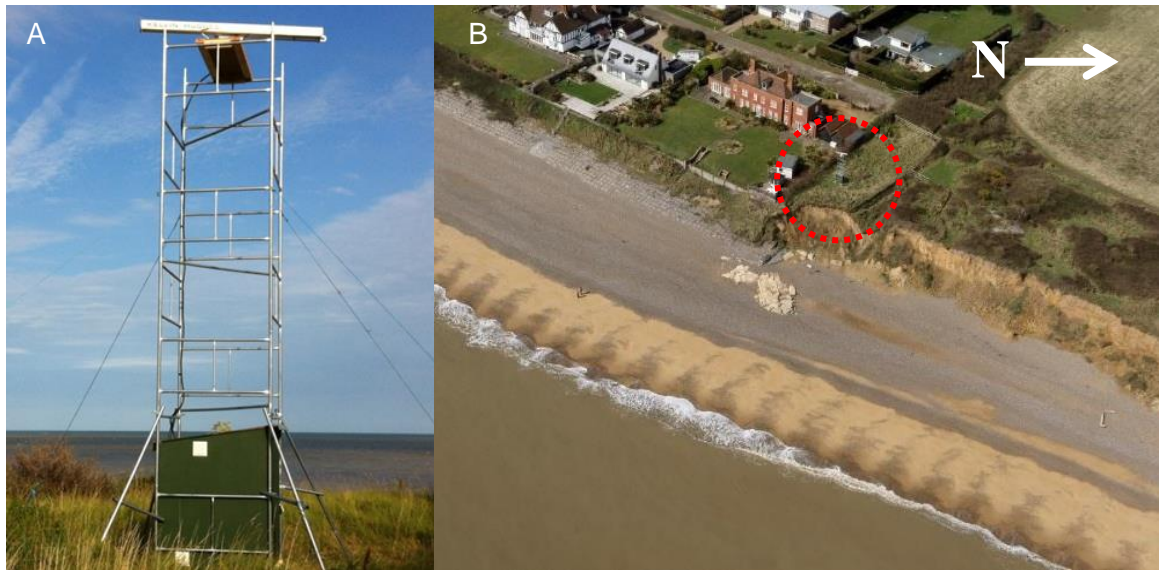


Figure 5.4. (A) The radar deployed on the cliff top and (B) position to the north of the village seen from above (with an approximate north direction indicated) on 13-Apr-2016 (Mike Page 2016)

Data were collected between 16-Sep-2015 and 18-Apr-2017, with a data return of 55.7% over a total of 614 days. The radar was set up to record data for 11 minutes (256 rotations, 2.63 seconds per rotation) every 30 minutes; generating a time series ‘image stack’ (sweeps of the radar) (Figure 5.3). These stacks were compressed and stored on an internal hard drive before being downloaded during service visits and processed offsite for the production of bathymetric maps.

Bathymetric maps were produced from radar data using algorithms developed by the NOC based on a bathymetric inversion method (Bell 1999; Bell and Osler 2011). The process is summarised in Figure 5.5, which identifies the key steps including: (a) calibration of wave heights and water levels; (b) validation of water depths; and (c) new data quality control methods developed as part of this research. Together the radar calibration and validation described here quantifies for the first-time errors and uncertainties associated with radar-derived data and provide the evidence to support the subsequent use of the data in the studies of morphodynamics at Thorpeness reported here.

¹ “X-band radar and evidence-based coastal management decisions” reference NE/M021564/1

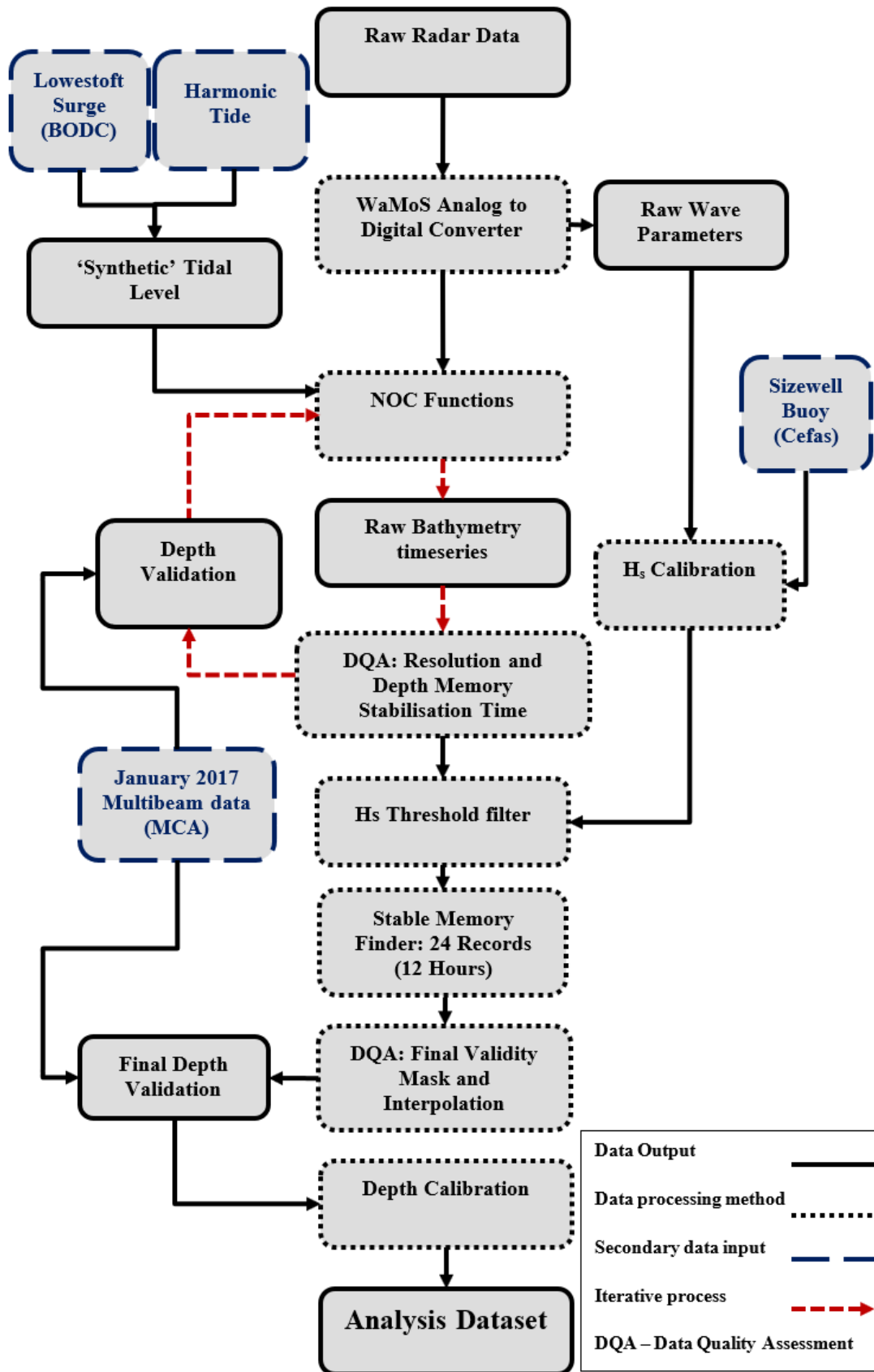


Figure 5.5. Schematic of the methodology employed to produce the radar dataset used in analysis.

5.2.2 Calibration of water levels

To relate radar-derived depth to Ordnance Datum Newlyn, ODN, the algorithms require tidal elevation data from a tidal model that includes astronomical and metrological forcing. Using a ‘*synthetic*’ tide approach (Bell et al. 2016), tidal residual information from the tide gauge at Lowestoft was added to POLPRED harmonic prediction close to the radar deployment field site. The resulting tidal elevation data were compared with measured water level from a pressure sensor deployed for 3 months (27-Apr-2016 and 31-Jul-2016) at a location 2 km south of Thorpeness (Figure 5.6a). A good agreement was obtained between the measured and synthetic tidal time-series. This is further reflected by the correlation coefficient ($R^2 = 0.75$ to 0.96) after applying the Lowestoft tidal residual value to the astronomical predictions (Figure 5.4b, c).

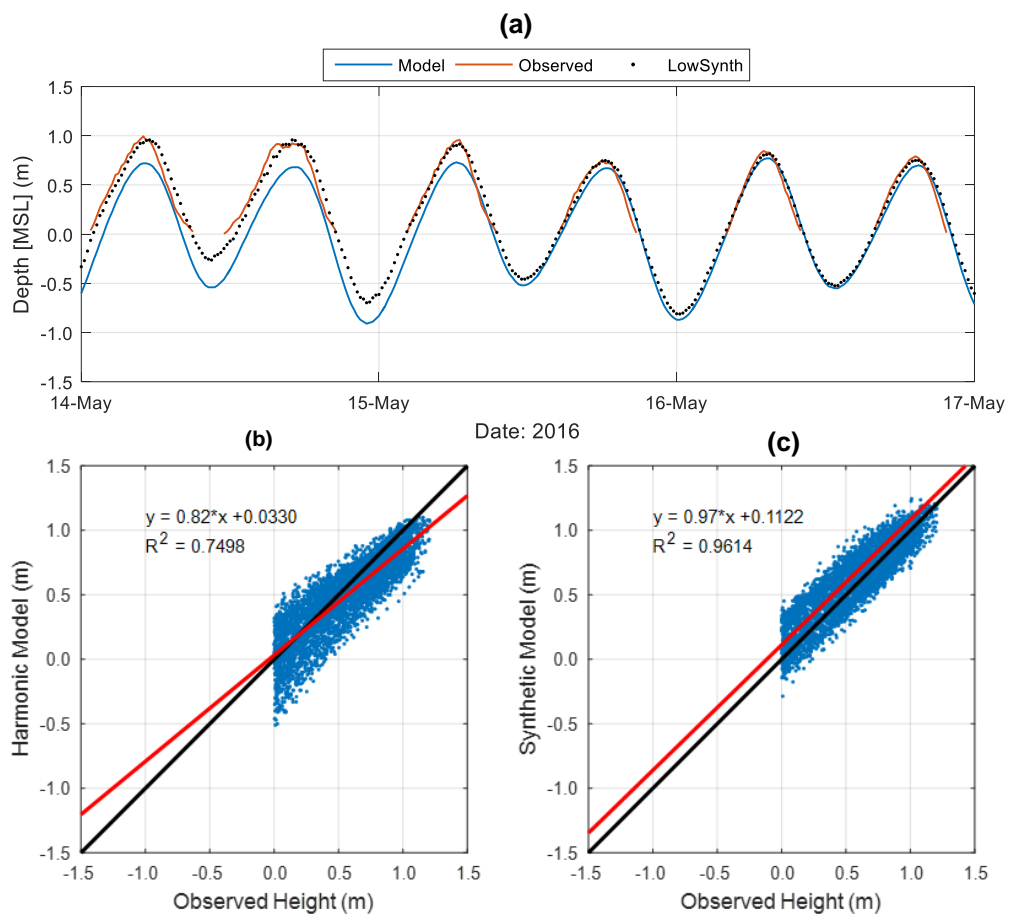


Figure 5.6. 3-day window where the synthetic model (Lowestoft) was seen to perform well (a) against the data recorded within the sluice. The bottom panels present (b) RMS analysis of harmonic model and (c) Synthetic model against observed height. Limited to $>0\text{m}$ for observed data due to tide gauge deployment position and data quality

5.2.3 Calibration of wave heights

Due to non-linearity of the radar imaging mechanism wave height cannot be directly inferred from the raw data (Borge et al. 1999). However a calibration can be applied to the radar data using coincident wave measurements from another instrument (Alpers and Hasselmann, 1982, equation 5.2). In the present study, wave data from the Cefas wave buoy located $\sim 1900\text{m}$ north and $\sim 3500\text{m}$

east of the radar provided an H_s time-series required to calibrate the radar (Figure 5.7) using the simple linear relationship

$$H_s = A + B \sqrt{SNR} \quad (5.2)$$

where A is the intercept and B the slope of the fit between Signal to Noise Ratio (SNR) and calibrated H_s . The resulting calibrated wave height information has been used subsequently in the radar data quality control process described in 5.2.4.2.

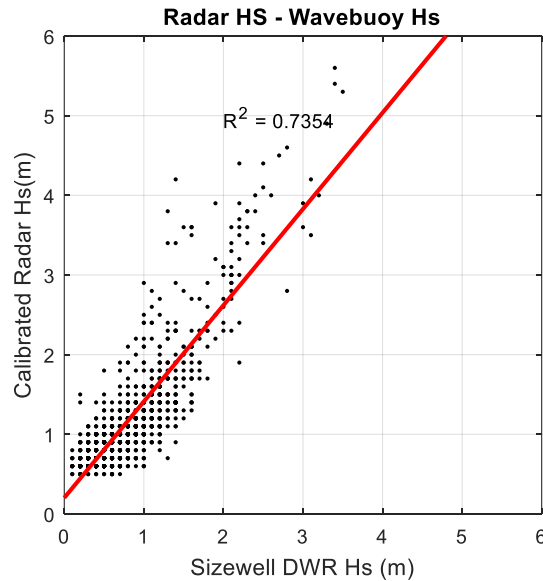


Figure 5.7. Radar derived wave height (calibrated) against wave buoy data.

5.2.4 Radar-derived bathymetry

The study has found that the accuracy of the bathymetric inversion used to obtain bathymetry data from the radar-derived wave measurements is highly dependent upon the prevailing wave conditions at any given time, specifically the wave length and period of the waves (Bell and Osler 2011). The inversion uses the wave dispersion relationship between wave frequency (σ), wave number (k_n) and mean water depth (h). Within a region defined by σ , the mean water depth directly affects k_n . To calculate these wave parameters the analysis considers a finite water surface area large enough to cover at least one wavelength in all directions and assumes that the area is homogenous with respect to both k and frequency spectra. This technique provides an ‘instantaneous’ estimation of the water depth as a probability density function (PDF) from which the peak describes the ‘most probable depth’ for each radar pixel. In real world conditions, these instantaneous measurements are generally noisy on an individual basis. To minimise this noise, the average from a sequence of PDFs (over a number of records) is taken to obtain the ‘most probable depth’. The easiest way to do this is to allow each individual probability density function to decay in importance with time in the manner of a radioactive half-life or ‘depth memory’ (Bell and Hessner 2009). The depth-memory half-life was

set to 24 records, which means after 24 records (12 hours) the first record makes up 1/24 (0.04) of the PDF.

Prior to any analysis and validation, a number of tests using a range of radar processing areas were assessed to establish the area size parameters that provide the best trade-off between processing time and data quality. The final dataset utilised a 160 x 160 m window for depth analysis, which was shifted in 40m increments throughout the radar view, resulting in a 40 x 40 m bathymetry grid.

The resulting depth data (Figure 5.8a) were then screened to establish the regions of low return. This was caused by the effects of distance from the radar, water depth, obscured radar view by the Ness foreland and a hardware issue (in which a ‘split’ in the radar view was caused by wear in a rotational gear cog of the radar, Figure 5.8b). Missing areas of data (caused by the faulty rotation) were replaced by interpolation using natural neighbour method (Sibson 1981; Figure 5.8c). This data quality control allowed identifying an area of consistently good data return within the radar view extending beyond the depth of closure (7.27m ODN), where the most significant changes in bathymetry occur (limited only in the north due to headland and beach orientation changes).

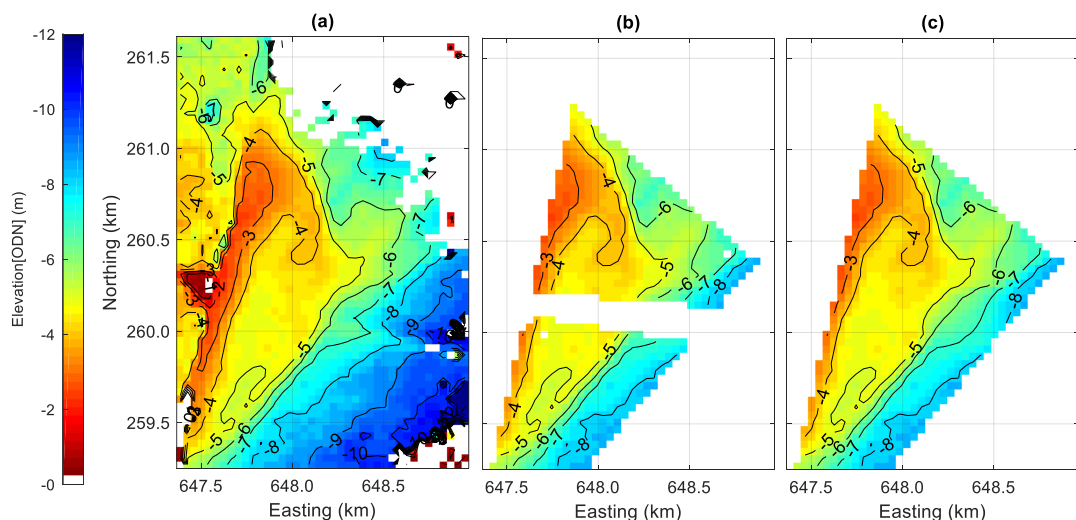


Figure 5.8 The radar derived bathymetric map (A, 11-Oct-2015 05:00) and stages of quality control to remove the ‘slice’ in the radar view and highly variable data due to depth and range (B) and natural neighbour interpolation (C).

5.2.4.1 Validation of radar-derived bathymetry

Validation of radar-derived bathymetry utilised data from multibeam bathymetric surveys². A comparison between multibeam measured and radar derived bathymetry (Figure 5.9) indicated a bias in which shallower depths were overestimated and deeper depths underestimated (similar to results reported by Rutten et al. 2017). A linear calibration correction was applied resulting in 96% of the radar-derived bathymetry being within ± 0.5 m of the measured data and 100% within ± 1 m of the measured data. Regions first thought to have the lowest accuracy were later confirmed to be the most

² MCA surveys undertaken during 30-Jan-2017 to 24-Feb-2017 in the north sector of the radar view and during 7-Jan-2017 to 15-Feb-2017 in the south sector. The method is outlined further in Atkinson et al. (2018).

dynamic with regards to bathymetric changes, including the beach foreshore and spit-like feature extending south and offshore from the Ness (see 5.3.3.2). Therefore, the differences are attributable to the natural changes in bathymetry that occurred during the survey period rather than the error of the radar methods.

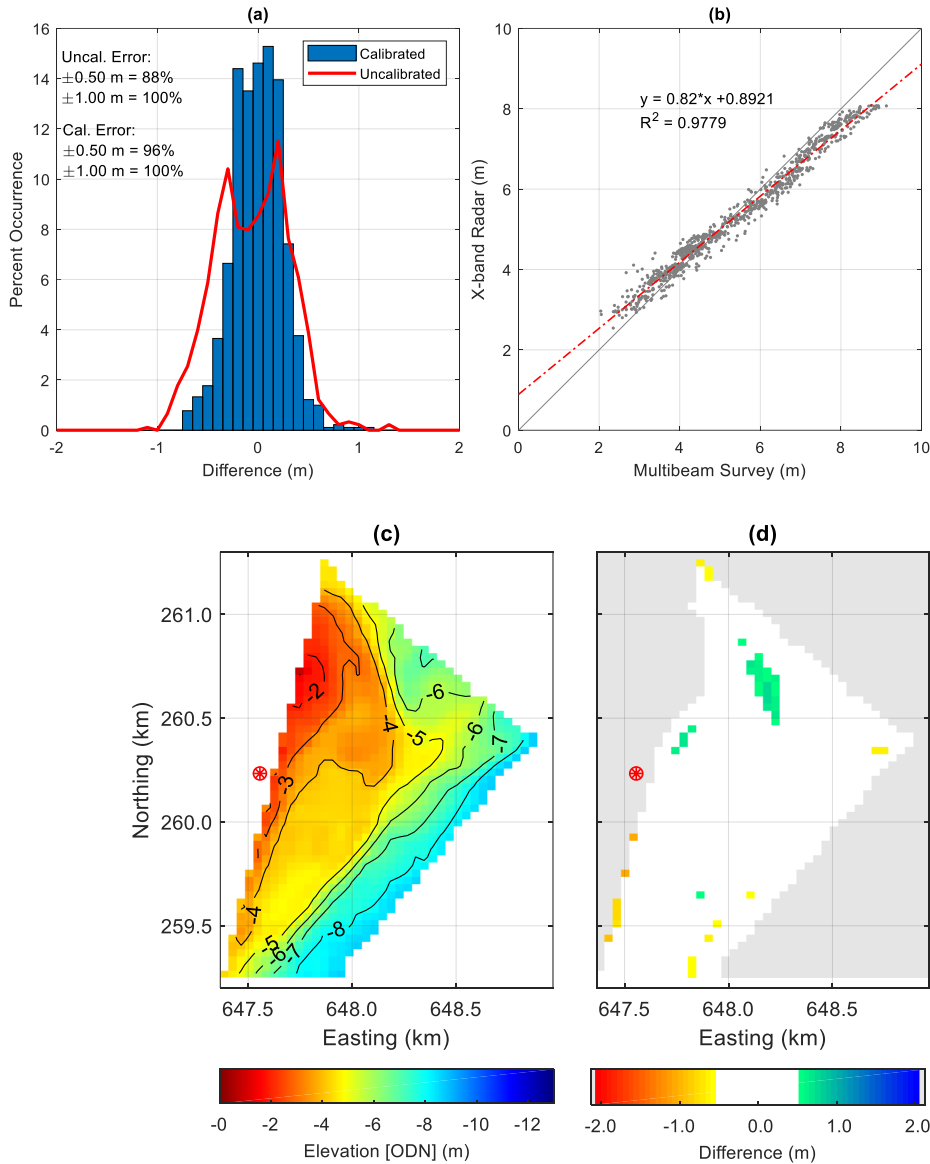


Figure 5.9. (A) Radar histogram of calibrated depths (blue) and the previous uncalibrated depth (red), (B) scatter plot of the multibeam and radar derived depths prior to calibration utilising the derived line equation, (C) the radar record used concurrent to the multibeam survey and (D) the resulting differences between multibeam and radar, where a negative value indicates an underestimation of the radar and orange an over estimation.

5.2.4.2 Data selection and quality control

The validation process established that radar data acquired in conditions where the offshore wave heights exceeded 1m for more than 12 hours gave the most reliable nearshore bathymetry. The following data processing steps were followed:

- The radar data was filtered to identify records showing calibrated radar-derived $H_s > 1$ m;

- These records were screened to identify periods in which H_s exceeded 1 m for at least 12 hours (24 records). This screening identified the first ‘data block’ in which the *depth memory* had stabilised (i.e. all cell depths within the PDF were calculated from data exceeding the wave height threshold in the previous 12 hours); and
- Bathymetric maps were then produced for each ‘data block’ fitting the criteria (12 hours of stabilised depth memory for periods when H_s exceeded 1m. If H_s dropped below the threshold, the block was closed, and a new block initiated when data fitted the criteria.

Using this data filtering method, a total of 53 ‘data blocks’ were identified over the radar deployment period (Figure 5.10). The longest data gap between ‘data blocks’ was 80 days (between 06-Mar-2016 and 25-May-2016).

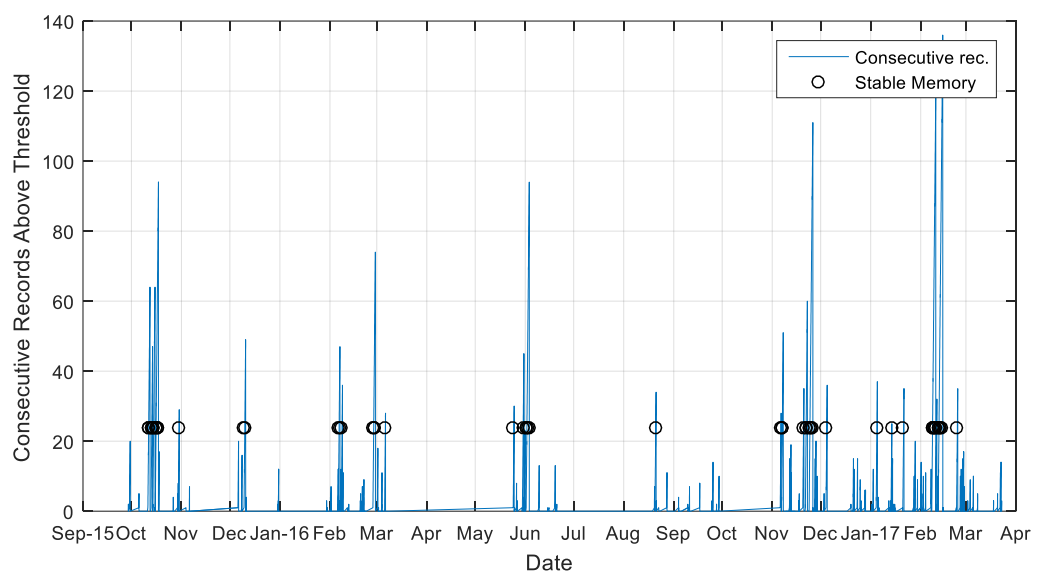


Figure 5.10. Time series analysis showing consecutive records above 1m H_s threshold (blue) and points in which 24 records were exceeded and record was defined as stable.

Within each ‘data block’ variance in depth was assessed to remove artefacts related to changes in water level, variations in wave direction and non-linearities in the wave climate across radar field-of-view. Using a tailor-made graphical user interface (GUI) developed in Matlab (Figure 5.11) the ‘data blocks’ were analysed iteratively in order to identify the records which showed changes in the radar-derived bathymetry in areas known to be more dynamic and minimal changes in areas known to be stable; as indicated in the analysis of the multibeam surveys. The bathymetry maps derived from radar data passing the quality control screening were then analysed to (a) quantify magnitudes of change, when and where they were more prominent; (b) identify the driving metocean conditions; and (c) linkages between nearshore and beach shoreline changes (Section 5.2.6).

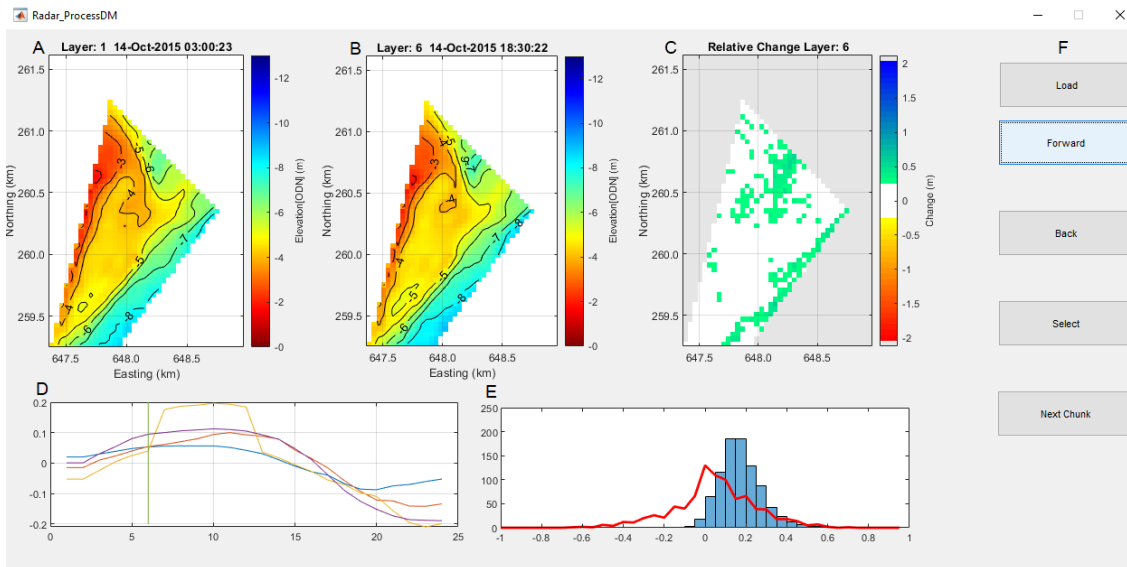


Figure 5.11. The developed GUI showing two bathymetric maps (A and B) from different 'blocks' of data, the calculated difference between them (C), a diagnostic for pixel variances through each block (D), a histogram of magnitudes of difference (E) and controls in which to cycle through and define each of the records for the time series (F).

5.2.5 Changes in nearshore bathymetry

The broad magnitude of changes in nearshore bathymetry were initially quantified by comparing multibeam surveys³ of the study area obtained in the summer 2014 and the winter 2017 (Figure 5.13). Changes in bathymetry were calculated only for the areas covered by both surveys with no extrapolation outside of the survey limits. To enable comparison with the radar data, the multibeam data were referenced to the OSGB36 coordinate system, using Ordnance Survey software GridInquest version 7.0, and corrected to ODN datum using the correction (Chart Datum -1.5 m) for Lowestoft (British Oceanographic Data Centre 2018). Using linear interpolation, data from the multibeam surveys were represented in a 0.5 m resolution grid. In cases where grid cells contained more than one data point, the arithmetic mean depth value was calculated.

Changes in radar-derived bathymetry (and estimated changes in sediment volume) were calculated only for the pixels where changes exceeded ± 0.5 m (i.e. the estimated error). The analysis then focussed on three areas where bathymetric changes were more prominent (Figure 5.12):

- Area 1 - the nearshore oblique Ness bar extending NW-SE at the north of the radar view;
- Area 2 - the area south of the Ness (N260900 m to N260300 m); and
- Area 3 - the area extending along the shoreline from the cliff line north of the radar installation (N260300 m) to the southern extent of the radar view (N259500 m).

³ Provided by the Environment Agency (EA) and the Maritime and Coastguard Agency (MCA), respectively.

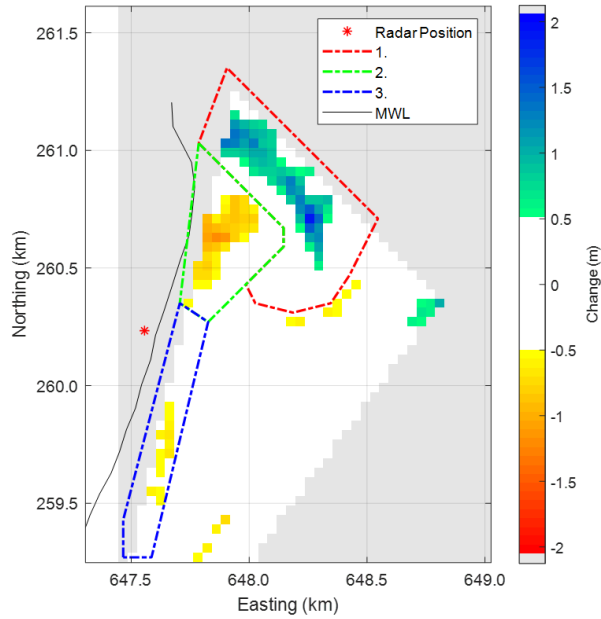


Figure 5.12. The three areas where largest changes in bathymetry were observed, which are the focus of the analysis, showing differences in bed level between 11-Oct-2015 and 08-Feb-2016.

5.2.6 Assessing linkages between nearshore and shoreline changes and wave conditions

Changes in nearshore bathymetry were compared with beach changes to establish whether there were noticeable linkages between the patterns of accretion and erosion. The analysis paired the available beach survey data collected on dates that most closely coincided with the radar-derived bathymetric changes beach survey data collected (Table 5.1). Changes were then calculated for the best matching periods of time at two scales: (a) at intervals of approximately 6 months (bi-annual changes); and (b) short-term changes, varying from 23 to 106 days (Table 5.2). Only a limited number of suitable matches were identified, particularly for the shorter-term changes, as the bathymetric changes must be large enough to exceed the ± 0.5 m error. Fortunately, changes measured during the winter of 2016-2017 proved to be sufficiently large to enabled short-term analysis.

Table 5.1. Best matching dates between beach surveys and radar-derived bathymetry.

Survey Date	Closest Radar Data Return	Days Difference
02-Aug-2015*	11-Oct-2015	70
02-Feb-2016*	06-Feb-2016	4
26-Jul-2016*	20-Aug-2016	25
02-Aug-2016	20-Aug-2016	18
22-Oct-2016	06-Nov-2016	15
06-Dec-2016	04-Dec-2016	-2
09-Jan-2017	13-Jan-2017	4
18-Jan-2017	21-Jan-2017	3
13-Feb-2017	12-Feb-2017	-1
06-Mar-2017*	23-Feb-2017	-11

*EA Surveys

Beach changes were analysed based on the relative position of MHWS at each available EA monitoring profile (between N261203 to 259469m, TN001 to TN036 respectively). This served as a

suitable proxy of beach volume as indicated by the strong significant and positive relationship between MHWS position and beach profile area above MLWS ($r = 0.75$ to 0.99) identified in 3.3.2. For the periods identified in Table 5.2, significant wave height and the proportion of northerly ($Dir_P: 300 - 60^\circ$) and southerly ($Dir_P: 120 - 240^\circ$) waves (in a moving 30-day window) were calculated from the nearest offshore wave buoy data (West Gabbard 1 and 2). These wave parameters were used to establish the effects of wave energy and direction on the observed nearshore and beach changes.

Table 5.2. Defined periods of analysis for bathymetry, each survey and wave climate.

	First Date	Second Date	Number of days between beach surveys
Biannual Surveys			
	11-Oct-2015	06-Feb-2016	118
	06-Feb-2016	20-Aug-2016	196
	20-Aug-2016	23-Feb-2017	176
Short-term changes			
	20-Aug-2016	04-Dec-2016	106
	04-Dec-2016	13-Feb-2017	71
	21-Jan-2017	13-Feb-2017	23

5.3 Results

5.3.1 Multibeam data analysis at radar resolution

The changes in bathymetry recorded by the multibeam surveys (Figure 5.13) help to discriminate the areas of immobile geology and those where changes in bathymetry indicate sediment movement. With the exception of the areas closest to the shore and within the central sector differences between bathymetry measured by the multibeam survey in 2014 (Figure 5.13a) and 2017 (Figure 5.13b) are small or zero (Figure 5.13c).

Three areas of largest bathymetric changes are identified (as 1, 2, and 3) in Figure 5.13c. Area 1 shows distinct erosion (-2 m) of the oblique bar present during the 2014 survey. This erosion is observed to extend north of the Ness towards the shoreline and the edge of the radar view. In Area 2 accretion occurs ($+2$ m) just south of Area 1. There is quite an abrupt transition between erosion (in Area 1) and accretion (in Area 2). Further offshore of Area 2, narrow bands of erosion and accretion alternate, suggesting a north westerly migration of large (c. 2 m high, 20-50 m wide) bedforms, such as sand waves, which seem to be constrained by the presence of the Coralline crag ridge (Figure 5.13). Although these are the largest changes in bathymetry observed in offshore areas, these features are too narrow to be adequately captured by the radar at the spatial resolution of analysis. Area 3 shows significant erosion in the surf zone along most of the southern half of the survey area, including the beach frontage of Thorpeness village.

It is also noted that the apparent bands of erosion (< 0.5 m) aligned approximately north-south in the north and south sectors are believed to be artefacts of the surveying method. They are seen to align with the survey lines (or the trajectory of the vessel) in 2014 and result in a band of erosion that perfectly follows the south-eastern edge of the survey coverage.

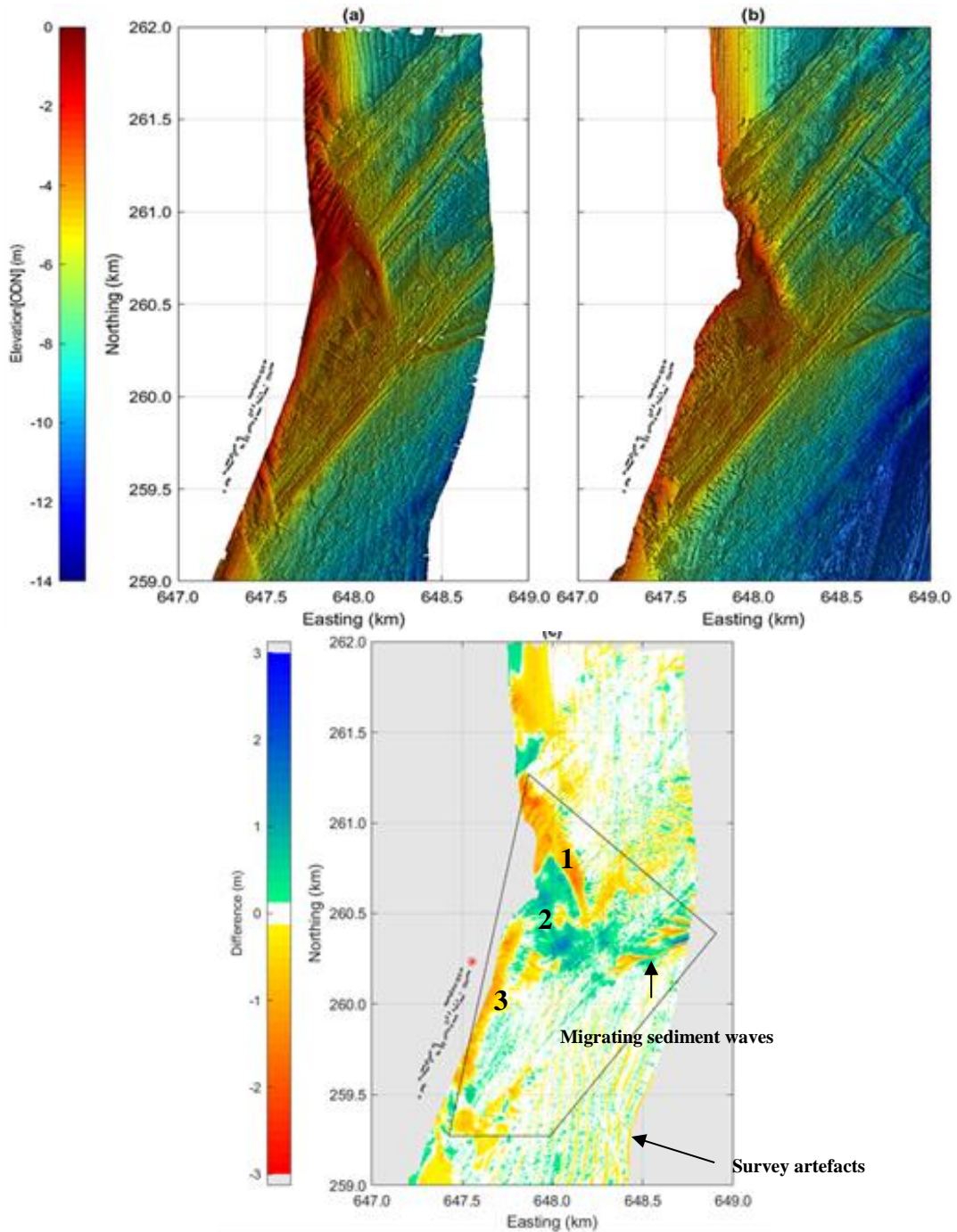


Figure 5.13. Bathymetry data from two multibeam surveys covering the study area: (A) obtained by the EA in June 2014 and (B) obtained by the MCA in January 2017. (C) Difference in the depths recorded between the 2014 and 2017 surveys. Negative values indicate an increase in depth (usually due to sediment loss) and positive values indicate a reduction in depth (usually due to sediment gain). Areas in white represent changes within ± 0.125 m. The black boundary indicates the radar coverage used in analysis. Thorpeness beach frontage buildings are identified in all figures.

5.3.2 Radar-derived nearshore volume changes

Figure 5.14 presents overall volume changes within the three areas of analysis (solid lines) in relation to the first valid radar record. Scattered markers indicate periods of rapid change, which are unlikely to be real sediment movement but instead noise in the radar signal. Larger changes in volume are most likely to occur during periods of sustained high waves, which is also when the radar

returns more data within the quality thresholds. However, these data are subject to noise and error due to wave variance in the radar view and so caution should be taken when interpreting the results.

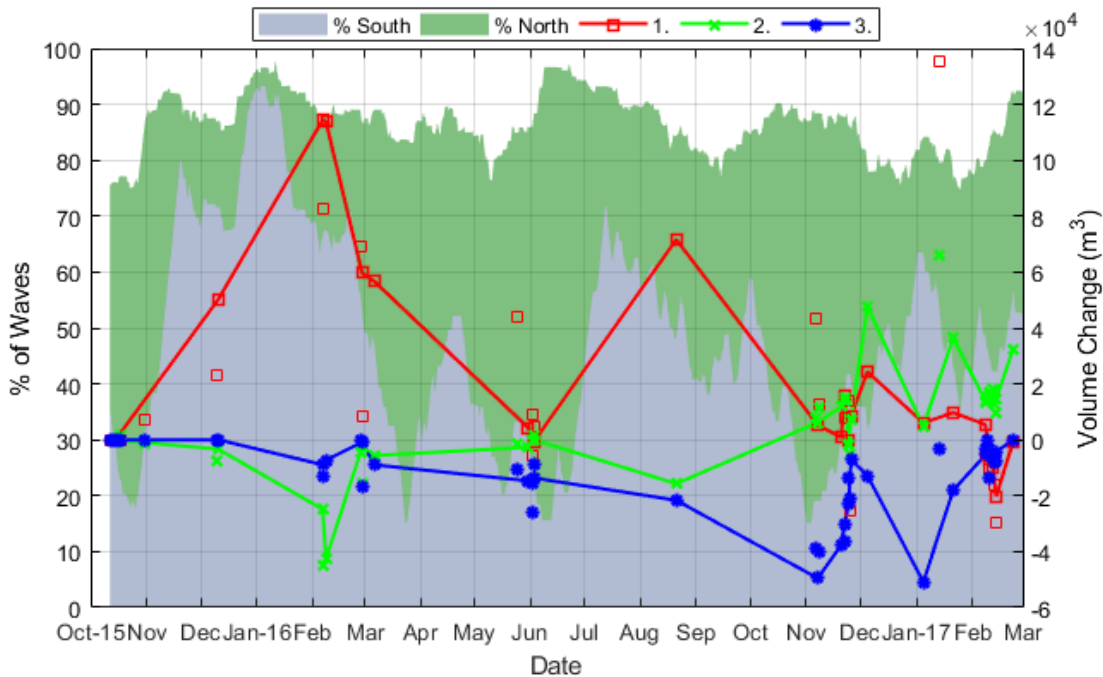


Figure 5.14. Area plot of the percentage of waves from northerly (Dir_P: 300 – 60°, grey area) and southerly (Dir_P: 120 – 240°, green area) directions calculated over a rolling 30-day window from the West Gabbard buoy (left, y-axis). Radar derived volume change within areas 1-3 relative to the starting record (11-Oct-2015, right y-axis), where a reduction in volume indicates erosion of the area and an increase suggests accretion.

Despite the issues outlined the observed trend in the volume changes shows correlations with the dominant wave climate, as well as the patterns of change observed between the two multibeam surveys. Area 1 accretes continually between October 2015 and February 2016 (50000-114000 m³) while Area 2 reduces in volume (by 45000 m³). This period showed strong dominance (between 70 and 90% of the time) of southerly waves.

Northerly waves dominate between February and June 2016 and Area 1 is seen to lose sediment returning to its original volume, whilst Area 2 increases in volume. This pattern seems to repeat at the biannual scale, as periods dominated by southerly waves seems to result in accretion in Area 1 and erosion in Area 2 over the period June-November 2016 (despite limited radar data return) and the reverse is observed when northerly waves dominate between August and November 2016.

The winter of 2016-2017 shows more of a balance between northerly and southerly waves when compared with the previous winter, and the resulting behaviour is more complex. The three areas show increases in volume over November (when northerly waves dominated) and decreases over December (when southerly waves dominate). By the end of the radar deployment Areas 1 and 3 are comparable to their starting volumes, whereas Area 2 has increase by 32000 m³ (Figure 5.12), despite the relative balance in the bimodal wave direction.

5.3.3 Nearshore and shoreline change analysis

It is important to note that the previous section analysed the volume changes of each relative to an initial radar record (11-Oct-2015), whereas the following sections assess the volume changes within periods of time for which both nearshore and beach data are available. This can affect the volume calculations primarily due to bathymetric changes of less than ± 0.5 m not being included in the calculations as they are within established error of the radar.

5.3.3.1 Bi-Annual changes

Changes occurring over the period of 6 months in the nearshore are distinct. As observed in the previous section Area 1 and 2 show the largest (and opposite) changes between records (Table 5.3), though changes at the shoreline are more complex.

Table 5.3. Nearshore volume changes over periods of approximately 6 months.

Date 1	Date 2	Change	Area 1		Area 2		Area 3	
			Area (m ²)	Volume (m ³)	Area (m ²)	Volume (m ³)	Area (m ²)	Volume (m ³)
11-Oct-2015	06-Feb-2016	Accretion	118400	112196	0	0	0	0
		Erosion	0	0	36800	-26063	19200	-11653
06-Feb-2016	20-Aug-2016	Accretion	0	0	25600	16818	0	0
		Erosion	48000	-36453	0	0	1600	-1068
20-Aug-2016	23-Feb-2017	Accretion	0	0	46400	35241	0	0
		Erosion	92800	-71343	0	0	0	0

From 11th October 2015 to 6th February 2016 southerly waves dominated resulting in a removal of 26063 m³ and 11653m³ of sediment from Areas 2 and 3, respectively, and accretion of 112196 m³ in Area 1 (Table 5.3) with changes reaching up to +1.75 m. This period is seen to coincide with the largest seaward extent of the Ness since 1992, and the shoreline advancing 37 m at the EA transect SO37 (N260948 m, advancing 37 m) and 30 m at Transect A (Figure 5.15a). Elsewhere the shoreline remains relatively stable (changes of <3 m) except the cliff toe in front of the radar which retreats 8.5 m.

As the dominance of the northerly waves increases between February and August 2016, erosion of 36453 m³ is observed in Area 1 (a maximum vertical change of -1.15 m) and accretion of 16818 m³ occurs in Area 2 (a maximum vertical change of +0.89 m). Although the pattern is a reversal from the previous 6 months, magnitudes of change are considerably lower. Coastal change seems to follow the nearshore changes, as the beach retreats around the Ness (as Area 1 erodes) and accretes further south adjacent to Area 2 (Figure 5.16a). The cliff line north of the radar retreats, while further south the beach width remains stable or accretes. The removal of sediment from Area 1 and an overall increased stability or accretion elsewhere in the nearshore and the shoreline to the south appears to occur due to a more balanced north-south wave distribution (Figure 5.16b), despite much of the larger waves still approaching from the south (Figure 5.16c).

With increased dominance from northerly waves between August 2016 and February 2017, erosion intensifies in Area 1 and accretion in Area 2 (Figure 5.17), a reduction of 71343 m³ and increase of

35241 m³, respectively (Table 5.3). During this period beach retreat reaching up to 16 m was observed across the study area.

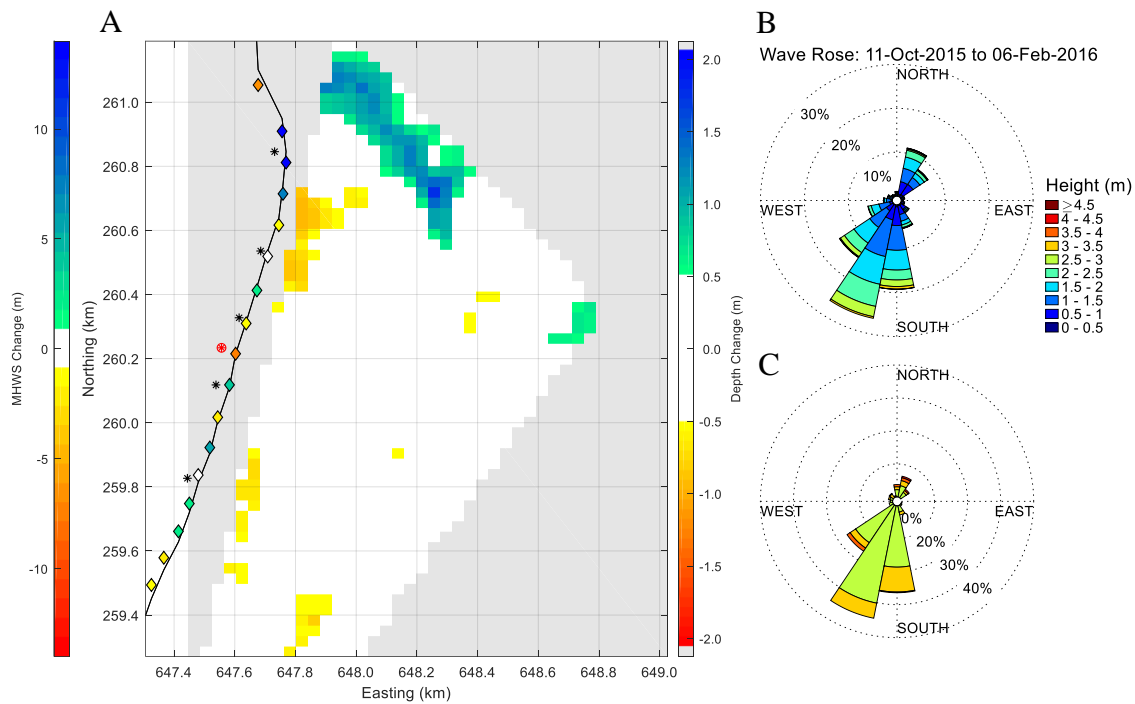


Figure 5.15. (A) Changes in radar-derived bathymetry between the 11-Oct-2015 and 06-Feb-2016. The black line indicates the shoreline position on 02-Feb-2016 and markers indicate changes in beach width at MHWs between 05-Aug-2015 and 02-Feb-2016 Wave roses for the period 11-Oct-2015 and 06-Feb-2016 for all waves (B) and for $H_s > 2.5$ m only (C).

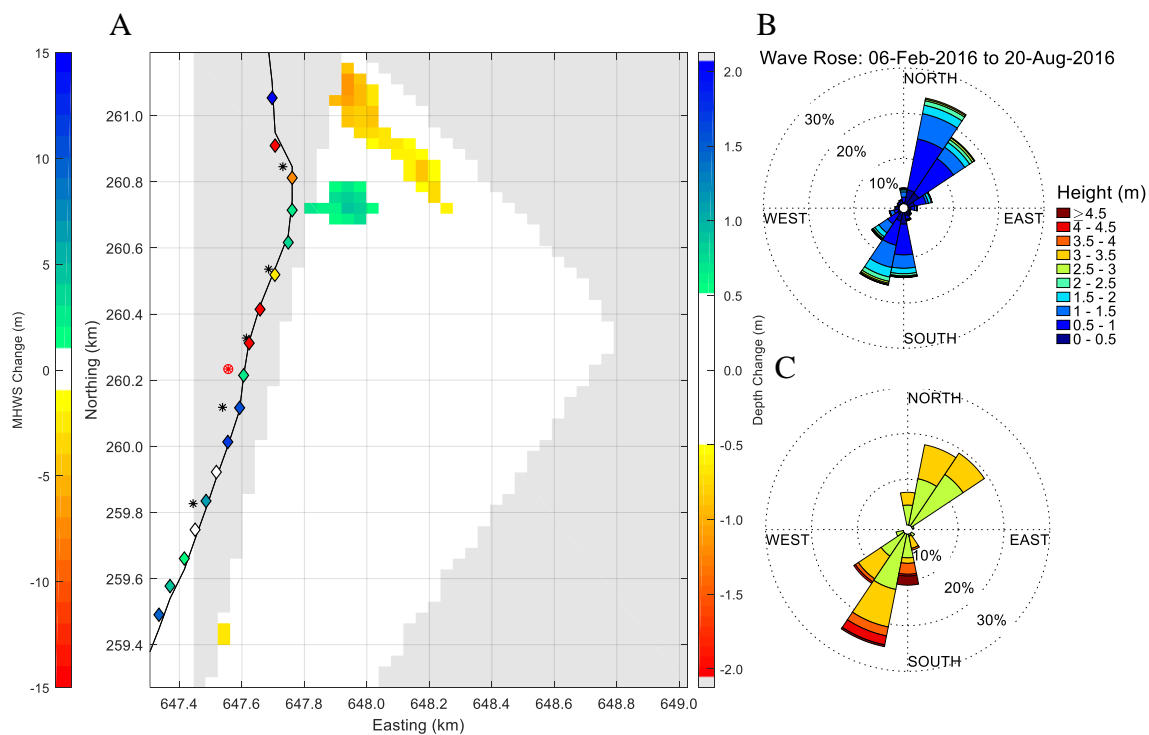


Figure 5.16. (A) Changes in radar-derived bathymetry between 06-Feb-2016 and 20-Aug-2016. The black line indicates the shoreline position on 27-Jul-2016 and markers indicate changes in beach width at MHWs between 02-Feb-2016 and 27-Jul-2016 Wave roses for the period 06-Feb-2016 and 20-Aug-2016 for all waves (B) and for $H_s > 2.5$ m only (C).

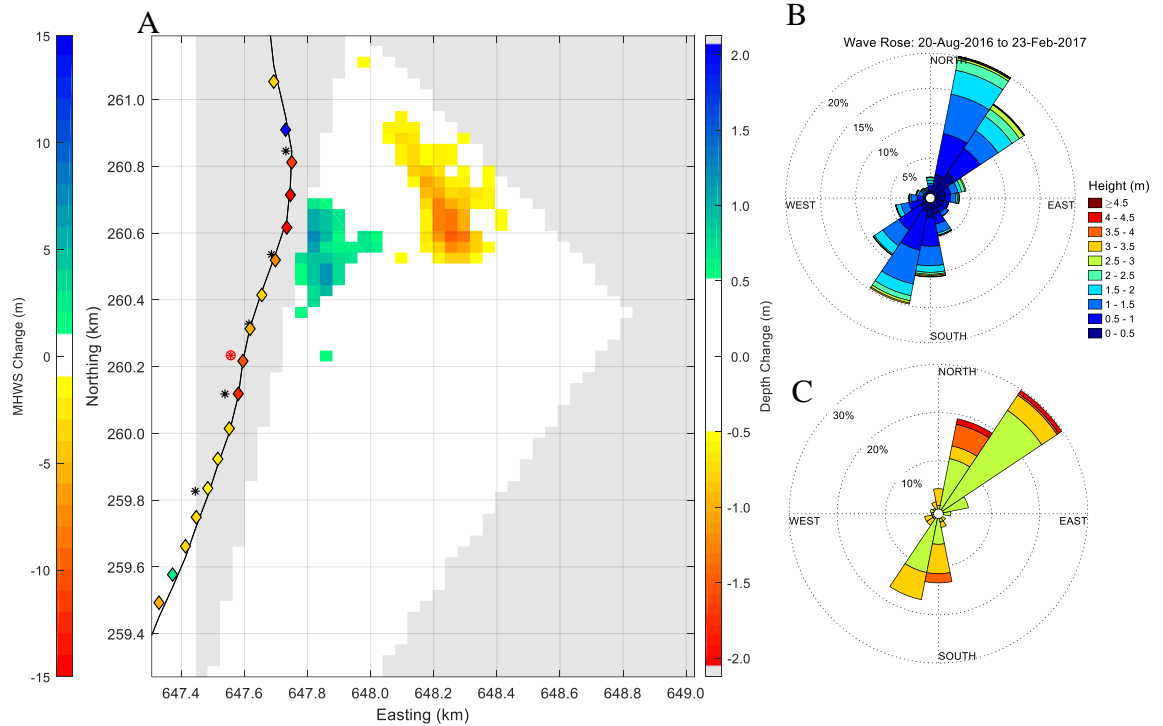


Figure 5.17. (A) Changes in radar-derived bathymetry between 20-Aug-2016 and 23-Feb-2017. The black line indicates the shoreline position on 06-Mar-2017 and markers indicate changes in beach width at MHWs between 27-Jul-2016 and 06-Mar-2017. Wave roses for the period 20-Aug-2016 and 23-Feb-2017 for all waves (B) and for $H_s > 2.5$ m only (C).

5.3.3.2 Short-term changes

Short-term analysis focused on three consecutive periods spanning from August 2016 to February 2017 when more frequent beach surveying occurred (Table 5.4). From August to December 2016 (106 days), northerly waves dominated resulting in accretion of Area 2 (55172 m³) and erosion (10951 m³) in Area 1 (Table 5.4). Beach retreat of up to 6 m is observed at the Ness and between Transect C and D (Figure 5.18), the area associated with a chronic erosion hot-spot. Much of the rest of the beach frontage and nearshore shows relative stability (changes of 1 m or less). Similarities exist with the changes observed from August 2015 to February 2016 (Figure 5.17). However, from August to December 2016, southerly waves are less frequent, which seems to increment accretion in Area 2 and the shoreline and reduce erosion in Area 2, when compared to changes observed between August 2015 and February 2016.

Table 5.4. Periods of focused shoreline-radar analysis and calculated volume changes between records.

Date 1	Date 2	Change	Area 1		Area 2		Area 3	
			Area (m ²)	Volume (m ³)	Area (m ²)	Volume (m ³)	Area (m ²)	Volume (m ³)
20-Aug-2016	04-Dec-2016	Accretion	12800	7708	67200	55172	4800	2774
		Erosion	16000	-10951	0	0	0	0
04-Dec-2016	21-Jan-2017	Accretion	0	0	0	0	0	0
		Erosion	1600	-870	1600	-985	0	0
21-Jan-2017	13-Feb-2017	Accretion	3200	1938	0	0	16000	10311
		Erosion	44800	-29735	1600	-842	0	0

Changes in the nearshore between December 2016 and January 2017 (Figure 5.19) observed by the radar are minimal (i.e. < 0.5 m and within the error band of radar-derived bathymetry). This may be

due to the balance between north and south wave energy, as southerly waves were more frequent (Figure 5.19a) but the larger waves approached from the north (Figure 5.19b). However, beach retreat seemed to dominate, except at the Ness where accretion was observed and localised areas of stability. The beach accretion of 1 m registered in Transect C is deceptive, as the adjacent cliff toe retreated 4 m (measured at 3m ODN), probably the source of material for the beach growth.

Between January and February 2017 (23 days) large changes occurred in both the nearshore and at the shoreline. This period was dominated by northerly waves, including all waves exceeding $H_s > 2.5$ m. Beach retreat of up to 6 m was observed along most of the shoreline (only accreting south of Transect E). Erosion (29735 m^3) is also observed in Area 1.

Interestingly the region of largest change over this period (Area 1) is the area of the radar view which had the largest errors during validation (Figure 5.9d), this analysis covers the same period as the multibeam survey so it can be assumed that the large errors observed in the radar validation are likely due to actual bed movement over the multibeam survey (which occurred between 30-Jan-2017 to 24-Feb-2017 in the north of the radar view) rather than a region of inaccuracy by the radar.

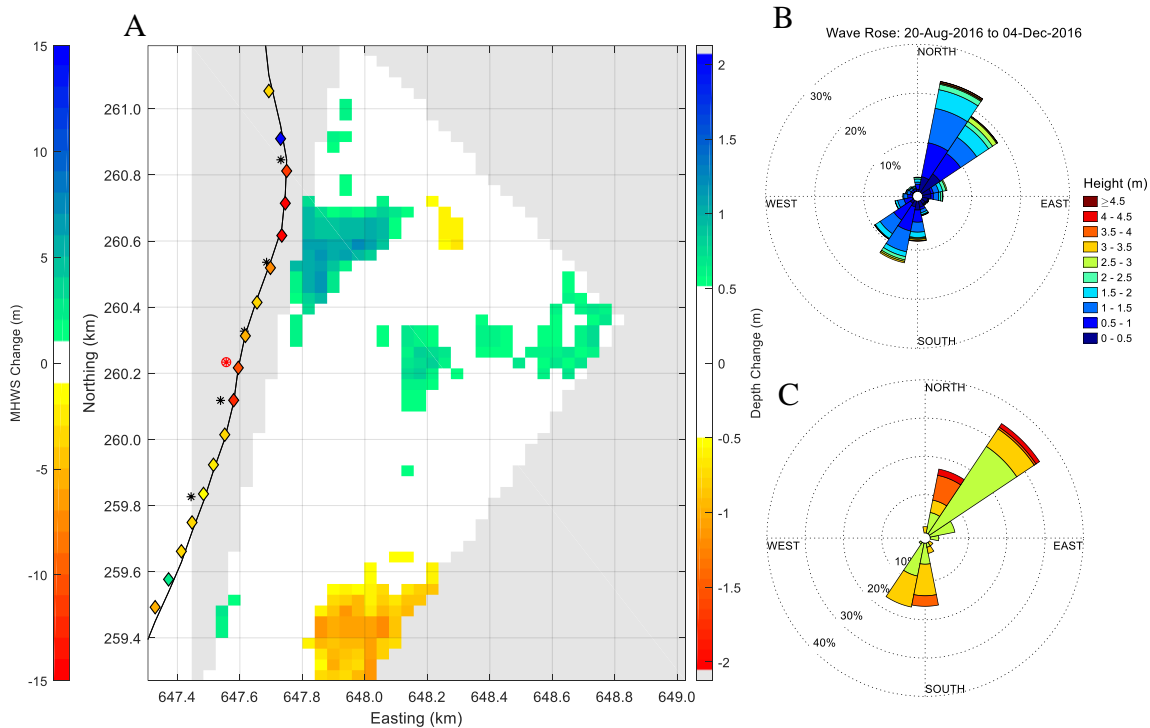


Figure 5.18. (A) Changes in radar-derived bathymetry between 20-Aug-2016 and 04-Dec-2016. The black line indicates the shoreline position on 06-Dec-2016 and markers indicate changes in beach width at MHWs between 03-Aug-2016 and 06-Dec-2016. Wave roses for the period 20-Aug-2016 and 04-Dec-2016 for all waves (B) and for $H_s > 2.5$ m only (C). Note large changes to the south east are likely to be artefacts of variable wave direction between records.

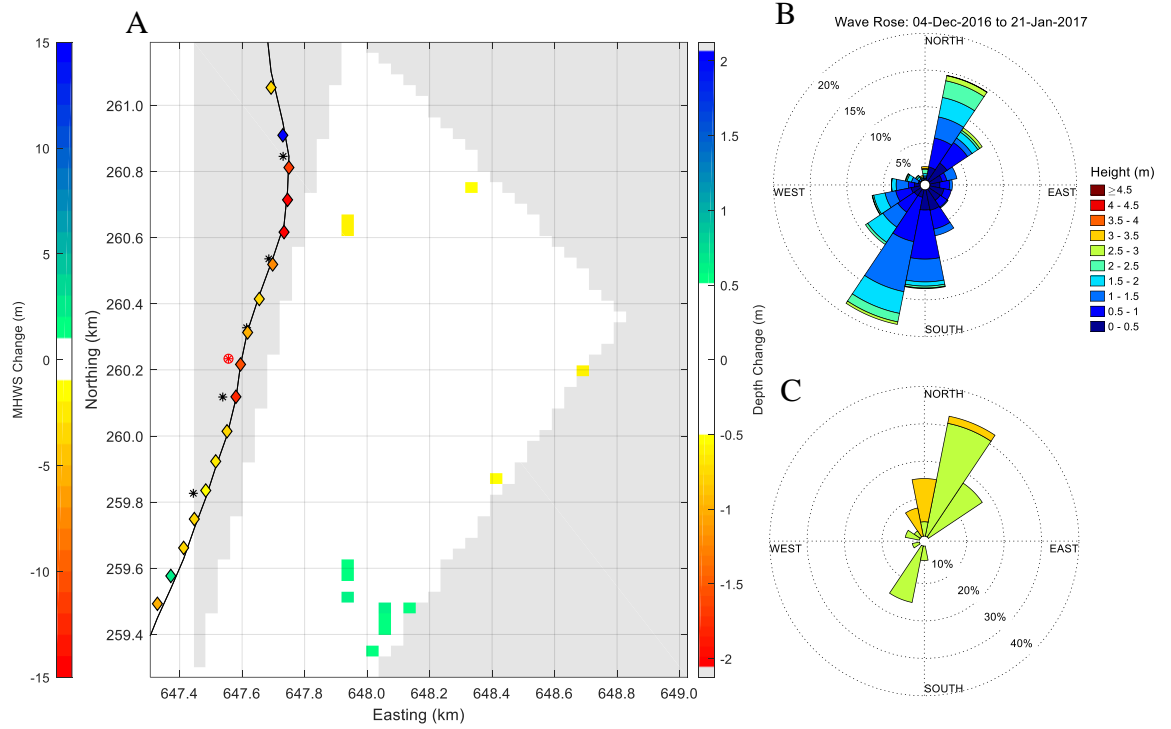


Figure 5.19. (A) Changes in radar-derived bathymetry between the 04-Dec-2016 and 21-Jan-2017. The black line indicates the shoreline position on 18-Jan-2017 and markers indicate changes in beach width at MHWS between 06-Dec-2016 and 18-Jan-2017. Wave roses for the period the 04-Dec-2016 and 21-Jan-2017 for all waves (B) and for $H_s > 2.5$ m only (C).

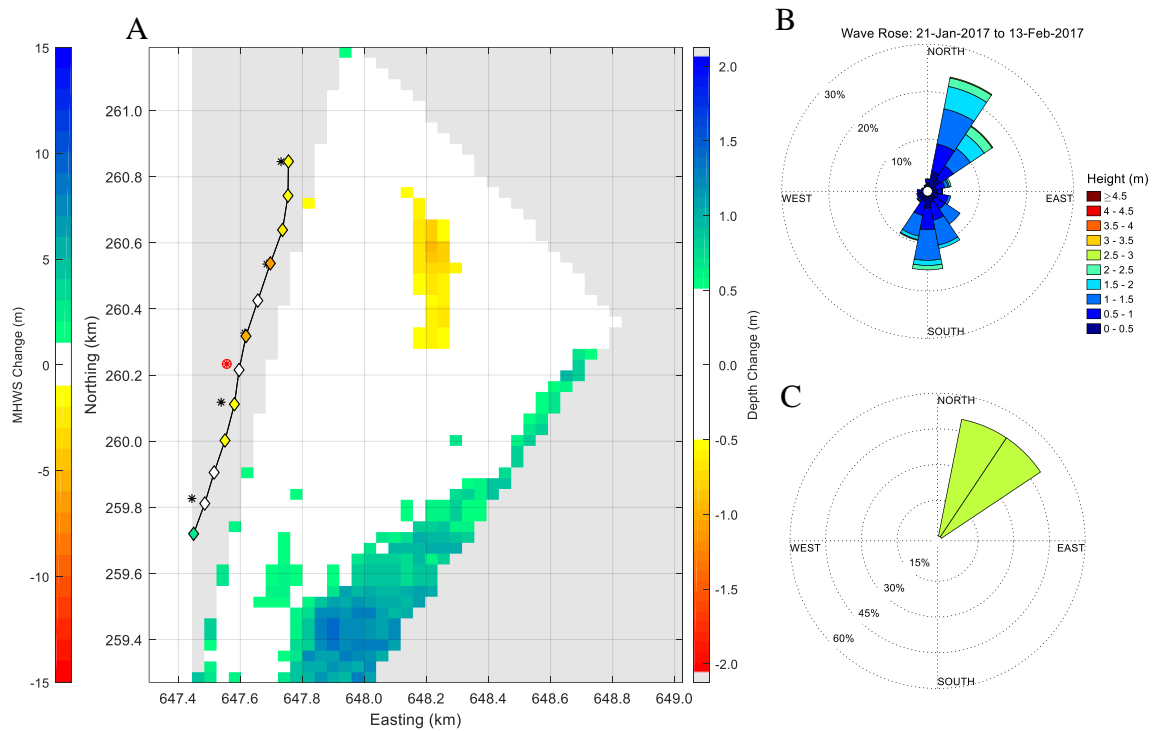


Figure 5.20. (A) Changes in radar-derived bathymetry between the 21-Jan-2017 and 13-Feb-2017. The black line indicates the shoreline position on 13-Feb-2017 and markers indicate changes in beach width at MHWS between 18-Jan-2017 and 13-Feb-2017. Wave roses for the period the 21-Jan-2017 and 13-Feb-2017 for all waves (B) and for $H_s > 2.5$ m only (C). Note after careful interrogation large changes to the south east are likely to be artefacts of variable wave direction between records.

5.4 Discussion

5.4.1 Nearshore dynamics and shoreline behaviour

The distinct shape and recurrence of nearshore features (observed in both the radar and multibeam analysis) suggests there are underlying controls on the formation and removal of these features. In the case of Thorpeness the underlying harder geology has been identified as an important control in the shoreline and nearshore behaviour (Burningham and French 2017) and so may be influencing the shape of the analysed areas (Area 1 being an oblique bar and enveloping Area 2, which covers a more rounded area at the Ness). Defined boundaries of separation in behaviour were identified in the radar which was supported by the same features observed between multibeam surveys. The features are not observed to migrate from one state to the other but instead volume exchanges appear to occur. Similar first-order geologic controls have been observed in a series of studies at North Carolina, USA (McNinch 2004; Browder and McNinch 2006; Schupp et al. 2006) in which vessel based surveying of nearshore processes identified links to both recurring and redevelopment of features and their link to the occurrence of focused erosion ‘hot-spots’ on the coast. Similar studies by Kirkpatrick and Green (2018, Namibia) and Jackson et al. (2005, Ireland) have identified similar links, describing the complex interaction between underlying geology and coastal state as important determinants of beach morphology. The majority of these studies have utilised, seismic techniques to understand subsurface structures and although the multibeam data at Thorpeness proved valuable in radar validation, the underlying geology is difficult to define. Insight could be obtained through establishing the hard geology and depth of sediment and in these areas, which in turn may provide greater understanding of the distinct patterns of nearshore formations.

The trends of erosion and accretion of these nearshore features are neither seasonal (with Area 1 being in its ‘accreted state’ in both June/July 2014 and February 2016) nor regularly spaced in time (in the period of time the radar was installed the bar at Area 1 formed over 6 months but took longer to be fully removed). This non-seasonal change appears to be primarily due to the wave bimodality and inter annual variance outlined in 3.3.1. The importance of a combination of bimodal wave climate and complex bathymetry on nearshore dynamics has not been studied extensively, with the research often focusing on smaller changes in direction due to climate change (Adams et al. 2011; McSweeney and Shulmeister 2018). In cases where bimodal direction changes are larger, the focus is often on the energy distribution caused by the directional difference and interaction with the sea bed (Burningham and French 2016; Hegermiller et al. 2017) rather than a combination of direction and nearshore change. This primarily is due to the lack of bathymetry data at temporally high resolutions. The variable wave climate over the radar and project period has allowed a number of scenarios to be outlined, though recurring patterns of wave climate did not occur (winters over the research being dominated by southerly, northerly and a mixed climate in 2015, 2016 and 2017 respectively). This variability of the processes over the deployment makes conceptualising these patterns of behaviour difficult. Longer term trends or interactions therefore require either extended

observation periods or numerical modelling to establish any cycles in behaviour longer than the current dataset.

The concept of the Ness area being a region LST divergence to the north and convergence to the south (Burningham and French 2016) is supported by the observations between 2015 and 2017. General trends in advance and retreat of the shoreline are often observed to switch around the Ness area suggesting changes in either LST, wave energy distribution along the shoreline or a combination of the two. However, the analyses in Burningham and French (2016) were based on longer term, large scale surveying over decades, rather than sub annual monitoring. At Thorpeness, where erosional and accretional trends are observed to change over the period of months rather than years, the temporal resolution of these traditional surveying methods is reduced in utility. These trends are also difficult to link with wave parameters over the periods of biannual beach monitoring and concurrent bathymetric maps. Though large increases in the volume of the Ness and the Ness bar occurred during winter 2015-16 which was dominated by southerly wave energy. This trend appeared to be against the correlations outlined in 3.3.5, where the Ness profile (Transect A) showed a negative correlation against the % of Southerly waves ($r=-0.622$, $p=0.018$, $N=14$), though this was from a dataset in which surveys were conducted in the order of 4 weeks rather than 6 months. The shorter-term analysis, over the winter of 2016-17 presented a number of shoreline links, with accretion in Area 2 linking with the stability of the shoreline in the area (August to December 2016), whilst to the south erosion continued.

5.4.2 Utility of Radar

This study of the radar in a complex environment presents the difficulties of producing a framework which can be adopted easily by an end user. The outputs presented in this chapter were developed from an iterative and lengthy process to understand the intricacies and sensitivities of the radar processing algorithms and are specific to the field site. Although intensive scrutiny of the data for quality control is required prior to analysis, the radar has provided valuable insight into the rates, patterns and volumes of change occurring in the nearshore. These analyses would not have been possible through traditional measurements without an extensive and expensive monitoring campaign. It is important to emphasise that, as with other remote sensing systems (Holman and Stanley 2007; Lopez et al. 2016), the radar-derived data require calibration and validation based on ground-truth measurements.

The study has provided the first comprehensive and critical assessment of the use of radar to inform coastal monitoring. The accuracy of the radar for bathymetric measurements during ideal conditions (sustained $H_s > 1$ m) is ± 0.5 m, which agrees with a number of papers in less complex environments (Hessner and Bell 2009; Ludeno et al. 2015). In contrast to Rutten et al. (2017) where greatest accuracy was achieved in waters deeper than 6 m below MSL, the methods employed in this study showed highest accuracy in shallower waters (0 to -8 m ODN) with the deeper regions of the radar view showing large inaccuracies and removed during processing. These differences are likely due to

the size of the analysis window (160 x 160 m in this study and 960 x 960 m in Rutten et al. 2017). The resolution utilised in this study is approaching the finest possible with the methods employed; limited by the characteristics of the waves (needing to incorporate multiple wavelengths in the analysis window). When compared to bathymetry derived from the Argus wave inversion method the error is similar (Holman et al. 2013) though the range of the radar extends much beyond that of the camera based system (500 m in Argus and exceeding 1 km for radar in this project) as well as being operational 24 hours a day. Further bathymetric measurements could be made in the intertidal zone using a waterline method (Bell et al. 2016) similar to those used for Argus video camera monitoring (Holman et al. 1991), though at Thorpeness, where the tidal range is relatively small, and the beach steep would have given limited coverage though becomes more viable in macro-tidal and dissipative environments.

The magnitude and regions of significant change identified by the radar and supported by the multibeam surveys suggests the radar can be used as a nearshore monitoring tool, not only for general trends (erosion/accretion in specific areas) but to define the sediment volume change at the temporal resolution of weeks and months. This contrasts with the conclusions of Rutten et al. (2017) who indicated that daily to monthly scale volume changes the X-band radar seem unrealistic, due to strong bias in shallower regions and the aforementioned measurement window size. These calculations have been possible in the present study due to the framework employed, focusing on the nearshore region with higher resolution at the cost of data quality loss in deeper water. Though limitations are highlighted when assessing the shorter-term (<6 months) changes, due to the inherent error of the radar causing more of an influence. An observed change of 1 m by the radar may (in optimum conditions) range from 0.5 to 1.5 m or $\pm 50\%$. When the changes are smaller (<0.5 m) the error becomes equivalent to the change. The shorter the time between records, the more likely changes will not be captured, and so future deployments need to consider the rate and magnitude of changes as well as conditions required for quality data return. In a site where changes are slow and of low magnitudes, or wave conditions rarely exceed $H_s > 1$ m the radar noise and accuracy issues will result in a data being unreliable and limit the conclusions that can be drawn. However, in sites where magnitudes of change exceed this error the radar can be utilised for both long- and short-term analysis.

6. Numerical Modelling of Coastal and MSG Beach Dynamics

6.1 Introduction

The aim of this chapter is to utilise the data and knowledge gained from previous chapters to inform focused numerical modelling simulations. This will assess the influence of varying wave conditions and nearshore bathymetry on the rates and direction of longshore sediment transport in the study area before exploring how this can be used to inform local management decisions.

Owing to the availability of suitable data, most numerical modelling of shoreline morphology has focused on sandy beaches (van Rijn et al. 2003; Smit et al. 2008; Roelvink et al. 2009; Stokes et al. 2015), with much less attention being given to gravel beaches (e.g. Jamal et al. 2014; McCall et al. 2014, 2015). While being largely overlooked in the past, MSG beaches are now also the subject of deterministic modelling investigations (e.g. McCall 2015; Bergillos et al. 2017a, 2017b, 2017c; Dornbusch 2017). Although the hydrodynamic and wave modelling aspects of this work provide a good representation of real-world conditions, longshore sediment transport (LST) processes for gravel and MSG beaches (e.g. Van Rijn 2014) are less developed and less validated than those for sand (Center 1984; Kamphuis 1991). Most recently, two approaches to predict LST for MSG beaches and associated morphological changes have been utilised: (a) using a representative unimodal sediment size which has been validated as the closest approximation to the mixed beach response (e.g. Bergillos et al. 2017a) and (b) computation of LST for the gravel and sand components independently (e.g. Martin-Grandes et al. 2017).

Evidence presented in previous chapters has indicated that interactions between the bimodal wave climate and the nearshore bathymetry may play a key role in determine the morphological response of the shoreline. The high variability in the nearshore bathymetry of the Suffolk coast was highlighted as being important for coastal evolution (Carr 1979, 1981; and Brooks 2010), and the impact of the bidirectional wave climate on LST rates was demonstrated though the use of numerical modelling (Burningham and French 2016). However, the role of bathymetric variability and bimodal wave directions on shoreline energy distribution has not been investigated.

Past studies have attempted to establish links between nearshore bathymetry, wave climate and shoreline processes (e.g. Hegermiller et al. 2017; Limber et al. 2017; Kirkpatrick and Green 2018). The broad consensus is that nearshore bathymetric changes can cause constructive or erosive beach responses. Further, studies aimed at quantifying geological and sedimentological controls of shoreline behaviour (e.g. Browder and McNinch 2006; Barnard et al. 2012) identify wave focusing as the primary cause of erosional ‘hot-spots’, such as the one at Thorpeness. Chapter 5 (5.3.1, 5.3.2) has drawn attention to the presence offshore of resistant Coralline crag ridges at Thorpeness and to

the changes in offshore bathymetry identified through the multibeam and radar analysis. Giving historical and contemporary evidence of localised erosion at Thorpeness, it is considered that shoreline behaviour is influenced to some degree by the spatial and temporal changes in nearshore bathymetry, which may in turn give rise to localised episodic erosional or accretional events along the shoreline, as reported from other sites.

To build on previous work reported here, numerical modelling has been undertaken to examine how changes in nearshore bathymetry affect the longshore distribution of wave energy, and how this influences the magnitude and direction of longshore sediment transport. The numerical modelling has three specific objectives:

1. To assess and quantify if bathymetric changes, measured by multibeam surveys and X-band radar, affect the distribution of wave energy arriving at shore;
2. To examine the response of the shoreline and nearshore bathymetric features to different wave climates; and
3. To establish, using the same long-term wave forcing conditions, if the direction and magnitude of LST along the Thorpeness frontage changes in response to near-shore bathymetric evolution.

6.2 Methods

The modelling approach is illustrated schematically in Figure 6.1 Coastal Area Models (CAMs), comprising MIKE by DHI flexible mesh (FM) modules, spectral waves (SW), hydrodynamics (HD) and sediment Transport (ST), were built using measured 2014 (CAM 1) and 2017 (CAM 2) nearshore bathymetry. The models were forced using the same global tidal model and offshore waves and were calibrated and validated using measured and modelled data. Model parameters were adjusted to meet coastal model performance criteria described by Williams and Esteves (2017).

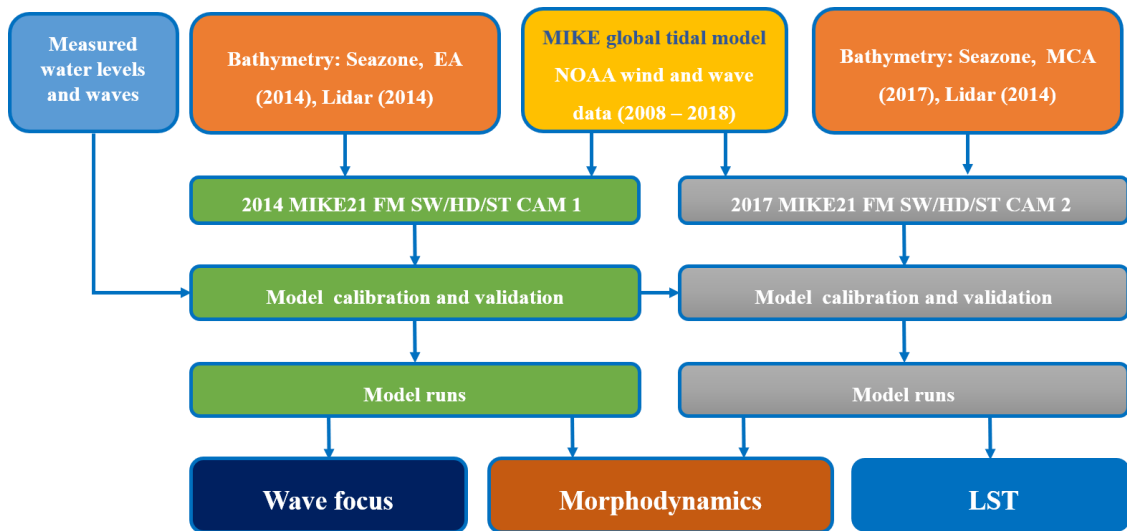


Figure 6.1. Schematic of model set up and summary of primary investigations using the models.

6.2.1 Model setup and resolution

CAM 1 and CAM 2 models used offshore bathymetric data provided by *Seazone*, complemented by nearshore swath bathymetry of the local study site from 2014 and 2017 (5.3.1), in both models the beach and intertidal areas utilised EA Lidar data (from 2014). These data were corrected to ODN and assessed for quality issues. The bathymetry was gridded using the MIKE FM tool. This enabled higher-resolution nesting towards the field site, with the shoreline between Sizewell and Aldeburgh having a maximum cell area of 50 m² (approximately 11 m side length, Table 6.1). The resulting gridded composite bathymetry for CAM 1 and CAM 2 and difference between them is shown in Figure 6.2.

Table 6.1. Maximum cell area, and indicative side length (based on an equilateral triangle) used in the model gridding.

	Region	Max. Area (m²)	Indicative Side Length (m)
Offshore	1	450000	1019
	2	150000	589
	3	50000	340
	4	5000	107
	5	1000	48
	6	150	19
Shoreline	7	50	11

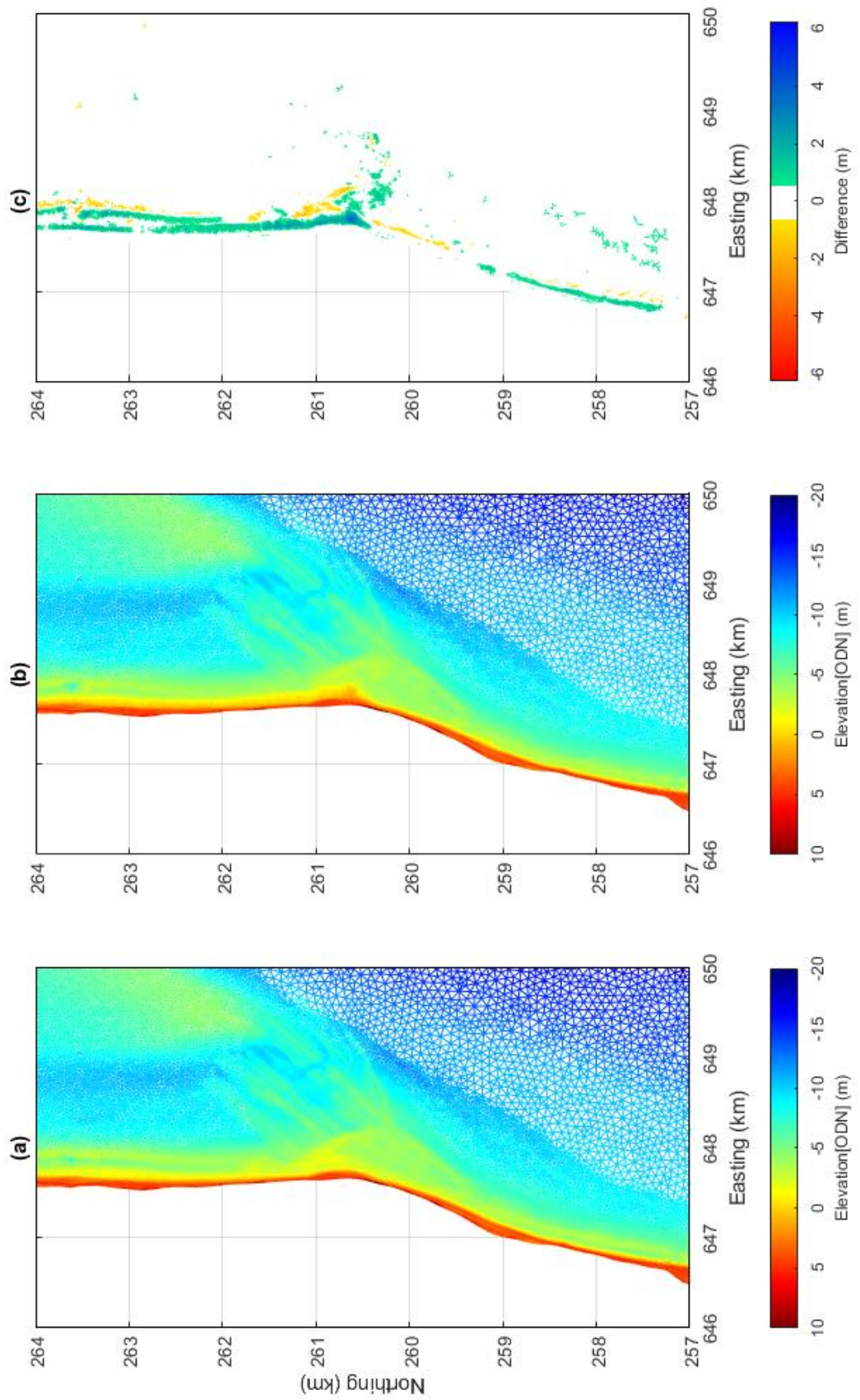


Figure 6.2. Gridded bathymetry in the nearshore region: (a) CAM 1 from the July 2014 EA multibeam survey, (b) CAM 2 from the January 2017 MCA survey; and (c) the difference between CAM 1 and CAM 2. Positive values (green-blue) indicate accretion between 2014 and 2017 and negative values (yellow-red) indicate erosion.

6.2.2 MIKE21 FMHD: Hydrodynamics

For both CAM 1 and CAM 2, the MIKE21 FMHD module utilised boundary conditions from the MIKE global water levels database, interpolated linearly along each boundary. The resulting water levels and tidal currents were validated against *Total Tide* points within the model domain (Figure 6.3a and Table 6.2) and water level data from a pressure sensor deployed at Thorpeness between April and July 2016 (See Section 5.3.1). Calibration was achieved using a +0.1 m offset along the northern boundary and a linear offset along the eastern boundary (+0.1 m to the north and 0 m to the south). Good model calibration was obtained as illustrated by the time-series plots from 5 location across the model domain showing comparisons between current speeds and direction from *Total Tide* data for the CAM 1 model (Appendix C1) and a Nash-Sutcliffe Efficiency score of 0.75 for model predictions of water level at the tide gauge deployment location a shows strong model performance (Appendix C1).

Table 6.2. Names, locations and temporal coverage of validation and boundary condition data sources for the SW and HD models.

Name	Latitude	Longitude	Data Coverage/Start date
NOAA WWIII Coordinates			
Point 1	52° 00.00'N	001° 30.00'E	2006 to 2018
Point 2	52° 00.00'N	002° 00.00'E	
Point 3	52° 30.00'N	002° 00.00'E	
Buoys Used in Boundary Validation			
Lowestoft	52°28.55'N	001°49.03'E	20-Apr-2016 to End
Felixstowe	51°56.30'N	001°23.64'E	04-Sep-2012 to End
West Gabbard	51°58.88'N	002°04.73'E	28-Aug-2002 to 10-May-2016
West Gabbard 2	51°57.17'N	002°06.53'E	10-May-2016 to End
Nearshore Wave Validation Points			
Sizewell	52°12.48'N	001°41.07'E	11-Feb-2008 to End
Total Tide Points			
SN014 D	52° 15.43'N	001° 48.78'E	01-Jan-2015 to 31-Dec-2015
SN014 Q	52° 12.73'N	001° 38.29'E	
SN014 A	52° 04.93'N	001° 38.29'E	
SN014 B	52° 02.03'N	001° 41.99'E	
SN013 N	51° 58.13'N	001° 33.99'E	
Thorpeness Tidal Gauge			
Gauge 1	52° 10.099'N	001° 36.46E	27-Apr-2016 to 31-Jul-2016

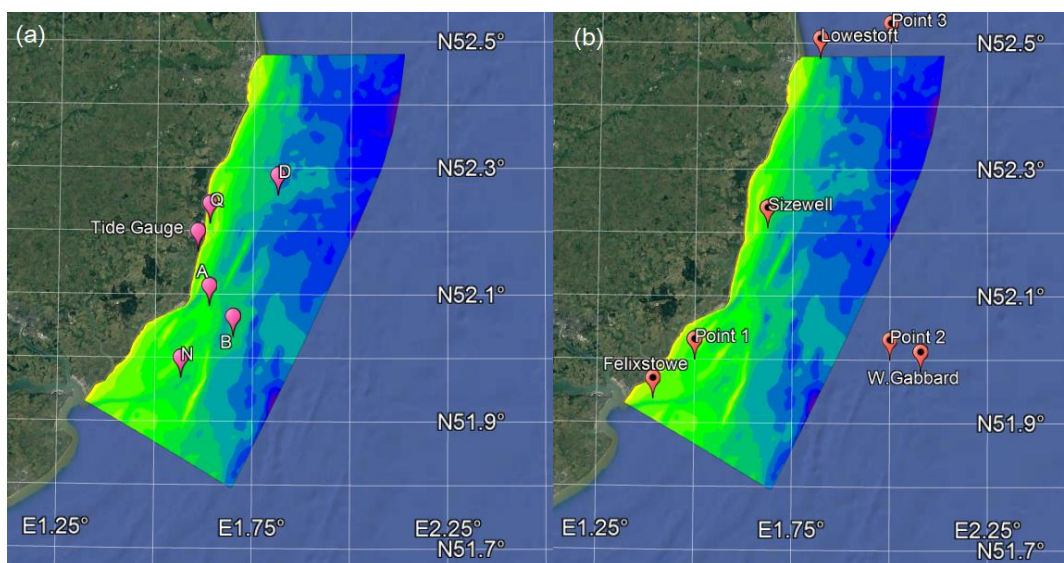


Figure 6.3. Google Earth © imagery overlaid with model coverage showing bathymetry and: (a) Total Tide and Tide gauge locations; and (b) NOAA WWIII points and wave buoy locations.

6.2.3 MIKE21 FMSW: Waves

The MIKE 21 FMSW model was driven along the offshore boundary by hindcast wave data from an offshore NOAA global WaveWatch III model data points spanning the period January 2006 to December 2017 (Figure 6.3b, Table 6.2). These data comprised values for significant wave height, H_s , peak, T_p , and mean, T_m , wave period, peak direction, Dir_p , and wind speed and direction at 3-hour intervals which were validated against the nearest Cefas Wavenet wave buoy (Appendix C2). A uniform wind field was applied across the model domain and the MIKE21 FMSW model was calibrated against wave buoy data by adjusting bed friction and wave breaking (e.g. white-capping). The following procedure was used to drive the appropriate wave conditions at the offshore boundaries of the MIKE 21 FMSW model: (a) wave conditions along the eastern offshore boundary were uniform and defined by the calibrated data from NOAA WaveWatch III Point 2; (b) to account for wave transformation, wave conditions along the northern boundary were linearly interpolated between Point 2 (offshore) and Point 3 (nearshore); and (c) linear interpolation between Point 2 (offshore) and Point 1 (nearshore) was used to define the wave conditions along the southern boundary of the model.

The calibrated model result was validated against the Sizewell buoy (5 km from the field site) for the year 2017 and results are presented in Appendix C3. It is considered that a Nash-Sutcliffe Efficiency score of 0.66 for model predictions of H_s at the Sizewell buoy demonstrates a reasonable model performance.

6.2.4 MIKE21 FMST: Sand transport

The MIKE21 FMST (sand transport) module setup for the study assumed a uniform offshore sediment size of 0.2 mm (British Geological Survey 1996), with porosity of 0.40. While this spatially invariant value simplifies the offshore sedimentary properties, there is insufficient data to define spatial changes in bottom sediment grain size; thus, this is a reasonable compromise based on the data available.

To correctly simulate wave-driven currents in the nearshore region, the sediment model was driven by the HD and SW modules in coupled mode. Following standard modelling practice, a sediment look-up table derived from the MIKE21 toolbox “*Generation of Q3D Sediment Tables*” was used to calculate sediment transport rates and thereby optimise model run times. The look-up table included the full range of wave height (0 to 5 m), period (3 to 18s), wave height/depth ratio (0.01 to 1.1) and current velocity (0.05 to 2.00m/s) values likely to be encountered at all locations in the model domain.

6.2.5 Effects of bathymetric change on shoreline wave energy

To investigate the impact of nearshore bathymetry on the wave energy distribution arriving at the shoreline of Thorpeness, two recent periods of beach erosion were selected for the simulations using the CAM models. The scenarios simulated are defined as Events A and B:

- A. 29th March – 3rd April 2010: A series of storms which contributed to the removal of sediment and the uncovering of geobag and gabion revetment at the northern end of the beach frontage; and
- B. 10th January – 15th January 2017: a storm event preceded by a period of southerly waves (between 1 and 2 m H_s , Figure 6.5) followed by northerly waves that reached a peak height of 3 m and resulted in significant erosion of the soft cliff line north of Thorpeness village.

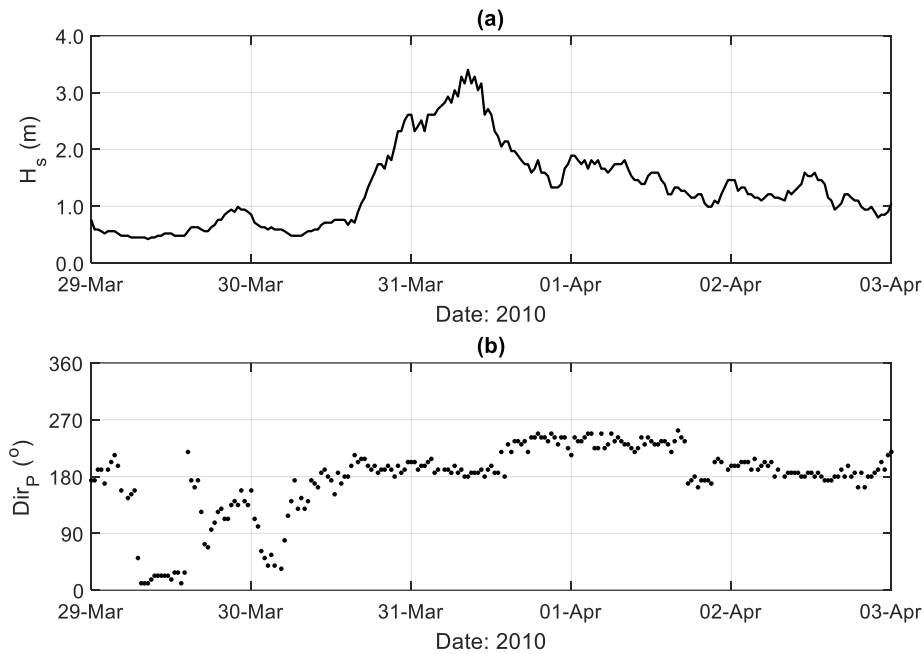


Figure 6.4. Time series of metocean conditions offshore (West Gabbard buoy) used for modelling the southerly scenario Event A: significant wave height (H_s , a) and peak wave direction (Dir_P , b) during a spring 2010 erosion event.

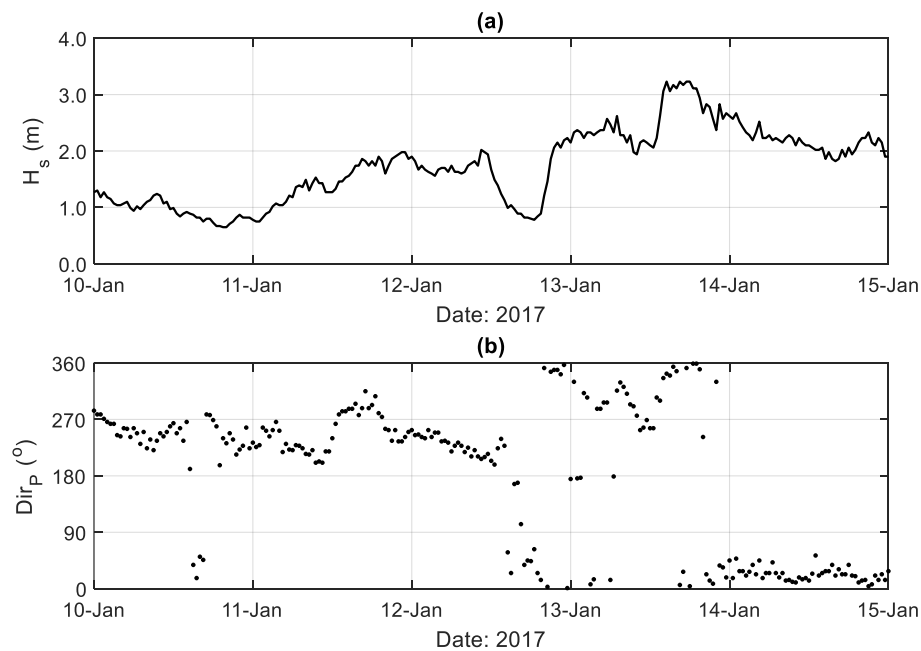


Figure 6.5. Event B: Time series of metocean conditions offshore (West Gabbard buoy) used for modelling the Winter 2016-17 erosion event (Event B).

6.2.6 Effects of wave direction on nearshore changes

It has been observed that prolonged periods of waves from either a southerly or northerly direction give rise to different beach responses. For example, in 2010 a period of southerly waves that preceded the main storm event in June resulted in beach drawdown and narrowing between Thorpeness and the Ness. As a consequence, the beach was made more vulnerable to subsequent storm impacts. The oblique bar-like feature that extends south and offshore from the Ness (hereafter termed the Ness bar) exhibits cycles of growth and retreat resulting from periods in which southerly and northerly waves dominate, respectively (See 5.3.3). This is demonstrated by the 2014 and 2017 bathymetry where the feature has quite different characteristics. To examine whether changes to the Ness bar affect wave refraction and dissipation leading to wave focusing (that could explain the formation of the erosion hot-spot at Thorpeness) when optimum bathymetry and wave conditions align.

Two CAM runs comprising of coupled HD, SW and ST modules were undertaken in order to assess these issues: The SW module was driven by wave boundary conditions representative of northerly and southerly wave events which caused significant erosion at the field site (Table 6.3): 19-Jun-2010 a northerly destructive event; and 31-Mar-2010 a southerly event which resulted in significant beach lowering (Williams 2014).

To enable morphological responses to be detected in the model results, the ST model used a morphological ‘speed-up’ factor of 10 so that the model run of 14 days (to cover a spring-neap tidal cycle) was equivalent to 140 days of persistent conditions. To moderate the morphological response of the model, bed changes were limited to a maximum of 5 m per day (which were never reached).

Table 6.3. Eastern boundary conditions for persistent northerly and southerly wave event assessment.

Model run	Start date	End date	Offshore wave and conditions				
			H _s (m)	T _p (s)	Dir _p (°)	Wind speed (m/s)	Wind direction (deg. N)
CAM 1	1-Apr-2010	15-Apr-2010	2.38	7.8	7	15.0	7
CAM 2	1-Apr-2010	15-Apr-2010	1.45	4.6	195	15.0	195

6.2.7 Effects on longshore sediment transport (LST)

Following the scenario focused CAM model runs, the modelling study then considered the longer-term coastal responses to an imposed wave climate using well-known equations to predict longshore sediment transport.

The shoreline between Aldeburgh and Sizewell was divided into 123 locally shore normal profiles distributed alongshore distances 4 km north and 4 km south of the field site and separated by 40 and 60 m depending of the rate of coastal orientation change. This ensured that the azimuth differences between adjacent profiles alongshore did not exceed 5 degrees, average beach slope values between MLWS and MHWS were calculated and interpolated using Environment Agency regional

monitoring profiles from the Thorpeness (coded TN), Sizewell (SZ) and Aldeburgh (AL), (Table 6.4).

Table 6.4. EA profiles used for the LST model. With sub cell references, longshore starting position and profile azimuth ranges indicated

Profile Set	Reference values	Profile Coverage: Northing (m)	Azimuth Range (°)
Aldeburgh	AL002 – AL027	257350 - 258755	107 – 110
Thorpeness	TN001 – TN047	258847 - 261203	90 - 110
Sizewell	SZ001 – SZ052	263962 - 261253	90

As an input to the LST model, a simplified version of the SW model was used in which the temporal resolution was reduced to the original 3-hour NOAA output, and the model was run in a directionally decoupled, parametric, quasi-stationary configuration between January 2007 and December 2017 (10-years) for both the CAM 1 (2014) and CAM 2 (2017) bathymetry cases. During this run, water level was modulated using a tidal curve derived using harmonic analysis of the data from tidal gauge deployed at Thorpeness.

The formulation of Battjes and Stive (1985), Equation (6.1) was used to define the height of breaking waves along each profile at each model time step (29224 records).

$$\frac{H_{sb}}{h} = 0.5 + 0.4 \tanh\left(\frac{33H_0}{L_0}\right) \quad (6.1)$$

where H_0 is the offshore significant wave height, H_{sb} is the breaking wave height, L_0 is the wavelength at the peak of the offshore wave spectrum (calculated based on linear wave theory, Equation (6.2) and h is the water depth. L_0 is defined as:

$$L_0 = \frac{g}{2\pi} T_0^2 \quad (6.2)$$

where, $g = 9.81 \text{ m/s}^2$ and T_0 is the deep-water peak period (at the eastern model boundary).

For each time step and offshore profile, the wave height and depth (relative to water level at that time) was extracted and the formulation used to define the value of H_s/h . Prior to calculating the LST rates, a smoothing filter (5 record moving average) was applied to the following wave breaking parameters: direction relative to shoreline θ , H_{sb} , T_{pb} and water depth.

LST transport rates for each profile were then calculated based on the Kamphuis (Kamphuis 1991, (6.3)), Coastal Engineering Research Center (CERC 1984, (6.4)) and van Rijn (Van Rijn 2014, (6.5)) formulations, with D_{50} values using the average of the sand ($D_{50} = 0.3 \text{ mm}$) and gravel fraction ($D_{50} = 14 \text{ mm}$):

$$Q_1 = \frac{2.27}{(\rho_s - \rho)} H_{sb}^2 T_{pb}^{1.5} (\tan\beta)^{0.75} D_{50}^{-0.25} (\sin(2\theta))^{0.6} \quad (6.3)$$

$$Q_2 = k * Pl = k \frac{(1 + n_e) \rho g H_{sb}^2 C_g \sin(2\theta)}{(\rho_s - \rho)g} \frac{1}{8} \frac{1}{2} \quad (6.4)$$

$$Q_3 = 0.00018 \rho_s g^{0.5} (\tan\beta)^{0.4} (d_{50})^{-0.6} (H_{sb})^{3.1} (\sin(2\theta)) \quad (6.5)$$

Here Q denotes the volumetric LST rate ($\text{m}^3 \text{s}^{-1}$), ρ_s is the sediment density (2650 kg m^3), ρ water density (1026 kg m^3), g is the acceleration due to gravity, n_e is the sediment porosity (0.40 and 0.45 for sand and gravel respectively), $\tan\beta$ is the beach slope, D_{50} is the median grain size, H_{sb} is the significant wave height at the breaking point, T_{pb} is peak period at the breaking point, C_g is the group velocity, θ is the wave angle to the shoreline and k is the coefficient in the CERC equation (assumed to be 0.39).

6.3 Results

6.3.1 Effects of bathymetric change on shoreline wave energy

Plots of wave energy at the 1 m isobath for both Event A and B (Figure 6.6a and b respectively) provide an overview of the wave power differences between Aldeburgh and Sizewell. Considering Event A (southerly direction), Figure 6.6a shows a reduction in wave power to the north of the Ness for both CAM 1 and CAM 2. South of the Ness (at the village frontage) wave energy is greater for the CAM 2. This is most likely attributable to the steepening of the nearshore profile that occurred between 2014 and 2017 (Figure 6.2, Figure 6.6d and e). North of the Ness, wave power reduction is noted in both runs suggesting shadowing from southerly events by the Ness. The longshore changes in wave power between the Ness and Aldeburgh shown in Event A have two primary features: (a) a large-scale modulation in wave power that gives rise to a significant reduction in wave energy north of the Ness and an increase south of the Ness; and (b) a series of wave power oscillations superimposed on the larger modulations which are especially evident for the CAM 2, which suggests variable wave power along the whole beach frontage during southerly storm events.

The longshore changes in wave power between the Ness and Aldeburgh for Event B (Figure 6.6b) show overall a lower wave power when compared with Event A, this is likely due to the dissipation of wave energy over Sizewell bank. A reduction in wave power is also observed to the north of the Ness only in CAM 1 (Figure 6.6b) while an increase in wave power is apparent for the CAM 2. The increase in wave power north of the Ness observed in CAM 2 may be due to the fact that the Ness bar present in 2014 is eroded in 2017. Changes to the south of the Ness are minor (Figure 6.6e), between CAM 1 and 2, and the large modulation of energy observed in the southerly event does not occur.

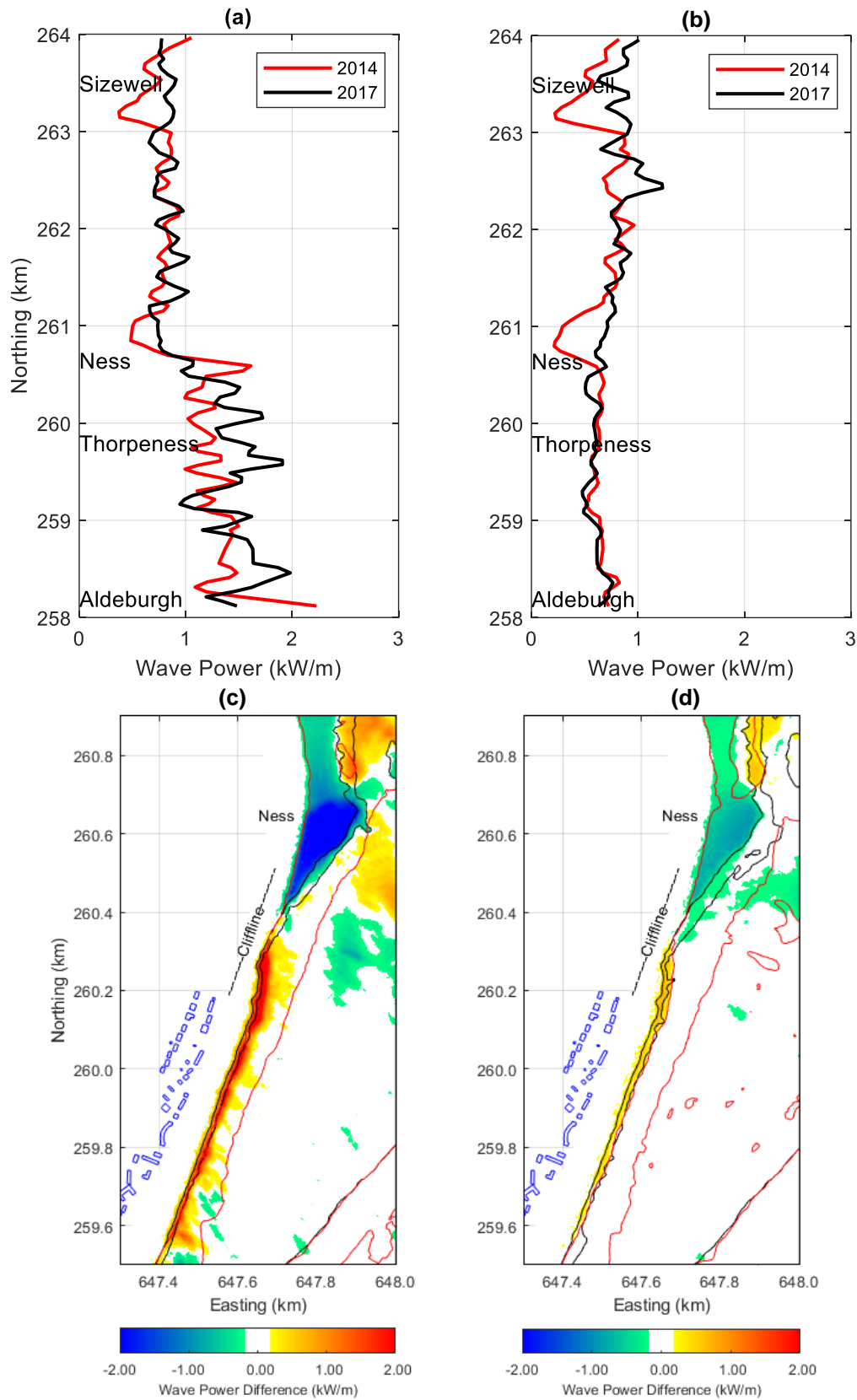


Figure 6.6. Wave power plots CAM 1 (2014) and CAM 2 (2017) between Aldeburgh and Sizewell at the peak wave height for (a) southerly Event A and (b) northerly Event B. Spatial plots focusing on the Ness and beach front of the wave power differences (positive indicates an increase in energy between CAM 1 and 2): (c) Event A; and (d) Event B. Contour lines indicate 1, 2 and 5 m depths for 2014 (red) and 2017 meshes (black).

While the features of the longshore wave power distribution are specific to the storm events in the CAM simulations, they demonstrate clearly how differences in the offshore bathymetry between 2014 and 2017 can result in variations in the longshore wave power distribution and, by implication, longshore variability in beach responses to wave action.

6.3.2 Effects of wave direction on nearshore changes

The impact of extended northerly wave conditions (Figure 6.7) results in the erosion of sediment in the range of 0.75 to 1.25 m depth in the offshore region north of the Ness (261 km, arrow A). The accretion on the Ness bar (260.7 km, arrow B) is contrary to what has been seen in the radar and multibeam assessment, this is likely due to the lack of defined hard geology in the model, and so northerly approaching waves instead bring sediment to the bar from the NE, where in reality the multibeam analysis indicated hard geology with little change between 2014 and 2017. The steepening of nearshore beach frontage (arrow C) is apparent and closely matches the region of nearshore changes identified by the multibeam surveys. The northerly waves also result in a double bar formation (approximately 1 m high) along much of the Thorpeness village frontage, evidence of this feature is observable in several of the measured beach transects

The impact of extended southerly waves to the north of the Ness (Figure 6.8, arrow A) is more variable, with accretion dominating the south of the area and relative stability elsewhere. The Ness bar shows significant accretion running N/S around 300 m. Though as per the northerly run, the accretion is observed to be outside the areas identified by the multibeam analysis, suggesting the lack of hard geology in the model is not constraining the bar as appears to be the case in the recurring formations in the multibeam and radar analysis (5.3.1 and 5.3.2). The Thorpeness village frontage and coast to the north shows widespread evidence of erosion (Figure 6.8, arrow C) though nearer to the shoreline, accretion of sediment is shown (2 to 3 m) with no double bar system present.

It is noted that the CAM models assume the model domain comprises entirely sand of unlimited depth. Areas of resistant Coralline Crag ridges and other hard geology are therefore subject to rates of erosion that far exceed what would occur naturally. This gives rise to the ‘false’ regions of sediment movement identified, particularly around the Ness bar, that in some cases do not match the changes seen in the multibeam data. Nevertheless, even with simple input parameters (single D_{50} used, no hard geology defined etc.), model results agree broadly with the changes observed between the multibeam surveys and the radar-derived data.

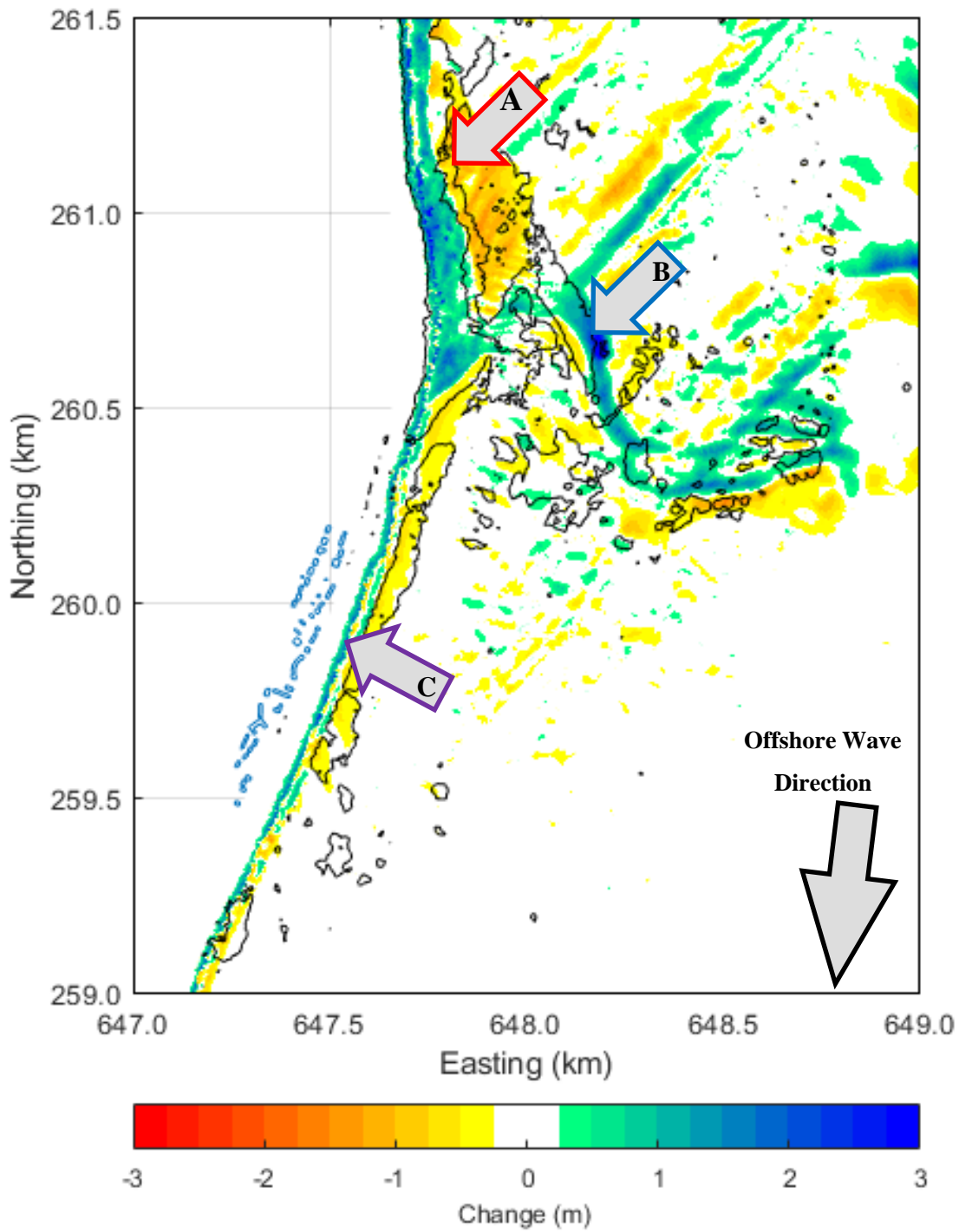


Figure 6.7. Total change of bed level (greater than ± 0.25 m) from northerly waves after 14-day coupled model run, black contour lines indicate changes $\geq \pm 0.5$ m between 2014 and 2017 by multibeam survey. Arrows indicate areas specifically discussed in the text.

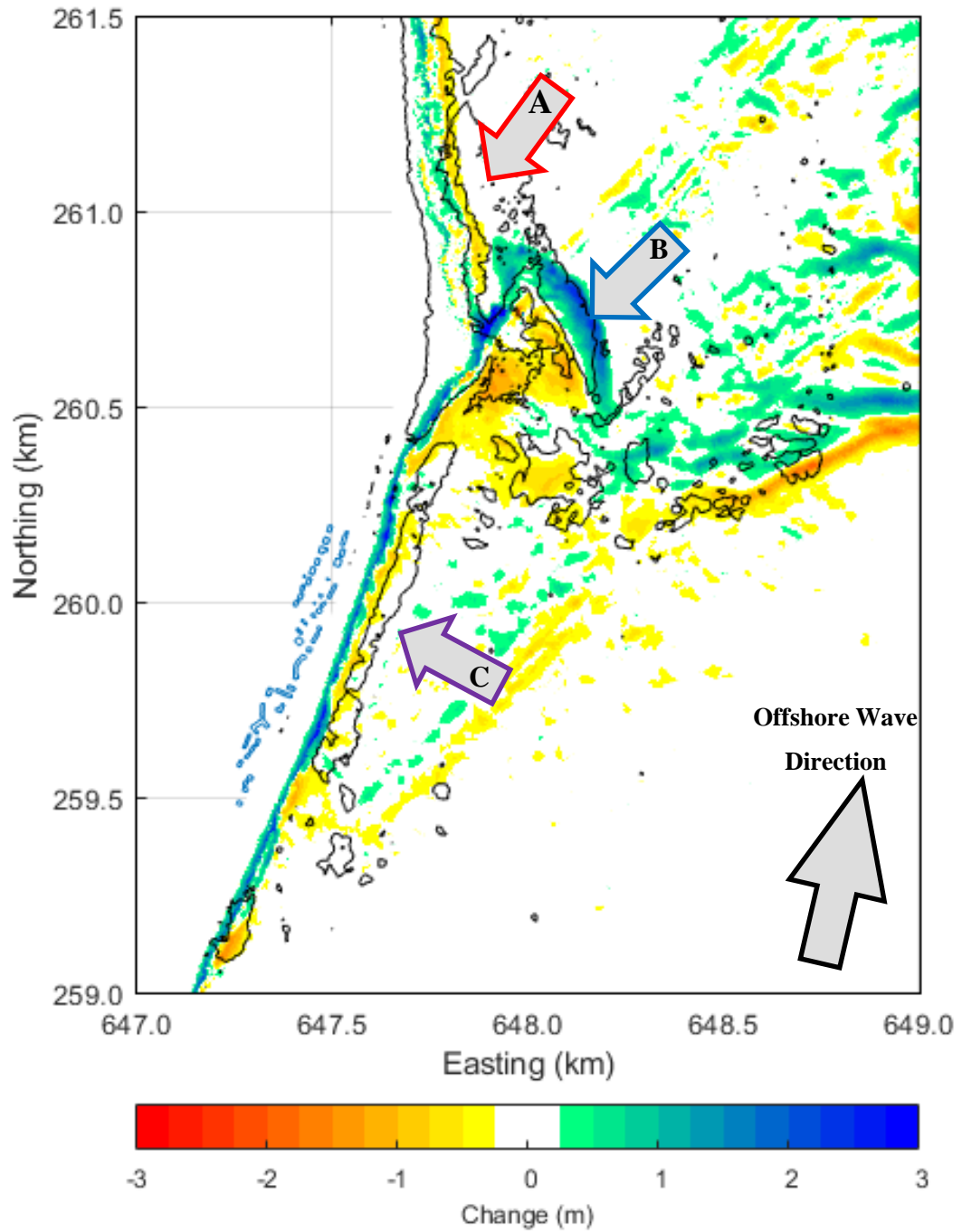


Figure 6.8. Total change of bed level (greater than ± 0.25 m) from southerly waves after 14-day coupled model run, black contour lines indicate changes $> \pm 0.5$ m between 2014 and 2017 by multibeam survey. Arrows indicate areas specifically discussed in the text.

6.3.3 Effects on longshore sediment transport (LST)

LST transport rates, expressed as an average annual flux (m^3/year) for each of the formulations and sediment sizes (Figure 6.9 and Figure 6.10) show similar trends. The Kamphuis formula prediction of LST are around 50% less than CERC and the Van Rijn formula predicts an order of magnitude difference in LST rates between the sand and gravel fractions. A prominent divergence at the Ness is observed for CAM scenarios, where the location of the sediment flux peak (northerly movement) lies between N260.3 and N260.6 km before reversing and attaining a peak negative value (southerly movement) at N261 km. The magnitude of these peaks in LST differs with each LST formulae.

Differences between the LST model runs results using the 2014 and 2017 bathymetry occur at a number of points along the shoreline. Results from the Van Rijn formula (Figure 6.9c and Figure 6.10c) show a notable increases in LST between 2014 and 2017 at N259 km ($5000 \text{ m}^3/\text{y}$), 260 km ($3500 \text{ m}^3/\text{y}$) and 260.4 km ($5000 \text{ m}^3/\text{y}$). North of the Ness, the Sizewell region shows variable LST rates and both northerly and southerly movement for 2014 and 2017 bathymetry. Here, the absolute magnitude of the LST rates are smaller than those south of the Ness, likely due to the wave energy dissipation over Sizewell Bank.

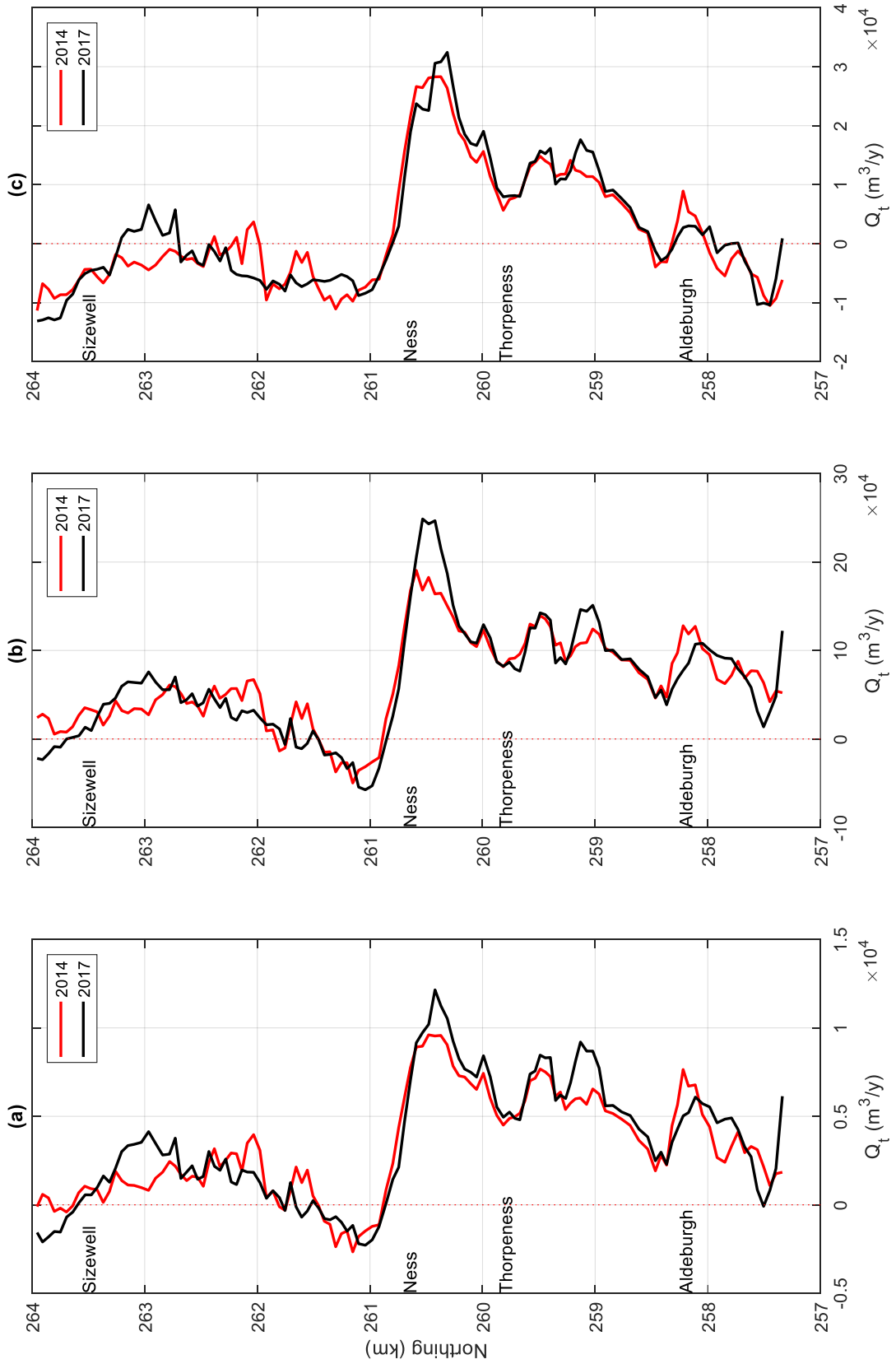


Figure 6.9. LST total average yearly flux of medium sand ($D_{50} = 0.3$ mm) for (a) Kamphuis, (b) CERC and (c) van Rijn formulations over the 10-year dataset where a positive value denotes northerly transport and a negative value southerly transport.

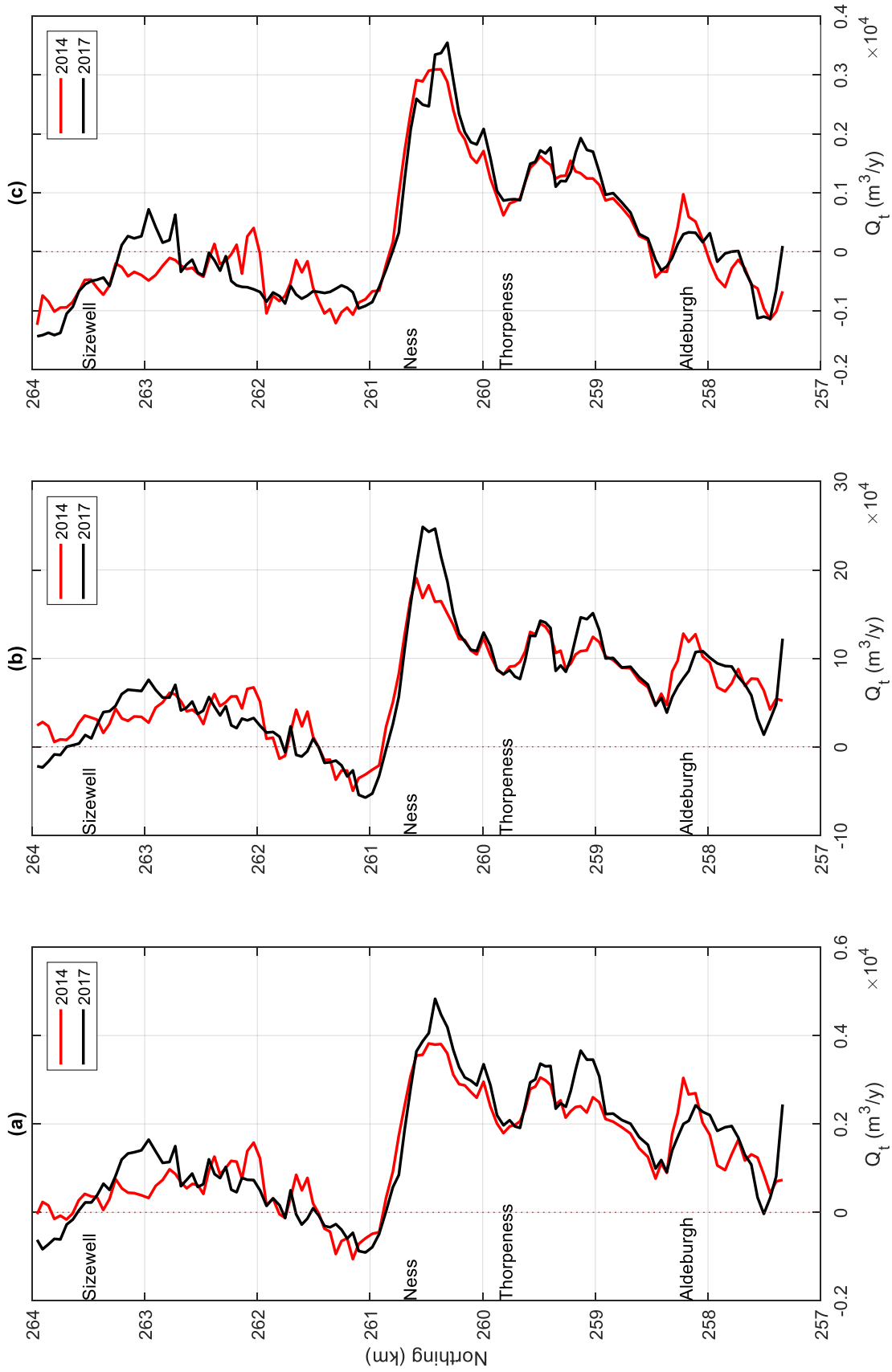


Figure 6.10. LST total average yearly flux of gravel fraction ($D_{50} = 14.0$ mm) for (a) Kamphuis, (b) CERC and (c) van Rijn formulations over the 10-year dataset where a positive value denotes northerly transport and a negative value southerly transport.

As previous studies have demonstrated, annual differences in northern and southern net LST can be substantial. To better understand LST along the Thorpeness coastline it is necessary to consider how periods of directionally dominant waves interact with the beach sediment and how bathymetric changes act to modify the incident wave climate and LST. This has been investigated by examining two contrasting winter periods each dominated by either northerly or southerly waves (Figure 6.11), and two high energy wave records within each of these winter periods (Figure 6.12).

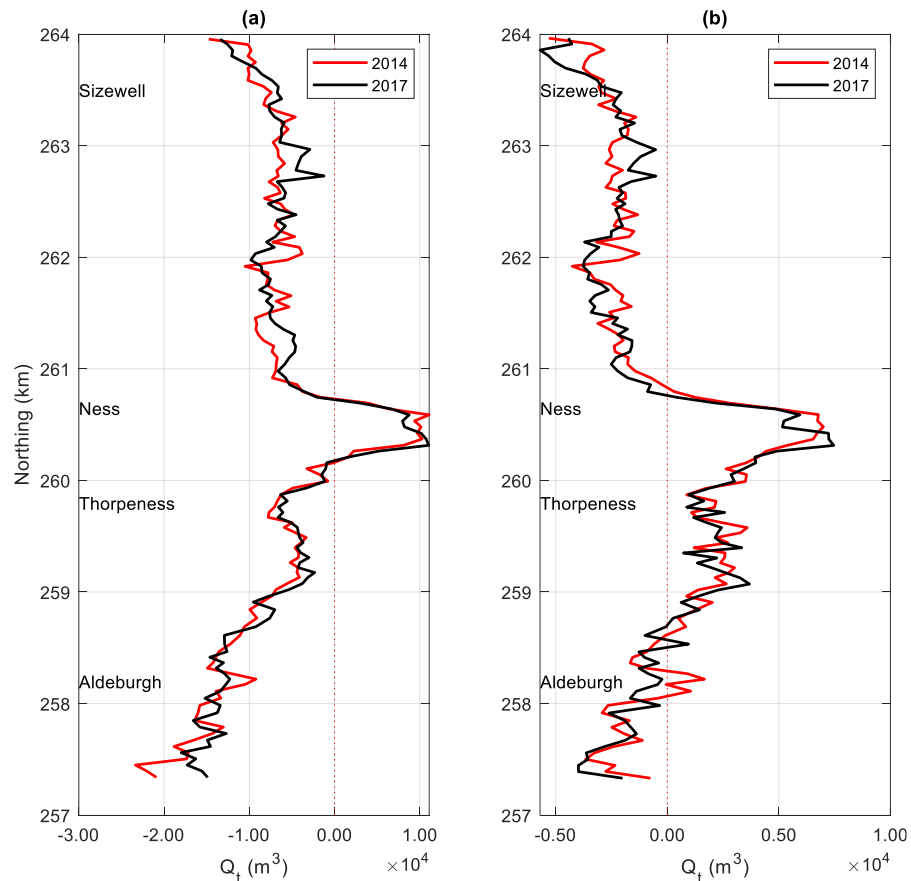


Figure 6.11. Van Rijn computed LST for medium sand ($D_{50} = 0.3$ mm) (a) northerly dominated winter (01-Dec-2009 to 28-Feb-2010); (b) southerly dominated winter (01-Dec-2015 to 28-Feb-2016).

The LST simulations show the following key features:

- For the northerly wave dominated winter (Figure 6.11a), the LST flux is primarily negative (southerly) for both CAM 1 and CAM 2 except in the region of the Ness, where the LST is positive (northerly). Therefore, the LST flux indicates a convergence of sediment to the north of the and a divergence of sediment to the south;
- For the southerly dominated winter (Figure 6.11b), the LST flux is dominantly positive for both CAM 1 and CAM 2, between the Ness and Aldeburgh, except for CAM 1 along a short coastal stretch north of the Ness, where a negative LST flux is observed. Therefore, for CAM 1, convergence of sediment continues to occur at the Ness and divergence now occurs north of the Ness; and

- The fluctuation of LST rates between Thorpeness and the Ness is lower in the northerly dominated winter. This is likely due the dissipation of wave energy due to the Sizewell bank as noted above. While spatial variability in LST flux rates are apparent for both the 2014 and 2017 bathymetries, the overall trends are similar.

The differences in LST flux associated with CAM 1 and CAM 2 bathymetry become even more apparent when individual wave events are examined. Here as examples, northerly waves on 17-Dec-2009 and southerly waves on 12-Dec-2014 are used to illustrate this (Figure 6.12). The principal results show that:

- High energy northerly wave conditions (Figure 6.12a) give rise to significant differences in sediment flux north of the Ness. This agrees well with results from the CAM 1 model which shows large changes of LST (varying between +10 and -70 m³/h). This contrasts with the less variable LST flux results from the CAM 2 model (flux of -20 to -60 m³/h);
- Around the Ness, differences in LST rates are reduced compared to adjacent areas irrespective of the bathymetry considered; and
- Although the direction of LST associated with the southerly event is exclusively to the north, the greatest variance is observed south of the Ness, where rates are observed to change from 40 m³/h in 2014 to 25 m³/h in 2017.

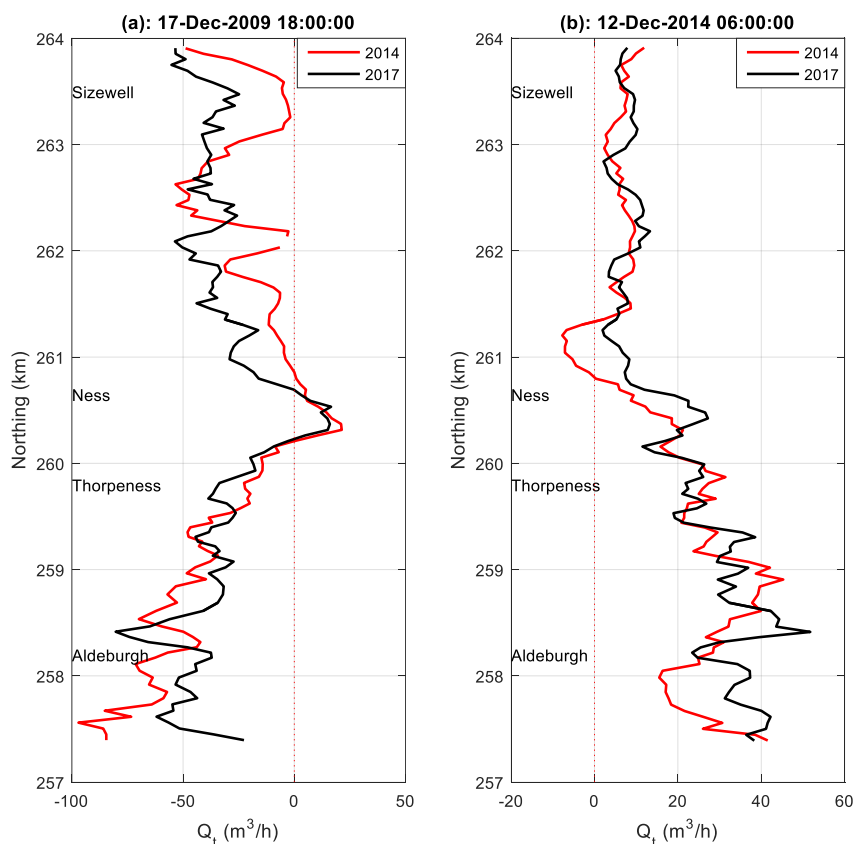


Figure 6.12. Van Rijn computed LST rates for single occurrences ($D_{50} = 0.3$ mm), (a) northerly event (17-Dec-2009 boundary conditions: $H_s = 3.67$, $Dir_p = 28$, $T_p = 8.19$) (b) southerly event (12-Dec-2014 boundary conditions: $H_s = 4.02$, $Dir_p = 210$, $T_p = 6.81$).

6.4 Discussion

Considering the wider coastal behaviour at Thorpeness, the LST modelling has provided insights on the effects of changes in bathymetry on the direction and magnitudes of the LST flux which result in convergence at the Ness and divergence either south or north of the Ness. The location of divergent LST can also shift alongshore in response to both bathymetric changes and the incident wave climate. Along with wave focus, areas of divergent LST are especially vulnerable to erosion in storms and thus LST may be a primary contributing factor to the occurrence of erosion hot-spots.

When the LST rates for the 10 year model are compared to the results of Burningham and French (2016, who present the Van Rijn LST formula outputs), the trends and magnitudes of the sediment flux are comparable despite the differences in the model setup which includes use of: (a) a finer alongshore profile resolution (40 m within this study compared to 100 m); and (b) a 10-year incident wave time-series compared to the simulated wave climate based on analysis and binning of the wave conditions between 2009 and 2016 used by Burningham and French. The resulting peak sediment flux at the Ness in Burningham and French was $\sim 20,000 \text{ m}^3/\text{y}$ northwards ($D_{50} = 0.4 \text{ mm}$) whereas this study ($D_{50} = 0.3 \text{ mm}$, based on field observations), indicates 28,000 to 32,000 m^3/y , (although this is reduced to 24,000 - 27,000 m^3/y with an identical $D_{50} = 0.4 \text{ mm}$). North and south of Ness the LST outputs show differing magnitudes to the north of the Ness where southerly directed transport reaches $\sim 80,000 \text{ m}^3/\text{y}$ in Burningham and French compared to 10,000 m^3/y in this study. To the south of the Ness, both studies indicate a steady shift to southerly dominant transport.

When comparing LST predictions for 2014 and 2017, the impact of bathymetric changes can be seen clearly. Variations in the magnitude and direction of LST flux between Thorpeness and the Ness provide a plausible explanation for the observed alongshore variability in beach response identified in previously in the thesis. The LST modelling has shown that irrespective of bathymetric changes, the Ness is a region of sediment convergence. However, apart from localised and temporary erosion and accretion phases, the total volume of the Ness remains relatively constant. This implies that there must be exchanges of sediment between the Ness and the nearshore. The observed growth of the Ness bar, and maintenance of the southern portion of Sizewell Bank may suggest a sediment exchange between the Ness and the offshore, previously hypothesised by McCave (1978) and Carr (1981).

The LST modelling suggests that the Ness may be a viable source of sediment for redistribution in reactive or pro-active coastal protection works. If sediment is taken from the active region of the Ness profile (MLWS to approximately 3 m ODN) the environmental impact would be minimised. However, the removal of sediment from these locations also carries a risk of removing the buffer and protection this sediment provides to the upper regions of the Ness. Being able to identify a 'tipping point' in which sediment removal may affect the natural accretion trend requires further investigation.

In a broader sense this chapter has highlighted the need to ensure that the bathymetry used in numerical models is accurate. All too often this is overlooked to save costs even when investments in coastal defences may be several millions of pounds (e.g. Dornbusch 2017). It is common for model bathymetry to comprise non-contemporaneous data of variable quality from multiple sources. The modelling results for this localised coastal area demonstrate clearly how subtle changes in offshore bathymetry impact on the wave field, shoreline behaviour and related processes. These results send a strong message to practitioners and funders that investments in bathymetric data acquisition will reduce risks and uncertainties, lessening the high costs associated either over-design or failed structures.

7. Discussion of Key Findings and Conclusions

This research has advanced the current knowledge of temporal and spatial variability of nearshore and shoreline changes in mixed sand and gravel coasts and the associated physical drivers, using the coast around Thorpeness (Suffolk, UK) as a study case. A multi-method approach was paramount to effectively understand the interactions between wave conditions, sediment transport, nearshore and beach changes in a dynamic and complex system. The range of methods used included: field data collection (sediment and beach topography), secondary data analysis (10 years of wave climate and beach profiles), remote sensing (using a land-based X-band radar) and numerical modelling. These techniques were used to quantify magnitudes of changes and investigate the combination of: (a) bimodal wave directions and varying energy; (b) the proportion of sand at the beach; and (c) nearshore bathymetry on beach mobility.

Multi-method approaches in characterising and understanding coastal dynamics have been conducted, though rarely in such complex environments. These studies have often been incorporated into longer-term monitoring sites such as Duck, North Carolina, USA (van Dongeren et al. 2008; Holman et al. 2013; Honegger et al. 2019) and Perranporth, Cornwall, UK (Austin et al. 2010; Masselink et al. 2014; Stokes 2015), or after major engineering works such as the sand engine in The Hague, Netherlands (Rutten et al. 2017), where the availability of bathymetric and topographic measurements facilitate the validation and calibration of remote sensing data and numerical models. In all these cases, the environment consisted of sandy coasts; similar comprehensive studies in mixed coasts have not occurred. Therefore, this project innovates for using multi-methods to investigate nearshore and beach dynamics at a highly complex MSG site where prior field data coverage was limited to regional beach morphology monitoring and sporadic bathymetric surveys. Previous studies highlighted the complexity of the study area and suggested that local nearshore processes have a large influence on the shoreline dynamics (Bamber 1965; Lees 1977, 1983; Williams 2014; Burningham and French 2016); however, actual measurements to support this were lacking. For these reasons, the methods utilised were driven by a need to characterise these complex interactions through a holistic but cost-effective manner to better inform future coastal management.

This chapter discusses the relevance of the key results presented in previous chapters to advance the current knowledge and research practices related to mixed beaches and implications to local coastal management. The content is organised to address each of the research objectives outlined in Section 1.2 and includes suggestions for future research. The key findings are summarised in the Conclusions.

7.1 Temporal and spatial variability of MSG beach morphology in relation to wave climate

This research has evidenced the great temporal and spatial variability in beach morphology and response to driving conditions within short distances (~300 m) alongshore. Previous studies have highlighted the variable morphology in this coastline (Pontee et al. 2004; Williams 2014) and simulated the impact of wave climate on shoreline position using numerical modelling (Burningham and French 2016). However, none have previously quantified these differences and responses based on field measurements nor evidenced that variability can occur within such short stretches of coastline.

Within the 2-km long coastline, beach behaviour was observed to parallel with the three conceptual models outlined by Pontee et al. (2004): 1) an unmanaged mixed beach (Transects A and B); 2) an unconsolidated cliff backed beach (Transect C), and 3) an engineered beach (Transects D and to some extent Transect E). Differences in response and mobility at the site and within these conceptual models are influenced by the presence and movement of gravel ridges across the system from the lower to the upper beach and their interaction with the back-beach (e.g. protected or unprotected cliff faces, natural gravel berms). The enhanced mobility and erosion hot-spot along the protected coastline at Thorpeness parallels with the engineered beach conceptual model. This model indicated that when losses over the whole profile occur (due to storm conditions) it is unlikely to recover without intervention. However, differences in behaviour occur between similar transects in this study (e.g. A and B or D and E) suggesting small differences in morphology and driving wave conditions may impact the overall behaviour.

The widely recognised relationship between enhanced wave energy and beach erosion in sandy (Short 1979; Loureiro et al. 2012; Angnuureng et al. 2017) and gravel coasts (Ruiz de Alegria-Arzaburu et al. 2010; McCall et al. 2015) is much less evident in the study area. Previous studies have suggested that the local interaction between the bimodal dominant wave direction and the nearshore results in alongshore variation in the wave energy distribution at the coast, altering sediment transport (Pye and Blott 2006; Burningham and French 2016; Pethick 2017). The observed variable behaviour at the shoreline at site was linked to the phase/state of the nearshore bathymetry through LST modelling. The results demonstrated the movement of sediment convergence and divergence regions with different nearshore states. These states were a result of the preceding, long-term wave conditions building upon the conclusions of Burningham and French (2016), showing the direct impact of nearshore change on shoreline response.

7.2 The effect of the proportion of sand in mixed beach mobility

The effect of the proportion of sand on the mobility of MSG beaches has been the focus of previous studies (López de San Román Blanco 2003; She et al. 2006, 2007; Horn and Walton 2007; Zarkogiannis et al. 2018). This project has highlighted the difficulty in making accurate estimates of

the proportion of sand and gravel in natural beach conditions and that assumptions need to be made to ensure such characterisation can be defined through more feasible and practical methods. Trade-offs between accuracy, speed and spatial coverage also need to be considered. Initial tests with automatic image processing for particle size analysis confirmed that large errors occur when grain sizes spanned orders of magnitude (Pentney and Dickson 2012). Therefore, an alternative and more feasible method was devised to quantify the proportion of sand and gravel and how it varies in space (including at surface and subsurface) and time, combining in situ measurements, digital image analysis and sediment sampling.

The results of the PSD analyses have highlighted the large sediment variability at the site which has also been identified in previous research at similar geographical (Pontee et al. 2004) and morphological environments (Dawe 2001). The study builds upon these studies through development of methods for assessing the relationship of sand proportion and beach mobility hypothesised by a number of earlier papers (Mason 1997; López de San Román Blanco 2003; She et al. 2007) which is driven by its impact on hydraulic conductivity (She et al. 2006, 2007). This simple relationship between proportion and mobility has been proven to be difficult to define in the field in comparison to previous laboratory tests.

Limitations of the methods employed were primarily due to the assumptions made of profile composition below the surface and of the sand and gravel mix. When using only surface proportions for analysis, the results were highly variable, the assuming depth analysis values of 34% sand and 66% gravel within the composite mix, resulted in bias toward these values in transects which were not gravel dominated. Unfortunately, it seems that regardless of accuracy, speed and efficiency of image analysis, the characterisation and understanding of sediment and its dynamics in MSG beaches will always rely on both surface and depth samples due to the large changes in sediment composition between surface and depth.

7.3 Utility of X-band radar

X-band radar data provided valuable information on the nearshore bathymetry at time-frames that would be prohibitive by other means. These data helped identifying the most dynamic nearshore areas and the understanding of linkages between beach and nearshore changes hypothesised in previous studies (Carr 1981; Williams 2014; Burningham and French 2016). In particular, the cyclical accretion and erosion phases of the oblique bar off the Ness, and the role of this feature in moderating wave climate and alongshore sediment transport has provided a new understanding of the local sediment budget. Net changes in seabed sediment volume can be large ($>700,000 \text{ m}^3$) even over periods of only few weeks and reach >5 million m^3 over longer periods (few months).

Concurrent multibeam survey data has enabled for the first time a critical assessment of the data derived using algorithms to analyse X-band radar data. This rigorous analysis has quantified the accuracy of the radar as well as identifying its limitations; producing a bathymetric map at a 40 x 40

m cell size (made from a 120 x 120 analysis window, shifted in 40 m increments) at an accuracy of ± 0.50 m. This accuracy is comparable to radar deployments elsewhere though often larger resolution (960 x 960 m analysis window in Rutten et al. 2017) or less bathymetrically complex sites are used (Honegger et al. 2019). The thesis has driven the use of radar for temporal change analysis, with the method employed demonstrating changes in the nearshore bathymetry can be reliably quantified and observed in the order of weeks. These results contrast with recent research (Rutten et al. 2017) concluding temporal change in the order of days and months is currently unrealistic.

The analyses of radar data employed in this study have overcome previous issues associated with data quality and variance due to the bi-directional wave climate and difficulties in defining the correct processing parameters in which to extract the highest quality data. These advances may lead in the future to a radar system that can be deployed and used by non-specialist end-users to deliver high-quality data required in many practical coastal applications. However, it is important to note that substantial investment in supporting data is required for the calibration and validation of the radar outputs, which limits its use as a 'stand-alone' system.

7.4 Nearshore variability, shoreline change and impact of a bimodal wave climate

Bi- and multi-modal wave climate studies tend to incorporate observed wave conditions with modelling of wave fields to understand longshore energy flux changes (e.g. Burningham and French 2016; Hegermiller et al. 2017). Though this study is the first to model a combination of a complex changing nearshore and wave conditions informed through remote sensing, similar techniques utilising remote sensing for predictive modelling have been accomplished in sandy regions (Stokes et al. 2015). The results of this study have shown the speed of nearshore change and the significant impact it can have on energy distribution at the shoreline.

The extensive multibeam and radar analysis highlighted two distinct nearshore states that tended to occur due to varying proportions of north and south wave energy. The fact the two states were distinct and recurring in shape suggested the underlying hard Coralline Crag geology also played a significant factor in repeated formation. Similar recurrence of sea bed features have been linked with underlying geology (McNinch 2004; Schupp et al. 2006; Kirkpatrick and Green 2018) but interestingly also focused erosional hot-spots (Browder and McNinch 2006). This study has built upon these works by linking the dominant wave direction to the phase of nearshore state and then investigating (through modelling) how this impacts shoreline energy distribution. These states are centred around the formation and removal of a 'Ness bar' which accretes during southerly dominated periods, eroding areas to the south. During northerly conditions, this bar is eroded and accretion forms to the south and west. Recurrence of these states observed in the radar data show that changes (exceeding 0.5 m) occur in periods of months, are non-seasonal and that the temporal coverage of available multibeam surveys does not accurately capture the full dynamism of the system.

The changes in the nearshore were numerically modelled to understand the short- (single event), seasonal (DJF) and long-term (10-year model run) impacts of the two bathymetry phases on shoreline processes as well as assessing the recurrence of nearshore features through a nearshore sediment transport model. The results indicated a strong link to the variance in wave energy at the shoreline and the associated direction and magnitude of LST. A distinct tendency for the recurring features to be developed also occurs within the model; though it is acknowledged that improvements to define hard geology may increase the accuracy further and result in the geologically constrained nearshore states observed both in the radar and multibeam analysis.

7.5 Informing coastal management decisions

Within the study area, the Ness seems the most favourable source of gravel for small-scale beach recharge operations benefitting the Thorpeness frontage. Particularly, if sediment extraction is limited to the dynamic part of the profile (below MHWS) and after periods of accretion. Material used to recharge the beach at Thorpeness is likely to return to the Ness naturally through longshore transport. Therefore, it is important to carefully consider the volume and timing of the operations to ensure that they will provide coastal protection at Thorpeness without causing detrimental impacts elsewhere.

The area south of the Ness where gravel has been extracted in the past has experienced considerable erosion since 2014. Although some recovery has been observed since 2017, gravel extraction from this area should be avoided at least until the profile area is returned to pre-2014 conditions. Numerical modelling studies may be useful to identify thresholds for beach stability in this area and the associated linkages to changes elsewhere.

The gabions and the geobags installed to protect the northern frontage have offered some protection to the beachfront properties. However, they have reduced the beach width and the level of natural dissipation of wave energy, increasing the exposure to the defences and the beachfront properties. Options proposed including the replacement of temporary geobags with a more permanent structure, such as a rock revetment (Williams and Herbert 2015), are very likely to enhance erosion to the north and result in further reduction in the beach width in front of the structure (Pontee et al. 2004). Therefore, exposure to waves and risk of erosion are likely to increase in the longer-term.

Results of the LST modelling suggest that the most sustainable and less detrimental option to reduce the impact of erosion at Thorpeness in the short-term is small-scale beach recharge using the Ness as a source of material as indicated above. However, if northerly waves become more dominant, this option may no longer be feasible due to changes in the local sediment budget. Further, as conditions may become more severe due to impacts of climate change, the protection of existing beachfront properties may require an increased frequency of operations and sediment volume. Therefore, for the longer-term economic and environmental sustainability of this area, management decisions need to consider measures that allow the coast to behave more naturally and prevent further occupation and

values at risk. Options may include a combination of setback lines, restrictions on property improvements that may enhance erosion or increase assets at risk, and managed realignment.

7.6 Further Research

In common with previous MSG beach research, the present work has identified the difficulties in quantifying and understanding the spatial and temporal variability of MSG sediment dynamics. The fieldwork methods employed in this study were an attempt to provide a non-destructive consistent approach to MSG beach characterisation to understand the effect of sand proportion on beach mobility. The present results indicate that higher temporal analysis of sedimentary change in high and low energy periods is required to improve understanding of how the proportion of sand and gravel affect hydraulic conductivity and related beach mobility. This is unlikely to be achieved through automated image analysis and so multi-method analyses are required, with further tests to refine and increase the accuracy of results.

Modelling the mixed beach dynamics was simplified in the thesis to the two LST formulations utilising two representative sediment sizes. Numerically modelling mixed beaches dynamics has had limited research, often utilising representative single D_{50} values validated against mixed beach observations (Bergillos et al. 2017a). Recent improvements in numerical models such as Xbeach-G have allowed multi-modal and spatially varying PSDs to be incorporated into simulations, though these are yet to be validated against field and laboratory measurements. The complexities of these mixed sediment interactions (such as conductivity and porosity effects) require further investment within existing models (McCall 2015) and their impact on morphologic change in mixed environments can then be better understood.

The research of X-band radar has historically focused on proving the technology as a viable and accurate option in observation. This thesis has established the system to be effective within coastal monitoring though the analysis and validation methods were substantial and required iterative processes to define the quality thresholds and analysis regimes. For the system to be more widely adopted outside of research, future effort needs to be focused on reducing the technical and time-consuming sensitivity testing, providing frameworks in which to more easily ground-truth the radar at a variety of sites with varying environmental conditions.

7.7 Conclusions

The overall aim of this research was to advance the understanding of the temporal and spatial variability of MSG beaches in response to driving factors, such as varying wave conditions and changes in nearshore bathymetry. The thesis has fulfilled this main aim through achieving the objectives outlined in Section 1.2 and provided new insights into MSG beach dynamics as well as the use of multi-method approaches to inform the characterisation of complex sites:

1. To advance the current knowledge on the spatial and temporal variability of MSG beach morphology and how these are influenced by wave conditions:

- The analysis in the thesis focused on five morphologically distinct transects over 2 km. Variability in these profiles' response made it difficult to directly link the widely recognised relationship between indicators of wave energy and shoreline change;
- The large differences in response and mobility in some cases were observed to be morphologically influenced by the presence and movement of gravel ridges from the lower to the upper beach. Where coastal engineering was present, the role of these gravel ridges was diminished, and beach mobility was enhanced, contributing to localised focused "erosion hot-spot";
- The variable behaviour along the shoreline appeared to be linked to the phase/state of the nearshore bathymetry, and the morphological features of the beachfront, which in turn appeared to be a result of the preceding, long-term wave conditions.

2. To assess MSG beach sediment characterisation and test whether there is an association between the calculated proportion of sand and beach mobility;

- Establishing sand proportion in mixed system field observations is highly complex and assumptions need to be taken when considering long-term monitoring in order to reduce the number of bulk samples required long- and cross-shore and at depth. The study utilised two distinct methodologies to characterise the sediment distributions and proportions through surface and depth analysis. The results showed that more accurate estimations of sand proportions require measurements at the surface and at depth, both in the intertidal and supratidal areas limiting the use of manual and automated image analysis methods;
- PSD variability at site is primarily based upon changes in the gravel fraction. The sand fraction is observed to vary little in the intertidal area (D_{50} change of less than 0.05 mm between all transects and samples), with change above the intertidal area attributed to over wash on berms and the influence of engineering works. Gravel sizing (D_{50}) at site ranges from very fine (3.39 mm) to very coarse (35.67 mm), with larger sized gravel occurring above MHWS for all transects (A-D) except E;
- A simple relationship between sand content and mixed beach mobility as hypothesised in laboratory experiments is difficult to identify in the field. Though correlation analysis established consistent relationships between sand proportion against wave conditions and profile change in two of the profiles (A and C). This was presumed to be due to significant sources of sediment available above MHWS resulting in erosion above MHWS, causing an increase of this sediment at the surface and through the depth of the profile.

3. To establish and apply a robust and cost-effective method to quantify changes in nearshore bathymetry, at temporal scales of weeks and seasons, using X-band radar technology, and quantify associated uncertainties;

- A robust quality control and analysis procedure was followed to produce a series of bathymetric maps over an 18-month X-band radar deployment. The data were validated against a concurrent multibeam survey in January 2017 which found the radar to be accurate to ± 0.50 m at a 40 x 40 m resolution (taken from a 120 x 120 m analysis window);
- During the deployment, two distinct nearshore states were observed within the radar data; these formations correlated with two similar states observed in multibeam surveys three years apart. However, in the case of the radar data, the formations were observed to form and be eroded over the period of 4-12 months;
- Limitations of the radar have been shown to be related to the wave climate (height and direction) and the spatial resolution pushing limits of the method. Nevertheless, the project has shown the technology to allow observation of changes and volume estimates exceeding the error of the instrument (± 0.5 m) in the temporal scales of months, and during ideal conditions (where morphologic change is large and wave height high) weeks.

4. To improve the understanding of the effects of bimodal wave directions on the temporal variability and interaction of MSG beaches with nearshore changes;

- The impact of the bimodal wave climate at site was not immediately apparent during initial profile analysis (objective 1), with the understanding of nearshore change provided by radar and multibeam analysis further conclusions could be drawn;
- The project and radar deployment allowed shoreline and nearshore analysis over a southerly dominated winter (DJF) 2015-2016 (20/70 N/S% for all waves and 1.65/8.24% for $H_s > 2.5$ m), which resulted in both the largest historic seaward extent of the Ness profiles (around Transect A) and a highly accreted nearshore Ness bar observed by the radar;
- A reduction in southerly dominance in the spring of 2017 resulted in the Ness bar formation eroding over the following 12 months. This was accompanied by landward migration of the Ness and lateral spreading of the accreted area alongshore (north and south).

5. To identify linkages between nearshore and shoreline changes, particularly the effects of antecedent nearshore bathymetry on longshore sediment transport;

- The changes in the nearshore were numerically modelled to understand the short- (single event), seasonal (DJF) and long-term (10-year model run) impacts of the two bathymetry phases on shoreline processes as well as assessing the recurrence of nearshore features through a nearshore sediment transport model. The results indicated a strong link to the variance in direction and magnitude of LST. The resulting patterns of LST convergence and divergence give an explanation to the variable alongshore beach response identified during the research;
- The numerical modelling showed strong variance in both transport rates and wave power at the shoreline between the two identified nearshore states. Wave power at the Thorpeness frontage was observed to be greatest during southerly events with the large variance of

power between the two models being attributed to the steepening of the nearshore profile between 2014 (CAM1) and 2017 (CAM2);

- The results establish the need for both beach and nearshore monitoring to understand changes occurring at the shoreline, particularly in sites consisting of multi-modal wave directions, complex nearshore geology and beach behaviour. It is recommended that any coastal processes modelling should quantify potential nearshore variability to establish if a number of distinct bathymetric meshes are required to accurately characterise coastline behaviour.

6. To utilise the evidenced-knowledge obtained in this research to inform coastal management decisions to mitigate the effects of erosion at Thorpeness;

- Historically the site has utilised 'shingle recycling' to redistribute sediment across the beach frontage. The area south of the Ness has been used as a source of gravel in the past. However, with the continued erosion of this area this method of nourishment cannot continue;
- The morphology of the Ness profile to the north of this region is highly dynamic below the elevation of ~3 m ODN, with migratory berms observed to move onshore, before being incorporated into the beach and increasing the volume of the profile. Above ~3 m a stable and semi-permanent (little change over ten years) berm is observed;
- LST modelling has shown the Ness is a consistent source of transport convergence over a ten-year analysis period in both identified nearshore states and for northerly and southerly dominated periods. This resilience of the Ness to directionally dominated winters and nearshore bathymetric changes indicates that shingle recycling may be a feasible approach to short-term and reactive beach nourishment at site. However, this is only feasible if the sediment is redistributed from the lower, active part of the profile, with minimal impact on the more stable (and ecologically important) areas of the Ness (above 3 m).

References

- Adams, J., 1979. Gravel Size Analysis from Photographs. *Journal of the Hydraulics Division*, 105 (10), 1247–1255.
- Adams, P. N., Inman, D. L., and Lovering, J. L., 2011. Effects of climate change and wave direction on longshore sediment transport patterns in Southern California. *Climatic Change*, 109 (SUPPL. 1), 211–228.
- Alpers, W. R. and Hasselmann, K., 1982. Spectral signal to clutter and thermal noise properties of ocean wave imaging synthetic aperture radars. *International Journal of Remote Sensing*, 3 (4), 423–446.
- Angnuureng, D. B., Almar, R., Senechal, N., Castelle, B., Addo, K. A., Marieu, V., and Ranasinghe, R., 2017. Shoreline resilience to individual storms and storm clusters on a meso-macrotidal barred beach. *Geomorphology*, 290 (April), 265–276.
- Antoniadis, C., 2012. Laboratory Investigation on Gravel and Mixed Beaches During an Oblique Wave Attack. *Journal of Coastal Development*, 16 (1), 68–83.
- Antoniadis, C., 2013. New Modified Equation of Longshore Current Velocity At the Breaking Point for Mixed and Gravel Beaches. *Journal of Coastal Development*, 16 (2), 121–134.
- Atkinson, J. and Esteves, L., 2018. Alongshore Variability in the Response of a Mixed Sand and Gravel Beach to Bimodal Wave Direction. *Geosciences*, 8 (12), 488.
- Atkinson, J., Esteves, L. S., Williams, J. W., McCann, D. L., and Bell, P. S., 2018. The Application of X-Band Radar for Characterization of Nearshore Dynamics on a Mixed Sand and Gravel Beach. *Journal of Coastal Research*, 85, 281–285.
- Austin, M., Scott, T., Brown, J., Brown, J., MacMahan, J., Masselink, G., and Russell, P., 2010. Temporal observations of rip current circulation on a macro-tidal beach. *Continental Shelf Research*, 30 (9), 1149–1165.
- Bamber, R. N., 1965. *Thorpeness: structure, topography and benthic communities. Consultancy report prepared for Nuclear Electric Plc.*
- Barnard, P. L., Hansen, J. E., and Erikson, L. H., 2012. Synthesis Study of an Erosion Hot Spot, Ocean Beach, California. *Journal of Coastal Research*, 283, 903–922.
- Battjes, J. A., 1974. Surf similarity. *Proceedings of of the 14th international conference on coastal engineering, ASCE*, (1), 466–480.
- Battjes, J. A. and Stive, M. J. F., 1985. Calibration and verification of a dissipation model for random breaking waves. *Journal of Geophysical Research*, 90 (C5), 9159.
- BEEMS, 2012. *Physical Science relating to possible Present and Future Coastal Geo-Hazards at the Sizewell New Nuclear Build Site. BEEMS Technical Report TR105, 190pp.*

- Bell, P. S., 1999. Shallow water bathymetry derived from an analysis of X-band marine radar images of waves. *Coastal Engineering*, 37 (3–4), 513–527.
- Bell, P. S., Bird, C. O., and Plater, A. J., 2016. A temporal waterline approach to mapping intertidal areas using X-band marine radar. *Coastal Engineering*, 107, 84–101.
- Bell, P. S. and Hessner, K., 2009. High resolution current & bathymetry determined by nautical X-Band radar in shallow waters, (August 2014).
- Bell, P. S. and Osler, J. C., 2011. Mapping bathymetry using X-band marine radar data recorded from a moving vessel. *Ocean Dynamics*, 61 (12), 2141–2156.
- Bell, P. S., Williams, J. J., Clark, S., Morris, B. D., and Vila-Concejo, A., 2004. Nested Radar Systems for Remote Coastal Observations. *J. Coastal Research: ICS 2004 Proceedings*, Special Is (39), 483–487.
- Bennett, W., Karunaratna, H., Mori, N., Reeve, D., Science, M., Url, E. C., Impacts, C. C., Climate, F. W., and Science, M., 2016. Climate Change Impacts on Future Wave Climate around the UK. *Journal of Marine Science and Engineering*, 4 (4), 78.
- Bergillos, R. J., Ortega-Sánchez, M., Masselink, G., and Losada, M. A., 2016. Morpho-sedimentary dynamics of a micro-tidal mixed sand and gravel beach, Playa Granada, southern Spain. *Marine Geology*, 379, 28–38.
- Bergillos, R. J., Masselink, G., and Ortega-Sánchez, M., 2017a. Coupling cross-shore and longshore sediment transport to model storm response along a mixed sand-gravel coast under varying wave directions. *Coastal Engineering*, 129 (September), 93–104.
- Bergillos, R. J., Masselink, G., McCall, R. T., and Ortega-Sánchez, M., 2017b. Modeling Overwash Vulnerability Along Mixed-Sand-Gravel Coasts With XBeach-G Case Study of Playa Granada, Southern Spain. *Coastal Engineering Proceedings*, 1 (35), 13.
- Bergillos, R. J., Rodríguez-Delgado, C., and Ortega-Sánchez, M., 2017c. Advances in management tools for modeling artificial nourishments in mixed beaches. *Journal of Marine Systems*, 172, 1–13.
- Bergsma, E. W. J., Conley, D. C., Davidson, M. A., and O'Hare, T. J., 2016. Video-based nearshore bathymetry estimation in macro-tidal environments. *Marine Geology*, 374, 31–41.
- Black, K., 2012. Using Sediment Tracers to Map Sediment Transport Pathways, 44, 1–18.
- Black, K. S., Athey, S., Wilson, P., and Evans, D., 2007. The use of particle tracking in sediment transport studies: a review. *Geological Society Special Publication*, 274 (1), 73–91.
- Bluck, B. J., 1967. Sedimentation of Beach Gravels: Examples from South Wales. *Journal of Sedimentary Petrology*, 37, 128–156.
- Borge, J. C. N., Hessner, K., and Reichert, K., 1999. Estimation of the Significant Wave Height With X-Band Nautical Radars. *Proc. 18th Int. Conf. Offshore Mech.*, (C), 1–8.

- Borge, J. C. N., Rodríguez Rodríguez, G., Hessner, K., and González, P. I., 2004. Inversion of marine radar images for surface wave analysis. *Journal of Atmospheric and Oceanic Technology*, 21 (8), 1291–1300.
- Bragg, W. H. and Bragg, W. L., 1913. The Reflection of X-rays by Crystals. *Proceedings of the Royal Society of London. Series A*, 88 (605), 428 LP – 438.
- Bramato, S., Ortega-Sánchez, M., Mans, C., Losada, M. A., 2012. Natural Recovery of a Mixed Sand and Gravel Beach after a Sequence of a Short Duration Storm and Moderate Sea States. *Journal of Coastal Research*, 28 (1), 89–101.
- British Crown and OceanWise, 2017. *Thorpeness and Nearshore*, 1:25,000 [online map], Using: EDINA Digimap Ordnance Survey Service, Created: March 2017. Available from: <https://digimap.edina.ac.uk/roam/map/chart> [accessed 01-Nov-2019].
- British Geological Survey (BGS), 1996. *BGS Geology: marine sediments 250k*.
- British Oceanographic Data Centre, 2018. *Download UK Tide Gauge Network data from BODC* [online].
- Brooks, S. M., 2010. *Coastal change in historic times - linking offshore bathymetric changes and cliff recession in Suffolk*.
- Brooks, S. M. and Spencer, T., 2012. Shoreline retreat and sediment release in response to accelerating sea level rise: Measuring and modelling cliffline dynamics on the Suffolk Coast, UK. *Global and Planetary Change*, 80–81, 165–179.
- Brooks, S. M. and Spencer, T., 2014. Importance of decadal scale variability in shoreline response: examples from soft rock cliffs, East Anglian coast, UK. *Journal of Coastal Conservation*, 18 (5), 581–593.
- Brooks, S. M., Spencer, T., and Christie, E. K., 2017. Storm impacts and shoreline recovery: Mechanisms and controls in the southern North Sea. *Geomorphology*, 283, 48–60.
- Browder, A. G. and McNinch, J. E., 2006. Linking framework geology and nearshore morphology: Correlation of paleo-channels with shore-oblique sandbars and gravel outcrops. *Marine Geology*, 231 (1–4), 141–162.
- Bunte, K. and Abt, S. R., 2001. Sampling Surface and Subsurface Particle-Size Distributions in Wadable Gravel- and Cobble-Bed Streams for Analyses in Sediment Transport, Hydraulics and Streambed Monitoring. *0*, 450.
- Burningham, H. and French, J., 2016. *Shoreline – Shoreface Dynamics on the Suffolk Coast*.
- Burningham, H. and French, J., 2017. Understanding coastal change using shoreline trend analysis supported by cluster-based segmentation. *Geomorphology*, 282, 131–149.
- Burvingt, O., Masselink, G., Russell, P., and Scott, T. M., 2017. Classification of beach response to extreme storms. *Geomorphology*, 295, 722–737.

- Buscombe, D., 2013. Transferable wavelet method for grain-size distribution from images of sediment surfaces and thin sections, and other natural granular patterns. *Sedimentology*, 60 (7), 1709–1732.
- Buscombe, D. and Masselink, G., 2006. Concepts in gravel beach dynamics. *Earth-Science Reviews*, 79 (1–2), 33–52.
- Buscombe, D. and Masselink, G., 2009. Grain-size information from the statistical properties of digital images of sediment, 421–438.
- Butler, J. B. and Place, D., 2001. Automated extraction of grain-size data from gravel surfaces using digital image processing Acquisition automatique des données de granulométrie des surfaces de gravier par un procédé d' imagerie numérique. *Journal of Hydraulic Research*, 39 (4), 1–11.
- Cancino-Solórzano, Y., Gutiérrez-Trashorras, A. J., and Xiberta-Bernat, J., 2010. Analytical methods for wind persistence: Their application in assessing the best site for a wind farm in the State of Veracruz, Mexico. *Renewable Energy*, 35 (12), 2844–2852.
- Carr, A. P., 1979. *Sizewell-Dunwich Banks field Study, Long-term changes in the coastline and offshore banks*.
- Carr, A. P., 1981. Evidence for the sediment circulation along the coast of East Anglia. *Marine Geology*, 40 (3), M9–M22.
- Carter, R. W. G. G., Orford, J. D., Forbes, D. L., and Taylor, R. B., 1990. Morphosedimentary development of drumlin-flank barriers with rapidly rising sea level, Story Head, Nova Scotia. *Sedimentary Geology*, 69 (1), 117–138.
- Chappell, J. and Eliot, I. G., 1979. Surf-beach dynamics in time and space — An Australian case study, and elements of a predictive model. *Marine Geology*, 32 (3), 231–250.
- Cheng, Z. and Liu, H., 2015. Digital grain-size analysis based on autocorrelation algorithm. *Sedimentary Geology*, 327, 21–31.
- Ciavola, P., Castiglione, E., and Ferrara, U., 2009. Sediment dynamics of mixed sand and gravel beaches at short time- scales. *Journal of Coastal Research*, 2009 (56), 1751–1755.
- Coastal Engineering Research Center, 1984. *Shore Protection Manual - Volume 1*. Department of the Army.
- Coates, T. T. and Hawkes, P. J., 1998. Beach Recharge Design and Bi-modal Wave Spectra. *Coastal Engineering Proceedings*, 1, 3036–3045.
- Cooper, J. A. G. and Navas, F., 2004. Natural bathymetric change as a control on century-scale shoreline behavior. *Geology*, 32 (6), 513.
- Curtiss, G. M., Osborne, P. D., and Horner-Devine, A. R., 2009. Seasonal patterns of coarse sediment transport on a mixed sand and gravel beach due to vessel wakes, wind waves, and tidal currents. *Marine Geology*, 259 (1–4), 73–85.

- Davidson-Arnott, R. G. D. and Greenwood, B., 2003. Waves and sediment transport in the nearshore zone. *In: Coastal Zones and Estuaries*. 43–60.
- Davidson, M. A., Van Koningsveld, M., de Kruif, A., Rawson, J., Holman, R. A., Lamberti, A., Medina, R., Kroon, A., and Aarninkhof, S., 2007. The CoastView project: Developing video-derived Coastal State Indicators in support of coastal zone management. *Coastal Engineering*, 54 (6–7), 463–475.
- Davidson, M. A., Splinter, K. D., and Turner, I. L., 2013. A simple equilibrium model for predicting shoreline change. *Coastal Engineering*, 73, 191–202.
- Dawe, I. N., 2001. Sediment Patterns on a Mixed Sand and Gravel Beach, Kaikoura, New Zealand. *Journal of Coastal Research*, 19 (Special Issue 34 (ICS 2000 New Zealand)), 267–277.
- DEFRA, 2003. *Development of predictive tools and design guidance for mixed beaches -FD1901 1*. Research Policy.
- Dickson, M. E., Kench, P. S., and Kantor, M. S., 2011. Longshore transport of cobbles on a mixed sand and gravel beach, southern Hawke Bay, New Zealand. *Marine Geology*, 287 (1–4), 31–42.
- Dissanayake, P., Brown, J., Wisse, P., and Karunaratna, H., 2015. Effects of storm clustering on beach/dune evolution. *Marine Geology*, 370, 63–75.
- van Dongeren, A., Plant, N., Cohen, A., Roelvink, D., Haller, M. C., and Catalán, P., 2008. Beach Wizard: Nearshore bathymetry estimation through assimilation of model computations and remote observations. *Coastal Engineering*, 55 (12), 1016–1027.
- Dornbusch, U., 2017. Design requirement for mixed sand and gravel beach defences under scenarios of sea level rise. *Coastal Engineering*, 124 (February), 12–24.
- Dornbusch, U., Williams, R., and Moses, C., 2005. Beach Materials Properties; BAR Phase 1, Science Report, (February 2003), 1–25.
- Duncan, R., 1964. Effect of water table and tide cycle on swash-backwash sediment distribution and beach profile development. *Marine Geology*, 2, 186–197.
- Dunkerley, D. L., 1994. Discussion: Bulk sampling of coarse clastic sediments for particle-size analysis. *Earth Surface Processes and Landforms*, 19 (3), 255–261.
- Eikaas, H. S. and Hemmingsen, M. A., 2006. A GIS approach to model sediment reduction susceptibility of mixed sand and gravel beaches. *Environmental Management*, 37 (6), 816–825.
- Elko, N., Feddersen, F., Foster, D., Hapke, C., Mcninch, J., Mulligan, R., Özkan-haller, H. T., Plant, N., Raubenheimer, B., Elko, N., Feddersen, F., Foster, D., Hapke, C., Mcninch, J., Mulligan, R., Özkan-haller, H. T., Plant, N., and Raubenheimer, B., 2014. *The future of nearshore processes research Edited by the future of nearshore processes research*.
- Elsner, P., Horn, D. P., Dornbusch, U., Thomas, I., and Amos, D. A. N., 2015. Monitoring Mixed Sand and Gravel Beaches Using Unmanned Aerial Systems. *In: Coastal sediments 2015*. 1–13.

- Environment Agency, 2010. *Coastal Morphology Report-Southwold to Benacre Denes (Suffolk) - RP016/S/2010*.
- Environment Agency, 2011. *Coastal Morphology Report Thorpeness (Phase 1), RP024/S/2011*.
- Ernstsen, V. B., Noormets, R., Hebbeln, D., Bartholomä, A., and Flemming, B. W., 2006. Precision of high-resolution multibeam echo sounding coupled with high-accuracy positioning in a shallow water coastal environment. *Geo-Marine Letters*, 26 (3), 141–149.
- Esteves, L. S., Brown, J. M., Williams, J. J., and Lymbery, G., 2012. Quantifying thresholds for significant dune erosion along the Sefton Coast, Northwest England. *Geomorphology*, 143–144 (MARCH 2012), 52–61.
- Esteves, L. S., Williams, J. J., and Bell, P. S., 2007. Assessing Nearshore Bar Movements during Storms Using Time-Averaged X-Band Radar Images. *In: Coastal Sediments '07*. Reston, VA: American Society of Civil Engineers, 1886–1899.
- Feld, G., Randell, D., Wu, Y., Ewans, K., and Jonathan, P., 2015. Estimation of Storm Peak and Intrastorm Directional–Seasonal Design Conditions in the North Sea. *Journal of Offshore Mechanics and Arctic Engineering*, 137 (2), 021102.
- Fisher, N. I. and Lee, A. J., 1994. Time Series Analysis of Circular Data. *Journal of the Royal Statistical Society. Series B (Methodological)*, 56 (2), 327–339.
- Folk, R. L. and Ward, W. C., 1957. Brazos River bar [Texas]; a study in the significance of grain size parameters. *Journal of Sedimentary Research*, 27 (1), 3–26.
- Forbes, D. L., Orford, J. D., Carter, R. W. G., Shaw, J., and Jennings, S. C., 1995. Morphodynamic evolution, self-organisation, and instability of coarse-clastic barriers on paraglacial coasts. *Marine Geology*, 126 (1–4), 63–85.
- Franzke, C. and Woollings, T., 2011. On the Persistence and Predictability Properties of North Atlantic Climate Variability. *Journal of Climate*, 24 (2), 466–472.
- Fugro Geos, 2001. *Wind and wave frequency distributions for sites around the British Isles: 2001/030*.
- Gomes, M., Santos, L., Pinho, J. L., and do Carmo, J. S. A., 2018. Hazard Assessment of Storm Events for the Portuguese Northern Coast. *Geosciences*, 8 (5), 178.
- H.R Wallingford, 2010. *Sizewell Power Station Extreme Sea Level Studies. Joint Probability of Waves and Sea Levels and Structure Response. Technical Note 01. Report to EDF Energy*.
- Harley, M. D., Turner, I. L., Kinsela, M. A., Middleton, J. H., Mumford, P. J., Splinter, K. D., Phillips, M. S., Simmons, J. A., Hanslow, D. J., and Short, A. D., 2017. Extreme coastal erosion enhanced by anomalous extratropical storm wave direction. *Scientific Reports*, 7 (1), 1–9.
- Hegermiller, C. A., Rueda, A., Erikson, L. H., Barnard, P. L., Antolinez, J. A. A., and Mendez, F. J., 2017. Controls of Multimodal Wave Conditions in a Complex Coastal Setting. *Geophysical*

Research Letters, 44 (24), 12,315-12,323.

- Hequette, A. and Aernouts, D., 2010. The influence of nearshore sand bank dynamics on shoreline evolution in a macrotidal coastal environment, Calais, northern France. *Continental Shelf Research*, 30 (12), 1349–1361.
- Hequette, A., Ruz, M. H., Maspataud, A., and Sipka, V., 2009. Effects Of Nearshore Sand Bank And Associated Channel On Beach Hydrodynamics: Implications For Beach And Shoreline Evolution. *Journal of Coastal Research*, 2009 (56), 59–63.
- Hessner, K. and Bell, P. S., 2009. High resolution current & bathymetry determined by nautical X-Band radar in shallow waters. *Oceans 2009-Europe*, (June), 1–5.
- Hessner, K., Reichert, K., Borge, J. C. N., Stevens, C. L., and Smith, M. J., 2014. High-resolution X-Band radar measurements of currents, bathymetry and sea state in highly inhomogeneous coastal areas. *Ocean Dynamics*, 64 (7), 989–998.
- Hessner, K., Wallbridge, S., and Dolphin, T., 2015. Validation of areal wave and current measurements based on X-band radar. *Current, Waves and Turbulence Measurement (CWTM), 2015 IEEE/OES Eleventh*, 0–9.
- Hey, R. D. and Thorne, C. R., 1983. Accuracy of surface samples from gravel bed material. *Journal of Hydraulic Engineering*, 109 (6), 842–851.
- Hill, P. R., 1990. Coastal geology of the King Point area, Yukon Territory, Canada. *Marine Geology*, 91 (1–2), 93–111.
- Holland, K. T. and Elmore, P. A., 2008. A review of heterogeneous sediments in coastal environments. *Earth-Science Reviews*, 89 (3–4), 116–134.
- Holman, R. ., Lippmann, T. ., O’Neill, P. ., and Hathaway, K., 1991. Video estimation of subaerial beach profiles. *Marine Geology*, 97 (1–2), 225–231.
- Holman, R. A., Plant, N., and Holland, T., 2013. CBathy: A robust algorithm for estimating nearshore bathymetry. *Journal of Geophysical Research: Oceans*, 118 (5), 2595–2609.
- Holman, R. A. and Stanley, J., 2007. The history and technical capabilities of Argus. *Coastal Engineering*, 54 (6–7), 477–491.
- Honegger, D. A., Haller, M. C., and Holman, R. A., 2019. High-resolution bathymetry estimates via X-band marine radar: 1. beaches. *Coastal Engineering*, 149 (December 2018), 39–48.
- Horn, D. P. and Walton, S. M., 2007. Spatial and temporal variations of sediment size on a mixed sand and gravel beach. *Sedimentary Geology*, 202 (3), 509–528.
- Horsburgh, K. J. and Wilson, C., 2007. Tide-surge interaction and its role in the distribution of surge residuals in the North Sea. *Journal of Geophysical Research: Oceans*, 112 (8), 1–13.

- Ingle, J. C., ed., 1966. Chapter 1 Introduction. *In: The Movement of Beach Sand*. Elsevier, 1–13.
- Ivamy, M. C. and Kench, P. S., 2006. Hydrodynamics and morphological adjustment of a mixed sand and gravel beach, Torere, Bay of Plenty, New Zealand. *Marine Geology*, 228 (1–4), 137–152.
- Jackson, D., Cooper, A., and Del Río, L., 2005. Geological control of beach morphodynamic state. *Marine Geology*, 216, 297–314.
- Jamal, M. H., Simmonds, D. J., and Magar, V., 2014. Modelling gravel beach dynamics with XBeach. *Coastal Engineering*, 89, 20–29.
- Jennings, R. and Shulmeister, J., 2002. A field based classification scheme for gravel beaches. *Marine Geology*, 186 (3–4), 211–228.
- Kamphuis, J. W., 1991. Alongshore Sediment Transport Rate. *Journal of Waterway, Port, Coastal, and Ocean Engineering*, 117 (6), 624–640.
- Karunaratna, H., Pender, D., Ranasinghe, R., Short, A. D., and Reeve, D. E., 2014. The effects of storm clustering on beach profile variability. *Marine Geology*, 348, 103–112.
- Kellerhals, R. and Bray, D., 1971. Sampling Procedures for Coarse Fluvial Sediments. *Journal of the Hydraulics Division*, 97 (8), 1165–1180.
- Kirk, R. M., 1975. Aspects of Surf and Runup Processes on Mixed Sand and Gravel Beaches. *Geografiska Annaler: Series A, Physical Geography*, 57 (1–2), 117–133.
- Kirk, R. M., 1980. Mixed sand and gravel beaches: morphology, processes and sediments. *Progress in Physical Geography*, 4 (2), 189–210.
- Kirk, R. M., 1992. Experimental beach reconstruction-renourishment on mixed sand and gravel beaches, Washdyke Lagoon, South Canterbury, New Zealand. *Coastal Engineering*, 17 (3–4), 253–277.
- Kirkpatrick, L. H. and Green, A. N., 2018. Antecedent geologic control on nearshore morphological development: The wave dominated, high sediment supply shoreface of southern Namibia. *Marine Geology*, 403 (June), 34–47.
- Kobayashi, N., Cox, D. T., and Wurjanto, A., 1991. Permeability Effects on Irregular Wave Runup and Reflection. *Journal of Coastal Research*, 7 (1), 127–136.
- Kobayashi, N. and Wurjanto, A., 1993. Irregular Wave Interaction with Permeable Slopes. *In: Coastal Engineering 1992*. New York, NY: American Society of Civil Engineers, 1299–1312.
- Koçak, K., 2008. Practical ways of evaluating wind speed persistence. *Energy*, 33 (1), 65–70.
- Koçak, K., 2009. Examination of persistence properties of wind speed records using detrended fluctuation analysis. *Energy*, 34 (11), 1980–1985.
- Kuhnle, R. A., 1993. Incipient Motion of Sand-Gravel Sediment Mixtures. *Journal of Hydraulic Engineering*, 119 (12), 1400–1415.

- Kulkarni, C. D., Levoy, F., Monfort, O., and Miles, J., 2004. Morphological variations of a mixed sediment beachface (Teignmouth, UK). *Continental Shelf Research*, 24 (11), 1203–1218.
- Kuwashima, S. and Hogben, N., 1986. The estimation of wave height and wind speed persistence statistics from cumulative probability distributions. *Coastal Engineering*, 9 (6), 563–590.
- Lamb, 1991. *Historic Storms of the North Sea, British Isles and Northwest Europe*. 1st ed. Cambridge University Press.
- Van Lancker, V., Lanckneus, J., Hearn, S., Hoekstra, P., Levoy, F., Miles, J., Moerkerke, G., Monfort, O., and Whitehouse, R., 2004. Coastal and nearshore morphology, bedforms and sediment transport pathways at Teignmouth (UK). *Continental Shelf Research*, 24 (11), 1171–1202.
- Lees, B. J., 1977. *Edwards forbes cruise 1977 - Sizewell - Dunwich Bank Field Study*. Unpublished Manuscript.
- Lees, B. J., 1983. *Sizewell-Dunwich Banks Field Study*. I.O.S.
- Lenton, T. M., Dakos, V., Bathiany, S., and Scheffer, M., 2017. Observed trends in the magnitude and persistence of monthly temperature variability. *Scientific Reports*, 7 (1), 5940.
- Limber, P. W., Adams, P. N., and Murray, A. B., 2017. Modeling large-scale shoreline change caused by complex bathymetry in low-angle wave climates. *Marine Geology*, 383, 55–64.
- Long, P. E. and Zalasiewicz, J. A., 2011. The molluscan fauna of the Coralline Crag (Pliocene, Zanclean) at Raydon Hall, Suffolk, UK: Palaeoecological significance reassessed. *Palaeogeography, Palaeoclimatology, Palaeoecology*, 309 (1–2), 53–72.
- López de San Román-Blanco, B., Coates, T. T., Holmes, P., Chadwick, A. J., Bradbury, A., Baldock, T. E., Pedrozo-Acuña, A., Lawrence, J., and Grüne, J., 2006. Large scale experiments on gravel and mixed beaches: Experimental procedure, data documentation and initial results. *Coastal Engineering*, 53 (4), 349–362.
- López de San Román Blanco, B., 2003. Dynamics of gravel and mixed, sand and gravel beaches. PhD Thesis, Imperial College, University of London. *Unpublished PhD Thesis, Imperial College, University of London*.
- Lopez, G., Conley, D. C., and Greaves, D., 2016. Calibration, Validation, and Analysis of an Empirical Algorithm for the Retrieval of Wave Spectra from HF Radar Sea Echo. *Journal of Atmospheric and Oceanic Technology*, 33 (2), 245–261.
- López, I., Aragonés, L., Villacampa, Y., Compañ, P., Satorre, R., Compan, P., Satorre, R., López, I., Aragonés, L., Villacampa, Y., Compañ, P., and Satorre, R., 2015. Morphological classification of microtidal sand and gravel beaches. *Ocean Engineering*, 109 (November), 309–319.
- Loureiro, C., Ferreira, Ó., and Cooper, J. A. G., 2012. Geologically constrained morphological variability and boundary effects on embayed beaches. *Marine Geology*, 329–331 (June 2018), 1–15.

- Ludeno, G., Reale, F., Dentale, F., Carratelli, E. P., Natale, A., Soldovieri, F., and Serafino, F., 2015. An X-band radar system for bathymetry and wave field analysis in a harbour area. *Sensors (Switzerland)*, 15 (1), 1691–1707.
- Malvarez, G. C. and Cooper, J. A. G., 2000. A whole surf zone modelling approach as an aid to investigation of nearshore and coastal morphodynamics. *Journal of Coastal Research*, 16 (3), 800–815.
- Martin-Grandes, I., Simmonds, D. J., Karunarathna, H., Horrillo-Caraballo, J. M., and Reeve, D. E., 2017. Assessing the Variability of Longshore Transport Rate Coefficient on a Mixed Beach. *Coastal Dynamics*, (243), 642–653.
- Mason, T., 1997. Hydrodynamics and Sediment Transport on a Macro-Tidal, Mixed (Sand and Shingle) Beach. Unpubl. PhD thesis, Department of Oceanography, University of Southampton.
- Mason, T. and Coates, T. T., 2001. Sediment Transport Processes on Mixed Beaches: A Review for Shoreline Management. *Journal of Coastal Research*, 17 (3), 645–657.
- Mason, T. and Dhoop, T., 2018. *Occurrence of Bimodal Seas around the English Coastline - Channel Coast Observatory Technical Note TN 02*.
- Masselink, G., Austin, M., Scott, T. M., Poate, T., and Russell, P., 2014. Role of wave forcing, storms and NAO in outer bar dynamics on a high-energy, macro-tidal beach. *Geomorphology*, 226, 76–93.
- Matthew, W., Edward, M., and Robert, O., 2011. Photographic Techniques for Characterizing Streambed Particle Sizes. *Transactions of the American Fisheries Society*, 132 (3), 605–610.
- Matthews, E. R., 1983. Measurements of beach pebble attrition in Palliser Bay, southern North Island, New Zealand. *Sedimentology*, 30 (6), 787–799.
- McCall, R. T., 2015. Process-based modelling of storm impacts on gravel coasts. PhD Thesis. Plymouth University.
- McCall, R. T., Masselink, G., Poate, T. G., Roelvink, J. A., and Almeida, L. P., 2015. Modelling the morphodynamics of gravel beaches during storms with XBeach-G. *Coastal Engineering*, 103, 52–66.
- McCall, R. T., Masselink, G., Poate, T. G., Roelvink, J. A., Almeida, L. P., Davidson, M. A., and Russell, P. E., 2014. Modelling storm hydrodynamics on gravel beaches with XBeach-G. *Coastal Engineering*, 91, 231–250.
- McCave, I. N., 1978. Grain-size trends and transport along beaches: Example from eastern England. *Marine Geology*, 28 (1), M43–M51.
- McComb, P. and Black, K., 2005. Detailed Observations of Littoral Transport Using Artificial Sediment Tracer, in a High-Energy, Rocky Reef and Iron Sand Environment. *Journal of Coastal Research*, 358–373.

- McFarland, S., Whitcombe, L., and Collins, M., 1994. Recent shingle beach renourishment schemes in the UK: Some preliminary observations. *Ocean and Coastal Management*, 25 (2), 143–149.
- McLean, R. F., 1970. Variations in grain-size and sorting on two kaikoura beaches. *New Zealand Journal of Marine and Freshwater Research*, 4 (2), 141–164.
- McLean, R. F. and Kirk, R. M., 1969. Relationships between grain size, size-sorting, and foreshore slope on mixed sand - shingle beaches. *New Zealand Journal of Geology and Geophysics*, 12 (1), 138–155.
- McNinch, J. E., 2004. Geologic control in the nearshore: Shore-oblique sandbars and shoreline erosional hotspots, Mid-Atlantic Bight, USA. *Marine Geology*, 211 (1–2), 121–141.
- McSweeney, S. and Shulmeister, J., 2018. Variations in wave climate as a driver of decadal scale shoreline change at the Inskip Peninsula, southeast Queensland, Australia. *Estuarine, Coastal and Shelf Science*, 209 (March), 56–69.
- Miles, J. R. and Russell, P. E., 2004. Dynamics of a reflective beach with a low tide terrace. *Continental Shelf Research*, 24 (11), 1219–1247.
- Miller, I. M. and Warrick, J. A., 2012. Measuring sediment transport and bed disturbance with tracers on a mixed beach. *Marine Geology*, 299–302, 1–17.
- Miller, I. M., Warrick, J. A., and Morgan, C., 2011. Observations of coarse sediment movements on the mixed beach of the Elwha Delta, Washington. *Marine Geology*, 282 (3–4), 201–214.
- Neal, A., Pontee, Nigel, I., Pye, K., and Richards, J., 2002. Internal structure of mixed sand and gravel beach deposits revealed using ground-penetrating radar. *Sedimentology*, 49, 789–804.
- Nolan, T. J., Kirk, R. M., and Shulmeister, J., 1999. Beach cusp morphology on sand and mixed sand and gravel beaches, South Island, New Zealand. *Marine Geology*, 157 (3–4), 185–198.
- Ordnance Survey, 2017. *Thorpeness*, 1:5,000 [online map], Using: *EDINA Digimap Ordnance Survey Service*, Created: July 2019. Available from: <https://digimap.edina.ac.uk/roam/map/os> [accessed 01-Nov-2019].
- Orford, J. D., 1975. Discrimination of particle zonation on a pebble beach. *Sedimentology*, 22 (3), 441–463.
- Osborne, P. D., 2005. Transport of gravel and cobble on a mixed-sediment inner bank shoreline of a large inlet, Grays Harbor, Washington. *Marine Geology*, 224 (1–4), 145–156.
- Pedrozo-Acuña, A., Simmonds, D. J., Chadwick, A. J., and Silva, R., 2007. A numerical-empirical approach for evaluating morphodynamic processes on gravel and mixed sand-gravel beaches. *Marine Geology*, 241 (1–4), 1–18.
- Pedrozo-Acuña, A., Simmonds, D. J., Otta, A. K., and Chadwick, A. J., 2006. On the cross-shore profile change of gravel beaches. *Coastal Engineering*, 53 (4), 335–347.

- Pentney, R. M. and Dickson, M. E., 2012. Digital Grain Size Analysis of a Mixed Sand and Gravel Beach. *Journal of Coastal Research*, 28 (1), 196–201.
- Pethick, J., 2017. *Sizewell Power Stations Shore Defences: Annual Report 2016 For Magnox Ltd and EDF Energy*.
- Pile, J., 2003. Analysis of Coastal Change: Erosion and Sedimentation Along the Suffolk Coast Between Lowestoft and Bawdsey. PhD Thesis. University Of London. University of London.
- Pontee, N., Pye, K., and Blott, S. J., 2004. Morphodynamic Behaviour and Sedimentary Variation of Mixed Sand and Gravel Beaches, Suffolk, UK. *Journal of Coastal Research*, 20 (1), 256–276.
- Powell, K. A., 1989. The Dynamic Response of Shingle Beaches to Random Waves. In: *Coastal Engineering 1988*. New York, NY: American Society of Civil Engineers, 1763–1773.
- Pye, K. and Blott, S. J., 2006. Coastal Processes and Morphological Change in the Dunwich-Sizewell Area, Suffolk, UK. *Journal of Coastal Research*, 223 (3), 453–473.
- Quick, M. C. and Dyksterhuis, P., 1994. Cross-shore transport for beaches of mixed sand and gravel. In: *International Symposium: Waves-Physical and Numerical Modelling (Canadian Society of Civil Engineers)*. 1443–1452.
- Reichert, K., Hessner, K., Borge, J. C. N., and Dittmer, J., 1999. WaMoS II: A radar based wave and current monitoring system. *Isop '99 Proceedings Vol. 3*, 3 (May), 1–5.
- van Rijn, L. ., Walstra, D. J. ., Grasmeijer, B., Sutherland, J., Pan, S., and Sierra, J. ., 2003. The predictability of cross-shore bed evolution of sandy beaches at the time scale of storms and seasons using process-based Profile models. *Coastal Engineering*, 47 (3), 295–327.
- Van Rijn, L. C., 2014. A simple general expression for longshore transport of sand, gravel and shingle. *Coastal Engineering*, 90, 23–39.
- Ritter, J. R. and Helley, E. J., 1969. Optical methods for determining particle sizes of coarse sediment. *Techniques of Water-Resources Investigations of the United States Geological Survey*, 5 (3), 33.
- Roberts, T. M., Wang, P., and Puleo, J. A., 2013. Storm-driven cyclic beach morphodynamics of a mixed sand and gravel beach along the Mid-Atlantic Coast, USA. *Marine Geology*, 346, 403–421.
- Robinson, A. H. W., 1980. Erosion and accretion along part of the Suffolk coast of East Anglia, England. *Marine Geology*, 37, 133–146.
- Rodil, I. and Lastra, M., 2004. Environmental factors affecting benthic macrofauna along a gradient of intermediate sandy beaches in northern Spain. *Estuarine, Coastal and Shelf Science*, 61, 37–44.
- Roelvink, D., Reniers, A., van Dongeren, A., van Thiel de Vries, J., McCall, R. T., and Lescinski, J., 2009. Modelling storm impacts on beaches, dunes and barrier islands. *Coastal Engineering*, 56 (11), 1133–1152.

- Royal Haskoning, 2010. *Thorpeness Erosion Response Works. Stage 1 Report for Suffolk Coastal District Council, 9W2244/R/303906/*.
- Rubin, D. M., 2004. A Simple Autocorrelation Algorithm for Determining Grain Size from Digital Images of Sediment. *Journal of Sedimentary Research*, 74 (1), 160–165.
- Ruessink, B. G., Van Enckevort, I. M. J., and Kuriyama, Y., 2004. Non-linear principal component analysis of nearshore bathymetry. *Marine Geology*, 203 (1–2), 185–197.
- Ruiz-Martinez, G., Rivillas-Ospina, G. D., Mariño-Tapia, I., and Posada-Vanegas, G., 2016. SANDY: A Matlab tool to estimate the sediment size distribution from a sieve analysis. *Computers and Geosciences*, 92 (July), 104–116.
- Ruiz de Alegria-Arzaburu, A., Masselink, G., Alegria-arzaburu, A. R. De, and Masselink, G., 2010. Storm response and beach rotation on a gravel beach, Slapton Sands, U.K. *Marine Geology*, 278 (1–4), 77–99.
- Rutten, J., de Jong, S. M., and Ruessink, G., 2017. Accuracy of Nearshore Bathymetry Inverted From X-Band Radar and Optical Video Data. *IEEE Transactions on Geoscience and Remote Sensing*, 55 (2), 1106–1116.
- Schupp, C. A., McNinch, J. E., and List, J. H., 2006. Nearshore shore-oblique bars, gravel outcrops, and their correlation to shoreline change. *Marine Geology*, 233 (1–4), 63–79.
- Scott, T. M., Masselink, G., and Russell, P., 2011. Morphodynamic characteristics and classification of beaches in England and Wales. *Marine Geology*, 286 (1–4), 1–20.
- She, K., Horn, D. P., and Canning, P., 2006. Porosity and Hydraulic Conductivity of Mixed Sand-Gravel Sediment. *Flood and Coastal Risk Management, At York*, (April), 1–16.
- She, K., Horn, D. P., and Canning, P., 2007. *R&D Technical Report FD1923/TR: Influence of permeability on the performance of shingle and mixed beaches*.
- Short, A. D., 1979. Three Dimensional Beach-Stage Model. *The Journal of Geology*, 87 (5), 553–571.
- Short, A. D., 2006. Australian Beach Systems—Nature and Distribution. *Journal of Coastal Research*, 221 (1), 11–27.
- Sibson, R., 1981. *Interpolating Multivariate Data*. Chichester: John Wiley.
- Sime, L. C. and Ferguson, R. I., 2003. Information on Grain Sizes in Gravel-Bed Rivers by Automated Image Analysis. *Journal of Sedimentary Research*, 73 (4), 630–636.
- Single, M. B. and Hemmingsen, M., 2001. Mixed sand and gravel barrier beaches of South Canterbury, New Zealand. *Ecology and Geomorphology of Coastal Shingle*, 261–276.
- Smit, M. W. J., Aarninkhof, S. G. J., Wijnberg, K. M., Gonz?lez, M., Kingston, K. S., Southgate, H. N., Ruessink, B. G., Holman, R. A., Siegle, E., Davidson, M. A., and Medina, R., 2007. The role of

- video imagery in predicting daily to monthly coastal evolution. *Coastal Engineering*, 54 (6–7), 539–553.
- Smit, M. W. J., Reniers, A. J. H. M., Ruessink, B. G., and Roelvink, J. A., 2008. The morphological response of a nearshore double sandbar system to constant wave forcing. *Coastal Engineering*, 55 (10), 761–770.
- Smith, G. H. S., Nicholas, A. P., and Ferguson, R. I., 1997. Measuring and defining bimodal sediments: Problems and implications. *Water Resources Research*, 33 (5), 1179–1185.
- Spencer, T., Brooks, S. M., Evans, B. R., Tempest, J. A., and Möller, I., 2015. Southern North Sea storm surge event of 5 December 2013: Water levels, waves and coastal impacts. *Earth-Science Reviews*, 146 (December 2013), 120–145.
- Stark, N. and Hay, A. E., 2016. Pebble and cobble transport on a steep, mega-tidal, mixed sand and gravel beach. *Marine Geology*, 382, 210–223.
- Stark, N., Hay, A. E., Cheel, R., and Lake, C. B., 2014. The impact of particle shape on the angle of internal friction and the implications for sediment dynamics at a steep, mixed sand-gravel beach. *Earth Surface Dynamics*, 2 (2), 469–480.
- Stokes, C., 2015. Coastal Impacts in the Lee of a Wave Energy Site: Waves, Beach Morphology and Water-Users (Wave Hub, Cornwall, UK). *School of Marine Sciences and Engineering*, Doctor of, 275.
- Stokes, C., Davidson, M. A., and Russell, P., 2015. Observation and prediction of three-dimensional morphology at a high-energy macrotidal beach. *Geomorphology*, 243, 1–13.
- Turley, M. D., Bilotta, G. S., Arbocuite, R. P., Chadd, R. P., Extence, C. A., and Brazier, R. E., 2016. Quantifying Submerged Deposited Fine Sedimentes in Rivers and Streams Using Digital Image Analysis. *River Research and Applications*, 30 (2), 307–328.
- Villegas, J. F., Ochoa, G. V., and Chamorro, M. V., 2017. Statistical Analysis of Wind Power and Analytical Methods for Wind Persistence in Magdalena and Cesar Departments in Colombia. *Indian Journal of Science and Technology*, 10 (36), 1–09.
- Vogel, C. A., Pendergrass, W. R., Division, D., Ridge, O., Oceanic, T. N., Adminis-, A., and Turbulence, N. A., 2007. Using autocorrelation to evaluate persistence forecasts for discrete wind vector fields in the national capital region. *Seventh Symposium on the Urban Environment, American Meteorological Society*, P1.15 (Figure 2), 2–4.
- Waddell, E., 1976. Swash-groundwater profile interactions. *Society of Economic and Paleontological Mineralogists Special Publication*, 24 (1), 115–125.
- Wadey, M. P., Brown, J. M., Haigh, I. D., Dolphin, T., and Wisse, P., 2015a. Assessment and comparison of extreme sea levels and waves during the 2013/14 storm season in two UK coastal regions. *Natural Hazards and Earth System Sciences*, 15 (10), 2209–2225.

- Wadey, M. P., Haigh, I. D., Nicholls, R. J., Brown, J. M., Horsburgh, K., Carroll, B., Gallop, S. L., Mason, T., and Bradshaw, E., 2015b. A comparison of the 31 January–1 February 1953 and 5–6 December 2013 coastal flood events around the UK. *Frontiers in Marine Science*, 2 (February 1953).
- Warrick, J. A., Rubin, D. M., Ruggiero, P., Harney, J. N., Draut, A. E., and Buscombe, D., 2009. Cobble cam : grain-size measurements of sand to boulder from digital photographs and autocorrelation analyses †, 1821, 1811–1821.
- Van Wellen, E., Chadwick, A. J., and Mason, T., 2000. A review and assessment of longshore sediment transport equations for coarse-grained beaches. *Coastal Engineering*, 40 (3), 243–275.
- Wentworth, C. K., 1922. A Scale of Grade and Class Terms for Clastic Sediments. *The Journal of Geology*, 30 (5), 377–392.
- Wilcock, P. R., 1993. Critical Shear Stress of Natural Sediments. *Journal of Hydraulic Engineering*, 119 (4), 491–505.
- Wilcock, P. R., Kenworthy, S. T., and Crowe, J. C., 2001. Experimental study of the transport of mixed sand and gravel. *Water Resources Research*, 37 (12), 3349–3358.
- Williams, J. J., 2014. *Thorpeness Coastal Erosion Appraisal*. MottMacDonald.
- Williams, J. J. and Esteves, L. S., 2017. Guidance on Setup, Calibration, and Validation of Hydrodynamic, Wave, and Sediment Models for Shelf Seas and Estuaries. *Advances in Civil Engineering*, 2017, 1–25.
- Williams, J. J. and Herbert, L., 2015. *Thorpeness Coastal Protection Options Appraisal*. MottMacDonald.
- Wolman, M. G., 1954. A method of sampling coarse river-bed material. *Transactions, American Geophysical Union*, 35 (6), 951.
- Wright, L. D. and Short, A. D., 1984. Morphodynamic variability of surf zones and beaches: A synthesis. *Marine Geology*, 56 (1–4), 93–118.
- Wyatt, L. R., Green, J. J., Gurgel, K. W., Borge, J. C. N., Reichert, K., Hessner, K., Günther, H., Rosenthal, W., Saetra, O., and Reistad, M., 2003. Validation and intercomparisons of wave measurements and models during the EuroROSE experiments. *Coastal Engineering*, 48 (1), 1–28.
- Wylie, D. P., Hinton, B. B., Howland, M. R., and Lord, R. J., 1985. Autocorrelation of Wind Observations. *Monthly Weather Review*.
- Young, I. R., Rosenthal, W., and Ziemer, F., 1985. A three-dimensional analysis of marine radar images for the determination of ocean wave directionality and surface currents. *Journal of Geophysical Research: Oceans*, 90 (C1), 1049–1059.
- Yuzyk, T. R. and Winkler, T., 1991. *Procedures for bed-material sampling. Lesson Package No. 28*.

Environment Canada, Water Resources Branch, Sediment Survey Section, Ottawa, Canada,.

Zarkogiannis, S. D. D., Kontakiotis, G., Vousdoukas, M. I. I., Velegrakis, A. F. F., Collins, M. B. B., and Antonarakou, A., 2018. Scarping of artificially-nourished mixed sand and gravel beaches: Sedimentological characteristics of Hayling Island beach, Southern England. *Coastal Engineering*, 133 (December 2016), 1–12.

Zenkovich, V., 1967. *Processes of coastal development*. Edinburgh; London: Oliver & Boyd.

Zhang, S. lin, Wu, G. jian, Yang, X. guo, Jiang, W. hong, and Zhou, J. wen, 2018. Digital Image-based Identification Method for the Determination of the Particle Size Distribution of Dam Granular Material. *KSCE Journal of Civil Engineering*, 22 (8), 2820–2833.

Appendix A – Volume change error evaluation

When combining different datasets and comparing different surveys temporally for volume analysis (in this study EA monitoring and project beach profiles), it is important to assess whether differences in the methods of data collection do not compromise comparability and validity of results. Two sources of error were identified in the method: (1) the horizontal and vertical accuracy of the DGPS used in the surveys, which were at a maximum of ± 0.02 m and ± 0.05 m respectively during the earliest (2009) measurements by the EA (Environment Agency 2010); and (2) differences resulting from the number and spacing of measurements taken along each cross-shore transect between the EA data and the data obtained in this research.

The horizontal error is considered negligible on the assumption that differences in elevation within < 0.05 m radius from any point are minimal and will not have an effect on the overall outcome. The objective here is to provide an assessment of relative changes rather than a very accurate estimate of actual volume. The error resulting from the vertical accuracy of the instrument (± 0.05 m) was calculated based on the relative percentage of the area within the error band (equivalent to a layer of 0.10 m across the cross-shore profile) in relation to the total profile cross-shore area. The errors range from 4.51% to 8.94% of the overall profile area and are higher for areas $> \text{MHWS}$ (Table A.1). The magnitudes of measured changes are much larger than the maximum potential error, as illustrated for Transect D (Figure A.1), suggesting that the comparison of the different datasets does not compromise the analysis in the thesis.

Table A.1. Mean average potential error range and percentage of profile area this equates to.

	Potential Error Range (m ²)			Potential Error Range (%)		
	>MHWS	>MWL	>MLWS	>MHWS	>MWL	>MLWS
Transect A	7.07	8.21	10.15	6.99	4.51	4.57
Transect B	6.88	7.74	10.77	8.94	6.10	6.84
Transect C	6.11	7.24	10.25	6.31	4.75	6.08
Transect D	3.74	4.49	5.48	8.79	7.12	7.33
Transect E	4.09	4.96	6.87	7.83	5.27	5.18

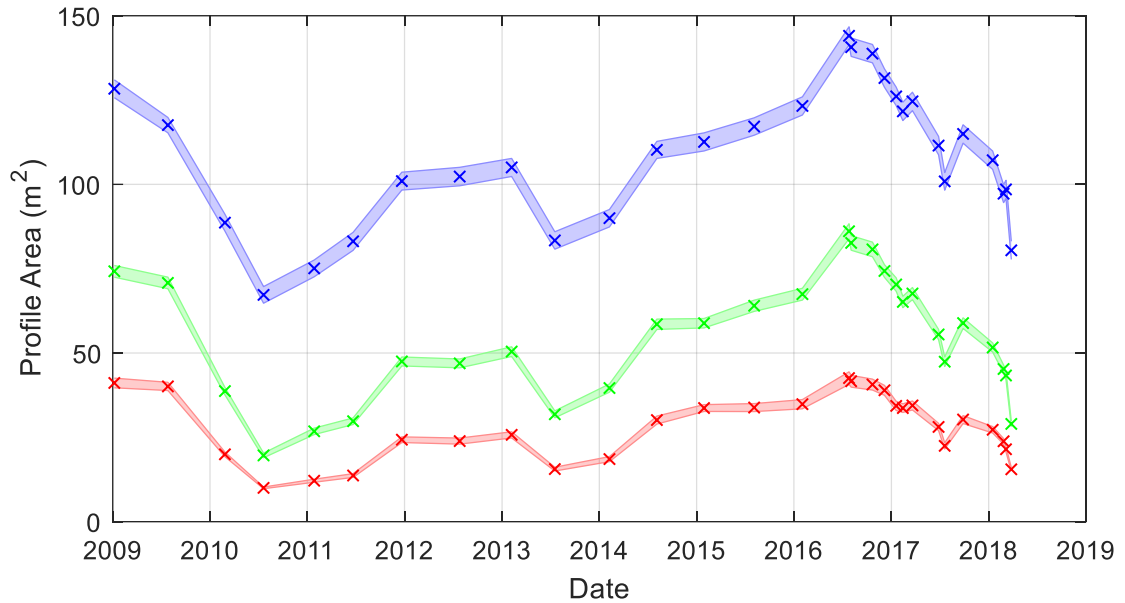


Figure A.1. Calculated profile areas for Transect D (>MLWS, >MWL, >MHWS) with error margins presented around points.

The beach profiles measured during this research recorded elevations every 2 s, using the automatic rover sampling method. The EA profiles were measured recording elevation at points of visible changes in slope/morphology. The average sampling distance was 2.9 m for the EA profiles and 0.43 m for the profiles collected in this project. The latter were then reproduced mimicking the coarser sampling of the EA profiles, the cross-sectional area was then recalculated. The differences between the original estimates and the recalculated areas provides a proxy to quantify the potential error due to sampling differences. Maximum differences were $\leq 2.67\%$ (Table A.2), except for Transect C above MWL (4.67%) and above MHWS (7.69%), an artefact of the resampling at the cliff top/face (Figure A.2), a difference unlikely to occur in real surveys aiming to capture key changes in morphology. In transects without a cliff face or steep slopes, errors are considerably smaller (Figure A.2), e.g. the maximum error in Transect A is 0.84% for the area above MLWS (Table A.2). The mean (absolute) error for all profiles was calculated as 0.62% which is acceptable and warrants comparability of the datasets.

Table A.2. Mean average potential error range and percentage of profile area this equates to.

		Area Difference (m ²)			Area Difference (%)		
		Min	Max	Mean	Min	Max	Mean
Transect A	>MHWS	0.03	0.72	0.22	0.03	0.71	0.21
	>MWL	0.06	0.70	0.22	0.04	0.45	0.13
	>MLWS	0.33	2.37	1.40	0.12	0.84	0.52
Transect B	>MHWS	0.02	0.31	0.11	0.05	0.87	0.36
	>MWL	0.05	0.25	0.11	0.09	0.50	0.19
	>MLWS	0.70	2.48	1.57	0.38	1.48	0.92
Transect C	>MHWS	0.05	3.78	1.25	0.09	7.69*	2.78*
	>MWL	0.14	3.80	1.26	0.16	4.67	1.68
	>MLWS	0.09	4.35	1.43	0.05	2.48	0.80
Transect D	>MHWS	0.01	0.51	0.16	0.09	1.80	0.57
	>MWL	0.01	0.51	0.20	0.01	0.93	0.40
	>MLWS	0.43	2.60	1.33	0.35	2.67	1.24
Transect E	>MHWS	0.01	0.49	0.25	0.03	0.98	0.52
	>MWL	0.05	0.45	0.24	0.06	0.54	0.28
	>MLWS	0.06	2.62	1.40	0.04	1.70	0.90

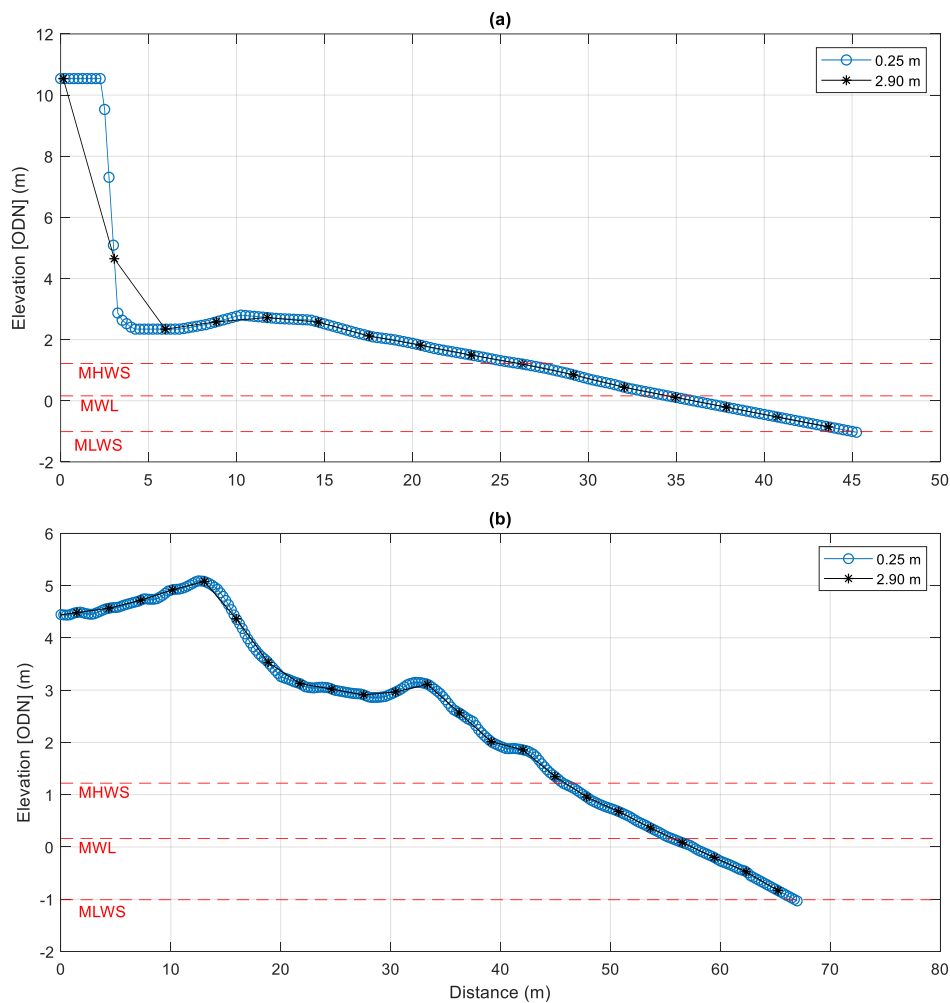


Figure A.2. Example subsampled profiles (07-Mar-2018) at (a) Transect C and (b) Transect A.

Appendix B – Supplementary sediment analysis tables and figures

Table B.1. Descriptive statistics of % of sand through surface and depth analysis at each Transect for all available surveys.

Transect	Proportion Sand Surface (%) >MLWS				Proportion Sand Depth (%) >MLWS			
	Min	Mean	Max	StDev	Min	Mean	Max	StDev
A	0.95	16.09	27.76	8.79	13.52	19.19	24.90	2.99
B	14.00	35.12	75.21	19.44	16.21	28.77	36.07	5.05
C	17.07	40.62	57.50	12.21	26.83	30.34	31.94	1.64
D	5.01	15.96	24.76	7.44	13.52	19.85	24.90	3.29
E	13.22	27.19	37.61	8.73	20.05	25.14	31.62	3.32

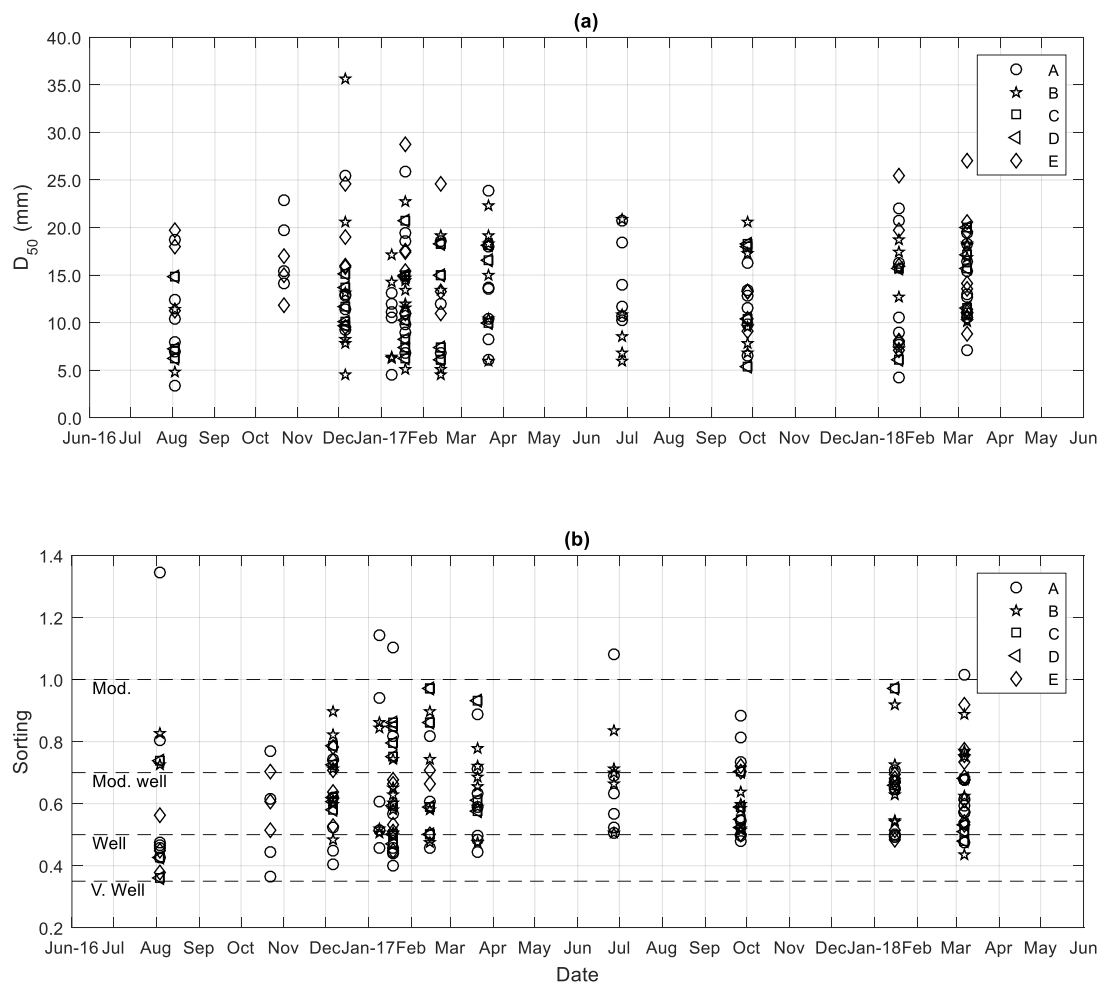


Figure B.1. Scatter-time series of gravel fraction (a) D50 and (b) sorting for all transects over the project period.

Table B.2. Gravel PSD statistics for samples above and MHWS.

Gravel>MHWS Transect	D ₅₀ (mm)				Sorting (σ)				Kurtosis (K_G)				Skewness (Sk_I)			
	Min	Mean	Max	StDev	Min	Mean	Max	StDev	Min	Mean	Max	StDev	Min	Mean	Max	StDev
A	3.39	13.75	25.88	5.25	0.37	0.60	1.14	0.17	0.7	1.04	1.52	0.16	-0.54	-0.02	0.16	0.13
B	5.15	13.40	22.76	5.23	0.44	0.64	0.89	0.12	0.73	1.01	1.28	0.13	-0.23	0.04	0.26	0.14
C	6.11	13.16	20.75	4.61	0.36	0.60	0.97	0.15	0.79	1.02	1.32	0.14	-0.22	0.04	0.18	0.10
D	4.02	14.85	24.30	5.30	0.41	0.57	0.85	0.10	0.82	1.02	1.34	0.13	-0.28	-0.02	0.14	0.10
E	7.05	15.07	28.73	5.76	0.38	0.62	0.92	0.12	0.79	1.05	1.39	0.14	-0.19	0.07	0.23	0.10

Gravel<MHWS Transect	D ₅₀ (mm)				Sorting (σ)				Kurtosis (K_G)				Skewness (Sk_I)			
	Min	Mean	Max	StDev	Min	Mean	Max	StDev	Min	Mean	Max	StDev	Min	Mean	Max	StDev
A	4.29	9.13	15.46	3.72	0.59	0.86	1.34	0.27	0.74	0.92	1.44	0.24	-0.16	-0.01	0.16	0.11
B	4.46	12.44	35.67	11.01	0.48	0.75	0.92	0.15	0.80	0.91	1.19	0.14	-0.4	-0.04	0.33	0.26
C	5.41	11.71	18.17	4.73	0.55	0.72	0.93	0.13	0.70	0.96	1.20	0.16	-0.39	-0.10	0.03	0.13
D	8.49	12.40	16.32	5.53	0.62	0.67	0.71	0.07	1.05	1.07	1.09	0.03	0.05	0.09	0.14	0.07
E	16.00	17.49	19.00	1.50	0.45	0.59	0.78	0.17	1.04	1.10	1.16	0.06	-0.09	0.14	0.32	0.21

Table B.3. Sand PSD statistics for samples above and below MHWS.

Sand Above MHWS Transect	D ₅₀ (mm)				Sorting (σ)				Kurtosis (K_G)				Skewness (Sk_I)			
	Min	Mean	Max	StDev	Min	Mean	Max	StDev	Min	Mean	Max	StDev	Min	Mean	Max	StDev
A	0.26	0.33	0.42	0.06	0.47	0.60	0.85	0.15	0.92	1.08	1.47	0.23	-0.05	0.07	0.30	0.14
B	0.32	0.39	0.44	0.04	0.46	0.58	0.75	0.10	0.94	1.00	1.09	0.05	-0.20	-0.04	0.05	0.09
C	0.21	0.26	0.32	0.08	0.43	0.47	0.51	0.06	0.93	0.94	0.96	0.03	-0.08	-0.01	0.06	0.10
D	0.33	0.39	0.48	0.06	0.46	0.56	0.75	0.13	0.95	0.98	1.04	0.04	-0.06	-0.02	0.04	0.04
E	-	-	-	-	-	-	-	-	-	-	-	-	-	-	-	-

Sand Below MHWS Transect	D ₅₀ (mm)				Sorting (σ)				Kurtosis (K_G)				Skewness (Sk_I)			
	Min	Mean	Max	StDev	Min	Mean	Max	StDev	Min	Mean	Max	StDev	Min	Mean	Max	StDev
A	0.30	0.34	0.40	0.05	0.44	0.49	0.56	0.06	0.84	0.91	1.00	0.09	-0.06	-0.03	-0.01	0.02
B	0.28	0.30	0.32	0.02	0.39	0.43	0.46	0.03	0.84	0.90	0.98	0.06	-0.08	0.00	0.05	0.06
C	0.30	0.32	0.37	0.03	0.41	0.43	0.46	0.02	0.85	0.91	1.05	0.10	-0.05	-0.01	0.04	0.04
D	0.31	0.31	0.31	0.00	0.43	0.44	0.45	0.01	0.85	0.87	0.90	0.03	-0.07	-0.05	-0.03	0.03
E	0.28	0.30	0.33	0.02	0.41	0.46	0.52	0.04	0.85	0.91	0.99	0.06	-0.07	-0.01	0.03	0.04

Appendix C – MIKE model supplementary information

C1 – HD validation

The model validation data used for the HD model comprised a local measurement of water level and predictions of current speed and direction from 5 Total Tide points. At locations across the model domain, water levels predicted by the HD model demonstrate good agreement with the validation data (Nash Sutcliffe Efficiency of 0.74, Figure C.1). The closest agreement between validation data and HD model predictions for current speed and direction are found at offshore locations (B and D, Figure C.2). Although closer to the shore at points N, A and Q, agreement is not as good, the model performance still meets criteria for coastal models defined by Williams & Esteves (2017) and can be attributed to: (a) changes in the nearshore bathymetry occurring after publication of the TotalTide data; and/or (b) limitations of the HD model. Nevertheless, agreement between HD model predictions and the validation data demonstrate two key features required of the model: (a) flow direction is reproduced well by the model, and (b) the maximum differences between the validation data and the predicted current speeds do not exceed 0.2 m s^{-1} showing the model is sufficiently accurate for the present investigations.

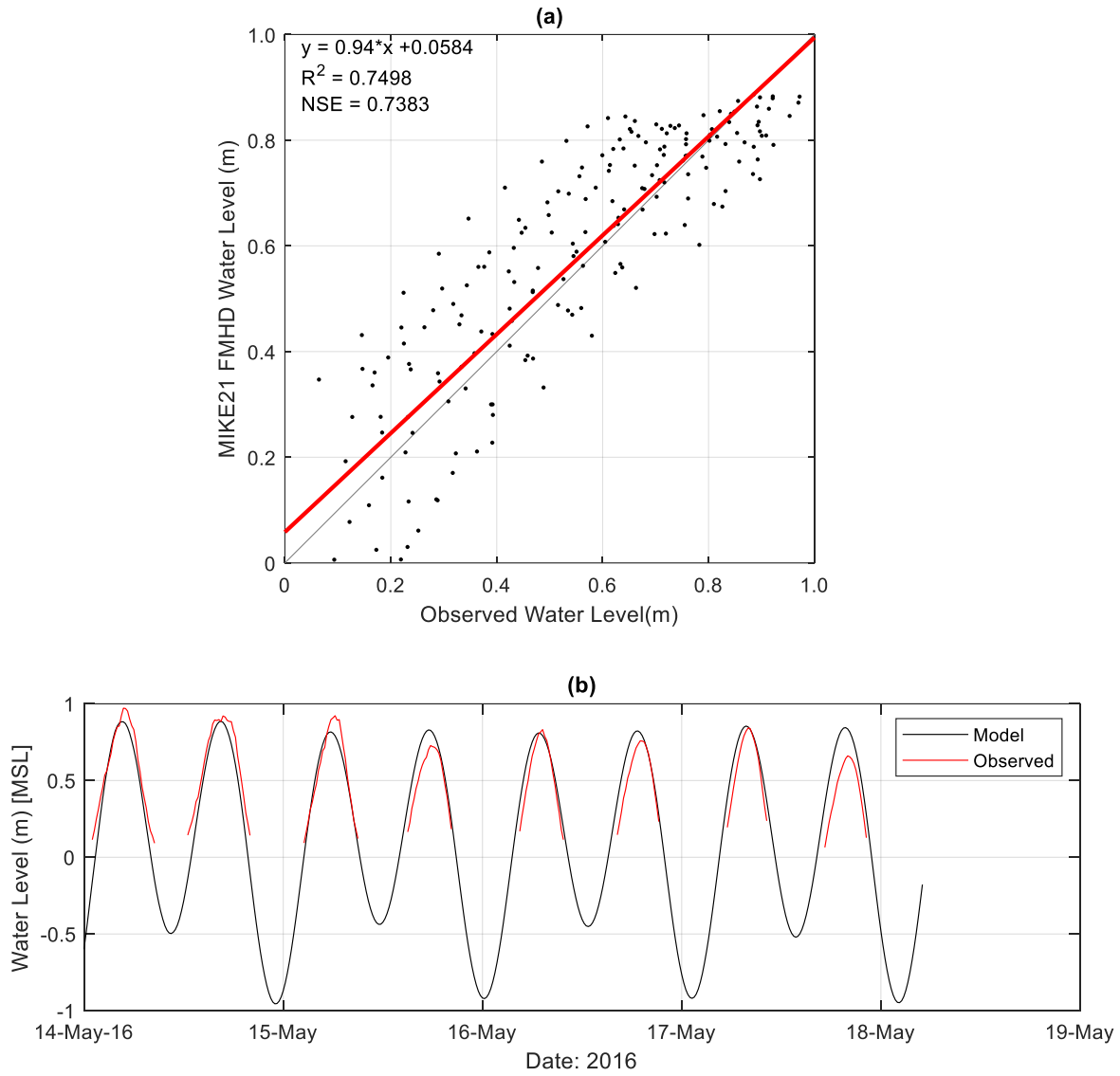


Figure C.1. (a) Scatter plot of modelled water level against Mike FMHD water level at the location of the deployed tide gauge between 14-May-2016 and 18-May-2016. (b) time series of water level observed by the pressure sensor and predicted modelled data (note that the gauge was deployed in a tidally influenced sluice and so only covers data from a height of approximately 0.1 m).

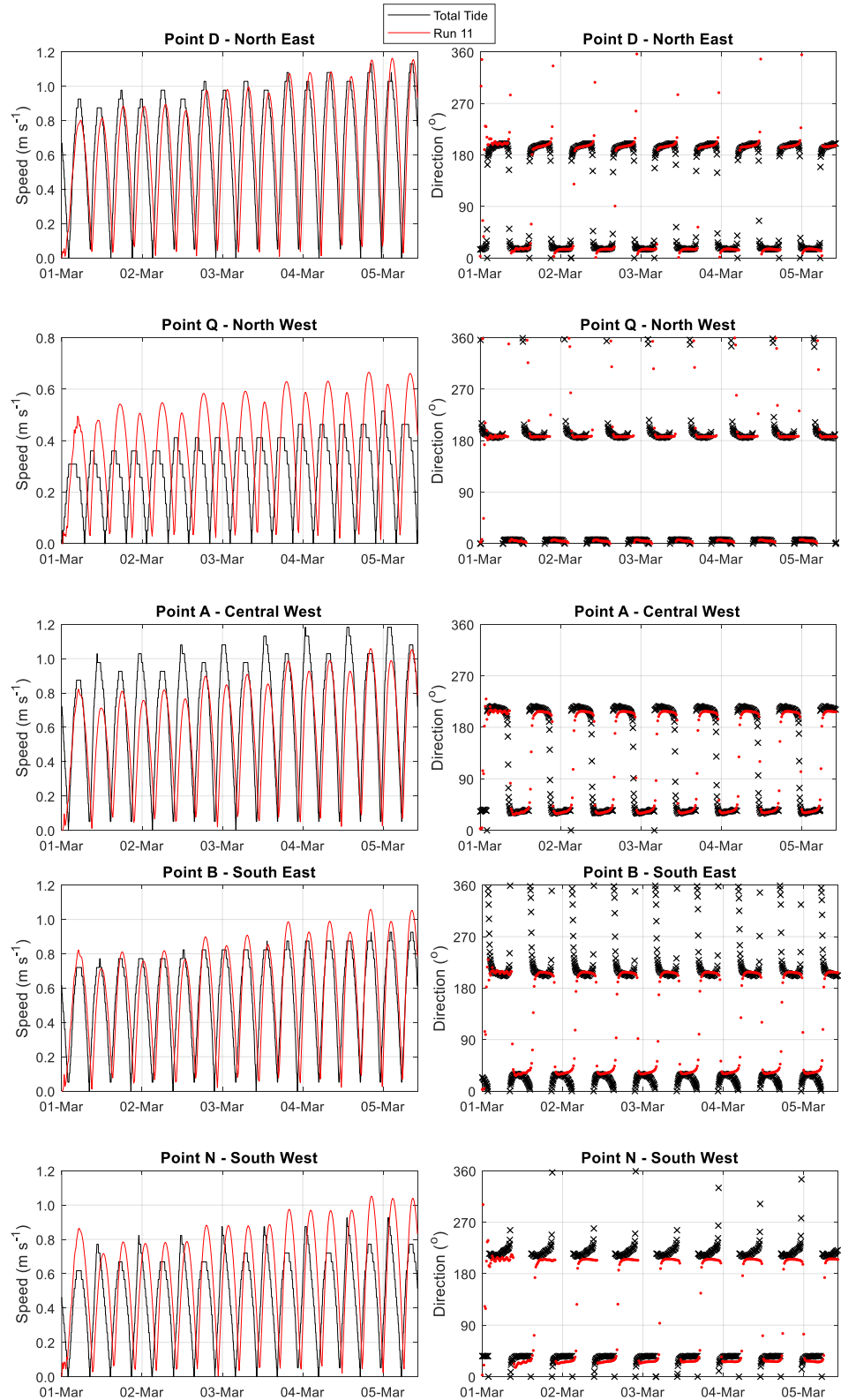


Figure C.2. Time-series of current magnitude (left column) and current direction (right column) for Total Tide points (D,Q, A, B and N) used in validation of the MIKE FMHD model.

C2 – SW model boundary Conditions

The MIKE FMSW model was driven along the offshore boundary by wave data from the NOAA WaveWatch III model. Adjustments were made to model parameters (primarily bed friction) to achieve the best possible agreement model predictions and wave buoy data from West Gabbard (eastern model boundary), Felixstowe (southern model boundary) and Lowestoft (northern model boundary) (see 6.2.1). The comparison between modelled and observed significant wave height (Figure C.3) and peak direction (Figure C.4) show strongest agreement with the West Gabbard buoy for both direction and wave height, with larger errors seen at the nearshore locations at Felixstowe and Lowestoft.

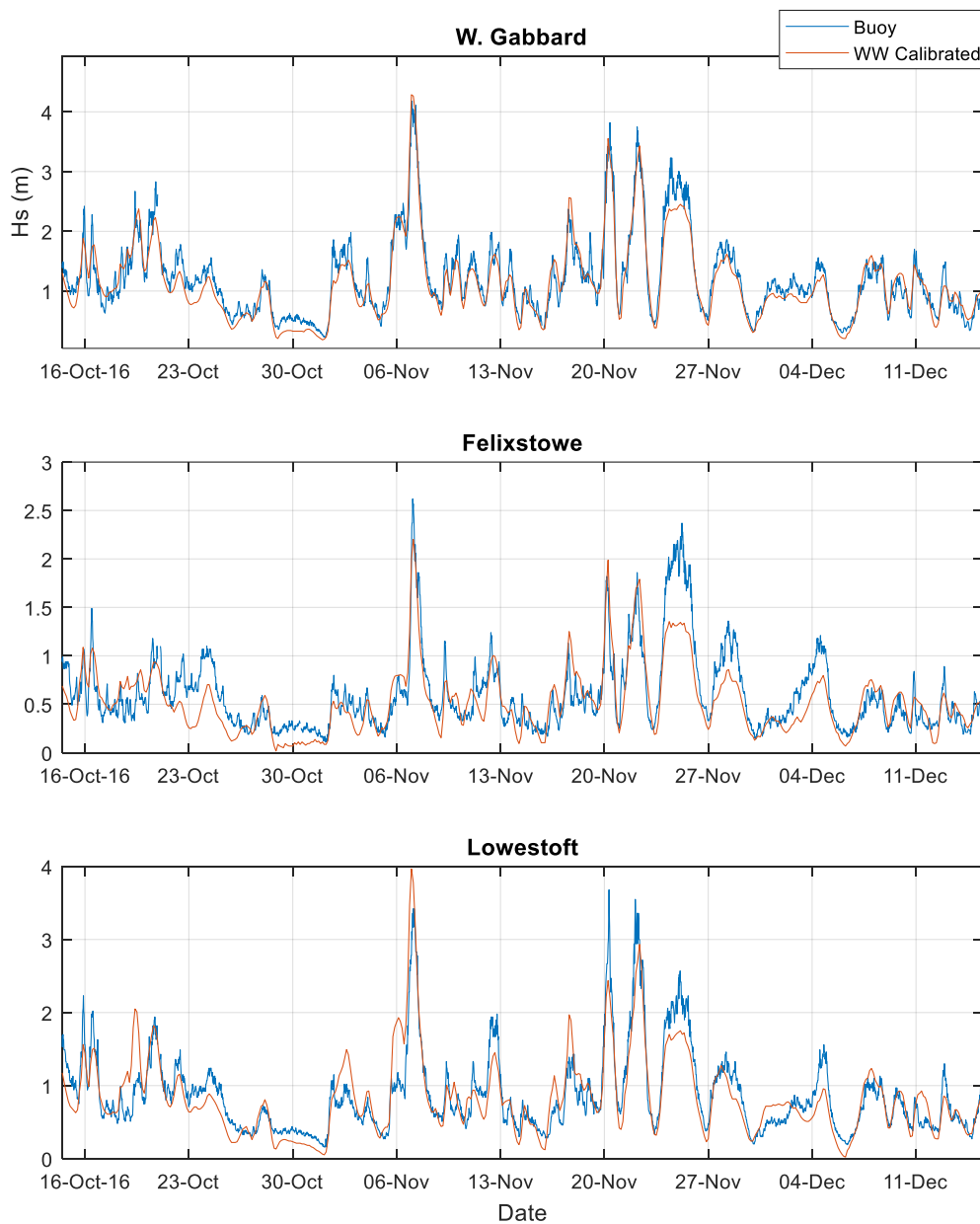


Figure C.3. Significant wave height (H_s) comparison between the calibrated NOAA WaveWatch III points used within the MIKE FMSW model and the nearest deployed wavebuoy. For West Gabbard (east boundary), Felixstowe (south boundary) and Lowestoft (north boundary).

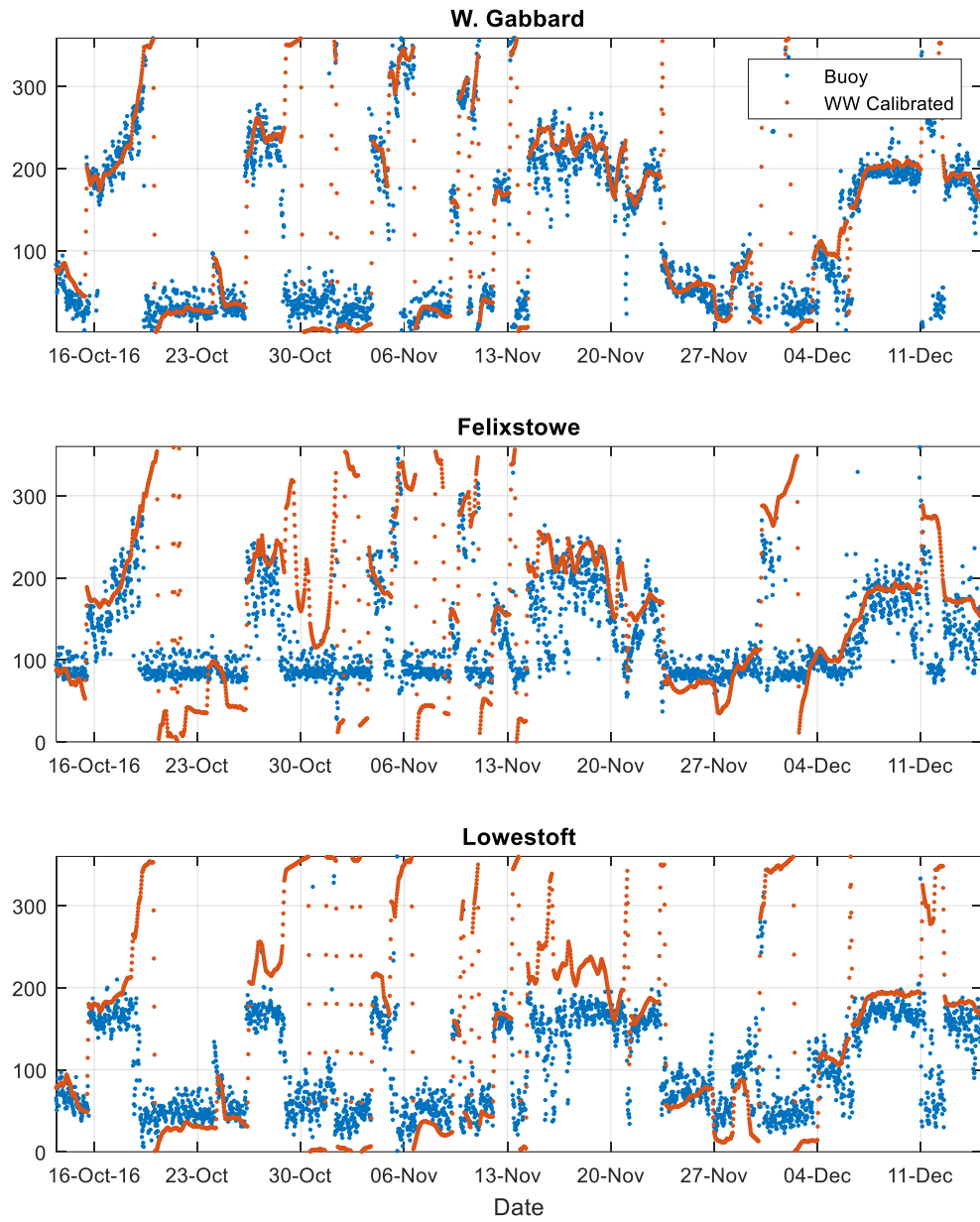


Figure C.4. Peak wave direction (Dir_p) comparison between the calibrated NOAA WaveWatch III points used within the MIKE FMSW model and the nearest deployed wavebuoy. For West Gabbard (east boundary), Felixstowe (south boundary) and Lowestoft (north boundary).

C3 – SW Validation

To meet the modelling objectives of the present study it is most important to predict as accurately as possible the wave conditions in the vicinity of Thorpeness. Through the MIKE FMSW calibration process this has been largely achieved and is demonstrated in Figure C.5 which shows a comparison between wave height measured by the nearshore Sizewell Waverider buoy and the MIKE 21 FMSW model predictions for a one month period from 01-Dec-2017 to 31-December-2017. While visually this shows that the MIKE 21 SW model tends to slightly underestimate nearshore wave heights at this location, a Nash-Sutcliffe Efficiency score of 0.66 (Figure C.6) indicates the model is performing reasonably well. Similar good model performance is also achieved for wave direction and wave period.

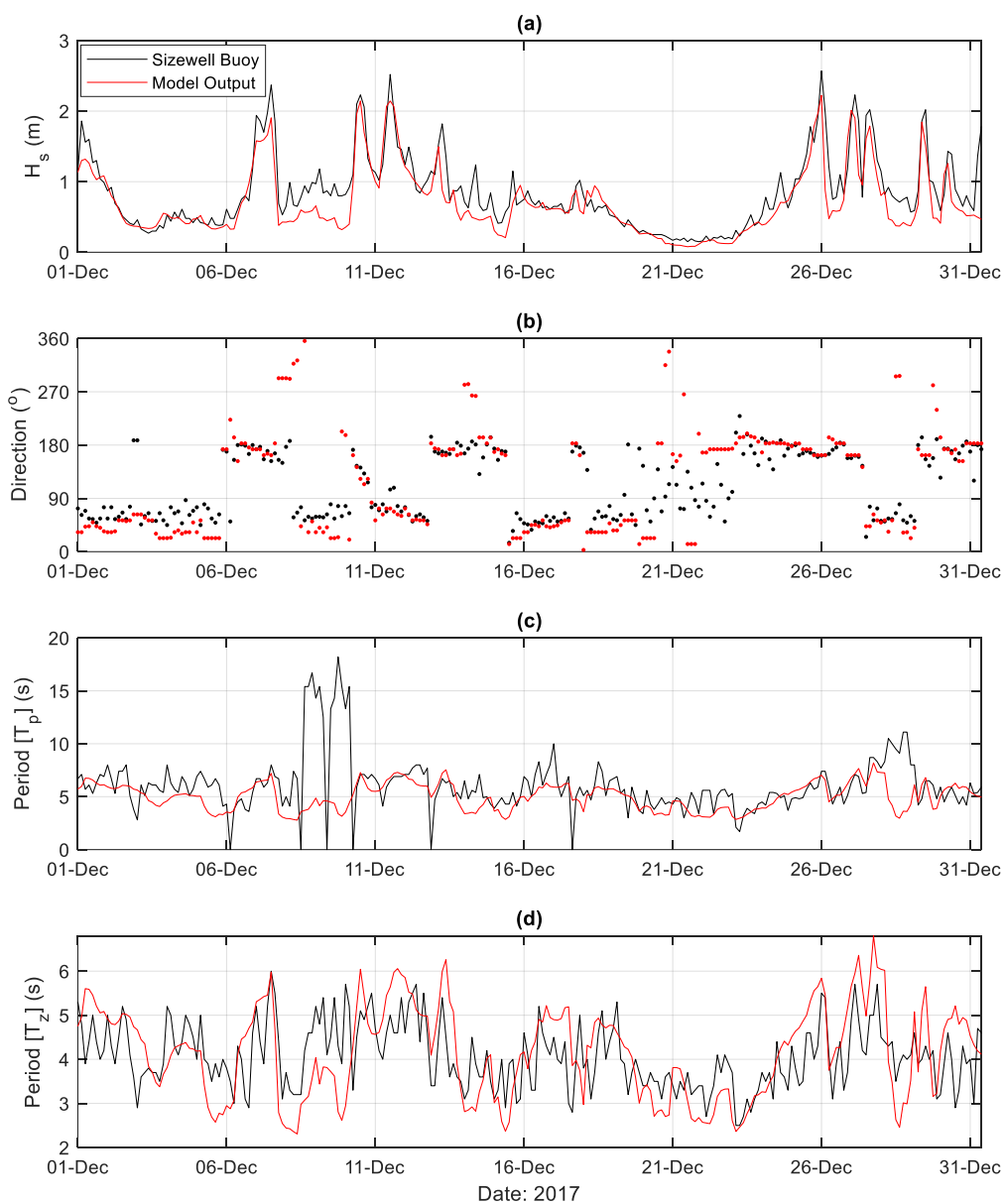


Figure C.5. Time-series plots showing a comparison between MIKE FMSW model predictions and Sizewell buoy data during December 2017 for: (a) significant wave height (H_s); (b) peak wave direction (Dir_p); (c) peak wave period (T_p); and (d) mean wave period (T_z).

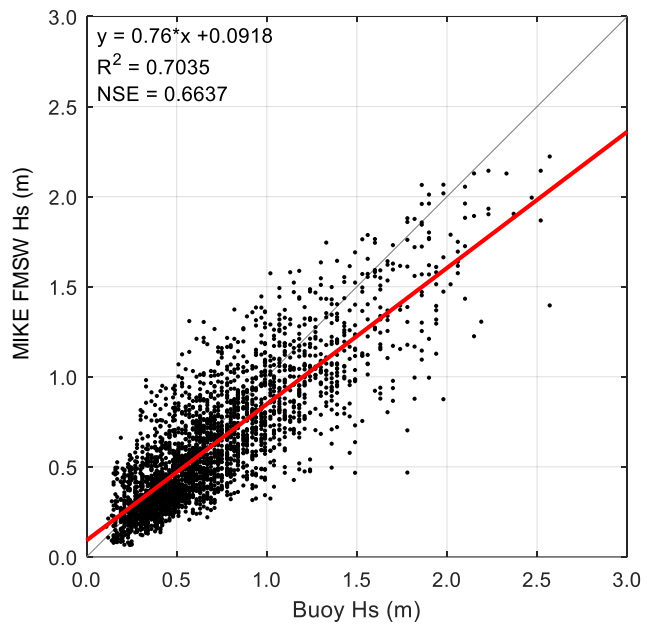


Figure C.6. MIKE 21 FMSW model: Scatter plot between Sizewell buoy and predicted significant wave height for the period 01-Jan-2017 to 31-Dec-2017. The Nash-Sutcliffe Efficiency score of 0.66 indicates acceptable MIKE FMSW model performance for the purposes of the present modelling studies.

Appendix D – Published Materials

Materials published as first author during the project period consist of:

Atkinson, J., Esteves, L. S., Williams, J. J., Bell, P. S., and McCann, D., 2017. Monitoring Nearshore Processes and Understanding Significant Coastal Change Using X-Band Radar. *Coastal Dynamics*, 3 (In: Coastal Dynamics 2017), 1506–1517.

Atkinson, J., Esteves, L. S., Williams, J. W., McCann, D. L., and Bell, P. S., 2018. The Application of X-Band Radar for Characterization of Nearshore Dynamics on a Mixed Sand and Gravel Beach. *Journal of Coastal Research*, 85, 281–285.

Atkinson, J. and Esteves, L., 2018. Alongshore Variability in the Response of a Mixed Sand and Gravel Beach to Bimodal Wave Direction. *Geosciences*, 8 (12), 488.